Doctoral theses at NTNU, 2020:364

Magnus Aashammer Gjennestad

Modelling of two-phase equilibrium, stability and steady-state flow in porous media

Doctoral thesis

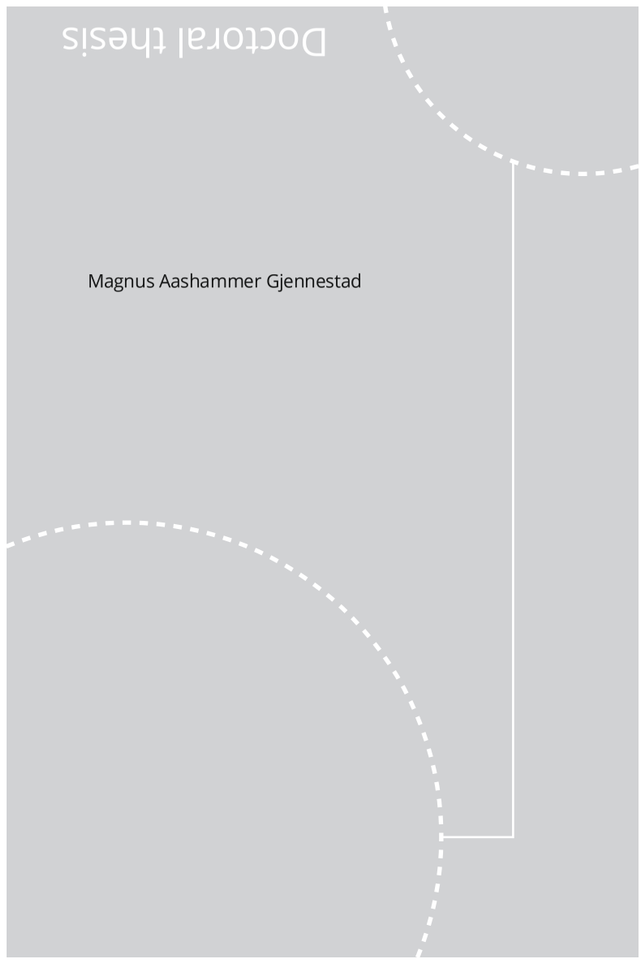

Magnus Aashammer Gjennestad

ISBN 978-82-326-5074-3 (printed ver.)
ISBN 978-82-326-5075-0 (electronic ver.)
ISSN 1503-8181

NTNU
Norwegian University of
Science and Technology

NTNU
Norwegian University of Science and Technology
Thesis for the Degree of
Philosophiae Doctor
Faculty of Natural Sciences
Department of Physics

Doctoral theses at NTNU, 2020:364

NTNU
Norwegian University of
Science and Technology

Magnus Aashammer Gjennestad

Modelling of two-phase equilibrium, stability and steady-state flow in porous media

Thesis for the Degree of Philosophiae Doctor

Trondheim, November 2020

Norwegian University of Science and Technology
Faculty of Natural Sciences
Department of Physics

NTNU
Norwegian University of
Science and Technology

NTNU
Norwegian University of Science and Technology

Thesis for the Degree of Philosophiae Doctor

Faculty of Natural Sciences
Department of Physics

ISBN 978-82-326-5074-3 (printed ver.)
ISBN 978-82-326-5075-0 (electronic ver.)
ISSN 1503-8181

Doctoral theses at NTNU, 2020:364

Printed by NTNU Grafisk senter

Abstract

This thesis concerns fundamental aspects of coexistence and flow of two fluid phases within porous media. Specifically, the focus is on thermodynamic stability and equilibrium on the scale of a single pore and on macroscopic steady-state properties of immiscible two-phase flow. In this work, macroscopic steady-state properties refers to time-averages of time-dependent quantities that describe flow through a volume element consisting of many pores.

Capillary models are derived for free and adsorbed droplets and bubbles, and thick films in a pore. The thermodynamic stability of these structures in a specific pore geometry is mapped out and the effect of pore size and the pore being open or closed w.r.t. exchange of particles with the surroundings is explored. Equilibrium structures are found. When structures are unstable, they are found to be unstable against perturbations that can be classified as either translation or as condensation/evaporation. Furthermore, stability of thin films and droplets on a flat solid surface is considered. It is found that the often-cited criterion for stability of a flat film, which states that the flat films are stable when the derivative of disjoining pressure w.r.t. film thickness is negative, applies in open systems. In closed systems, however, stability is governed by mechanical instabilities that require a large enough substrate size to render the film unstable. Unstable droplets in both the open and closed containers are found to represent saddle points and activation barriers in their respective energy landscapes.

Numerical methods are presented that enable stable and fast time integration of a pore network model. These eliminate previous problems with numerical instabilities observed at low capillary numbers. The new methods extend the range of capillary numbers for which the pore network model is a tractable alternative and enables e.g. future studies of Haines jumps in the low capillary number regime.

By pore network modelling and lattice-Boltzmann simulations in the high capillary number limit, it is found that the total flow rate follows a Darcy-type equation where the fluid viscosity is replaced by an effective viscosity. This effective viscosity can be modelled by the Lichtenecker–Rother equation. Results from more than 6000 steady-state simulations using the pore network model are presented that range from the high capil-

lary number limit and down to $\sim 10^{-4}$. Variation in dimensionless output from the model is shown to be explainable by three dimensionless variables: the wetting fluid saturation, the viscosity ratio and a dimensionless pressure gradient. In the high capillary number limit, the model gives relative permeabilities that do not form straight lines when the viscosity ratio is different from one.

This thesis also addresses the computational challenges associated with calculating the thermodynamic stability limits of multi-component mixtures and the identification of extrema as minima, maxima or saddle points in variational calculus.

Preface

This thesis was submitted to the Department of Physics at the Norwegian University of Science and Technology (NTNU) in partial fulfilment of the requirements for the degree of philosophiae doctor (PhD). The thesis represents four years of work, in which teaching, courses and parental leave equivalent to approximately 18 months in total are included. The work was financed by the Faculty of Natural Sciences at NTNU and, partly, by the Research Council of Norway through its Centres of Excellence funding scheme (project number 262644). The thesis supervisors have been Professor Alex Hansen, Professor Signe Kjelstrup and Senior Research Scientist/Professor II Øivind Wilhelmsen.

I am very grateful to Alex Hansen for accepting me as a PhD student and for his help in acquiring funding. Alex deserves thanks for including me in his research projects, for our many discussions and for sharing some of his vast knowledge of physics. Also, it was in large part attending his lectures in computational physics as a student, almost ten years ago now, that inspired me to pursue a career as a researcher.

Many, many thanks are due to Signe Kjelstrup for her never-ending enthusiasm and optimism, her confidence in me, her lightening fast reading and feedback and her deep care for her students. Attending her course in irreversible thermodynamics has been one of the most enlightening experiences in my time at NTNU.

I am truly grateful to Øivind Wilhelmsen for being a good friend and office mate, and for introducing me to capillary models. Øivind's sense for details and rigour makes working with him an undivided pleasure, and he has helped me navigate through the nitty-gritty details of many problems. Without him, I do not think this thesis would have been completed.

Also, I am of course indebted to all collaborators and coauthors and in particular to Ailo Aasen, Eskil Aursand, Peder Aursand, Anders Austegard, Dick Bedeaux, Raffaela Cabriolu, Eirik Grude Flekkøy, Morten Hammer, Karl Yngve Lervåg, Gaute Linga, Halvor Lund, Elisa Magnanelli, Svend Tollak Munkejord, Jon Pharoah, Santanu Sinha, Geir Skaugen, Morten Vassvik and Mathias Winkler. Furthermore, I would like to offer thanks to everyone at PoreLab and at the Gas Technology department at SINTEF Energy Research for excellent discussions during lunches and coffee breaks, although I have not been able to attend as many of them

as I would have liked.

Finally, I would like to thank my parents, for more than 30 years of love and support, and my dear Ida and our children Vilma and Martin. Ida's support, emotional counselling and love have been inspiring when work has gone well and indispensable all the times it has not. Vilma and Martin have helped me keep a healthy distance to the thesis work. Their smiles and laughter have duly reminded me of the things that are truly important in life, and have done so every single day.

Trondheim, August 2020
Magnus Aa. Gjennestad

Contents

Chapter 1

Introduction

Porous media are ubiquitous both in nature and technology. For instance, naturally occurring substances, e.g. soils and rocks, and synthetic materials, e.g. concrete, ceramics, paper and various fibrous materials, are porous. Even biological materials such as wood, bone and the matrix of cells that make up the human body may be considered porous materials. Knowledge about their properties, and in particular the distribution and flow of fluids through them, is critical for applications such as ground water flow, spreading of contaminants in the ground, nuclear waste disposal, geothermal energy, oil and natural gas recovery, drug delivery for cancer treatment, catalysis and so on.

Perhaps the greatest challenge facing the world today is increased global warming. To meet it, strategies both for adapting to the consequences and eliminating net emissions of green house gases are required. One expected consequence is more heavy rainfall. This increases the risk of flooding and landslides [1]. Understanding how water flows into and through the ground is critical for dealing with these threats. Such knowledge is also important for drilling of water wells in areas that face droughts to ensure supply of clean drinking water [2]. Many technologies to reduce green house gas emissions also rely on porous media. Examples include geological sequestration of CO_2 [3, 4], CO_2 capture using porous absorbents [5], porous components of fuel cells [6] and H_2 storage [7, 8].

The pores of a porous material can be quite small, on the order of millimetres or even nanometres. However, some applications, e.g. flow in

soils and rocks, may require knowledge about flows on a length scale of kilometres. Porous media are therefore often described either on the pore scale, where the distribution of fluids within each pore is resolved, or on the continuum scale[1], where fluids and solid are described as superimposed continua and each point in space contain a mixture of some or all phases. Single-phase flow refers to the situation where a single fluid phase flows within the solid porous medium and the term two-phase flow is used when there are two fluid phases.

Two fluids that coexist in the pore space share common interfaces and may also have interfaces toward the solid. Thermodynamic properties of interfaces have been studied using density functional theories, square gradient theory and capillary models, see e.g. [9]. There is still much left to explore regarding the application of such approaches to porous media.

Experiments to study flow on the pore scale have used micromodels consisting of small flow channels. These are often two-dimensional to ease viewing and are made e.g. by etching in glass or using glass beads [10, 11, 12, 13]. Recently, advances in x-ray microcomputed tomography have also allowed the resolution of pore scale fluid distributions in three dimensions [14, 15].

Several modelling approaches have also been applied to the pore scale. These include direct numerical simulation approaches that solve the Navier–Stokes equations in the pore space and use e.g. the level-set method [16] or the volume-of-fluid method [17] to keep track of any fluid-fluid interfaces. Another widely used approach is the lattice-Boltzmann method [18, 19]. These methods provide detailed information, but are computationally expensive. An alternative approach is pore network models which treat the porous medium as a simplified network of volume elements that are often the size of a single pore or throat. The average flow properties in these elements are then considered, without taking into account the variation in flow properties within each element. Such models are classified as either quasi-static models [20, 21], which account for capillary forces, or dynamic models [22], which account for both capillary and viscous forces.

[1]The continuum scale is often also referred to as the Darcy scale. In this thesis, we use the term continuum scale to emphasize that fluids and solid are described as superimposed continua. Continuum mechanical descriptions, however, can be and are used to describe flow also on the pore scale. One example are the Navier–Stokes equations.

On the continuum scale, flow may be described by balance equations for mass, momentum and energy [23]. The prevailing modelling frameworks are Darcy's law for single-phase flow and the extended Darcy equations for two-phase flow. The limitations of the latter and the proper description of two-phase flow on the continuum scale is still a matter of debate [24]. A large effort has gone into measuring the parameters of the extended Darcy equations, the relative permeabilities and the capillary pressure, for different situations, see e.g. [25, 26].

1.1 Scope of work

This thesis concerns fundamental aspects of coexistence and flow of two fluid phases within in porous media. Specifically, the main focus is on thermodynamic stability and equilibrium on the scale of a single pore and on macroscopic steady-state properties of immiscible two-phase flow. By macroscopic steady-state properties we here refer to time-averages of, possibly, fluctuating quantities that describe flow through a volume element consisting of many pores. The research is disseminated in six published journal articles.

Equilibrium states can be described thermodynamically as global minima of an appropriate potential. A state is locally stable if it is a local minimum, and unstable otherwise. Whether a particular state is a minimum or not, may be strongly dependent on the choice of ensemble, e.g. whether the system is allowed to exchange particles with its surroundings or not. This thesis seeks to explore what the consequences of this are for stability of heterogeneous structures such as droplets, bubbles and films in a pore. The results are documented in **Paper II**. An extension of this work is the thermodynamic description and stability of thin films and droplets, which is the topic of **Paper III**. Prerequisites for the work both in **Paper II** and **Paper III** are thermodynamic descriptions and stability limits of homogeneous fluids and this is the topic of **Paper I**.

Single-phase flow in porous media is, at this point, reasonably well understood. Two-phase flow, on the other hand, is not and its description of the continuum scale is still debated [24]. While this thesis is, of course, not able to resolve this discussion, it seeks to add to it and to provide tools for further studies. These contributions are published in **Paper IV**,

Paper V and **Paper VI**.

The methods applied are theoretical and numerical, and the models used and approaches taken are, to a large degree, well-established. Example models are equations of state that describe the behaviour of bulk fluids, capillary models to describe heterogeneous structures with interfaces, the disjoining pressure for thin films and a pore network model. A large part of the thesis describes results from applying these theories and models to specific situations. To be able to do so, however, there was a need to address certain computational challenges. For instance, calculating the thermodynamic stability limits homogeneous multi-component mixtures, doing stable and fast time integration of the pore network model and the identification of extrema as minima, maxima and saddle points in variational calculus. The resolution of these challenges are documented as well in, respectively, **Paper I**, **Paper IV** and **Paper II**.

1.2 Outline of thesis

This thesis is made up of five chapters, followed by the six journal articles. Chapter 2 concerns thermodynamic description of fluids and Chapter 3 is about porous media flow. The purpose of chapters 2 and 3 is to provide a basic introduction to these subjects, or at least the parts of these subjects that are relevant to the papers. The intention is that a person who is an expert in one area and not the other should be able to read the entire thesis without unnecessary obstacles. The introduction is provided here as it is too basic to be included in the research articles, but may be highly non-trivial to someone without some experience in the fields. Chapter 4 gives a summary of the findings in the research papers. Perspectives and outlook for the future are given in Chapter 5.

1.3 List of papers

The following papers are included in the thesis:

Paper I. P. Aursand, M. Aa. Gjennestad, E. Aursand, M. Hammer, and Ø. Wilhelmsen. The spinodal of single- and multi-component fluids and its role in the development of modern equations of state. *Fluid*

Phase Equilibria 436 (2017), pp. 98–112. DOI: 10.1016/j.fluid.2016.12.018

Paper II. M. Aa. Gjennestad and Ø. Wilhelmsen. Thermodynamic stability of droplets, bubbles and thick films in open and closed pores. *Fluid Phase Equilibria* 505 (2020), p. 112351. DOI: 10.1016/j.fluid.2019.112351

Paper III. M. Aa. Gjennestad and Ø. Wilhelmsen. Thermodynamic stability of volatile droplets and thin films governed by the disjoining pressure in open and closed containers. *Langmuir* 36 (2020), pp. 7879–7893. DOI: 10.1021/acs.langmuir.0c00960

Paper IV. M. Aa. Gjennestad, M. Vassvik, S. Kjelstrup, and A. Hansen. Stable and efficient time integration at low capillary numbers of a dynamic pore network model for immiscible two-phase flow in porous media. *Frontiers in Physics* 6 (2018), p. 56. DOI: 10.3389/fphy.2018.00056

Paper V. S. Sinha, M. Aa. Gjennestad, M. Vassvik, M. Winkler, A. Hansen, and E. G. Flekkøy. Rheology of high-capillary number flow in porous media. *Frontiers in Physics* 7 (2019), p. 65. DOI: 10.3389/fphy.2019.00065

Paper VI. M. Aa. Gjennestad, M. Winkler, and A. Hansen. Pore network modeling of the effects of viscosity ratio and pressure gradient on steady-state incompressible two-phase flow in porous media. *Transport in Porous Media* 132 (2020), pp. 355–379. DOI: 10.1007/s11242-020-01395-z

During time the author has been a PhD student, he has in addition contributed to papers that are not part of this thesis. In chronological order of publication, these include:

Paper VII. Ø. Wilhelmsen, A. Aasen, G. Skaugen, P. Aursand, A. Austegard, E. Aursand, M. Aa. Gjennestad, H. Lund, G. Linga, and M. Hammer. Thermodynamic modeling with equations of state: Present challenges with established methods. *Industrial & Engineering Chemistry Research* 56.13 (2017), pp. 3503–3515. DOI: 10.1021/acs.iecr.7b00317

Paper VIII. M. Aa. Gjennestad, E. Aursand, E. Magnanelli, and J. Pharoah. Performance analysis of heat and energy recovery ventilators using exergy analysis and nonequilibrium thermodynamics. *Energy and Buildings* 170 (2018), pp. 195–205. DOI: 10.1016/j.enbuild.2018.04.013

Paper IX. A. Hansen, S. Sinha, D. Bedeaux, S. Kjelstrup, M. Aa. Gjennestad, and M. Vassvik. Relations between seepage velocities in immiscible, incompressible two-phase flow in porous media. *Transport in Porous Media* 125 (2018), pp. 565–587. DOI: 10.1007/s11242-018-1139-6

Paper X. M. Winkler, M. Aa. Gjennestad, D. Bedeaux, S. Kjelstrup, R. Cabriolu, and A. Hansen. Onsager-symmetry obeyed in athermal mesoscopic systems: Two-phase flow in porous media. *Frontiers in Physics* 8 (2020), p. 60. DOI: 10.3389/fphy.2020.00060

Chapter 2

Thermodynamics of fluids

This chapter reviews some basic aspects of the thermodynamics of bulk fluids and fluids with interfaces. The treatment of such systems is a vast field that employs also far more advanced theory than what is covered here. It is not the objective of this chapter to provide a comprehensive review, but to give the reader an introduction to the topics treated and the concepts used in **Paper I**, **Paper II** and **Paper III**. Furthermore, fluid equations of state such as those presented may be used as closure relations in continuum-scale modelling of multi-phase flows [23] and the concept of interfacial tension, which is a critical parameter in two-phase porous media flow, has its origins in the thermodynamic theory presented here. The contents of this chapter thus also serve as a basis for the discussion of porous media flow in Chapter 3. We use single-component fluids as examples as these are studied in **Paper II** and **Paper III**.

2.1 Bulk fluids

The internal energy differential of a simple homogeneous bulk fluid is [36, p. 36]

$$\mathrm{d}U = T\mathrm{d}S - p\mathrm{d}V + \mu\mathrm{d}N, \tag{2.1}$$

where S is the entropy, V is the volume and N is the number of particles. The intensive[1] properties temperature T, pressure p and chemical potential μ are thus partial derivatives of U w.r.t. S, $-V$ and N, respectively. The term $T\mathrm{d}S$ accounts for the flow of heat into the system, $-p\mathrm{d}V$ for the mechanical work done on the system and $\mu\mathrm{d}N$ for the energy associated with any new particles introduced into the system. Since the internal energy is extensive[2] it follows from Euler's theorem of homogeneous functions that it can be expressed as [36, p. 60]

$$U = TS - pV + \mu N. \tag{2.2}$$

An expression for a thermodynamic potential in terms of its natural variables (S, V and N for the internal energy) is a fundamental relation that can be differentiated to yield the remaining thermodynamic properties of the system [36, pp. 28, 41]. It is thus advantageous to have a thermodynamic model for fluids on this form. Furthermore, it is often practical to formulate such models in terms of the Helmholtz energy

$$F = U - TS, \tag{2.3}$$

whose natural variables are T, V and N. Taking the differential and using (2.1), the Helmholtz energy differential is

$$\mathrm{d}F = -S\mathrm{d}T - p\mathrm{d}V + \mu\mathrm{d}N. \tag{2.4}$$

We then see that the entropy, pressure and chemical potential can be obtained from F by differentiation,

$$S = -\left(\frac{\partial F}{\partial T}\right)_{V,N}, \tag{2.5}$$

$$p = -\left(\frac{\partial F}{\partial V}\right)_{T,N}, \tag{2.6}$$

$$\mu = \left(\frac{\partial F}{\partial N}\right)_{T,V}. \tag{2.7}$$

[1] Intensive properties do not change with a scaling of the system size, e.g. $p\left(\beta S, \beta V, \beta N\right) = p\left(S, V, N\right)$.

[2] Extensive properties scale with the system size, e.g. $U\left(\beta S, \beta V, \beta N\right) = \beta U\left(S, V, N\right)$.

It can be shown[3] that the molar Helmholtz energy f is a function of the temperature and the molar volume $v = V/N$ only, i.e.

$$f(T, v) = F(T, V, N)/N. \tag{2.8}$$

The differential of f is thus,[4]

$$\mathrm{d}f = \left(\frac{\partial f}{\partial T}\right)_v \mathrm{d}T + \left(\frac{\partial f}{\partial v}\right)_T \mathrm{d}v = -s\mathrm{d}T - p\mathrm{d}v. \tag{2.9}$$

Since $f = u - Ts$, the differential of u is

$$\mathrm{d}u = T\mathrm{d}s - p\mathrm{d}v, \tag{2.10}$$

which can be equivalently expressed as

$$\mathrm{d}u = T\mathrm{d}s - \left\{p/\rho^2\right\}\mathrm{d}\rho, \tag{2.11}$$

where $\rho = 1/v$ is the density. Dividing (2.2) by N, we get

$$u = Ts - pv + \mu = Ts - p/\rho + \mu. \tag{2.12}$$

2.1.1 Equations of state

A fundamental relation needs to have some physical content. This may be provided through a mechanical equation of state (EOS). One of the simplest equations of this kind, that describes both gas and liquid behaviour, is the van der Waals equation of state,

$$p(T, V, N) = \frac{RT}{V - Nb} - \frac{N^2 a}{V^2}, \tag{2.13}$$

for which Johannes Diderik van der Waals received the 1910 Nobel prize in physics. Example isotherms of this equation for CO_2 are shown in Figure 2.1.

[3] Since the Helmholtz energy is extensive, $F(T, \beta V, \beta N) = \beta F(T, V, N)$. Subsequently choosing $\beta = 1/N$ yields $f(T, v) = F(T, V/N, 1) = F(T, V, N)/N$.

[4] The latter equality follows from $(\partial f/\partial T)_v = (\partial \{F/N\}/\partial T)_{V,N} = -S/N = -s$ and $(\partial f/\partial v)_T = (\partial F/\partial V)_{T,N} = -p$.

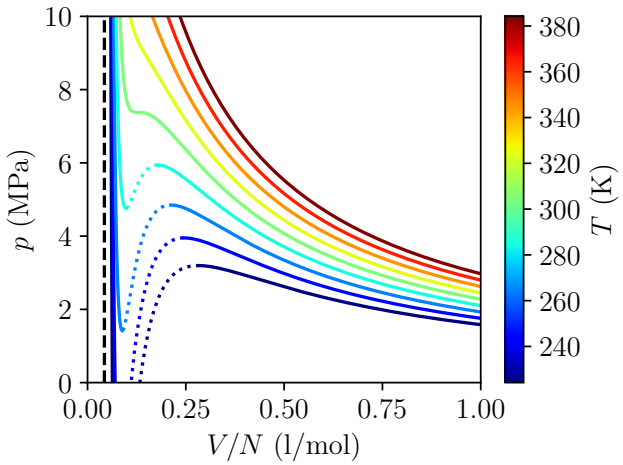

Figure 2.1: Isotherms of the van der Waals EOS (2.13) for CO_2, with parameters $a = 0.37\,\mathrm{Nm}^4/\mathrm{mol}^2$ and $b = 0.043\,\mathrm{l/mol}$ (dashed vertical line). The dotted parts of the isotherms represent locally unstable phases (see Section 2.1.3). For isotherms below the critical temperature (304.1 K) there are pressures for which the EOS predicts three possible volumes, one small (liquid phase), one large (gas phase) and one intermediate (unstable phase).

In (2.13), R is the universal gas constant. The co-volume parameter b accounts for the finite size of the particles in the fluid and makes the pressure diverge towards infinity as $V/N \to b$. The a parameter accounts for intermolecular attraction between particles. Below the critical temperature, the term $-N^2a/V^2$ introduces a local minimum in the isotherms. Thus the EOS predicts three possible volumes of the system for a specified temperature and pressure: one small volume, corresponding to a liquid phase, one large volume, corresponding to a gas phase, and one intermediate volume, corresponding to a locally unstable phase (see Section 2.1.3). In the limit $V/N \to \infty$, the van der Waals equation reduces to the ideal gas law.

This type of mechanical EOS, which gives p as a function of T, V and N, alone does not provide enough information to derive a fundamental relation. It will, however, if combined with a description of how the fluid behaves in the rarefied limit with molar volume v_∞ where the particles

are too far apart to interact. In this rarefied state the system behaves as an ideal gas and its Helmholtz energy is given by F^{i}. An expression for F^{i} may be derived by assuming a model for the ideal gas heat capacity at constant pressure or volume. We may then integrate to obtain the Helmholtz energy at any volume V,

$$F\left(T,V,N\right)=F^{\mathrm{i}}\left(T,v_{\infty}N,N\right)+\int_{v_{\infty}N}^{V}\left(\frac{\partial F}{\partial V}\right)_{T,N}\mathrm{d}V. \tag{2.14}$$

The partial derivative being integrated is equal to $-p$ and thus,

$$F\left(T,V,N\right)=F^{\mathrm{i}}\left(T,v_{\infty}N,N\right)-\int_{v_{\infty}N}^{V}p\ \mathrm{d}V. \tag{2.15}$$

Adding and subtracting an integral over the ideal gas pressure $p^{\mathrm{i}}=NRT/V$, and absorbing the subtracted integral into F^{i}, we get

$$F\left(T,V,N\right)=F^{\mathrm{i}}\left(T,V,N\right)-\int_{v_{\infty}N}^{V}\left\{p-p^{\mathrm{i}}\right\}\mathrm{d}V. \tag{2.16}$$

The integral term on the right-hand-side describes the deviation of the Helmholtz energy from that of an ideal gas and is called the residual Helmholtz energy [37, p. 21],

$$F^{\mathrm{r}}\left(T,V,N\right)=-\int_{v_{\infty}N}^{V}\left\{p-p^{\mathrm{i}}\right\}\mathrm{d}V. \tag{2.17}$$

There are a number of different EOS in the literature that are more sophisticated and accurate than the van der Waals EOS. Still, other cubic equations, such as Soave–Redlich–Kwong (SRK) [38] and Peng–Robinson (PR) [39], may be subjected to the same kind of integration procedure in order to obtain a fundamental relation. This also applies for e.g. the cubic-plus-association equation (CPA) [40], which uses a cubic equation for the pressure with an added term to account for association effects. It is the CPA EOS that is used in **Paper II** and **Paper III**.

Some modern EOS, e.g. the perturbed-chain statistically associating fluid theory (PC-SAFT) EOS [41], the multi-parameter equation of state for combustion gases and combustion gas-like mixtures (EOS-CG) [42] and the multi-parameter equation GERG-2008 [43], are given as models the Helmholtz energy (or the residual part) rather than as expressions for pressure that need to be integrated.

2.1.2 Gas-liquid coexistence

For a fluid system contained in a box with a fixed volume V and number of particles N, that is kept at constant temperature T by exchanging heat with its surroundings, the equilibrium state is one that maximizes the total entropy of the system and the surroundings. This state will correspond to a global minimum in the Helmholtz energy of the system [36, p. 155]. For the fluids described by one of the EOS mentioned in Section 2.1.1, that are below the critical temperature, this equilibrium state is either a gaseous state, a liquid state or a state in which a gaseous phase and a liquid phase coexists.

A necessary condition for gas-liquid coexistence at equilibrium is that the total Helmholtz energy differential,

$$\mathrm{d}F = \mathrm{d}F_{\mathrm{g}} + \mathrm{d}F_{\ell}, \tag{2.18}$$

$$= -p_{\mathrm{g}}\mathrm{d}V_{\mathrm{g}} + \mu_{\mathrm{g}}\mathrm{d}N_{\mathrm{g}} - p_{\ell}\mathrm{d}V_{\ell} + \mu_{\ell}\mathrm{d}N_{\ell}. \tag{2.19}$$

is zero. Since $N = N_{\mathrm{g}} + N_{\ell}$ and $V = V_{\mathrm{g}} + V_{\ell}$, then $\mathrm{d}N_{\mathrm{g}} = -\mathrm{d}N_{\ell}$ and $\mathrm{d}V_{\mathrm{g}} = -\mathrm{d}V_{\ell}$, and

$$\mathrm{d}F = -\left\{p_{\mathrm{g}} - p_{\ell}\right\}\mathrm{d}V_{\mathrm{g}} + \left\{\mu_{\mathrm{g}} - \mu_{\ell}\right\}\mathrm{d}N_{\mathrm{g}}. \tag{2.20}$$

A necessary condition for a gas-liquid equilibrium is thus that

$$p_{\ell} = p_{\mathrm{g}}, \tag{2.21}$$

$$\mu_{\ell} = \mu_{\mathrm{g}}. \tag{2.22}$$

The criteria (2.21) and (2.22) define the phase envelope. Such an envelope is illustrated in Figure 2.2 for CO_2, described by the van der Waals EOS. It terminates at the critical point where the gas and liquid densities converge and the two phases become indistinguishable.

An excellent and much more general treatment of phase equilibria in mixtures is given by Michelsen and Mollerup [37].

2.1.3 Phase stability

An equilibrium state is a global minimum in the relevant thermodynamic potential. A metastable state, on the other hand, represents a local minimum. A state that is not a minimum may have its free energy reduced by infinitesimally small perturbations and is thus unstable.

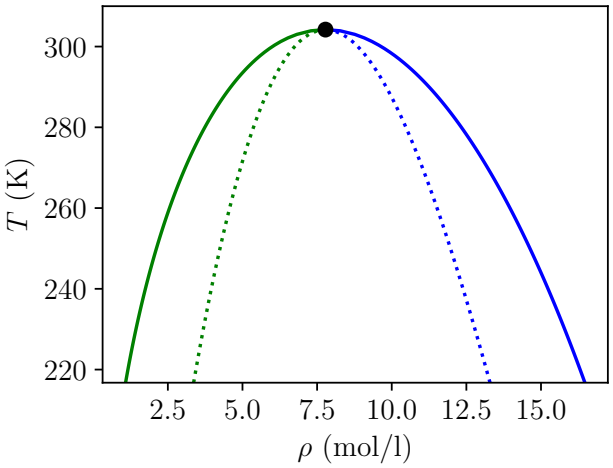

Figure 2.2: Phase envelope for CO_2, as modelled by the van der Waals EOS. Gas and liquid coexistence densities are shown in solid green and solid blue, respectively. The equilibrium state is gas and liquid in coexistence for temperatures and total densities $\rho = N/V$ inside the envelope. The gas and liquid spinodal curves are shown in dotted green and dotted blue. All curves terminate at the critical point (black circle).

The general question of phase stability is surprisingly technical and complex. We therefore treat only the special case of stability of a single-component phase at fixed temperature, volume and number of particles here. This is the specific case relevant for the homogeneous phases considered in **Paper II** and **Paper III**. A more comprehensive discussion, that considers mixtures and other ensembles, is given in [44], **Paper I** and the references therein. A conceptually similar approach to that taken here is used to analyse stability of heterogeneous systems in **Paper II** and **Paper III**.

Consider a homogeneous phase with a fixed temperature T, volume V and number of particles N and partition the phase into two parts, called 1 and 2. The two subsystems have volumes V_1 and V_2, respectively, contain N_1 and N_2 particles and can freely exchange volume and particles with each other, so that $\mathrm{d}N_1 = -\mathrm{d}N_2$ and $\mathrm{d}V_1 = -\mathrm{d}V_2$. Since the whole system is homogeneous, the intensive variables of the two subsystems are initially equal, e.g. $p_1 = p_2$ and $\mu_1 = \mu_2$.

The question of local stability of the homogeneous phase is then: Can the total system system reduce its Helmholtz energy by small, local perturbations in such a way that the two parts 1 and 2 attain different intensive variables? Physically, this would mean that the system would spontaneously split into two phases with different intensive properties. To address this question, we set up the Helmholtz energy differential to second order,

$$\begin{aligned} \mathrm{d}F &= \mathrm{d}F_1 + \mathrm{d}F_2, && (2.23)\\ &= \mathrm{d}\mathbf{x}_1^{\mathrm{T}} \frac{\mathrm{d}F_1}{\mathrm{d}\mathbf{x}_1} + \mathrm{d}\mathbf{x}_2^{\mathrm{T}} \frac{\mathrm{d}F_2}{\mathrm{d}\mathbf{x}_2} \\ &\quad + \mathrm{d}\mathbf{x}_1^{\mathrm{T}} \frac{\mathrm{d}^2F_1}{\mathrm{d}\mathbf{x}_1^2} \mathrm{d}\mathbf{x}_1 + \mathrm{d}\mathbf{x}_2^{\mathrm{T}} \frac{\mathrm{d}^2F_2}{\mathrm{d}\mathbf{x}_2^2} \mathrm{d}\mathbf{x}_2. && (2.24) \end{aligned}$$

Herein, $\mathbf{x}_1 = [V_1, N_1]^{\mathrm{T}}$ and $\mathbf{x}_2 = [V_2, N_2]^{\mathrm{T}}$. Since the total volume and the total number of particles are constant, we have that $\mathrm{d}\mathbf{x}_1 = -\mathrm{d}\mathbf{x}_2$ and thus

$$\mathrm{d}F = \mathrm{d}\mathbf{x}_1^{\mathrm{T}} \left\{ \frac{\mathrm{d}F_1}{\mathrm{d}\mathbf{x}_1} - \frac{\mathrm{d}F_2}{\mathrm{d}\mathbf{x}_2} \right\} + \mathrm{d}\mathbf{x}_1^{\mathrm{T}} \left\{ \frac{\mathrm{d}^2F_1}{\mathrm{d}\mathbf{x}_1^2} + \frac{\mathrm{d}^2F_2}{\mathrm{d}\mathbf{x}_2^2} \right\} \mathrm{d}\mathbf{x}_1. \qquad (2.25)$$

The first derivatives of the Helmholtz energy w.r.t. volume and number of particles are equal to the negative pressure and the chemical potential, respectively, see (2.6) and (2.7). Since the system is initially homogeneous, $p_1 = p_2$ and $\mu_1 = \mu_2$ and the first-order term in $\mathrm{d}F$ is zero. Furthermore, it may be shown[5] that $N_1\ \mathrm{d}^2F_1/\mathrm{d}\mathbf{x}_1^2 = N_2\ \mathrm{d}^2F_2/\mathrm{d}\mathbf{x}_2^2$ and the Helmholtz energy differential may then be reduced to

$$\mathrm{d}F = \frac{N}{N_2}\mathrm{d}\mathbf{x}_1^{\mathrm{T}}\ \frac{\mathrm{d}^2F_1}{\mathrm{d}\mathbf{x}_1^2}\ \mathrm{d}\mathbf{x}_1. \tag{2.26}$$

The Hessian matrix of F_1 is

$$\frac{\mathrm{d}^2F_1}{\mathrm{d}\mathbf{x}_1^2} = \begin{bmatrix} \left(\frac{\partial^2 F_1}{\partial V_1^2}\right)_{T,N_1} & \left(\frac{\partial}{\partial N_1}\left(\frac{\partial F_1}{\partial V_1}\right)_{T,N_1}\right)_{T,V_1} \\ \left(\frac{\partial}{\partial V_1}\left(\frac{\partial F_1}{\partial N_1}\right)_{T,V_1}\right)_{T,N_1} & \left(\frac{\partial^2 F_1}{\partial N_1^2}\right)_{T,V_1} \end{bmatrix}, \tag{2.27}$$

and may be further simplified[6] to

$$\frac{\mathrm{d}^2F_1}{\mathrm{d}\mathbf{x}_1^2} = \frac{1}{N_1}\left(\frac{\partial^2 f_1}{\partial v_1^2}\right)_T \begin{bmatrix} 1 & -v_1 \\ -v_1 & v_1^2 \end{bmatrix}. \tag{2.28}$$

The matrix in this expression is symmetric and may be decomposed as $\mathbf{Q}\mathbf{\Lambda}\mathbf{Q}^{\mathrm{T}}$, where $\mathbf{\Lambda}$ is the diagonal matrix of eigenvalues and $\mathbf{Q}$ is a matrix whose ith column $\mathbf{q}_i$ is the eigenvector associated with the eigenvalue Λ_i.

[5] Intensive variables are zeroth-order homogeneous in the extensive variables of the system, e.g. $p\left(T,V,N\right) = p\left(T,\beta V,\beta N\right)$. By setting $\beta = 1/N$, we get that the pressure can be considered a function of T and v, $p\left(T,v\right) = p\left(T,V/N,1\right) = p\left(T,V,N\right)$. Thus $\left(\partial^2 F/\partial V^2\right)_{T,N} = -\left(\partial p/\partial V\right)_{T,N} = -\left(\partial p/\partial v\right)_T/N$. Since subsystems 1 and 2 initially have equal intensive variables, $\left(\partial p_1/\partial v_1\right)_T = \left(\partial p_2/\partial v_2\right)_T$, and $N_1\left(\partial^2 F_1/\partial V_1^2\right)_{T,N_1} = N_2\left(\partial^2 F_2/\partial V_2^2\right)_{T,N_2}$ follows. A similar argument may be used for the other elements of the Hessian matrix.

[6] According to (2.8), the molar Helmholtz energy is a function of T and v only. In terms of the molar Helmholtz energy, we can write $\left(\partial F_1/\partial N_1\right)_{T,V_1} = f_1 - v_1\left(\partial f_1/\partial v_1\right)_T$, since $N_1 = V_1/v_1$ and the the partial derivative is taken at constant V_1. Differentiating one more time w.r.t. N_1 yields $\left(\partial^2 F_1/\partial N_1^2\right)_{T,V_1} = \left(\partial/\partial N_1\left\{f_1 - v_1\left(\partial f_1/\partial v_1\right)_T\right\}\right)_{T,N_1} = v_1^2\left(\partial^2 f_1/\partial v_1^2\right)_T/N_1$. Similar arguments may be followed for the other elements of the Hessian matrix.

Introducing the simplified Hessian, with the eigenvalue decomposition of the matrix, the Helmholtz differential becomes

$$\mathrm{d}F = \frac{N}{N_1 N_2}\left(\frac{\partial^2 f_1}{\partial v_1^2}\right)_T \mathrm{d}\mathbf{x}_1^{\mathrm{T}}\mathbf{Q}\mathbf{\Lambda}\mathbf{Q}^{\mathrm{T}}\mathrm{d}\mathbf{x}_1. \tag{2.29}$$

The Helmholtz energy F is at a local minimum if $\mathrm{d}F$ is positive for all possible $\mathrm{d}\mathbf{x}_1$. This will be the case if all eigenvalues Λ_i have the same sign as $\left(\partial^2 f_1/\partial v_1^2\right)_T$. If the signs are opposite for one or more eigenvalues, $\mathrm{d}\mathbf{x}_1$ may be chosen along one of the corresponding eigenvectors to give a negative $\mathrm{d}F$ and a reduction in the Helmholtz energy. The state is then locally unstable. If an eigenvalue is zero, the variation in F along the corresponding eigenvector is zero to second order and more information is required in order to assess local stability.

The eigenvalues Λ_i satisfy the characteristic polynomial

$$\Lambda_i^2 = \Lambda_i\left(1 + v_1^2\right), \tag{2.30}$$

and we therefore have the two eigenvalues $\Lambda_1 = 0$ and $\Lambda_2 = 1+v_1^2$. Letting $\mathrm{d}\mathbf{x}_1$ be in the direction of the eigenvector $\mathbf{q}_1$ corresponds to perturbations with $\mathrm{d}V_1 = v_1\mathrm{d}N_1$. Such perturbations amount to moving in the mathematical boundary between subsystems 1 and 2, with no physical change to the system as a whole, including its Helmholtz energy, or to the intensive variables of either subsystem. We can therefore ignore the eigenvalue Λ_1 when assessing stability.

The remaining condition for stability is that $\mathrm{d}F$ is positive for perturbations along the eigenvector $\mathbf{q}_2$. Since Λ_2 is always positive, this is true when

$$\left(\frac{\partial^2 f_1}{\partial v_1^2}\right)_T > 0. \tag{2.31}$$

Since the partitioning of the system is arbitrary, and we could let $N_1 \to N$, we can drop the subscripts, multiply by the positive number $1/N$ and write

$$\frac{1}{N}\left(\frac{\partial^2 f}{\partial v^2}\right)_T = \left(\frac{\partial^2 F}{\partial V^2}\right)_{T,N} = -\left(\frac{\partial p}{\partial V}\right)_{T,N} > 0, \tag{2.32}$$

as the criterion for stability of the homogeneous phase. Multiplying instead with the positive number v^2/N, the criterion may also be formulated as

$$\frac{v^2}{N}\left(\frac{\partial^2 f}{\partial v^2}\right)_T = \left(\frac{\partial^2 F}{\partial N^2}\right)_{T,V} = \left(\frac{\partial \mu}{\partial N}\right)_{T,V} > 0. \tag{2.33}$$

A fluid phase that does not satisfy these two equivalent relations corresponds to one located on a dashed curve in Figure 2.1 and it will spontaneously decompose into a gas and a liquid phase.

The spinodals represent the limits of thermodynamic stability, i.e. the curves where the stable phases become unstable and the stability criteria (2.32) and (2.33) are satisfied as equalities. The gas and liquid spinodal limits are shown in Figure 2.2 for CO_2 modelled by the van der Waals EOS. Spinodal limits of mixtures are treated in **Paper I**.

Some EOS may predict states that satisfy stability criteria between the gas and liquid spinodals. We call such states pseudo-stable. To the best of the author's knowledge, they have never been observed they are thus, when they appear, unfortunate artefacts of the EOS. Pseudo-stable states are discussed further in **Paper I**.

2.2 Fluids with interfaces

The previous section treated the thermodynamic description of homogeneous bulk fluids. When a gas and liquid phase are in coexistence, however, they share an interfacial region where intensive properties such as density and pressure may be different from the two bulk phases. In many cases, and especially for small systems, treating the combined gas and liquid system as the sum of the bulk gas phase and the bulk liquid phase is insufficient for an accurate description.

In this section, we review the Gibbs interface model and the capillary approach for describing heterogeneous systems. Furthermore, we briefly mention the concept of disjoining pressure used to describe thin films, i.e. heterogeneous systems with two interfaces in close proximity.

2.2.1 Gibbs interface model

An illustration of a density profile in the interfacial region in a gas-liquid system of CO_2 is shown in Figure 2.3. In the narrow, but finite, interfacial region there is a continuously varying density profile that connects the bulk densities in the gas and liquid phases. We will consider only planar interfaces in this section.

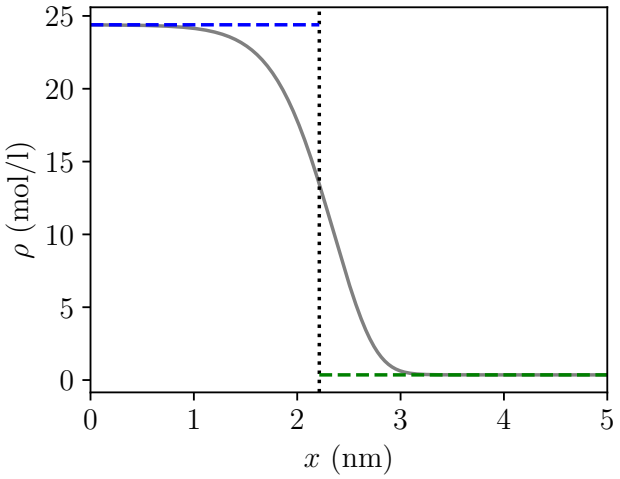

Figure 2.3: Illustration of the density profile (solid grey) around a planar gas-liquid interface in CO_2 at $T = 220\,\mathrm{K}$. The bulk liquid density ρ_ℓ and the bulk gas density ρ_g are indicated by blue and green dashed lines, respectively. The location of the equimolar Gibbs surface is shown as a dotted black line.

A thermodynamic treatment of such interfaces was introduced by Josiah Willard Gibbs. His approach was to describe the interface as a two-dimensional thermodynamic system that is separate from the bulk phases [45]. The combined system, with continuously varying properties, is thus modelled in a discontinuous manner by two homogeneous bulk systems and an interfacial system. To the interface are assigned extensive quantities such as an internal energy $U_{\mathrm{g}\ell}$, an entropy $S_{\mathrm{g}\ell}$, a particle number $N_{\mathrm{g}\ell}$ and an area $A_{\mathrm{g}\ell}$. The total internal energy of the gas-liquid

system, including the interface, is thus

$$U = U_{\mathrm{g}} + U_{\ell} + U_{\mathrm{g}\ell}. \tag{2.34}$$

Similar sums apply for the total entropy S and the total number of particles N,

$$S = S_{\mathrm{g}} + S_{\ell} + S_{\mathrm{g}\ell}, \tag{2.35}$$

$$N = N_{\mathrm{g}} + N_{\ell} + N_{\mathrm{g}\ell}. \tag{2.36}$$

Since the interface is modelled as a two-dimensional surface, it has no volume and the total volume is thus

$$V = V_{\mathrm{g}} + V_{\ell}. \tag{2.37}$$

The internal energy differential of the interfacial subsystem is

$$\mathrm{d}U_{\mathrm{g}\ell} = T_{\mathrm{g}\ell}\mathrm{d}S_{\mathrm{g}\ell} + \gamma_{\mathrm{g}\ell}\mathrm{d}A_{\mathrm{g}\ell} + \mu_{\mathrm{g}\ell}\mathrm{d}N_{\mathrm{g}\ell}, \tag{2.38}$$

where the partial derivative $\gamma_{\mathrm{g}\ell}$ is the interfacial tension. From the extensivity of $U_{\mathrm{g}\ell}$, we get the Euler relation,

$$U_{\mathrm{g}\ell} = T_{\mathrm{g}\ell}S_{\mathrm{g}\ell} + \gamma_{\mathrm{g}\ell}A_{\mathrm{g}\ell} + \mu_{\mathrm{g}\ell}N_{\mathrm{g}\ell}. \tag{2.39}$$

From the example system in Figure 2.3, it is evident that the total number of particles in the gas-liquid system can be obtained by integrating the density profile

$$N = A_{\mathrm{g}\ell} \int_{-L/2}^{L/2} \rho \, \mathrm{d}x, \tag{2.40}$$

over the length L of the system. Since two bulk systems are assumed homogeneous, with spatially constant densities ρ_{ℓ} and ρ_{g},

$$N_{\ell} = A_{\mathrm{g}\ell} \left\{x^* + L/2\right\} \rho_{\ell} = A_{\mathrm{g}\ell} \int_{-L/2}^{x^*} \rho_{\ell} \, \mathrm{d}x, \tag{2.41}$$

$$N_{\mathrm{g}} = A_{\mathrm{g}\ell} \left\{L/2 - x^*\right\} \rho_{\mathrm{g}} = A_{\mathrm{g}\ell} \int_{x^*}^{L/2} \rho_{\mathrm{g}} \, \mathrm{d}x, \tag{2.42}$$

where x^* is the location of the interface. Inserting these integrals into (2.36) and solving for $N_{g\ell}$, we get that

$$N_{g\ell} = A_{g\ell} \int_{-L/2}^{x^*} \{\rho - \rho_\ell\} \, \mathrm{d}x + A_{g\ell} \int_{x^*}^{L/2} \{\rho - \rho_g\} \, \mathrm{d}x. \tag{2.43}$$

The dividing surface location x^* may be chosen in a number of different ways. One choice is such that $N_{g\ell} = 0$ and this defines the equimolar Gibbs surface, illustrated in Figure 2.3.

2.2.2 Capillary model

The internal energy of the two-dimensional Gibbs model of the interface was given by (2.38). Performing now a Legendre transformation, $F_{g\ell} = U_{g\ell} - TS_{g\ell}$, the Helmholtz energy of the interface is

$$F_{g\ell} = \gamma_{g\ell} A_{g\ell} + \mu_{g\ell} N_{g\ell}. \tag{2.44}$$

By choosing the dividing surface such that $N_{g\ell} = 0$, the second term in this expression can be set to zero.

A capillary model for the Helmholtz energy of the total gas-liquid system can thus be set up as the sum of two bulk-phase contributions plus an interfacial tension term,

$$F = F_g + F_\ell + \gamma_{g\ell} A_{g\ell}. \tag{2.45}$$

To use such a capillary model to do calculations requires a model for the bulk phases, usually and equation of state of the kind described in Section 2.1.1, and a model for the interfacial tension.

The capillary modelling approach is a simple, yet powerful model for the gas-liquid system. Wilhelmsen et al. [46] used it to study stability of droplets and bubbles. They found that it accurately reproduced the solutions from the more sophisticated square gradient model, which models the spatially varying density profiles, except in the vicinity of the spinodals. Furthermore, earlier works have established that stability of droplets and bubbles is strongly affected by whether the system can exchange particles with its surroundings or not, i.e. if it is open or closed. This work has, in part, relied the capillary model [47, 48, 49].

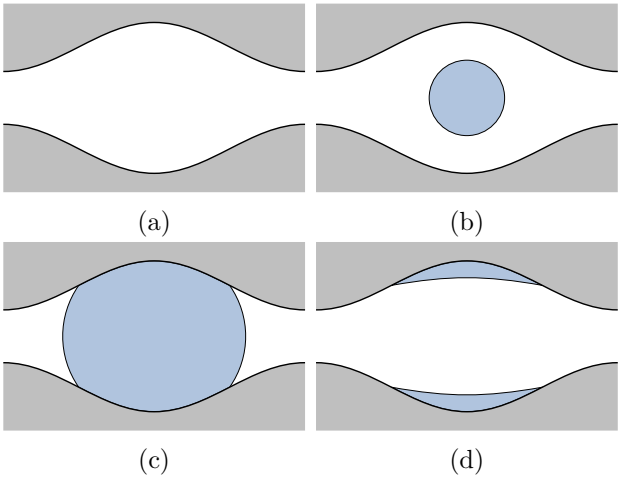

Figure 2.4: Illustration of the fluid structures considered in **Paper II**: (a) a homogeneous fluid phase, (b) a free droplet or bubble that is not in contact with the pore walls, (c) a droplet or bubble filling the entire cross-section of some part pore and (d) a thick film of gas or liquid.

The capillary model may be used to describe heterogeneous structures in pores by including also gas-solid and liquid-solid interfaces, so that the total Helmholtz energy is[7]

$$F = F_{\mathrm{g}} + F_{\ell} + \gamma_{\mathrm{g}\ell} A_{\mathrm{g}\ell} + \gamma_{\mathrm{gs}} A_{\mathrm{gs}} + \gamma_{\ell\mathrm{s}} A_{\ell\mathrm{s}}. \tag{2.46}$$

The motivation for doing this is to extend the earlier analysis [47, 49] of stability of droplets and bubbles to structures in pores. From these earlier works, it is expected that pore size and whether the pore is open or closed could affect stability and this is investigated in **Paper II**. The extended capillary model could also be used to study e.g. capillary condensation in porous media, where liquid phases may form at pressures below saturation.

In **Paper II**, models are derived that describe the Helmholtz energies (2.46) of each of the structures illustrated in Figure 2.4: (a) a homogeneous fluid phase, (b) a free droplet or bubble that is not in contact with the pore walls, (c) a droplet or bubble filling the entire cross-section of some

[7]The energy of the three-phase contact line is not considered, but this could easily be included in the analysis.

part pore and (d) a thick film of gas or liquid. The equilibrium state of a system corresponds to a minimum in some thermodynamic potential. By computing the value of this potential, and evaluating stability, for each of the structures (a)-(d), the equilibrium state for a specified set of conditions is identified. Which thermodynamic potential should be minimized depends on the boundary conditions. In a closed pore kept at constant temperature, the Helmholtz energy should be minimized. In an open pore that can exchange particles with is surroundings at a constant chemical potential, the grand canonical energy

$$\Omega = F - \mu N, \tag{2.47}$$

should be minimized. Herein, μ is the chemical potential of the surroundings and N is the number of particles in the pore.

The derived Helmholtz energy models for the bubbles and droplets, i.e. (b) and (c), are each a functions of a set of variables that describe the configuration. The film Helmholtz energy model, on the other hand, is a functional of the continuously varying film thickness along the pore. For a particular film state to be stable, it is necessary to have a vanishing first variation and a second variation which is positive for all possible perturbations of that film profile. To establish that this is the case, or not, can be very demanding. There was thus a need to address this computational problem in order to asses stability of films. Its resolution is documented in **Paper II**.

2.2.3 Thin films

The previous two sections treated modelling of interfaces separating two bulk phases. In thin films, on the other hand, two interfacial regions may be so close together that they begin to overlap and to interact. The properties of the film phase located between the two interfaces may then differ from the properties of a bulk phase. One approach to modelling this situation is through the concept of the disjoining pressure Π, developed by Boris Vladimirovich Derjaguin [50].

The disjoining pressure may be defined using the two containers illustrated in Figure 2.5, where there is a bulk gas phase and a thin liquid film in the left container and there is a bulk liquid phase in the right. The thin

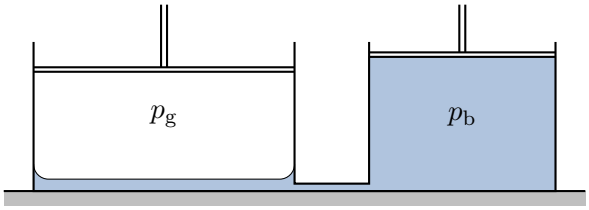

Figure 2.5: Two containers, where the left holds a thin liquid film (blue) and a bulk gas phase (white) with pressure p_g and the right holds a bulk liquid phase with pressure p_b. The film is connected to and in chemical equilibrium with the bulk liquid. Furthermore, the system is in force balance, but the two pressures p_g and p_b are not, in general, equal.

film and the bulk liquid phase are connected and in chemical equilibrium. Furthermore, the system is in force balance, so the gas pressure p_g is equal to the normal pressure $p_\perp$ in the film. Due to anisotropic stresses in the film, however, the gas pressure is, in general, not equal to the bulk liquid pressure p_b. The disjoining pressure is defined as [50]

$$\Pi = p_\perp - p_\mathrm{b}. \tag{2.48}$$

Further details on the disjoining pressure are given in **Paper III** and [50, 51]. For a specific temperature and set of materials, e.g. a water film on a graphite surface [52, 53], the disjoining pressure is often assumed to be a function of the film thickness h only. The curve obtained by plotting Π vs. h is called a disjoining pressure isotherm.

The stability of flat liquid films that are assumed non-volatile, by neglecting condensation and evaporation of the film, have been extensively studied in the literature, see e.g. [54, 55, 56, 57]. One result is that flat films are stable when $\mathrm{d}\Pi/\mathrm{d}h < 0$. When, $\mathrm{d}\Pi/\mathrm{d}h > 0$ on the other hand, interfacial tension acts to suppress perturbations with short wavelengths, whereas perturbations with wavelengths

$$\lambda > \lambda_0 = 2\pi\sqrt{\frac{\gamma_{\mathrm{g}\ell}^\infty}{\mathrm{d}\Pi/\mathrm{d}h}}, \tag{2.49}$$

can grow. Herein, $\gamma_{\mathrm{g}\ell}^\infty$ denotes the gas-liquid interfacial tension of an infinitely thick film. Films that form droplets by succumbing to such instabilities are said to undergo spinodal dewetting. Non-volatile films confined

on substrates that are smaller than λ_0 may be stable [58, 59]. By dynamic considerations, Sharma [60] found the stability criterion $\mathrm{d}\Pi/\mathrm{d}h < 0$ applied also to evaporating films, when a specific model for the evaporation rate was assumed.

Another phenomenon that can be described by the disjoining pressure is the wetting properties of droplets in coexistence with thin, flat films. A particularly well-known result is that the contact angle θ of a large droplet is related to the film thickness and the disjoining pressure by [50, 61]

$$\gamma_{\mathrm{g}\ell}^{\infty} \cos(\theta) = \gamma_{\mathrm{g}\ell}^{\infty} + \Pi h - \int_{\infty}^{h} \Pi \, \mathrm{d}h. \tag{2.50}$$

The stability of non-volatile and evaporating droplets has been studied e.g. by Dörfler, Rauscher, and Dietrich [59] and Sharma [60], respectively.

Paper III discusses, consistently and on equal terms, the thermodynamic stability of thin flat films and flat films in combination with droplets in open and closed systems. These films are allowed to exchange particles with a surrounding gas phase and may thus evaporate or condense. In the open system, the gas may also exchange particles with an external particle reservoir. Previous works have shown that stability of droplets and bubbles depends on whether the system is open or closed [47, 49]. Based on the existing concept of disjoining pressure, a fundamental relation for a liquid film phase is derived and used in a capillary modelling approach. In this respect, **Paper III** is an extension of the work in **Paper II**, where effects of overlapping interfacial regions were neglected.

As for the thick-film description in **Paper II**, the capillary approach gives a Helmholtz energy model for the thin film which is a functional of the continuously varying film thickness. The same computational challenges in determining whether or not a particular film profile is a local minimum in the Helmholtz energy are therefore encountered in **Paper III**, and they are resolved by the same method.

Chapter 3

Flow in porous media

Flow in porous media is a vast subject that has been studied and described with a wide variety of approaches. We shall here focus mostly two example continuum-scale models: One model for single-phase flow and one for two-phase flow. To form a natural continuation of the previous chapter, we shall use the single-phase model place concepts like Darcy's law and permeability in a thermodynamic context. These concepts are central to the findings in **Paper V**. Subsequently, we use the two-phase model to introduce the traditional way of describing two-phase flow on the continuum scale, in terms of the extended Darcy equations, relative permeabilities and the capillary pressure. Relative permeabilities form part of the framework used to present the results in **Paper VI**. These results are obtained by computer simulations using the pore network model and new numerical solution procedures described in **Paper IV**. The concept of Haines jumps, which are an important part of the background for the new solution procedures, is also discussed.

In Chapter 2, u, s, v and ρ represented molar quantities. In this chapter, we shall use the same symbols with the understanding that they now represent mass-specific quantities.

3.1 Single-phase flow

We first consider a relatively simple one-dimensional case of a single-component liquid phase flowing through a porous medium and use a

continuum-scale model to describe it. On this scale, each point in space represents an average over many pores and therefore has both liquid and solid in it. The solid phase is here assumed incompressible and chemically inert and is characterized by a constant density ρ_s and a temperature T_s. The volume fraction of solid α_s is constant in time, but may vary in space. The porosity φ and liquid volume fraction α_ℓ are both equal to $1 - \alpha_\mathrm{s}$ and are assumed known. A more general model which includes also e.g. elasticity of the solid can be found in [62].

Liquid mass is conserved and this is expressed by

$$\partial_t \{\alpha_\ell \rho_\ell\} + \partial_x \{\alpha_\ell \rho_\ell w_\ell\} = 0, \tag{3.1}$$

where ρ_ℓ is the liquid mass density and w_ℓ is the average flow velocity.

Momentum balance for the liquid phase is expressed as

$$\partial_t \{\alpha_\ell \rho_\ell w_\ell\} + \partial_x \{w_\ell \alpha_\ell \rho_\ell w_\ell\} + \alpha_\ell \partial_x \{p_\ell\} = \alpha_\ell \rho_\ell g_x + \tau_{\ell\mathrm{s}}, \tag{3.2}$$

where p_ℓ is the pressure, g_x is the x-component of the gravitational acceleration vector and $\tau_{\ell\mathrm{s}}$ represents the frictional force between the solid and the liquid phase. The terms of the right-hand side of the momentum equation are thus $\alpha_\ell \rho_\ell g_x$ due to gravitational forces and $\tau_{\ell\mathrm{s}}$ due to friction. Any other forces acting on the liquid are ignored here.

Energy balance for the liquid phase is expressed as

$$\partial_t \{\alpha_\ell \rho_\ell e_\ell\} + \partial_x \{w_\ell \alpha_\ell \rho_\ell e_\ell + w_\ell \alpha_\ell p_\ell + j_\ell\} = \alpha_\ell \rho_\ell g_x w_\ell + \epsilon_{\ell\mathrm{s}}, \tag{3.3}$$

where $e_\ell = u_\ell + w_\ell^2/2$ is the sum of the internal and kinetic energy per liquid mass. The term $\epsilon_{\ell\mathrm{s}}$ accounts for flow of heat from the solid phase and j_ℓ is the heat flux from e.g. thermal conduction through the liquid.

Since the solid is rigid, incompressible and chemically inert, it only has an energy equation

$$\partial_t \{\alpha_\mathrm{s} \rho_\mathrm{s} u_\mathrm{s}\} + \partial_x \{j_\mathrm{s}\} = -\epsilon_{\ell\mathrm{s}}, \tag{3.4}$$

where j_s is the heat flux through the solid.

The unknown quantities in this description are T_ℓ, T_s, u_ℓ, u_s, ρ_ℓ, w_ℓ, p_ℓ, $\tau_{\ell\mathrm{s}}$, $\epsilon_{\ell\mathrm{s}}$ j_ℓ and j_s, giving the a total of eleven unknowns. To determine these, we have the four balance equations: liquid mass (3.1), liquid momentum (3.2), liquid energy (3.3) and solid energy (3.4). Assuming local

equilibrium and that the liquid and solid can be described at every point by one bulk-phase equation of state (EOS) each, we also have three constitutive relations provided by these EOS: $u_\ell\left(T_\ell, \rho_\ell\right)$, $u_\mathrm{s}\left(T_\mathrm{s}\right)$, $p_\ell\left(T_\ell, \rho_\ell\right)$. To close the system, models for $\tau_{\ell\mathrm{s}}$, $\epsilon_{\ell\mathrm{s}}$, j_ℓ and j_s may be selected. The second law of thermodynamics requires a positive local entropy production and this gives constraints on what kind of models for that are acceptable.

3.1.1 Entropy production

We start the derivation of the entropy production by combining the liquid mass and momentum equations, (3.1) and (3.2), to get a balance equation for the kinetic energy,

$$\begin{aligned}\partial_t\left\{\frac{1}{2}\alpha_\ell\rho_\ell\left\{w_\ell\right\}^2\right\}+\partial_x\left\{w_\ell\frac{1}{2}\alpha_\ell\rho_\ell\left\{w_\ell\right\}^2\right\}\\ =\alpha_\ell\rho_\ell g_x w_\ell+\tau_{\ell\mathrm{s}}w_\ell-w_\ell\alpha_\ell\partial_x\left\{p_\ell\right\}.\end{aligned}\tag{3.5}$$

Introducing this into the energy equation (3.3) gives a balance equation for the internal energy,

$$\begin{aligned}\partial_t\left\{\alpha_\ell\rho_\ell u_\ell\right\}+\partial_x\left\{w_\ell\alpha_\ell\rho_\ell u_\ell\right\}\\ =\epsilon^{\mathrm{s}\ell}-\partial_x\left\{j_\ell\right\}-\tau_{\ell\mathrm{s}}w_\ell-p_\ell\partial_x\left\{w_\ell\alpha_\ell\right\}.\end{aligned}\tag{3.6}$$

The terms on the right-hand side are, respectively, due to heat flow into the liquid from the solid, heat flow through the liquid, dissipation of kinetic energy due to friction and compression.

The entropy equation for the liquid can now be obtained by introducing (2.11)[1], the internal energy differential $\mathrm{d}u_\ell = T_\ell \mathrm{d}s_\ell + \left\{p_\ell/\rho_\ell^2\right\}\mathrm{d}\rho_\ell$, in combination with the mass balance equation (3.2) into the internal energy equation (3.6). This yields

$$\partial_t\left\{\alpha_\ell\rho_\ell s_\ell\right\}+\partial_x\left\{w_\ell\rho_\ell s_\ell+\frac{j_\ell}{T_\ell}\right\}=\frac{\epsilon_{\ell\mathrm{s}}}{T_\ell}-\frac{\tau_{\ell\mathrm{s}}w_\ell}{T_\ell}+j_\ell\partial_x\left\{\frac{1}{T_\ell}\right\}.\tag{3.7}$$

[1]Equation (2.11) has the same form when expressed in terms of mass-specific rather than molar quantities. This can be seen by dividing it by the molar mass m and letting $u/m \mapsto u$, $s/m \mapsto s$ and $\rho m \mapsto \rho$.

A similar approach for the solid phase, where $\mathrm{d}u_\mathrm{s} = T_\mathrm{s}\mathrm{d}s_\mathrm{s}$, yields the entropy equation,

$$\partial_t \left\{\alpha_\mathrm{s}\rho_\mathrm{s}s_\mathrm{s}\right\} + \partial_x \left\{\frac{j_\mathrm{s}}{T_\mathrm{s}}\right\} = -\frac{\epsilon_{\ell\mathrm{s}}}{T_\mathrm{s}} + j_\mathrm{s}\partial_x \left\{\frac{1}{T_\mathrm{s}}\right\}. \tag{3.8}$$

Adding together the two entropy equations, the sum of the right-hand sides give the local entropy production,

$$\sigma = \epsilon_{\ell\mathrm{s}} \left\{\frac{1}{T_\ell} - \frac{1}{T_\mathrm{s}}\right\} - \frac{\tau_{\ell\mathrm{s}}w_\ell}{T_\ell} + j_\ell\partial_x \left\{\frac{1}{T_\ell}\right\} + j_\mathrm{s}\partial_x \left\{\frac{1}{T_\mathrm{s}}\right\}. \tag{3.9}$$

The current model should, of course, obey the second law of thermodynamics and have a positive σ. Choosing the constitutive models for $\tau_{\ell\mathrm{s}}$, $\epsilon_{\ell\mathrm{s}}$, j_ℓ and j_s such that all terms in (3.9) are positive is sufficient to ensure this. The first term is positive if heat flows from the hotter to the cooler phase. The second term is positive if the frictional force always acts in the direction opposite to the flow velocity. The final two terms are positive if the heat flux within each phase is against temperature gradient.

3.1.2 Darcy's law

In this section, we give a brief motivation for Darcy's law. For more formal derivations based on volume averaging, we refer to [63, 62].

The dimensionless Reynolds number is [64, p. 57],

$$\mathrm{Re} = \frac{\rho w l}{\eta}, \tag{3.10}$$

where ρ, w, l and η are, respectively, the characteristic density, flow velocity, length scale and viscosity. In porous media flow, l may be chosen as the typical pore diameter. The Reynolds number represents the ratio of inertial to viscous forces.

If the porous medium we are considering has relatively small pores and the liquid flowing through it is relatively viscous, the flow will be characterized by a low Reynolds number. At low Reynolds numbers, the flow in each pore is laminar and, inspired by the case of Poiseuille flow [64, pp. 51, 58], we may model the average frictional force per volume of liquid as proportional to the viscosity η_ℓ and to the flow velocity w_ℓ. If we

then choose the constant of proportionality as φ/κ, and thus define the permeability κ, we can set

$$\frac{\tau_{\ell \mathrm{s}}}{\alpha_\ell} = -\frac{\varphi}{\kappa}\eta_\ell w_\ell. \tag{3.11}$$

From (3.9) it is easily confirmed that this model for $\tau_{\ell \mathrm{s}}$ leads to positive entropy production from the frictional force term.

Since the Reynolds numbers are low, we may also neglect the inertial term in the momentum equation (3.2). Steady-state flow is then governed by a much simplified version of the momentum balance equation (3.2),

$$\frac{\tau_{\ell \mathrm{s}}}{\alpha_\ell} = \partial_x \left\{p_\ell\right\} - \rho_\ell g_x. \tag{3.12}$$

Combining (3.12) and (3.11) we get Darcy's law

$$q_\ell = -\frac{\kappa}{\eta_\ell}\left\{\partial_x \left\{p_\ell\right\} - \rho_\ell g_x\right\}, \tag{3.13}$$

where the volumetric flux $q_\ell = w_\ell \alpha_\ell$ has been introduced. This equation is named after the French hydraulic engineer and scientist Henry Philibert Gaspard Darcy.[2]

One important feature of (3.13) is that it separates the proportionally factor κ/η_ℓ in two numbers, where the viscosity η_ℓ is a property of the liquid and the permeability κ is a property of the porous medium. Therefore, if the permeability of a porous medium is measured using one liquid, the flow rate of another fluid is easily calculated, if its viscosity is known.[3]

In many cases, it is reasonable to assume that the liquid is incompressible, i.e. that ρ_ℓ is a constant. In such a case, the steady-state mass conservation equation is $\partial_x \left\{w_\ell \alpha_\ell\right\} = 0$, stating that the volume flux q_ℓ is

[2]Darcy is famously credited for designing the public water system of Dijon, France in the 1840s [65]. The design and construction was documented in his book with the English title "The Public Fountains of the City of Dijon" [66], published in 1856. In this book, Darcy's formulation of (3.13) appears in Appendix D, a part concerned with water filters utilizing sand.

[3]A necessary condition for this to hold is that the no-slip condition on the solid surfaces is satisfied, which it typically is for liquids, but is not always for gases. Gases may slip at the solid walls when their mean free path is not small w.r.t. the pore size. This is known as the Klinkenberg effect. Darcy's law is then invalid or the permeability must be corrected [67].

constant along the x-direction. Equation (3.13) is then easily integrated over a finite length L with uniform κ to yield

$$q_\ell = -\frac{\kappa}{\eta_\ell}\left\{\frac{\Delta p_\ell}{L} - \rho_\ell g_x\right\}, \tag{3.14}$$

where Δp_ℓ is the pressure difference over the length L.

This section has treated the case of single-phase flow in porous media. The problem of two-phase flow is considerably more complex. This is, in part, due to the presence of interfaces between the two fluids and the existence of two different kinds of fluid-solid interface [68]. At high flow rates, however, where the viscous forces are much larger than the interfacial forces, these interfacial forces should not be important for the fluid flow. By simulations with a pore network model and the lattice-Boltzmann method, **Paper V** finds that horizontal two-phase flow can be described by Darcy-type equation similar to (3.14), where the viscosity η_ℓ is replaced by an effective viscosity.

3.2 Immiscible two-phase flow

Compared to the case of single-phase flow, two-phase flow in porous media is much more complex and exhibits a richer range of physical effects. The two phases can have different viscosities and densities, and viscous and gravitational forces may thus affect them differently. Furthermore, three types of interface are now present [68]. This results in interfacial, i.e. capillary, forces that affect the flow. Capillary forces tend to dominate when flow rates are low and viscous forces are small. One phase will usually wet the solid to a lager degree than the other. We therefore adopt a widely used convention and label the most wetting phase "wetting" (w) and the least wetting phase "non-wetting" (n). We restrict the attention to immiscible flow, where particles from one phase may not be transferred to the other. The terms phase and fluid will be used interchangeably in this section.

To characterize two-phase flow, the dimensionless capillary number and the viscosity ratio are often used. The capillary number describes the

ratio of viscous to capillary forces,

$$\mathrm{Ca} = \frac{\eta w}{\gamma_{\mathrm{wn}}}, \tag{3.15}$$

where η is the characteristic fluid viscosity, γ_{wn} is the fluid-fluid interfacial tension and w is a characteristic flow velocity. The viscosity ratio is

$$M = \frac{\eta_{\mathrm{n}}}{\eta_{\mathrm{w}}}. \tag{3.16}$$

In their seminal work, Lenormand, Touboul, and Zarcone [11] set up maps in terms Ca and M to describe drainage processes. In drainage, the non-wetting fluid flows into a porous medium and displaces the wetting fluid. The opposite process is called imbibition. For drainage, they identified three types of displacement regime: (i) Stable displacement, which occurs when the viscous forces in the injected fluid dominate. This results in a more or less flat displacement front. (ii) Viscous fingering is obtained when viscous forces in the displaced fluid dominate. Tree-like structures then emerge, which grow in direction of the outlet. (iii) Capillary fingering occurs when capillary forces dominate. This regime is characterized by tree-like structures that grow in all directions, also backwards toward the inlet. Example drainage processes representing these three regimes simulated with the pore network model from **Paper IV** are shown in Figure 3.1. An example of a practical consequence of these displacement regimes is their effect on the storage efficiency of CO_2 in geological sequestration, see e.g. [4].

3.2.1 Haines jumps

One important concept in drainage is Haines jumps [69]. An illustration of such jumps, simulated by the pore network model in **Paper IV**, is shown in Figure 3.2. As non-wetting fluid is injected into a porous medium at constant flow rate, the external pressure needed to drive the flow fluctuates [70]. Due to capillary forces, an increasingly larger pressure is needed when the invasion front moves into narrowing necks. When the non-wetting fluid front breaks through a neck and invades a new pore, there is a sudden drop in the driving pressure. For low injection rates, it has been observed that the invasion front retracts near the point of

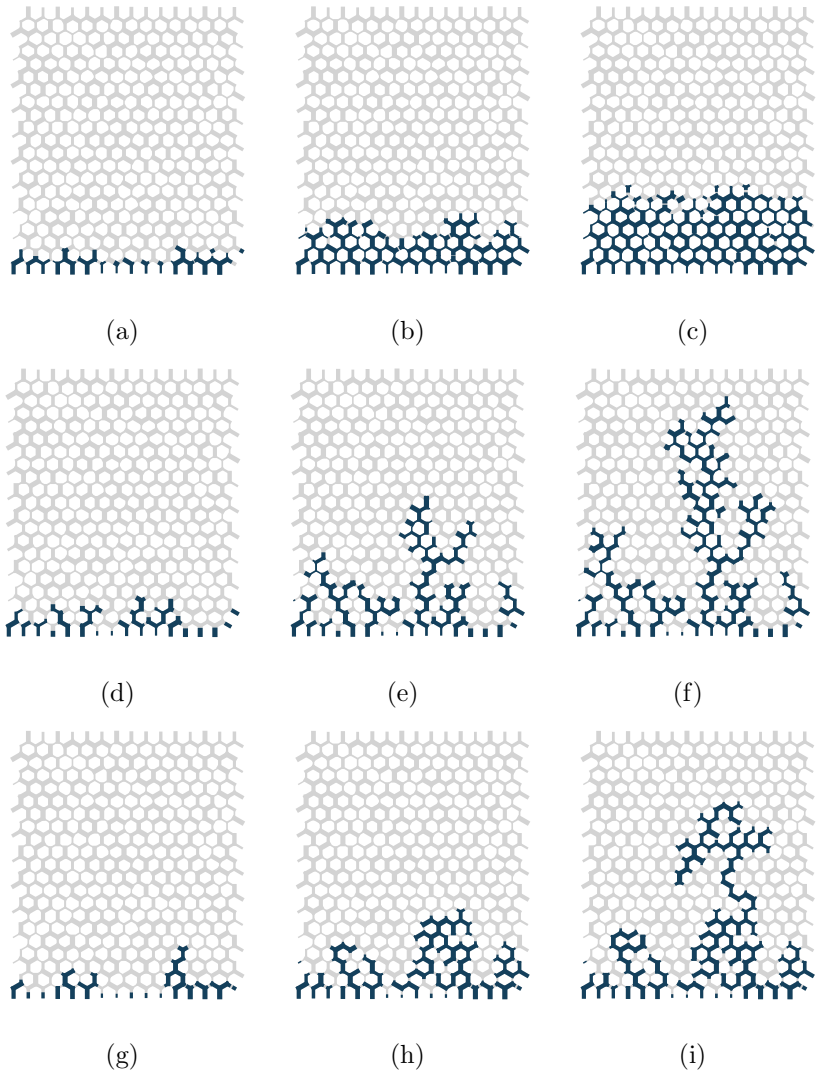

Figure 3.1: Example displacement patterns simulated with the pore network model from **Paper IV**. Figures (a)-(c) show an example drainage process from the stable displacement regime ($\mathrm{Ca} = 10^{-1}$, $M = 10^{2}$), (d)-(f) show one from the viscous fingering regime ($\mathrm{Ca} = 10^{-4}$, $M = 10^{-3}$) and (g)-(i) one from the capillary fingering regime ($\mathrm{Ca} = 10^{-6}$, $M = 1$). The networks are periodic in the horizontal direction. Drawn link widths are chosen for illustrative purposes and are not to scale.

break-through [70, 71], because the non-wetting fluid volume needed to fill the newly invaded pores must be supplied internally rather than from the external feed. Local flow velocities during these events may be large, even though the injected flow rate is small. They may thus contribute significantly to viscous dissipation [72, 4] and to entropy production and the detriment of energy efficiency in the drainage process.

The capillary number in Figure 3.2 is 10^{-5}. Numerical instabilities at low capillary numbers is a long-known problem for various types of dynamic pore network models [73], and a whole section was devoted to this topic in the comprehensive review by Joekar-Niasar and Hassanizadeh [22]. The pore network model in **Paper IV** is of the Aker type [74]. When this kind of model is used, numerical instabilities are observed as interfaces jumping back and forth between consecutive time steps, in a manner that is unphysical and certainly not observed in experiments. This has restricted use of the model to relatively high capillary numbers. Proper resolution two-phase flow at low capillary numbers, and Haines jumps in particular, require stable simulations. **Paper IV** describes how this can be achieved and uses a Haines jump test case to demonstrate that simulations are indeed stabilized.

3.2.2 The extended Darcy equations

On the continuum scale, the fine pore-scale details of displacement patterns such as those in Figure 3.1 are averaged out. Each point in space represents an average over many pores and therefore has both wetting fluid, non-wetting fluid and solid in it. Their respective volume fractions are α_{w}, α_{n} and α_{s}. A fundamental variable in porous media literature is the saturation. The saturation of phase i is the fraction of the pore volume occupied by that phase, i.e. α_i/ϕ.[4] The volumetric flow rate of phase i per area of porous medium is q_i. The average flow velocity is $w_i = q_i/\alpha_i$.

One treatment of two-phase flow on the continuum scale, that seeks to have a large degree of generality, can be found in [75, 76]. This approach explicitly considers interfaces and employs macroscopic balance equations for mass, momentum and energy for each phase and each interface. To

[4] To avoid a notational conflict with the entropy, we do not give the saturation its own symbol here and use instead α_i/ϕ.

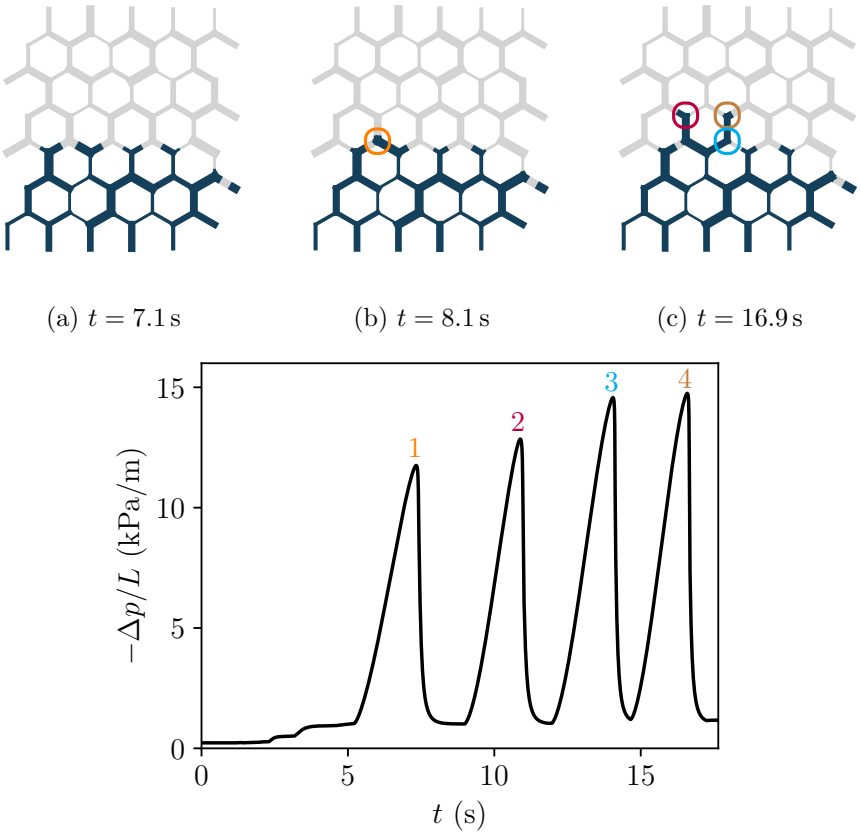

(a) $t = 7.1\,\mathrm{s}$ (b) $t = 8.1\,\mathrm{s}$ (c) $t = 16.9\,\mathrm{s}$

(d)

Figure 3.2: Illustration of Haines jumps simulated with the pore network model from **Paper IV**, with Ca $= 10^{-5}$ and $M = 1$. Non-wetting fluid (blue) is injected at the bottom of the networks in (a)-(c) at a constant rate and displaces the wetting fluid (grey). The pressure at the top of the network is fixed while that at the bottom is varied in order to get the specified flow rate. The drainage process proceeds by successive invasion of pores. The invaded pores are indicated by circles in (a)-(c). Each invasion is here associated with a spike in driving pressure (d). The network is periodic in the horizontal direction. Drawn link widths are chosen for illustrative purposes and are not to scale.

make predictions, however, constitutive relations are needed and, in most practical cases, some simplifying assumptions. The extended Darcy equations represent one such choice of assumptions and constitutive relations. Another approach to the description of flow on the continuum scale was given by Kjelstrup et al. [77].

We discuss here a much less general case with an incompressible, rigid and chemically inert solid phase and two fluid phases, w and n, that are immiscible and do not exchange particles. As in the single-phase case, the solid density ρ_s is a constant and the solid volume fraction α_s and the porosity φ are a known quantities that vary only in space and not in time. Furthermore, we assume thermal equilibrium between all phases and they thus have the same temperature T at every point.

Fluid mass is conserved, and this is expressed on the continuum scale as [23]

$$\partial_t \left\{\alpha_i \rho_i\right\} + \partial_x \left\{w_i \alpha_i \rho_i\right\} = 0, \tag{3.17}$$

for each phase $i \in \{\mathrm{w}, \mathrm{n}\}$. The traditional way of modelling the fluid flow is to use a two-phase extension of Darcy's law (3.13) [23],

$$w_i \alpha_i = -\frac{\kappa \kappa_i^\mathrm{r}}{\eta_i} \left\{\partial_x \left\{p_i\right\} - \rho_i g_x\right\}, \tag{3.18}$$

where κ_i^r is the relative permeability of phase i. In this approach, it is assumed that the flow of each fluid can be described by Darcy's law, where the effective permeability of the porous medium to one fluid is reduced by a factor, the relative permeability, due to the presence of the other. This idea dates back to the experimental work of Wyckoff and Botset [78] from the 1930s. They studied the simultaneous flow of CO_2 and water through sand and recorded the reduction in effective permeability of both fluids, relative to the single-phase flow cases, for different water saturations.

In the flow description consisting of (3.17) and (3.18), η_w, η_w, κ, φ and g_x may be assumed known. There are then eleven unknown quantities: T, α_w, α_n, ρ_w, ρ_n, p_w, p_n, w_w, w_n, $\kappa_\mathrm{w}^\mathrm{r}$ and $\kappa_\mathrm{n}^\mathrm{r}$. To determine these, we have two mass conservation equations (3.17), two constitutive relations for the flow rate (3.18) and $\alpha_\mathrm{w} + \alpha_\mathrm{n} = \varphi$. With the additional assumption of local equilibrium and the applicability of bulk-phase EOS, the relations $p_\mathrm{w}\left(T, \rho_\mathrm{w}\right)$ and $p_\mathrm{n}\left(T, \rho_\mathrm{n}\right)$ may be provided. We then need an additional four

constitutive equations to close the system. One is obtained by specifying a known temperature T, or an energy equation. The other three are often functional relationships for $\kappa_{\mathrm{w}}^{\mathrm{r}}$, $\kappa_{\mathrm{n}}^{\mathrm{r}}$, and $p_{\mathrm{n}} - p_{\mathrm{w}}$, in terms of the other variables in the problem. The quantity $p_{\mathrm{n}} - p_{\mathrm{w}}$ is often identified as the capillary pressure p^{c} [24].

When closure is obtained using the capillary pressure, it often assumed to be a function of saturation, i.e. $p^{\mathrm{c}}(\alpha_{\mathrm{w}}/\varphi)$. In this case, p^{c} may depend on the history of the porous medium and be different for e.g. a drainage process and an imbibition process following it. It has been suggested that the reason for this is, in part, the incomplete functional dependence of the capillary pressure and that more variables must be introduced to represent the fluid distribution in the porous medium [24, 79, 68].

If the fluids are assumed incompressible and isothermal, so that ρ_{w}, ρ_{n} and T are known constants, the mass conservation equations (3.17) and the extended Darcy equations (3.18) may be combined to give

$$\partial_t \{\alpha_{\mathrm{w}}\} + \partial_x \{w_{\mathrm{w}} \alpha_{\mathrm{w}}\} = 0, \tag{3.19}$$

and

$$\partial_x \left\{ \frac{\kappa \kappa_{\mathrm{w}}^{\mathrm{r}}}{\eta_{\mathrm{w}}} \{\partial_x \{p_{\mathrm{w}}\} - \rho_{\mathrm{w}} g_x\} + \frac{\kappa \kappa_{\mathrm{n}}^{\mathrm{r}}}{\eta_{\mathrm{n}}} \{\partial_x \{p_{\mathrm{n}}\} - \rho_{\mathrm{n}} g_x\} \right\} = 0, \tag{3.20}$$

with unknowns α_{w}, α_{n}, p_{w}, p_{n}, w_{w}, w_{n}, $\kappa_{\mathrm{w}}^{\mathrm{r}}$ and $\kappa_{\mathrm{n}}^{\mathrm{r}}$. A closed system may be obtained by combining the two equations above with $\alpha_{\mathrm{w}} + \alpha_{\mathrm{n}} = \varphi$, (3.18) and constitutive relations for $\kappa_{\mathrm{w}}^{\mathrm{r}}$, $\kappa_{\mathrm{n}}^{\mathrm{r}}$, and $p_{\mathrm{n}} - p_{\mathrm{w}}$.

Although the extended Darcy equations are widely used and have, arguably, been useful in many engineering applications, see e.g. [3, 80, 81], their theoretical foundation is not as sound as that of Darcy's law for single-phase flow. As stated by Miller et al. [23], "While the relationship between this approach and a formal momentum balance approach has been established for the limiting case of low Reynolds number in single-fluid systems, the common multiphase extension of Darcy's law to multiphase systems is not rigorously based.".

Hassanizadeh and Gray [76] do give a derivation of the extended Darcy equations, based on formal averaging and explicit consideration of interfaces. To obtain them, however, they rely on a number of simplifying assumptions. Among them is a first-order expansion of the dissipative

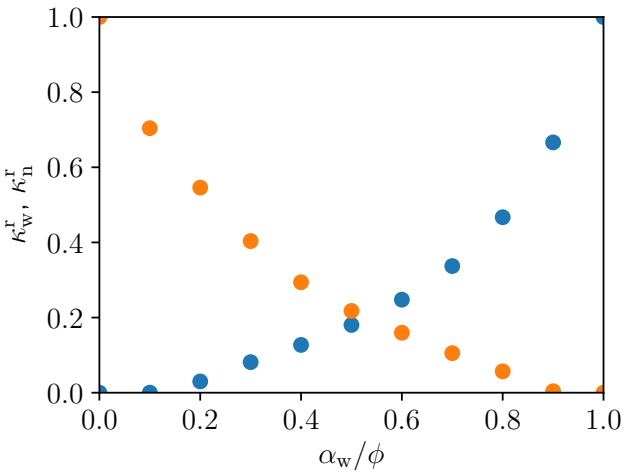

Figure 3.3: Example relative permeabilities for the network shown in Figure 3.1 computed with the pore network model described in **Paper IV** and a constant pressure gradient. Fluid viscosities are equal, i.e. $M = 1$.

friction forces in the velocities of the fluids and interfaces, relative to the solid. This should be valid close to equilibrium, when these velocities are small, but the linear relation between flow rate and pressure gradient is nonetheless an assumption in the derivation and not a result of it. Further necessary assumptions include that coupling between velocities can be ignored. Other approaches to a derivation of the extended Darcy equations are given in e.g. [82, 83].

Relative permeabilities are often assumed to be functions of the saturations only, and an illustration of how relative permeabilities may vary with saturation is provided in Figure 3.3. It is, however, well established that this is not generally the case, see e.g. [84, 12, 85, 14, 86]. In particular, dependence on capillary number and on fluid properties such as fluid-fluid interfacial tension and viscosity ratio has been reported. The dependence of relative permeabilities on fluid properties makes them very different from the absolute permeability κ, which is a property of the porous medium.

Using the extended Darcy equations is thus complicated by the need

for a number of assumptions to be valid. It may be difficult to know for, say, a given experiment, that they are. The view may then be taken that the extended Darcy equations define the relative permeabilities. The equations are thus valid, regardless of the validity of the underlying assumptions, because the relative permeabilities take on any value that satisfies the equations. They thus obtain a complex functional dependence that may be explored and correlated experimentally or using computer simulations. The relative permeabilities may in this case be understood as dimensionless quantities that can be used descriptively and the extended Darcy equations as a framework in which to present results of experiments and computer simulations. This seems to be the view taken in practice by many works.

The work in **Paper V** and **Paper VI** both represent efforts to extract information about continuum-scale two-phase flow in steady-state. The approach is to use, mainly,[5] the pore network model described in **Paper IV**, which resolves the flow on the pore scale, and subsequently compute time-averaged quantities for the entire network. In **Paper VI**, steady-state flow rates are computed for a number of different pressure gradients, wetting fluid saturations, pore sizes, fluid viscosities and fluid-fluid interfacial tensions. The results are presented and discussed using dimensionless numbers and the relative permeabilities are two of them. Incompressible flow is considered in a macroscopically one-dimensional case with no gravity and periodic boundary conditions. As a result of the boundary conditions, there is no difference between the pressure gradients in the two fluids.

The pore network model used is of the Aker type, which has been used extensively to study various aspects of steady-state flow [87, 88, 89, 90, 91]. In particular, Knudsen, Aker, and Hansen [87] performed simulations with equal viscosities, i.e. $M = 1$, and one value for the interfacial tension, and studied the effect of changing total flow rate on fractional flow and relative permeabilities. **Paper VI** is an extension of this work, which considers the effect of viscosity ratio and discusses the results in light of the findings at high capillary numbers in **Paper V**.

[5] Lattice-Boltzmann simulations are also used in **Paper V**.

Chapter 4

Summary of results and conclusions

This chapter reviews the most important results and contributions of the papers included in this thesis and their conclusions.

4.1 Paper I

> P. Aursand, M. Aa. Gjennestad, E. Aursand, M. Hammer, and Ø. Wilhelmsen. The spinodal of single- and multi-component fluids and its role in the development of modern equations of state. *Fluid Phase Equilibria* 436 (2017), pp. 98–112. DOI: 10.1016/j.fluid.2016.12.018

The criteria for thermodynamic stability of a single-component homogeneous phase, at constant temperature, volume and number of particles, were derived in Section 2.1.3. **Paper I** considers the thermodynamic stability of mixtures and considers also different ensembles. While the stability criteria for these cases are known, see e.g. [44], **Paper I** presents a robust methodology for calculating the spinodal curves and applies this method to several advanced equations of state (EOS), including PC-SAFT [41] and GERG-2008 [43]. The spinodal curve represents the limit of thermodynamic stability, where a stable homogeneous phase becomes unstable. Gas and liquid spinodals are calculated and compared for

a range of different EOS and large differences are observed, particularly for the gas spinodals. If the locations of the spinodals can be determined, this could be used in the fitting of EOS and improve predictions in the metastable regions.

EOS may predict pseudo-stable single-component states, between the gas and liquid spinodals. Such states are perhaps most easily recognized in some modern EOS like GERG-2008, as they are manifested in this case in the slope of the pressure-volume isotherm, but it is found in **Paper I** that they are present also in the much simpler van der Waals equation of state (2.13). As such states have, to the authors' knowledge at least, never been observed, they should not be predicted by an EOS either. **Paper I** presents inequality constraints that could be used in the fitting of single-component EOS parameters to avoid them. If satisfied, the constrains guarantee no pseudo-stable states between the spinodals, regardless of choice of ensemble.

In bulk-phase experiments to measure properties of homogeneous phases, thermal fluctuations will trigger homogeneous nucleation before the spinodal is reached. This occurs at the limit of superheat for liquids and at the limit of supersaturation for gases. The region between the limit of superheat/supersaturation and the spinodals is thus inaccessible in such experiments. In **Paper I**, superheat and supersaturation limits are calculated using classical nucleation theory and superheat limits are found to agree well with experimental data. Despite being unable to predict nucleation rates accurately, classical nucleation theory works well to predict superheat limits because these are insensitive to errors in the nucleation rate.

4.2 Paper II

> M. Aa. Gjennestad and Ø. Wilhelmsen. Thermodynamic stability of droplets, bubbles and thick films in open and closed pores. *Fluid Phase Equilibria* 505 (2020), p. 112351. DOI: 10.1016/j.fluid.2019.112351

Paper I was concerned with the stability of homogeneous phases. **Paper II** considers the thermodynamic stability of heterogeneous structures in

a pore, i.e. free and adsorbed droplets and bubbles and thick films, see Figure 2.4. This is done by employing capillary models for each structure. These models were briefly introduced in Section 2.2.2, and include up to three types of interface: liquid-solid, gas-liquid and gas-solid. The examined systems are isothermal and the effects on stability of pore size and whether or not the pore is closed, i.e. containing a fixed number of particles, or open, and allowed to exchange particles with a reservoir with constant chemical potential, is examined. Water at 358 K, as described by the cubic-plus-association modification of the Soave–Redlich–Kwoing EOS, is used as the example fluid.

The capillary model describing the film is formulated as a functional integral representing its Helmholtz energy. While identification of stationary states (with vanishing first variation) of this functional can be done by solving the Euler–Lagrange equation [92], this approach does not give any information about the stability of such states. A new methodology is therefore presented, and documented in detail in the supplementary material, that can be used to discretize the functional integrals and thus asses stability. The procedure is general and can be applied to many problems in variational calculus. It is utilized also in **Paper III**.

It is found that the observed instabilities for the films and the adsorbed droplets/bubbles belong to one of two distinct classes: (1) translation and (2) condensation/evaporation. The general trend is that translation instabilities are observed in the closed pores while both translation and condensation/evaporation instabilities are seen in the open pores, but some exceptions are seen.

The thermodynamic stability limit of adsorbed droplets and bubbles in both large open and large closed pores is determined by their mechanical stability. Mechanical stability is closely linked to the pore shape. This is also the case for a film in a closed pore. In open pores, the film is chemically unstable except for very low film-phase contact angles and for a limited range in external pressure. The difference in thermodynamic stability in open and closed pores and the presence of condensation/evaporation instabilities emphasizes the importance of not restricting the focus to mechanical force balance and mechanical stability and instead use a more complete thermodynamic analysis.

Phase diagrams are presented that show the stable structures with

the lowest free energy, the equilibrium structures. For the closed pore, the phase diagram is mapped out in terms of contact angles and average particle density. An important feature is the appearance and increase in size of regions in the phase diagram where the homogeneous phase is the equilibrium structure, as pore size is reduced.

4.3 Paper III

> M. Aa. Gjennestad and Ø. Wilhelmsen. Thermodynamic stability of volatile droplets and thin films governed by the disjoining pressure in open and closed containers. *Langmuir* 36 (2020), pp. 7879–7893. DOI: 10.1021/acs.langmuir.0c00960

Paper III is focused on systems consisting of thin liquid films and droplets adsorbed on the flat solid surface of a container's inside wall. A gas phase fills the volume of the container that is not occupied by liquid, and the gas and liquid phases may exchange particles with each other. The systems are considered isothermal and water at 293.15 K is used as the example fluid.

A capillary-type description is used and this is based on an EOS that models the bulk-phase liquid behaviour and a model for the disjoining pressure [50] as a function of film thickness. The fundamental assumption is that any departure from bulk-phase behaviour exhibited by the film is captured by the disjoining pressure. Two analytically obtainable results from the relation is that the film-solid interfacial tension depends on the film thickness and the reproduction of Derjaguin's equation (2.50) for the contact angle of a large droplet in mechanical force balance with a thin film.

The same discretization approach as in **Paper II** is applied to numerically evaluate the thermodynamic stability of both flat films and droplets in coexistence with flat films. The often-cited criterion for stability of a flat film is that the film is stable when the derivative of disjoining pressure w.r.t. film thickness is negative. It is found that this criterion applies in open systems due to the presence of a condensation/evaporation instability whenever the criterion is not satisfied. In closed systems, however, stability is governed by mechanical instabilities of a similar type as those

responsible for spinodal dewetting in non-volatile systems. Such instabilities require a substrate size that is large enough to support the minimum unstable wavelength, see (2.49). Flat films are thus stable when the substrate size is smaller than this wavelength.

Droplets that are in coexistence with thin films are found to be unstable for all the considered examples when the container is open. In a closed system, on the other hand, such droplets may be stable under specific conditions. Unstable droplets in both the open and closed containers represent saddle points in their respective energy landscapes. In the closed system, they represent the activation barrier for the transition between a stable flat film and a stable droplet. In the open system, the unstable droplet represents the activation barrier for the creation of a bulk liquid phase from a flat film.

By comparing the Helmholtz energy of flat films and droplets at different values of average density in the container, it is found that flat films are the equilibrium configuration up to a certain value of the average density. At this value, there is a morphological phase transition and above it the equilibrium configuration is a droplet.

4.4 Paper IV

> M. Aa. Gjennestad, M. Vassvik, S. Kjelstrup, and A. Hansen. Stable and efficient time integration at low capillary numbers of a dynamic pore network model for immiscible two-phase flow in porous media. *Frontiers in Physics* 6 (2018), p. 56. DOI: 10.3389/fphy.2018.00056

The pore network model used in **Paper V** and **Paper VI** is of the Aker type [74]. This kind of model is dynamic and takes both viscous and capillary forces into account. The location of each fluid-fluid interface is kept track of and evolved in time, according to the calculated pressures and flow rates in each pore, by integrating one ordinary differential equation (ODE) per interface. Previously, this model suffered from numerical instabilities when integrated with explicit methods at low capillary numbers. These were artefacts of the numerical methods and resulted in interfaces jumping back and forth between consecutive time steps. This restricted

use of the model to relatively high capillary numbers. **Paper IV** presents two strategies to eliminate the instabilities.

The first is a new time step criterion used to control the maximum length of time steps used when integrating the ODEs in time. It is demonstrated that this criterion stabilizes the two explicit methods considered in the paper, the forward Euler method and the midpoint method. The new time step criterion is independent of flow rate and therefore becomes quite severe when flow rates are low and this typically results in long simulation wall times for such cases.

The second strategy is a semi-implicit method. This approach achieves stabilization without the need to enforce the severe time step restriction. The result is superior efficiency at capillary numbers lower than $\sim 10^{-5}$ for the test case run. The range of capillary numbers for which the pore network model is a tractable alternative is thus vastly increased. The cost of the semi-implicit method is the need to solve a non-linear system of equations in every time step, instead of the linear systems required by the explicit methods.

A Haines jump case is simulated. This shows that all three methods were able to resolve both the pressure build-up and the subsequent fluid redistribution, including interfacial retraction along the invasion front, in a stable manner. These are phenomena which occur on vastly different time scales when capillary numbers are low.

4.5 Paper V

> S. Sinha, M. Aa. Gjennestad, M. Vassvik, M. Winkler, A. Hansen, and E. G. Flekkøy. Rheology of high-capillary number flow in porous media. *Frontiers in Physics* 7 (2019), p. 65. DOI: 10.3389/fphy.2019.00065

As briefly discussed in Section 3.2, two-phase flow in porous media is a complex topic and its continuum-scale description is still a topic of debate. **Paper V** finds, however, that in the high-capillary number limit, the total flux $q = q_{\mathrm{w}} + q_{\mathrm{n}}$ in steady-state can be described by an equation similar to Darcy's law for single-phase flow (3.14), where the viscosity η_ℓ is replaced by an effective viscosity. The effective viscosity $\bar{\eta}$ is given in terms of

the viscosities of each fluid by the Lichtenecker–Rother equation and its exponent ε,

$$\bar{\eta}^{\varepsilon} = \frac{\alpha_{\mathrm{w}}}{\phi}\eta_{\mathrm{w}}^{\varepsilon} + \frac{\alpha_{\mathrm{n}}}{\phi}\eta_{\mathrm{n}}^{\varepsilon}. \tag{4.1}$$

Simulations are performed using both the pore network model from **Paper IV** and the lattice-Boltzmann method. The pore network model simulations are time-dependent and resolve flow and interface locations in each pore. Continuum-scale steady-state time-averaged flow rates and pressure drops are calculated by time-averaging flow rates and pressure drops for the entire network. Periodic boundary conditions are applied.

The ε-exponent is found to depend on the degree of coupling and intermixing between the two fluids. For well intermixed flow with small bubbles, $\varepsilon = 1$ is found both with the pore network model and with the lattice-Boltzmann method. An exponent $\varepsilon = 0.6$ is found in the pore network model if bubbles are larger and the fluids thus less intermixed. A regime with lubrication layers and some degree of parallel flow in the pores is also obtained from another set of lattice-Boltzmann simulations, and this regime results in $\varepsilon = -0.5$.

4.6 Paper VI

> M. Aa. Gjennestad, M. Winkler, and A. Hansen. Pore network modeling of the effects of viscosity ratio and pressure gradient on steady-state incompressible two-phase flow in porous media. *Transport in Porous Media* 132 (2020), pp. 355–379. DOI: 10.1007/s11242-020-01395-z

Paper VI presents results from 6048 steady-state pore network model simulations corresponding to a large span in viscosity ratios and capillary numbers. The simulations are similar those in **Paper V**, except that they are run at finite capillary numbers. Dimensionless steady-state time-averaged quantities, such as relative permeabilities, residual saturations, mobility ratios and fractional flows, are computed from these simulations. It is found that these computed quantities depend on three dimensionless variables, the wetting fluid saturation α_{w}/ϕ, the viscosity ratio M and a

dimensionless pressure gradient. Effects of wettability, gravity and inertia are not considered.

The calculated relative permeabilities and residual saturations show many of the same qualitative features observed in other computational and experimental studies. In particular, the relative permeabilities increase with capillary numbers and converge to a limit, which depends on viscosity ratio and saturation, at high capillary numbers. However, while the consensus in the literature seems to be that relative permeabilities converge to straight lines at high capillary numbers, this is not the case for the results from the network model when $M \neq 1$. It is concluded that this is because high capillary numbers are not here obtained by running simulations in the near-critical region. In this region, interfacial tension is very small and phase properties, including viscosities, are similar.[1] Instead the two fluids considered in **Paper VI** may have different viscosities and, in the simulations run, the fluids intermix and do not form decoupled flow channels.

The average mobility is here defined as $\{q_{\mathrm{w}} + q_{\mathrm{n}}\} L/\phi\Delta p$. Ratios of average mobility to their high capillary number limit values are also considered. These ratios vary, roughly, between 0 and 1, but values larger than 1 were also observed. For a given saturation, the mobilities are not always monotonically increasing with the pressure gradient. Increasing the pressure gradient mobilizes more fluid and activates more flow paths. However, when the mobilized fluid is more viscous, the effective viscosity of the moving fluid is increased by this mobilization and a reduction in average mobility may occur instead.

[1] That gas and liquid densities become similar near the critical point is illustrated in Figure 2.2 for CO_2.

Chapter 5

Perspectives and outlook

The present thesis has considered fundamental aspects related to thermodynamic stability of homogeneous systems and heterogeneous two-phase systems at the pore scale and steady-state immiscible two-phase flow on the continuum scale. This final chapter provides a discussion of possible consequences and applications of, and future research avenues based on, the results obtained and procedures developed.

Equations of state (EOS) are frequently used to predict behaviour of phases that would be metastable in a bulk system. Examples are classical nucleation theory [93] and, indeed, the capillary models that describe heterogeneous systems with interfaces in **Paper II** and **Paper III**. Mass-based density functional theories rely in addition on information from the unstable region [32]. It is therefore important to have EOS that give accurate, or at least thermodynamically consistent, predictions in these regions. **Paper I** discussed how information about the spinodals could be used to improve accuracy in metastable region. Furthermore, inequality constrains were presented that could be used to eliminate pseudo-stable states between the spinodal lines. Such states were found to be present even in the simple van der Waals EOS (2.13).

The capillary models developed in **Paper II** modelled single-component fluids only. An obvious future extension would therefore be to consider mixtures also. The models could then be used to study capillary condensation of e.g. water from air. Furthermore, the thermodynamic stability of bubbles, both w.r.t. translation and dissolution into the other phase,

could influence capillary trapping [94] and long-term storage of CO_2 in geological formations. Another possible extension is to include line tension in the capillary models.

The fundamental relation for film phases developed in **Paper III** considered films on flat solid surfaces. This could be extended to consider films on fibres, along the lines of Neimark [53]. In this regard, it would be advantageous to also extend the discrete variational procedure to two dimensions, so that the assumption of cylindrical symmetry could be avoided. A possible avenue to follow is to study wetting of fibres. This has applications in water management in fuel cells, where accumulation of liquid water may block reactant pathways and be detrimental to performance [6], and moisture in thermal insulation materials for buildings and process equipment.

In both **Paper II** and **Paper III** systems were considered either open or closed w.r.t. exchange of particles with the surroundings. However, because migration of particles takes time, an open system may remain effectively closed at short time scales. Future work could seek to establish the time scale at which an open system remains effectively closed.

The new numerical solution procedures developed in **Paper IV** make dynamic pore network modelling computationally feasible at low capillary numbers. One phenomenon of interest in this regime is Haines jumps. **Paper IV** demonstrated that the new methods make it possible to resolve both the pressure build-up before such jumps and the subsequent pore invasion and interface retraction, even though these occur at vastly different time scales. In particular, statistics of single jumps and avalanche sizes for larger systems than accessible through direct numerical simulations or lattice-Boltzmann could be obtained. As discussed in Section 3.2, Haines jumps may involve locally large flow velocities and thus contribute significantly to viscous dissipation [72, 4]. Furthermore, they may have influence on storage and energy efficiency in CO_2 sequestration [4].

Paper VI was an effort to map out and discuss the steady-state flow properties of two-phase flow in porous media, as modelled by the dynamic pore network model described in **Paper IV**. It was observed that the studied dimensionless flow properties depended on three dimensionless variables, saturation α_w/ϕ, viscosity ratio M and a dimensionless pressure gradient. In the high-Ca limit, there was only a dependence of α_w/ϕ and

M. In future, one could explore what can be learned about the connection between macroscopic flow properties and flow regimes. As discussed by Avraam and Payatakes [12], four different flow regimes were observed in their micromodel experiments: large-ganglion dynamics, small-ganglion dynamics, drop-traffic flow and connected pathway flow. Such knowledge could be key to develop new theories for two-phase flow in porous media that go beyond the extended Darcy equations. Research along these lines could possibly also tie into ongoing efforts to characterize fluid configurations by integral geometry, see e.g. [95, 15, 19].

Another observation in **Paper VI** was that relative permeabilities did not form straight lines in the high-Ca limit when the viscosity ratio was different from unity. It was concluded that this was due to the intermixing and coupling of flow of the two fluids. Even though such intermixing behaviour has been observed also in lattice-Boltzmann simulations (**Paper V**) and, to some extent, in experiments [12], it would be very interesting to see experimental studies specifically designed to induce varying degrees of intermixing and measure steady-state properties at high capillary numbers. In particular, when would such experiments produce relative permeability curves that are nonlinear in saturation and what would the functional form be?

Bibliography

[1] S. L. Gariano and F. Guzzetti. Landslides in a changing climate. *Earth-Science Reviews* 162 (2016), pp. 227–252. DOI: 10.1016/j.earscirev.2016.08.011.

[2] S. S. Bakari, P. Aagaard, R. D. Vogt, F. Ruden, I. Johansen, and S. A. Vuai. Delineation of groundwater provenance in a coastal aquifer using statistical and isotopic methods, southeast Tanzania. *Environmental Earth Sciences* 66.3 (2012), pp. 889–902. DOI: 10.1007/s12665-011-1299-y.

[3] X. Jiang. A review of physical modelling and numerical simulation of long-term geological storage of CO_2. *Applied Energy* 88.11 (2011), pp. 3557–3566. DOI: 10.1016/j.apenergy.2011.05.004.

[4] I. Zacharoudiou, E. S. Boek, and J. Crawshaw. The impact of drainage displacement patterns and Haines jumps on CO_2 storage efficiency. *Scientific Reports* 8.1 (2018), pp. 1–13. DOI: 10.1038/s41598-018-33502-y.

[5] M. Oschatz and M. Antonietti. A search for selectivity to enable CO_2 capture with porous adsorbents. *Energy & Environmental Science* 11.1 (2018), pp. 57–70. DOI: 10.1039/c7ee02110k.

[6] H. Li, Y. Tang, Z. Wang, Z. Shi, S. Wu, D. Song, J. Zhang, K. Fatih, J. Zhang, H. Wang, et al. A review of water flooding issues in the proton exchange membrane fuel cell. *Journal of Power Sources* 178.1 (2008), pp. 103–117. DOI: 10.1016/j.jpowsour.2007.12.068.

[7] N. C. Gallego, L. He, D. Saha, C. I. Contescu, and Y. B. Melnichenko. Hydrogen confinement in carbon nanopores: Extreme den-

sification at ambient temperature. *Journal of the American Chemical Society* 133.35 (2011), pp. 13794–13797. DOI: 10.1021/ja202432x.

[8] K. Cousins and R. Zhang. Highly porous organic polymers for hydrogen fuel storage. *Polymers* 11.4 (2019), p. 690. DOI: 10.3390/polym11040690.

[9] Ø. Wilhelmsen. Equilibrium and nonequilibrium thermodynamics of planar and curved interfaces. PhD thesis. Norwegian University of Science and Technology, 2015.

[10] K. J. Måløy, J. Feder, and T. Jøssang. Viscous fingering fractals in porous media. *Physical Review Letters* 55.24 (1985), p. 2688. DOI: 10.1103/PhysRevLett.55.2688.

[11] R. Lenormand, E. Touboul, and C. Zarcone. Numerical models and experiments on immiscible displacements in porous media. *Journal of Fluid Mechanics* 189 (1988), pp. 165–187. DOI: 10.1017/S0022112088000953.

[12] D. Avraam and A. Payatakes. Flow regimes and relative permeabilities during steady-state two-phase flow in porous media. *Journal of Fluid Mechanics* 293 (1995), pp. 207–236. DOI: 10.1017/S0022112095001698.

[13] M. Moura, E. G. Flekkøy, K. J. Måløy, G. Schäfer, and R. Toussaint. Connectivity enhancement due to film flow in porous media. *Physical Review Fluids* 4.9 (2019), p. 094102. DOI: 10.1103/PhysRevFluids.4.094102.

[14] R. T. Armstrong, J. E. McClure, M. A. Berrill, M. Rücker, S. Schlüter, and S. Berg. Beyond Darcy's law: The role of phase topology and ganglion dynamics for two-fluid flow. *Physical Review E* 94.4 (2016), p. 043113. DOI: 10.1103/PhysRevE.94.043113.

[15] H. H. Khanamiri, C. F. Berg, P. A. Slotte, S. Schlüter, and O. Torsæter. Description of free energy for immiscible two-fluid flow in porous media by integral geometry and thermodynamics. *Water Resources Research* 54.11 (2018), pp. 9045–9059. DOI: 10.1029/2018WR023619.

[16] E. Jettestuen, J. O. Helland, and M. Prodanović. A level set method for simulating capillary-controlled displacements at the pore scale with nonzero contact angles. *Water Resources Research* 49.8 (2013), pp. 4645–4661. DOI: 10.1002/wrcr.20334.

[17] A. Q. Raeini, M. J. Blunt, and B. Bijeljic. Modelling two-phase flow in porous media at the pore scale using the volume-of-fluid method. *Journal of Computational Physics* 231.17 (2012), pp. 5653–5668. DOI: 10.1016/j.jcp.2012.04.011.

[18] S. Sinha, M. Aa. Gjennestad, M. Vassvik, M. Winkler, A. Hansen, and E. G. Flekkøy. Rheology of high-capillary number flow in porous media. *Frontiers in Physics* 7 (2019), p. 65. DOI: 10.3389/fphy.2019.00065.

[19] J. E. McClure, T. Ramstad, Z. Li, R. T. Armstrong, and S. Berg. Modeling geometric state for fluids in porous media: Evolution of the Euler characteristic. *Transport in Porous Media* 133 (2020), pp. 229–250. DOI: 10.1007/s11242-020-01420-1.

[20] D. Wilkinson and J. F. Willemsen. Invasion percolation: A new form of percolation theory. *Journal of Physics A: Mathematical and General* 16.14 (1983), p. 3365. DOI: 10.1088/0305-4470/16/14/028.

[21] M. J. Blunt. Physically-based network modeling of multiphase flow in intermediate-wet porous media. *Journal of Petroleum Science and Engineering* 20.3-4 (1998), pp. 117–125. DOI: 10.1016/S0920-4105(98)00010-2.

[22] V. Joekar-Niasar and S. Hassanizadeh. Analysis of fundamentals of two-phase flow in porous media using dynamic pore-network models: A review. *Critical Reviews in Environmental Science and Technology* 42.18 (2012), pp. 1895–1976. DOI: 10.1080/10643389.2011.574101.

[23] C. T. Miller, G. Christakos, P. T. Imhoff, J. F. McBride, J. A. Pedit, and J. A. Trangenstein. Multiphase flow and transport modeling in heterogeneous porous media: Challenges and approaches. *Advances in Water Resources* 21.2 (1998), pp. 77–120. DOI: 10.1016/S0309-1708(96)00036-X.

[24] W. G. Gray, K. Bruning, and C. T. Miller. Non-hysteretic functional form of capillary pressure in porous media. *Journal of Hydraulic Research* 57.6 (2019), pp. 747–759. DOI: 10.1080/00221686.2019.1671520.

[25] M. J. Oak, L. E. Baker, and D. C. Thomas. Three-phase relative permeability of Berea sandstone. *Journal of Petroleum Technology* 42.08 (1990), pp. 1054–1061. DOI: 10.2118/17370-PA.

[26] B. Bennion and S. Bachu. Relative permeability characteristics for supercritical CO_2 displacing water in a variety of potential sequestration zones. In: *SPE Annual Technical Conference and Exhibition*. Society of Petroleum Engineers. 2005. DOI: 10.2118/95547-MS.

[27] P. Aursand, M. Aa. Gjennestad, E. Aursand, M. Hammer, and Ø. Wilhelmsen. The spinodal of single- and multi-component fluids and its role in the development of modern equations of state. *Fluid Phase Equilibria* 436 (2017), pp. 98–112. DOI: 10.1016/j.fluid.2016.12.018.

[28] M. Aa. Gjennestad and Ø. Wilhelmsen. Thermodynamic stability of droplets, bubbles and thick films in open and closed pores. *Fluid Phase Equilibria* 505 (2020), p. 112351. DOI: 10.1016/j.fluid.2019.112351.

[29] M. Aa. Gjennestad and Ø. Wilhelmsen. Thermodynamic stability of volatile droplets and thin films governed by the disjoining pressure in open and closed containers. *Langmuir* 36 (2020), pp. 7879–7893. DOI: 10.1021/acs.langmuir.0c00960.

[30] M. Aa. Gjennestad, M. Vassvik, S. Kjelstrup, and A. Hansen. Stable and efficient time integration at low capillary numbers of a dynamic pore network model for immiscible two-phase flow in porous media. *Frontiers in Physics* 6 (2018), p. 56. DOI: 10.3389/fphy.2018.00056.

[31] M. Aa. Gjennestad, M. Winkler, and A. Hansen. Pore network modeling of the effects of viscosity ratio and pressure gradient on steady-state incompressible two-phase flow in porous media. *Transport in Porous Media* 132 (2020), pp. 355–379. DOI: 10.1007/s11242-020-01395-z.

[32] Ø. Wilhelmsen, A. Aasen, G. Skaugen, P. Aursand, A. Austegard, E. Aursand, M. Aa. Gjennestad, H. Lund, G. Linga, and M. Hammer. Thermodynamic modeling with equations of state: Present challenges with established methods. *Industrial & Engineering Chemistry Research* 56.13 (2017), pp. 3503–3515. DOI: 10.1021/acs.iecr.7b00317.

[33] M. Aa. Gjennestad, E. Aursand, E. Magnanelli, and J. Pharoah. Performance analysis of heat and energy recovery ventilators using exergy analysis and nonequilibrium thermodynamics. *Energy and Buildings* 170 (2018), pp. 195–205. DOI: 10.1016/j.enbuild.2018.04.013.

[34] A. Hansen, S. Sinha, D. Bedeaux, S. Kjelstrup, M. Aa. Gjennestad, and M. Vassvik. Relations between seepage velocities in immiscible, incompressible two-phase flow in porous media. *Transport in Porous Media* 125 (2018), pp. 565–587. DOI: 10.1007/s11242-018-1139-6.

[35] M. Winkler, M. Aa. Gjennestad, D. Bedeaux, S. Kjelstrup, R. Cabriolu, and A. Hansen. Onsager-symmetry obeyed in athermal mesoscopic systems: Two-phase flow in porous media. *Frontiers in Physics* 8 (2020), p. 60. DOI: 10.3389/fphy.2020.00060.

[36] H. B. Callen. Thermodynamics and an introduction to thermostatistics. 2nd ed. John Wiley & Sons, 1987.

[37] M. L. Michelsen and J. M. Mollerup. Thermodynamic models: Fundamentals & computational aspects. 2nd ed. Tie-Line Publications, 2007.

[38] G. Soave. Equilibrium constants from a modified Redlich–Kwong equation of state. *Chemical Engineering Science* 27.6 (1972), pp. 1197–1203. DOI: 10.1016/0009-2509(72)80096-4.

[39] D.-Y. Peng and D. B. Robinson. A new two-constant equation of state. *Industrial & Engineering Chemistry Fundamentals* 15.1 (1976), pp. 59–64. DOI: 10.1021/i160057a011.

[40] G. M. Kontogeorgis, E. C. Voutsas, I. V. Yakoumis, and D. P. Tassios. An equation of state for associating fluids. *Industrial & Engineering Chemistry Research* 35.11 (1996), pp. 4310–4318. DOI: 10.1021/ie9600203.

[41] J. Gross and G. Sadowski. Perturbed-chain SAFT: An equation of state based on a perturbation theory for chain molecules. *Industrial & Engineering Chemistry Research* 40.4 (2001), pp. 1244–1260. DOI: 10.1021/ie0003887.

[42] J. Gernert and R. Span. EOS–CG: A Helmholtz energy mixture model for humid gases and CCS mixtures. *The Journal of Chemical Thermodynamics* 93 (2016), pp. 274–293. DOI: 10.1016/j.jct.2015.05.015.

[43] O. Kunz and W. Wagner. The GERG-2008 wide-range equation of state for natural gases and other mixtures: An expansion of GERG-2004. *Journal of Chemical & Engineering Data* 57.11 (2012), pp. 3032–3091. DOI: 10.1021/je300655b.

[44] J. W. Tester and M. Modell. Thermodynamics and its applications. Prentice Hall, 1996.

[45] S. Kjelstrup and D. Bedeaux. Non-equilibrium thermodynamics of heterogeneous systems. Vol. 16. Series on advances in statistical mechanics. World Scientific, 2008.

[46] Ø. Wilhelmsen, D. Bedeaux, S. Kjelstrup, and D. Reguera. Thermodynamic stability of nanosized multicomponent bubbles/droplets: The square gradient theory and the capillary approach. *The Journal of Chemical Physics* 140.2 (2014), p. 024704. DOI: 10.1063/1.4860495.

[47] A. J.-M. Yang. The thermodynamical stability of the heterogeneous system with a spherical interface. *The Journal of Chemical Physics* 82.4 (1985), pp. 2082–2085. DOI: 10.1063/1.448344.

[48] L. G. MacDowell, V. K. Shen, and J. R. Errington. Nucleation and cavitation of spherical, cylindrical, and slablike droplets and bubbles in small systems. *The Journal of Chemical Physics* 125.3 (2006), p. 034705. DOI: 10.1063/1.2218845.

[49] Ø. Wilhelmsen, D. Bedeaux, S. Kjelstrup, and D. Reguera. Communication: Superstabilization of fluids in nanocontainers. *The Journal of Chemical Physics* 141.7 (2014). DOI: 10.1063/1.4893701.

[50] B. V. Derjaguin, N. V. Churaev, and V. M. Muller. Surface forces. Ed. by J. A. Kitchener. Trans. by V. I. Kisin. Springer, 1987.

[51] P.-G. de Gennes. Wetting: statics and dynamics. *Reviews of Modern Physics* 57.3 (1985), p. 827. DOI: 10.1103/RevModPhys.57.827.

[52] U. Thiele, M. Mertig, and W. Pompe. Dewetting of an evaporating thin liquid film: Heterogeneous nucleation and surface instability. *Physical Review Letters* 80.13 (1998), p. 2869. DOI: 10.1103/PhysRevLett.80.2869.

[53] A. V. Neimark. Thermodynamic equilibrium and stability of liquid films and droplets on fibers. *Journal of Adhesion Science and Technology* 13.10 (1999), pp. 1137–1154. DOI: 10.1163/156856199X00839.

[54] A. Vrij. Possible mechanism for the spontaneous rupture of thin, free liquid films. *Discussions of the Faraday Society* 42 (1966), pp. 23–33. DOI: 10.1039/DF9664200023.

[55] E. Ruckenstein and R. K. Jain. Spontaneous rupture of thin liquid films. *Journal of the Chemical Society, Faraday Transactions 2* 70 (1974), pp. 132–147. DOI: 10.1039/F29747000132.

[56] H. S. Kheshgi and L. Scriven. Dewetting: Nucleation and growth of dry regions. *Chemical Engineering Science* 46.2 (1991), pp. 519–526. DOI: 10.1016/0009-2509(91)80012-N.

[57] A. Alizadeh Pahlavan, L. Cueto-Felgueroso Landeira, A. E. Hosoi, G. H. McKinley, and R. Juanes. Thin films in partial wetting: Stability, dewetting and coarsening. *Journal of Fluid Mechanics* 845 (2018), pp. 642–681. DOI: 10.1017/jfm.2018.255.

[58] L. G. MacDowell. Computer simulation of interface potentials: Towards a first principle description of complex interfaces? *The European Physical Journal Special Topics* 197.1 (2011), pp. 131–145. DOI: 10.1140/epjst/e2011-01447-6.

[59] F. Dörfler, M. Rauscher, and S. Dietrich. Stability of thin liquid films and sessile droplets under confinement. *Physical Review E* 88.1 (2013), p. 012402. DOI: 10.1103/PhysRevE.88.012402.

[60] A. Sharma. Equilibrium and dynamics of evaporating or condensing thin fluid domains: thin film stability and heterogeneous nucleation. *Langmuir* 14.17 (1998), pp. 4915–4928. DOI: 10.1021/la971389f.

[61] L. Boinovich and A. Emelyanenko. Wetting and surface forces. *Advances in Colloid and Interface Science* 165.2 (2011), pp. 60–69. DOI: 10.1016/j.cis.2011.03.002.

[62] M. Hassanizadeh and W. G. Gray. General conservation equations for multi-phase systems: 3. Constitutive theory for porous media flow. *Advances in Water Resources* 3.1 (1980), pp. 25–40. DOI: 10.1016/0309-1708(80)90016-0.

[63] S. Whitaker. Flow in porous media I: A theoretical derivation of Darcy's law. *Transport in Porous Media* 1.1 (1986), pp. 3–25. DOI: 10.1007/BF01036523.

[64] L. D. Landau and E. M. Lifshitz. Fluid mechanics. 2nd ed. Vol. 6. Course of Theoretical Physics. Trans. by J. B. Sykes and W. H. Reid. Butterworth–Heinemann, 1987.

[65] C. T. Simmons. Henry Darcy (1803–1858): Immortalised by his scientific legacy. *Hydrogeology Journal* 16.6 (2008), p. 1023. DOI: 10.1007/s10040-008-0304-3.

[66] H. Darcy. The public fountains of the city of Dijon. Trans. by P. Bobeck. Kendall Hunt Publishing Company, 2004.

[67] A. S. Ziarani and R. Aguilera. Knudsen's permeability correction for tight porous media. *Transport in Porous Media* 91.1 (2012), pp. 239–260. DOI: 10.1007/s11242-011-9842-6.

[68] S. M. Hassanizadeh and W. G. Gray. Thermodynamic basis of capillary pressure in porous media. *Water Resources Research* 29.10 (1993), pp. 3389–3405. DOI: 10.1029/93WR01495.

[69] W. B. Haines. Studies in the physical properties of soil. V. The hysteresis effect in capillary properties, and the modes of moisture distribution associated therewith. *The Journal of Agricultural Science* 20.1 (1930), pp. 97–116. DOI: 10.1017/S002185960008864X.

[70] K. J. Måløy, L. Furuberg, J. Feder, and T. Jøssang. Dynamics of slow drainage in porous media. *Physical Review Letters* 68.14 (1992), p. 2161. DOI: 10.1103/PhysRevLett.68.2161.

[71] R. T. Armstrong and S. Berg. Interfacial velocities and capillary pressure gradients during Haines jumps. *Physical Review E* 88.4 (2013), p. 043010. DOI: 10.1103/PhysRevE.88.043010.

[72] S. Berg, H. Ott, S. A. Klapp, A. Schwing, R. Neiteler, N. Brussee, A. Makurat, L. Leu, F. Enzmann, J.-O. Schwarz, et al. Real-time 3D imaging of Haines jumps in porous media flow. *Proceedings of the National Academy of Sciences* 110.10 (2013), pp. 3755–3759. DOI: 10.1073/pnas.1221373110.

[73] J. Koplik and T. Lasseter. Two-phase flow in random network models of porous media. *Society of Petroleum Engineers Journal* 25.01 (1985), pp. 89–100. DOI: 10.2118/11014-PA.

[74] E. Aker, K. J. Måløy, A. Hansen, and G. G. Batrouni. A two-dimensional network simulator for two-phase flow in porous media. *Transport in Porous Media* 32.2 (1998), pp. 163–186. DOI: 10.1023/A:1006510106194.

[75] W. Gray and S. Hassanizadeh. Averaging theorems and averaged equations for transport of interface properties in multiphase systems. *International Journal of Multiphase Flow* 15.1 (1989), pp. 81–95. DOI: 10.1016/0301-9322(89)90087-6.

[76] S. M. Hassanizadeh and W. G. Gray. Mechanics and thermodynamics of multiphase flow in porous media including interphase boundaries. *Advances in Water Resources* 13.4 (1990), pp. 169–186. DOI: 10.1016/0309-1708(90)90040-B.

[77] S. Kjelstrup, D. Bedeaux, A. Hansen, B. Hafskjold, and O. Galteland. Non-isothermal transport of multi-phase fluids in porous media. Constitutive equations. *Frontiers in Physics* 6 (2019), p. 150. DOI: 10.3389/fphy.2018.00150.

[78] R. Wyckoff and H. Botset. The flow of gas-liquid mixtures through unconsolidated sands. *Physics* 7.9 (1936), pp. 325–345. DOI: 10.1063/1.1745402.

[79] S. Manthey, S. M. Hassanizadeh, R. Helmig, and R. Hilfer. Dimensional analysis of two-phase flow including a rate-dependent capillary pressure–saturation relationship. *Advances in Water Resources* 31.9 (2008), pp. 1137–1150. DOI: 10.1016/j.advwatres.2008.01.021.

[80] L. M. Abriola. Modeling multiphase migration of organic chemicals in groundwater systems – A review and assessment. *Environmental Health Perspectives* 83 (1989), pp. 117–143. DOI: 10.1289/ehp.8983117.

[81] G. Zhang and K. Jiao. Multi-phase models for water and thermal management of proton exchange membrane fuel cell: A review. *Journal of Power Sources* 391 (2018), pp. 120–133. DOI: 10.1016/j.jpowsour.2018.04.071.

[82] M. B. Allen. Mechanics of multiphase fluid flows in variably saturated porous media. *International Journal of Engineering Science* 24.3 (1986), pp. 339–351. DOI: 10.1016/0020-7225(86)90090-X.

[83] F. Kalaydjian. A macroscopic description of multiphase flow in porous media involving spacetime evolution of fluid/fluid interface. *Transport in Porous Media* 2.6 (1987), pp. 537–552. DOI: 10.1007/BF00192154.

[84] C. Bardon and D. G. Longeron. Influence of very low interfacial tensions on relative permeability. *Society of Petroleum Engineers Journal* 20.05 (1980), pp. 391–401. DOI: 10.2118/7609-PA.

[85] S. S. Datta, T. Ramakrishnan, and D. A. Weitz. Mobilization of a trapped non-wetting fluid from a three-dimensional porous medium. *Physics of Fluids* 26.2 (2014), p. 022002. DOI: 10.1063/1.4866641.

[86] D. Picchi and I. Battiato. Relative permeability scaling from pore-scale flow regimes. *Water Resources Research* 55.4 (2019), pp. 3215–3233. DOI: 10.1029/2018WR024251.

[87] H. A. Knudsen, E. Aker, and A. Hansen. Bulk flow regimes and fractional flow in 2D porous media by numerical simulations. *Transport in Porous Media* 47.1 (2002), pp. 99–121. DOI: 10.1023/A:1015039503551.

[88] H. A. Knudsen and A. Hansen. Relation between pressure and fractional flow in two-phase flow in porous media. *Physical Review E* 65.5 (2002), p. 056310. DOI: 10.1103/PhysRevE.65.056310.

[89] T. Ramstad and A. Hansen. Cluster evolution in steady-state two-phase flow in porous media. *Physical review E* 73.2 (2006), p. 026306. DOI: 10.1103/PhysRevE.73.026306.

[90] G. Tørå, T. Ramstad, and A. Hansen. Anomalous diffusion on clusters in steady-state two-phase flow in porous media in two dimensions. *Europhysics Letters* 87.5 (2009), p. 54002. DOI: 10.1209/0295-5075/87/54002.

[91] S. Sinha, A. T. Bender, M. Danczyk, K. Keepseagle, C. A. Prather, J. M. Bray, L. W. Thrane, J. D. Seymour, S. L. Codd, and A. Hansen. Effective rheology of two-phase flow in three-dimensional porous media: Experiment and simulation. *Transport in Porous Media* 119.1 (2017), pp. 77–94. DOI: 10.1007/s11242-017-0874-4.

[92] J. L. Troutman. Variational calculus and optimal control: Optimization with elementary convexity. 2nd ed. Springer Science & Business Media, 1996.

[93] H. Vehkamäki. Classical nucleation theory in multicomponent systems. Springer Science & Business Media, 2006.

[94] U. C. Bandara, A. M. Tartakovsky, and B. J. Palmer. Pore-scale study of capillary trapping mechanism during CO_2 injection in geological formations. *International Journal of Greenhouse Gas Control* 5.6 (2011), pp. 1566–1577. DOI: 10.1016/j.ijggc.2011.08.014.

[95] J. E. McClure, R. T. Armstrong, M. A. Berrill, S. Schlüter, S. Berg, W. G. Gray, and C. T. Miller. Geometric state function for two-fluid flow in porous media. *Physical Review Fluids* 3.8 (2018), p. 084306. DOI: 10.1103/PhysRevFluids.3.084306.

Paper I

P. Aursand, M. Aa. Gjennestad, E. Aursand, M. Hammer, and Ø. Wilhelmsen. The spinodal of single- and multi-component fluids and its role in the development of modern equations of state. *Fluid Phase Equilibria* 436 (2017), pp. 98–112. DOI: 10.1016/j.fluid.2016.12.018

Fluid Phase Equilibria 436 (2017) 98–112

Contents lists available at ScienceDirect

Fluid Phase Equilibria

journal homepage: www.elsevier.com/locate/fluid

The spinodal of single- and multi-component fluids and its role in the development of modern equations of state

Peder Aursand [a], Magnus Aa. Gjennestad [a], Eskil Aursand [a, b], Morten Hammer [a], Øivind Wilhelmsen [a, c, *]

[a] SINTEF Energy Research, Sem Sælands vei 11, NO-7034 Trondheim, Norway
[b] NTNU, Department of Energy and Process Engineering, Kolbjørn Hejes vei 1B, NO-7491 Trondheim, Norway
[c] NTNU, Department of Electrical Engineering and Renewable Energy, Gunnerus Gate 1, NO-7491 Trondheim, Norway

ARTICLE INFO

Article history:
Received 24 October 2016
Received in revised form
7 December 2016
Accepted 19 December 2016
Available online 26 December 2016

Keywords:
Thermodynamics
Equation of state
Spinodal
Nucleation
Phase stability
Superheat limit

ABSTRACT

The spinodal represents the limit of thermodynamic stability of a homogeneous fluid. In this work, we present a robust methodology to obtain the spinodal of multicomponent fluids described even with the most sophisticated equations of state (EoS) available. We elaborate how information about the spinodal and its uncertainty can contribute both in the development of modern EoS and to estimate their uncertainty in the metastable regions. Inequality constraints are presented that can be exploited in the fitting of modern EoS of single-component fluids to avoid inadmissible pseudo-stable states between the vapor and liquid spinodals. We find that even cubic EoS violate some of these constraints.

With the use of a selection of EoS representative of modern applications, we compare vapor and liquid spinodal curves, superheat and supersaturation limits from classic nucleation theory (CNT), and available experimental data for the superheat limit. Computations are performed with pure species found in natural gas, binary mixtures, as well as a multi-component natural gas mixture in order to demonstrate the scalability of the approach. We demonstrate that there are large inconsistencies in predicted spinodals from a wide range of EoS such as cubic EoS, extended corresponding state EoS, SAFT and multiparameter EoS. The overall standard deviation in the prediction of the spinodal temperatures were 1.4 K and 2.7 K for single- and multi-component liquid-spinodals and 6.3 K and 26.9 K for single- and multi-component vapor spinodals.

The relationship between the measurable limit of superheat, or supersaturation, and the theoretical concept of the spinodal is discussed. While nucleation rates from CNT can deviate orders of magnitude from experiments, we find that the limit of superheat from experiments agree within 1.0 K and 2.4 K with predictions from CNT for single- and multi-component fluids respectively. We demonstrate that a large part of the metastable domain of the phase diagram is currently unavailable to experiments, in particular for metastable vapor. Novel techniques, experimental or with computational simulations, should be developed to characterize the thermodynamic properties in these regions, and to identify the thermodynamic states that define the spinodal.

1. Introduction

Metastable fluids can be found everywhere and continue to attract attention [1]. Recent examples include the ongoing discussion on cavitation of water at large negative pressures [2–6], magma erupting from volcanoes [7] and violent vapor-explosions from liquids spills in contact with a substantially warmer substance [8–11]. It is challenging to measure the properties of highly metastable fluids. By their own labile nature, they transform into a more stable phase via nucleation, where the nucleation process is triggered by thermal fluctuations. These fluctuations occur naturally, even in perfectly homogeneous fluids at equilibrium [12].

Properties of metastable fluids are central in the description of many processes. An important example is nucleation, which is ubiquitous in a wide range of physical, chemical, and biological processes. In nucleation theory, the thermodynamic state of the

* Corresponding author. SINTEF Energy Research, Sem Sælands vei 11, NO-7034 Trondheim, Norway.
E-mail address: oivind.wilhelmsen@ntnu.no (Ø. Wilhelmsen).

http://dx.doi.org/10.1016/j.fluid.2016.12.018

critical embryo is within the metastable region of the fluid [12]. Even for the simple case of condensation of the noble gas argon, predictions of nucleation rates from classical nucleation theory (CNT) deviate more than 20 orders of magnitude from experiments. In contrast, we will here show that CNT predicts accurately the "limit of superheat" for many hydrocarbons, which represents the experimentally available limit of metastability of liquids. Some of the deviation between several theories [13,14] and experimental data is likely because of inaccuracies in current equations of state (EoS) in the metastable regions [13].

In the development of modern multiparameter EoS, for example for water [15], the thermodynamic properties of metastable fluid phases such as subcooled liquid (metastable with respect to solid-liquid) and superheated liquid (metastable with respect to the vapor-liquid) are included in the fitting procedure. The extrema for metastability are defined by the spinodal. At the spinodal, the homogeneous fluid becomes intrinsically unstable and the activation barrier for nucleation disappears. The unstable fluid will then spontaneously decompose into the more stable phases. From a thermodynamic point of view, much is known about the state of the fluid at the spinodal. For instance, for single-component fluids, several thermodynamic properties such as the bulk modulus and the inverse isobaric heat capacity equal zero. Therefore, information about the spinodal is valuable, both in the development of modern EoS and to estimate their uncertainty in the metastable regions. Moreover, a thermodynamically consistent behavior of the EoS in the unstable domain of the homogeneous fluid is a prerequisite for combining them with mass based density functional theory for studying interfacial phenomena [16].

A major challenge in the study of metastable fluids is that there are limitations to how close to the spinodal one can get in experiments with real fluids. No matter how careful an experiment has been carried out, thermal fluctuations that occur naturally in the fluid will trigger homogeneous nucleation before the spinodal has been reached, even though the metastable domain extends significantly further. Highly metastable states that are experimentally unavailable for bulk fluids can still be encountered in small cavities, or within the critical cluster or cavity during nucleation, and are thus of practical relevance. The experimentally attainable limit where a superheated liquid spontaneously transforms into vapor is known as the *limit of superheat* [1]. The most popular experimental technique for measuring the limit of superheat is the droplet explosion method, a technique dating back to the early work of Wakeshima and Takata [17] and Moore [18]. The droplet explosion method remains the most popular technique to date [8,11], and represents one of the techniques that can bring the liquid closest to the spinodal [19]. We shall in this work discuss how close to the spinodal it is possible to get experimentally, and how to get even closer.

From a theoretical perspective, we shall elaborate how information about the spinodal and its uncertainty can contribute both in the development of modern EoS and to estimate their uncertainty in the metastable regions. With the use of a selection of EoS with varying degree of complexity, we predict the spinodal curves for pure species and mixtures. The predicted spinodals are compared to both the limit of superheated liquid and supersaturated vapor from CNT and available experimental data. The present paper extends previous work on the topic spanning the last three decades [9,20–24]. Whereas previous studies have focused on cubic EoS, where obtaining the spinodal curve is straightforward, we present a general and robust approach based on thermodynamic stability analysis. This allows us to calculate and compare spinodals from a number of EoS with very different functional forms and levels of complexity. Moreover, while previous works have focused mostly on pure species, we calculate spinodals for hydrocarbon mixtures with up to five components. We show that the functional form of the EoS can have a significant influence on the predicted spinodal.

2. Theory

In this section, we present the theoretical foundation for the work. We start in Sec. 2.1 by describing the different types of EoS that will be used. In Sec. 2.2, we discuss how the spinodal can be characterized, before we in Sec. 2.3 explain how to estimate the experimental limit of stability for a homogeneous fluid with classical nucleation theory.

2.1. Equations of state

2.1.1. Cubic EoS (PR, SRK)

The simplest type of EoS that can still predict the spinodal are the cubic EoS. These can in general be represented as

$$P = \frac{RT}{v-b} - \frac{a\alpha(T)}{(v-bm_1)(v-bm_2)}. \tag{1}$$

Here, P is the pressure, T is the temperature, R the universal gas constant, v the molar volume, and a, α, and b are parameters of the EoS. The constants m_1 and m_2 characterize various two-parameter cubic EoS. For instance, for the van der Waals (VdW) EoS, $m_1 = m_2 = 0$, for the Soave–Redlich–Kwong (SRK) EoS [25], $m_1 = 1$ and $m_2 = 0$, and for the Peng–Robinson (PR) EoS [26], $m_1 = -1 + \sqrt{2}$ and $m_2 = -1 - \sqrt{2}$. All these EoS are two-parameter cubic EoS in the sense that they use the two parameters a and b. For fluids with several components, mixing rules are used to compute the parameters a and b, which then depend on the composition.

2.1.2. Extended corresponding state EoS (SPUNG)

An extension of the corresponding state (CSP) methodology was initiated by Leach, Rowlinson and Watson as elaborated in Ref. [27], by including so-called "shape factors" that take into account how the mixture in consideration differs from the reference fluid(s). For pure components, this extension has a basis in statistical mechanics. If cubic EoS are used to calculate the shape factors, one may combine the strength of cubic EoS observed in VLE calculations with improved prediction of bulk properties obtained from a very accurate reference EoS. This methodology has also been referred to as the SPUNG EoS, and has proven to be both computationally fast as well as accurate [28]. We refer to Chapter 4 in Ref. [29] for further details.

2.1.3. Statistical associating fluid theory (SAFT)

Statistical Associating Fluid Theory (SAFT) gives EoS that are founded on statistical mechanics [30]. The perhaps most commonly used formulation is PC-SAFT [31] that has, in general, substantially improved accuracy in comparison with cubic EoS. Since PC-SAFT is founded on statistical mechanics and accounts for sizes and shapes of molecules, it is also expected to be the EoS with the largest predictive ability of the EoS considered in this work, in particular for polar substances and associating substances.

2.1.4. Multiparameter equations of state (GERG-2008)

Multiparameter EoS are today the most accurate EoS for the regions where thermodynamic property data are available. The EoS are founded on a comprehensive analysis of experimental data and a diligent optimization procedure, with functional forms optimized for accuracy. They have been devised for single-component fluids [15,32–36] and mixtures [37]. For some of these EoS, the thermodynamic properties of metastable fluid phases such as

supersaturated vapor and superheated liquid have been included in the fitting procedure [15]. In this work, we will use the multiparameter EoS for natural gas called GERG-2008 [37]. It is defined in terms of a reduced Helmholtz energy function:

$$\alpha(\rho,T,\boldsymbol{x}) = \alpha^0(\rho,T,\boldsymbol{x}) + \sum_{i=1}^{N_c} x_i \alpha_i^{\mathrm{r}}(\rho,T) + \Delta\alpha^{\mathrm{r}}(\rho,T,\boldsymbol{x}), \tag{2}$$

where the superscripts 0 and r refer to the ideal gas and the residual contributions respectively, subscript i refers to species i, N_c is the number of components, ρ is the density and x_i is the mole fraction of component i. The last term on the right-hand-side, $\Delta\alpha^{\mathrm{r}}$ is the departure function that takes into account the deviation from ideal mixture.

2.2. Thermodynamic stability and the spinodal

The spinodal represents the limit of intrinsic stability of a single-phase fluid. The spinodal is a theoretical limit, since thermal fluctuations will lead to homogeneous nucleation long before the spinodal has been reached in experiments, as explained in Sec. 1.

2.2.1. Thermodynamic stability in terms of the eigenvalues of the Hessian matrices of the energy state functions

Classical thermodynamics states that at equilibrium, the entropy of an isolated system is at its maximum. By considering an isolated composite system consisting of a subsystem that interacts with a thermal, pressure or particle reservoir, this criterion can be reformulated in terms of minima of various energy state functions for the subsystem [38]. The identity of the energy state function depends on the surroundings of the subsystem, or alternatively which state variables that have been fixed. Some examples are:

$$\min\{U(S,V,\mathbf{N})\} \quad \text{at fixed } S,V \text{ and } \mathbf{N} \tag{3}$$

$$\min\{A(T,V,\mathbf{N})\} \quad \text{at fixed } T,V \text{ and } \mathbf{N} \tag{4}$$

$$\min\{H(S,P,\mathbf{N})\} \quad \text{at fixed } S,P \text{ and } \mathbf{N} \tag{5}$$

$$\min\{G(T,P,\mathbf{N})\} \quad \text{at fixed } T,P \text{ and } \mathbf{N} \tag{6}$$

where U is the internal energy, A is the Helmholtz energy, H is the enthalpy, G is the Gibbs energy, S is the entropy, V is the total volume, and $\mathbf{N}$ is the mole numbers, where boldface symbols are vectors. In addition, in a single-component system, $U^* = U - N\mu$ is the Legendre transform of the internal energy with respect to the mole number, where μ is the chemical potential. Even if U^* is not commonly used in engineering applications, we shall refer to it in subsequent discussions. The energy state functions A, U^* and H are Legendre transforms of the internal energy with respect to one variable, while G is a Legendre transform of the internal energy with respect to two variables.

The thermodynamic stability of a stationary homogeneous system can be examined by evaluating the change in internal energy when decomposing into two phases, denoted with subscripts α and β (the initial system has no subscript). Let us start with an isolated system where U is a minimum at equilibrium, meaning that $\mathrm{d}U = \mathrm{d}(U_\alpha + U_\beta) = 0$, i.e. the system is in a *stationary* state. This condition implies uniform intensive variables: T, P and μ_i, where subscript i refers to component i (see Chapters 5 and 6 in Ref. [38]). However, a *stationary* state can be a minimum, maximum or saddle point. For the energy state function to be a minimum, the lowest order of non-vanishing variation must be positive. In most cases, this is the second order variation:

$$\mathrm{d}^2U = \mathrm{d}^2U_\alpha + \mathrm{d}^2U_\beta = \mathrm{d}\mathbf{x}_\alpha^T\ \nabla\nabla U_\alpha\ \mathrm{d}\mathbf{x}_\alpha + \mathrm{d}\mathbf{x}_\beta^T\ \nabla\nabla U_\beta\ \mathrm{d}\mathbf{x}_\beta \geq 0, \tag{7}$$

where $\mathrm{d}\mathbf{x}^T = [\mathrm{d}S, \mathrm{d}V, \mathrm{d}N_1, \ldots, \mathrm{d}N_{N_c}]$ represents an arbitrary change in the state variables and $\nabla\nabla U$ is the Hessian matrix of the internal energy, i.e. the matrix containing the second order partial derivatives of U with respect to the variables in $\mathbf{x}$. Since the system is isolated, $\mathrm{d}\mathbf{x}_\alpha = -\mathrm{d}\mathbf{x}_\beta$ and since the α and the β phases have uniform intensive variables, Eq. (7) can be reformulated as [39]:

$$\mathrm{d}\mathbf{x}^T\ \nabla\nabla U\ \mathrm{d}\mathbf{x} \geq 0, \tag{8}$$

where we have omitted subscript α and a scaling factor of N/N_β. Equation (8) can be rewritten in terms of the eigenvalues of $\nabla\nabla U$, λ_j:

$$\sum_{j=1}^{N_c+2} c_j^2 \lambda_j \geq 0, \tag{9}$$

where $\mathrm{d}\mathbf{x} = \sum_j^{N_c+2} c_j e_j$ and $e_1, \ldots, e_{N_c+2}$ are the eigenvectors of the Hessian matrix. Here, we have expressed the vector $\mathrm{d}\mathbf{x}$ in terms of the eigenvector-space of the Hessian matrix and the parameters, c_j, which can take any value. Since c_j^2 is always positive for any real number, the criterion for thermodynamic stability of an isolated system expressed by Eq. (7) can be reformulated as:

$$\min\{\mathrm{eig}(\nabla\nabla U)\} \geq 0, \tag{10}$$

i.e., the Hessian matrix of U should be positive-semidefinite. Legendre transforming the internal energy gives other energy state functions, and equivalent thermodynamic stability criteria can be formulated for these by following a similar approach as elaborated above:

$$\min\{\mathrm{eig}(\nabla_{V,\mathbf{N}}\nabla_{V,\mathbf{N}}\ A(T,V,\mathbf{N}))\} \geq 0 \quad \text{at fixed } T,V \text{ and } \mathbf{N} \tag{11}$$

$$\min\{\mathrm{eig}(\nabla_{S,\mathbf{N}}\nabla_{S,\mathbf{N}}\ H(S,P,\mathbf{N}))\} \geq 0 \quad \text{at fixed } S,P \text{ and } \mathbf{N} \tag{12}$$

$$\min\{\mathrm{eig}(\nabla_{\mathbf{N}}\nabla_{\mathbf{N}}\ G(T,P,\mathbf{N}))\} \geq 0 \quad \text{at fixed } T,P \text{ and } \mathbf{N} \tag{13}$$

where the subscripts indicate which variables are included in the del-operator, i.e. only the extensive variables of the respective potentials are included. In fact, at equilibrium, the Legendre transformed energy state functions are concave functions of their intensive canonical variables, and they are only a minimum if these variables are fixed [38] (see Eqs. (3)–(6)). The spinodal can thus be identified by investigating the eigenvalues of the Hessian matrices above. The criteria above are completely general, however, the typical textbook treatment defines an alternative way of identifying the spinodal in terms of a set of thermodynamic quantities that become zero at the spinodal. Since this method can give further insight, we shall discuss it next.

2.2.2. Thermodynamic stability in terms of selected thermodynamic derivatives

In conventional textbook literature on thermodynamic stability analysis, the approach outlined by Beegle et al. is often referred to [40], where the inner product between the Hessian matrices and $\mathrm{d}\mathbf{x}$ is examined in more detail. In particular, they show that some thermodynamic quantities go to zero before any other properties at the spinodal. In their textbook on classical thermodynamics, Tester and Modell state that a necessary and sufficient condition for thermodynamic stability is that [39]:

$$\frac{\partial^2 U^{(N_c)}}{\partial x_{N_c+1}\partial x_{N_c+1}} > 0, \tag{14}$$

where the superscript in $U^{(k)}$ denotes that the internal energy has been Legendre transformed with respect to the number k, of the first variables in the vector $\mathbf{x}^T = [S, V, N_1, \ldots, N_{N_c}]$. Moreover, x_l defines index l of the vector $\mathbf{x}$. The spinodal is then defined in terms of the following equation:

$$\frac{\partial^2 U^{(N_c)}}{\partial x_{N_c+1}\partial x_{N_c+1}} = 0. \tag{15}$$

However, the order of the variables in $\mathbf{x}$ can be chosen arbitrarily. Therefore, Eq. (15) results in several thermodynamic identities that equal zero at the spinodal. For a single-component system, these are:

$$\frac{\partial^2 A}{\partial x_k^2} : -\left(\frac{\partial P}{\partial V}\right)_{T,N} = 0 \quad \text{and} \quad \left(\frac{\partial \mu}{\partial N}\right)_{T,V} = 0 \tag{16}$$

$$\frac{\partial^2 U^*}{\partial x_k^2} : \left(\frac{\partial T}{\partial S}\right)_{\mu,V} = 0 \quad \text{and} \quad -\left(\frac{\partial P}{\partial V}\right)_{\mu,S} = 0 \tag{17}$$

$$\frac{\partial^2 H}{\partial x_k^2} : \left(\frac{\partial \mu}{\partial N}\right)_{P,S} = 0 \quad \text{and} \quad \left(\frac{\partial T}{\partial S}\right)_{P,N} = 0 \tag{18}$$

where Eq. (16) contains the diagonal entries of $\nabla_{V,N}\nabla_{V,N}\, A$, Eq. (17) of $\nabla_{S,V}\nabla_{S,V}\, U^*$ and Eq. (18) of $\nabla_{S,N}\nabla_{S,N}\, H$. All of these equations are satisfied simultaneously at the spinodal, where they change from positive to negative. An interesting question we shall discuss in Sec. 3.1 is whether the left-hand-side of Eqs. (16)–(18) should remain negative between the vapor and liquid spinodals. Such information is useful in the development of modern EoS, because if one can argue that thermodynamic quantities such as those defined in Eqs. (16)–(18) should remain negative, they can be exploited as inequality constraints in the fitting of single-component EoS to avoid inadmissible pseudo-stable states between the vapor and liquid spinodals. Any of the thermodynamic quantities in Eqs. (16)–(18) can be used equivalently to locate the spinodal of a single-component fluid.

2.2.3. The numerical algorithm used to identify the spinodal in this work

The Hessian matrices of all the energy state functions are singular, i.e. one of their eigenvalues is always zero. The reason for this is that the energy state functions are Euler homogeneous functions of first degree with respect to their extensive variables, while the Hessian matrices contain derivatives of only intensive variables (see Theorem 4, Chapter 1 in Ref. [41]). In practice, the spinodal can be found by eliminating one row and one column of the Hessian matrix of an appropriate energy state function to construct the matrix Φ. In the stable domain, Φ is non-singular, and the smallest eigenvalue becomes 0 at the spinodal (see Theorem 6, Chapter 1 in Ref. [41]). In this work, we have used the following criterion to identify the spinodal:

$$\min\{\mathrm{eig}(\Phi)\} = 0 \quad \text{where} \quad \Phi = \nabla_{\mathbf{N}}\nabla_{\mathbf{N}}\, A(T, V, \mathbf{N}). \tag{19}$$

The use of the Helmholtz energy formulation has proven numerically robust when solving for critical points [42]. Applying the Hessian scaling suggested by Michelsen [43], the spinodal is found by solving for the temperature at a given specific volume. A second-order method that uses numerical differentials for the minimum eigenvalue, $\lambda_{\min}$ is used. The eigenvalue calculation of a symmetric matrix can be performed with high numerical efficiency. With a given initial point on the spinodal, the entire spinodal curve can easily be traversed with the use of uniform steps in $\ln(V)$. Extrapolation from a known spinodal point can be achieved by utilizing:

$$\mathrm{d}\lambda_{\min} = \left(\frac{\partial \lambda_{\min}}{\partial T}\right)_V \mathrm{d}T + \left(\frac{\partial \lambda_{\min}}{\partial V}\right)_T \mathrm{d}V = 0, \tag{20}$$

which provides a good initial value for the temperature at the next spinodal point.

2.3. The experimentally available limit of stability of a homogeneous fluid as predicted by classical nucleation theory (CNT)

When a liquid has been sufficiently superheated, the homogeneous nucleation rate becomes at some point so large that the liquid transforms into two phases in a much shorter time than the characteristic time of the experiment. This corresponds to the observed superheat limit, and nucleation theory can thus be used to predict this.

Nucleation is an activated process where an energy barrier must be overcome by thermal fluctuations. Accordingly, the nucleation rate J depends exponentially on the height of the nucleation barrier according to a standard Arrhenius rate law,

$$J = K\exp\left(-\frac{\Delta G^*}{k_B T}\right), \tag{21}$$

where ΔG^* is the nucleation barrier, k_B is Boltzmann's constant, and K is the kinetic prefactor. Equation (21) can be used both to describe the formation of bubbles and droplets; however, the expression for K and ΔG^* differ in the two cases. The nucleation barrier, ΔG^*, is:

$$\Delta G^* = \frac{4\pi\sigma r^{*2}}{3}, \tag{22}$$

where the radius of the critical cluster or cavity r^*, for bubble formation in a liquid [1], is

$$r^* = \frac{2\sigma}{P_{\mathrm{sat}}(T) - P_{\mathrm{l}}}, \tag{23}$$

or for droplet formation in a gas [1],

$$r^* = \frac{2\sigma}{\tilde{\rho}_{\mathrm{l}} k_B T \ln(P_{\mathrm{g}}/P_{\mathrm{sat}})}, \tag{24}$$

where $\tilde{\rho}_{\mathrm{l}}$ is the number density of the liquid phase. Further, the kinetic prefactors can be approximated by following a range of approaches. In this work, we have used the following expressions to calculate the kinetic prefactor for bubble formation in a liquid [1]:

$$K \approx \tilde{\rho}_{\mathrm{l}}\sqrt{\frac{2\sigma}{\pi m}}, \tag{25}$$

where $\tilde{\rho}_{\mathrm{l}}$ is the number density of the liquid phase and m is the mass of one molecule. For droplet formation in a gas, we have used [1]:

$$K \approx \frac{\tilde{\rho}_{\mathrm{g}}^2}{\tilde{\rho}_{\mathrm{l}}}\sqrt{\frac{2\sigma}{\pi m}}, \tag{26}$$

where $\tilde{\rho}_{\mathrm{g}}$ is the number density of the vapor-phase, i.e. Eqs. (25) and (26) differ by the factor $(\tilde{\rho}_{\mathrm{g}}/\tilde{\rho}_{\mathrm{l}})^2$. We have in this work provided only

the necessary formulas, and we refer to Refs. [1,44] for details and derivations. Once the nucleation barrier has been found and the kinetic prefactors have been estimated based on properties at saturation, the nucleation rate can be calculated by use of Eq. (21). However, to set a specific limit of superheat or supersaturation, one must decide on a *critical* nucleation rate that represents the observed sudden phase change. Experiments indicate values of J_{crit} in the range $10^2 - 10^6$ cm^{-3} s^{-1} [1]. Since the exact value of the critical nucleation rate has very little influence on the predicted limit of superheat (See Fig. 3.13 in Ref. [1]) we use $J_{\text{crit}} = 10^6$ cm^{-3} s^{-1} in this work.

Given a value for J_{crit}, we find the superheat/supersaturation temperature limits for a given pressure and composition by solving

$$J(T) = J_{\text{crit}}, \tag{27}$$

for T. In order to complete this model, thermodynamic properties are needed. The pressures and densities are supplied by an EoS, and in this work we have used the most accurate EoS for the components in natural gas, GERG2008 [37]. Pure component surface tensions were modeled by the corresponding state correlation recommended in Ref. [45] (see Chapter 12). The deviation between this correlation and experiments is below 5% for most fluids according to Tables 12–1 in Ref. [45]. The procedure for finding the limits of superheat/supersaturation is described above for pure components. We extend it to mixtures by replacing the saturation properties by the properties at the bubble line (superheat limit) or at the dew line (subcool limit) of the mixture. The molecule mass m is then replaced by the mole fraction averaged molecule mass. Also, we use the mole fraction weighted average of the pure component surface tensions.

3. Results

We shall in Secs. 3.1 and 3.2 discuss the vapor and liquid spinodals from a theoretical perspective and their relevance in the development of EoS. Next, we evaluate in Sec. 3.3 how much the spinodals predicted from various EoS differ, and the implications of this on prediction of properties in the metastable regions. Eventually, we discuss in Sec. 3.4 how close to the spinodal that current experiments can bring us. In the following, we will focus on hydrocarbons and their mixtures.

3.1. The spinodals and their relevance for developing EoS

Properties of metastable fluids have received much attention in recent literature, partly because such states are ubiquitous in nature, including in important processes such as nucleation of droplets or bubbles in condensation and evaporation processes. It is therefore important to develop EoS that give an accurate representation of the metastable regions of the fluid.

Fig. 1a shows the pressure as a function of the density for methane at $T = 175$ K, as predicted by the Peng–Robinson cubic EoS. The figure highlights five regimes, one regime with single-phase gas at low densities (green solid line), one regime with single-phase liquid at high densities (blue solid line), two regimes where the single-phase fluid is metastable (dashed lines) and one regime where it is unstable (dotted line). If the inequality, $(\partial P/\partial \rho) < 0$, is satisfied where ρ is the density (equivalent to Eq. (16)-left), the single-phase fluid is mechanically unstable and will spontaneously decompose into liquid and vapor.

The shape of the pressure, P plotted as a function of the density, ρ displayed in Fig. 1a with a local maximum followed by a local minimum is called a Maxwell loop. Many EoS have a single Maxwell loop, but some EoS have a second, artificial Maxwell loop in the two-phase region. One example is shown in Fig. 1b, where GERG2008 (blue solid line) exhibits a second loop. Since $(\partial P/\partial \rho) > 0$ (mechanically stable) and also other thermodynamic stability criteria are satisfied, the EoS predicts a pseudo-stable single-phase fluid within a region where experiments show a coexistence between vapor and liquid. For many fluids and conditions, the pseudo-stable phase has even a lower energy than the vapor-liquid coexistence [16]. The second Maxwell loop is an artifact of the functional form and parameters of the GERG2008 EoS, and is a general problem/challenge in the present development of multiparameter EoS.

Fig. 1b shows the behavior of several EoS in the metastable and unstable regions, and elucidates some important points:

- The exact location of the spinodals (the maxima and minima) varies much with the choice of EoS.
- The EoS have different behaviors between the spinodals; some EoS exhibit a thermodynamically consistent behavior (a single Maxwell loop), while other EoS do not.
- The behavior of the metastable regions depends much on the choice of EoS.

A goal should be to develop EoS that are accurate and thermodynamically consistent, also in the metastable and unstable regions of the phase diagram of the single-phase fluid. A future goal should be to develop EoS without inadmissible pseudo-stable states in the unstable domain of the single-phase fluid. This is of importance, both for combining them with mass based density functional theory and to develop thermodynamically consistent mixing rules with a physical interpretation as elaborated in detail in Ref. [16].

Fig. 1b shows that GERG2008 and PC-SAFT follow each other closely in the first part of the metastable regions. This is expected, as their Taylor-expansions of the pressure as a function of density about the saturation state are very similar, because they both reproduce well the thermodynamic properties at saturation from experiments. Therefore, accurate prediction of equilibrium properties at the saturation curve is a prerequisite for accurately predicting properties in the metastable regions. However, the figure also shows that GERG2008 and PC-SAFT predict very different pressures for the onset of the liquid-spinodal (the minima of the curves). Since equilibrium measurements at saturation can provide the right slope of, for instance P as a function of ρ into the metastable regions, the location of the spinodal would provide a reference for this extrapolation. Therefore, if it was possible to find the precise onset of the spinodal, either through experiments or computations, it would be possible to characterize the whole metastable region with good accuracy. Moreover, if the spinodal could be determined to some degree of uncertainty it would be possible, based on the known uncertainty of properties at coexistence, to make statements about how accurate extrapolations to the metastable regions from various EoS are. We shall discuss the current uncertainty in the prediction of the liquid and vapor spinodals in Sec. 3.3.

One of the more urgent challenges in the development of EoS is to remove the second artificial Maxwell loop in the two-phase region, an artifact characteristic for so-called multiparameter EoS (see Sec. 2.1.4). Multiparameter EoS are founded on a comprehensive analysis of experimental data and a diligent optimization procedure, with functional forms optimized for accuracy. By adding new terms to the Helmholtz energy functional of multiparameter EoS and with the use of additional constraints in the nonlinear fitting routine, Lemmon and Jacobsen managed to reduce the magnitude of the second Maxwell loop in the multiparameter EoS for the fluid R125 [46] from $\sim 10^6$ MPa to below $\sim 10^2$ MPa. In 2009, Lemmon et al. presented a multiparameter EoS for propane,

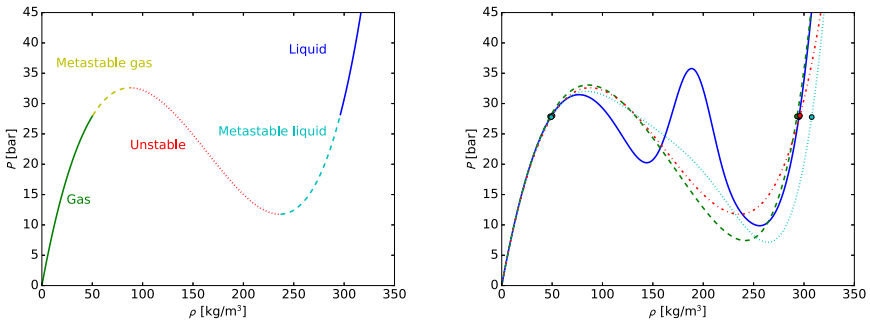

Fig. 1. Pure methane isotherms at 175 K. (a), the stable, metastable and unstable regions are illustrated by an isotherm as predicted by the PR EoS. (b), isotherms are drawn with different EoS: GERG2008 (solid blue), PC-SAFT (dashed green), PR (dash-dot red) and extended CSP (dotted cyan). The saturation points are indicated by circles. (For interpretation of the references to colour in this figure legend, the reader is referred to the web version of this article.)

where they reverted back to the functional form with Gaussian bell shaped terms [47]. With the use of the new fitting techniques and constraints from Ref. [46], they were able to reduce the magnitude of the artificial Maxwell loop. Recent multiparameter EoS are formulated with the functional form presented in Ref. [47]. Lemmon and Jacobsen implemented the constraint discussed by Elhassan et al. [48]:

$$a(\rho) - a_{\text{tang}}(\rho) \geq 0 \tag{28}$$

where a is the Helmholtz energy and subscript tang means the Helmholtz energy evaluated at the equilibrium tangent line. Despite what Elhassan and coauthors claim in their work [48], the constraint in Eq. (28) does not "remove any inconsistencies between thermodynamic stability and physical reality". Even if Eq. (28) guarantees that both the Helmholtz energy and the Gibbs energy of the vapor-liquid coexistence state is lower than the Gibbs energy of a pseudo-stable state coming from a second Maxwell loop [48], the pseudo-stable state can still be stable in other ensembles such as in an isolated system. We have elaborated in detail on this in Ref. [16].

3.2. Inequality constraints to avoid inadmissible pseudo-stable states between the spinodals

Since the inequality in Eq. (28) is insufficient for constraining EoS to avoid inadmissible pseudo-stable states in the unstable-region of the single-phase fluid (between the spinodals), we shall next discuss which inequality constraints that can be used instead. The derivatives in Eqs. (16–18) are natural candidates for such inequality constraints for the single-component fluid, since they reach zero before any other thermodynamic identities at the spinodals. We note that similar thermodynamic quantities can be defined for multicomponent fluids [39], and exploited in the fitting of multiparameter EoS for mixtures, such as GERG2008. We shall now evaluate Eqs. (16–18) for an EoS that is considered, from a qualitative perspective, to have a physically admissible behavior in the two-phase region: the Van der Waals cubic (VdW) EoS.

Fig. 2 plots Eqs. (16–18) for methane at 92 K through the metastable and unstable regions of the single-phase fluid, as predicted by the VdW EoS. The figure shows that all six of the thermodynamic quantities in Eqs. (16–18) reach zero at exactly the same two densities ($\rho = 32$ kg/m^3 and $\rho = 251$ kg/m^3), as shown by the vertical red dashed lines. These two densities define the vapor and liquid spinodals. At constant temperature, these are the only two densities where the thermodynamic quantities in Eqs. (16–18) equal zero.

If we examine the sign of the thermodynamic relations in Eqs. (16) and (18), only four of them remain negative between the vapor and liquid spinodals (vertical red dashed lines). The two thermodynamic relations that represent the diagonal entries of the Hessian matrix of the enthalpy, $(\partial\mu/\partial N)_{P,S}$ and $(\partial T/\partial S)_{P,N}$ shown in Figs. 2e and f, have asymptotes at densities just after the vapor spinodal and right before the liquid spinodal, and are positive in a region between the asymptotes. One of these thermodynamic relations has a clear physical interpretation:

$$\left(\frac{\partial T}{\partial S}\right)_{P,N} = \frac{T}{N\left(C_p^0 + C_p^{\text{r}}\right)}, \tag{29}$$

where the isobaric heat capacity, C_p, is split into an ideal gas contribution (superscript 0) and a residual contribution (superscript r). While C_p^{r} goes to $\pm\infty$ at the spinodals, C_p^0 is positive and depends only on the temperature. It is thus constant in Figs. 2 and 3. While $C_p^0(T)$ can be determined experimentally and is well-known for methane, $C_p^{\text{r}}(T,\rho)$ is unknown between the spinodals. The asymptotes of Eq. (29) correspond to the points where

$$C_p^{\text{r}}(T,\rho) = -C_p^0(T), \tag{30}$$

which can occur only between the spinodals. Interestingly, whether Eq. (30) is satisfied between the spinodals depends on which parameters that are used in the VdW EoS, and at which temperature the EoS is used. For instance, for methane at 92 K, Eq. (30) is clearly satisfied at two densities (see the asymptotes in Figs. 2e and f). However, for methane at 157 K, the same EoS predicts that $C_p^{\text{r}}(T,\rho) < -C_p^0(T)$ for all densities between the spinodals, where both of the thermodynamic relations in Eq. (18) remain negative between the spinodals, as shown in Fig. 3.

We shall next discuss if there are any physical arguments for why the thermodynamic quantities in Eqs. (16–18) should remain negative between the spinodals. To examine thermodynamic stability, we evaluate the sign of the eigenvalues of the Hessian matrices, since they define whether a stationary point of the energy state function is a minimum (only positive eigenvalues), a

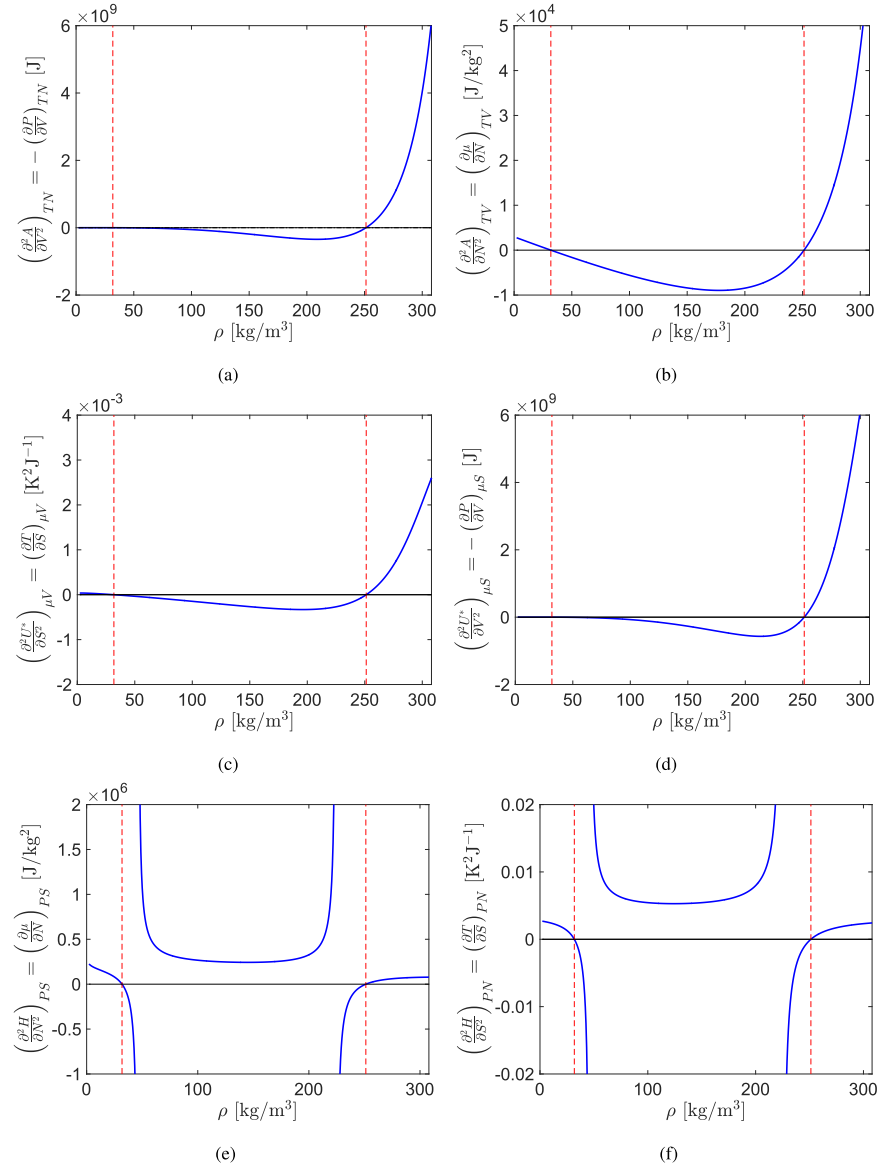

Fig. 2. A plot of Eqs. (16–18) through the two-phase region in the case of methane at 92 K as predicted by the Van der Waals cubic EoS (blue solid lines). The vertical red dashed lines show where the quantities pass through zero. The reported values are for 1 kmol of fluid. (For interpretation of the references to colour in this figure legend, the reader is referred to the web version of this article.)

maximum (only negative eigenvalues) or a saddle point (positive and negative eigenvalues).

First, let us discuss the rank of Hessian matrices and hence how many non-zero eigenvalues we expect. Since the energy state functions are Euler homogeneous functions of first degree in their extensive variables, the highest possible rank of their Hessian matrices is $r - 1$, where r is the number of extensive variables (we refer to Sec. 1.3 in Ref. [41] for details). Thus, for all the Hessian matrices, we expect at least one eigenvalue to be zero since they are singular [41]. For a single-component fluid, this gives a maximum

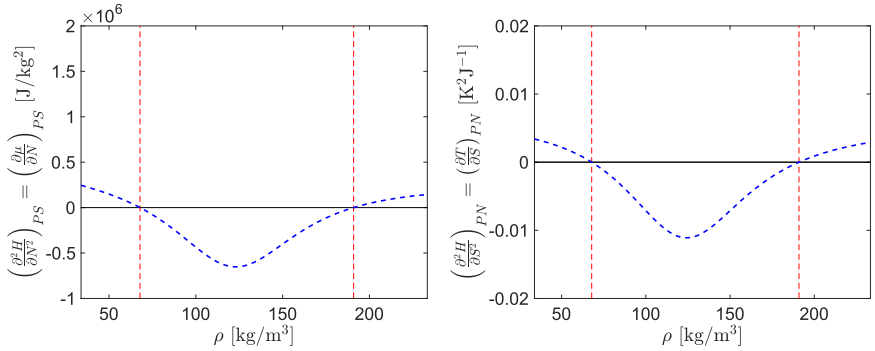

Fig. 3. A plot of two of the thermodynamic relations in Eq (18) through the two-phase region in the case of methane at 157 K as predicted by the VdW EoS (blue dashed lines). The vertical red dashed lines show where the quantities pass through zero. The reported values are for 1 kmol^3 of fluid. (For interpretation of the references to colour in this figure legend, the reader is referred to the web version of this article.)

of two non-zero eigenvalues for U and one non-zero eigenvalue for U^*, H and A. We have plotted the non-zero eigenvalues in Fig. 4 for methane, as described by the VdW EoS at 92 K (solid lines). In the figure, the eigenvalues have been divided by the eigenvalue of the liquid phase at saturation, and the subscripts refer to which energy state function the eigenvalues come from.

Fig. 4 shows that except for one of the eigenvalues of the Hessian matrix of U, $\lambda_{U,1}$, all eigenvalues go from positive to negative at the spinodals. This means that the internal energy goes from being a *local* minimum to a saddle point at the spinodals (one positive and one negative eigenvalue), while U^*, H and A go from local minima to maxima at the spinodals. Except for the eigenvalue of the Hessian matrix of the enthalpy displayed in Fig. 4c, the eigenvalues look very similar at 157 K and have not been plotted.

The asymptotes in the diagonal elements of the Hessian matrix of H at 92 K displayed in Fig. 2e and f are also reflected in asymptotes at the same densities in λ_H. In fact, Fig. 4c shows that the eigenvalue of $\nabla_{S,N}\nabla_{S,N}$ H goes from negative to positive in a region between the spinodals. When the asymptotes in the diagonal elements of the Hessian matrix of H disappear, such as at 157 K (see Fig. 3), then λ_H remains negative between the spinodals, similar to $\lambda_{U,2}$, λ_{U^*} and λ_A, as shown by the blue dashed lines in Fig. 4d.

Since all eigenvalues of the Hessian matrix of the enthalpy are non-negative in a region between the spinodals, the energy state function is a minimum. The VdW EoS thus predicts a uniform phase between the spinodals to be "pseudo-stable" in an adiabatic system kept at constant pressure, since the enthalpy is then the appropriate energy state function to examine.

In a macroscopic, single-phase system of arbitrary size, the thermodynamic stability of a sub-volume within the fluid should be independent of the choice of surroundings. Moreover, a pseudo-stable phase has never been observed experimentally between the spinodals, regardless of which experimental conditions that have been chosen. Therefore, the positive value of λ_H between the spinodals is an artifact of the VdW EoS and its parameters. We find a similar behavior of other cubic EoS, such as SRK and PR, where λ_H becomes positive between the spinodals at low temperatures. This is surprising, as its shows that even cubic EoS that have been considered to have a "physically admissible" behavior between the spinodals exhibit inconsistencies in the unstable domain of the single-phase fluid. To summarize: If one can find a state between the spinodals where, for any choice of energy state function, all eigenvalues of the Hessian are positive (one eigenvalue is always zero), one has found a pseudo-stable phase in that region. On the contrary, if at least one eigenvalue stays negative, such states are thermodynamically unstable. Thus, if we assume that such states are physically inadmissible, we arrive at the following statement:

> A sufficient condition for EoS to avoid inadmissible pseudo-stable states between the vapor and liquid spinodals is that at least one eigenvalue of the Hessian of the energy state function goes from positive to negative at, and remains negative between, the spinodals, for any choice of energy state function.

Fig. 2 shows that even if the EoS exhibits a physically admissible behavior for many of the state functions, this does not guarantee a physically admissible behavior for all energy state functions, unlike what is suggested in the work by Elhassan and coauthors [48]. We can also make some statements about the suitability of using Eqs. (16–18) as inequality constraints in fitting an EoS for a single-component fluid (similar statements can be made about multi-component fluids).

We know the following about the Hessian matrices of the energy state functions: They are singular, meaning that one of the eigenvalues is always zero and they are symmetric. Since the sum of the eigenvalues of a matrix equals the sum of the diagonal elements, one can prove mathematically that the two thermodynamic quantities in each of Eqs. (16–18) will always have the same sign for a single-component fluid. Therefore, it is only necessary to use one thermodynamic relation in each of the pairs in Eqs. (16–18) as an inequality constraint between the spinodals, where they have to be negative for a physically admissible behavior in the unstable region of the single-component fluid.

3.3. The spinodals and the limit of homogeneous nucleation

In Sec. 3.1 we argue that it is important to determine the spinodal precisely to arrive at EoS that are accurate in the metastable domain. In what follows, we investigate to which extent the EoS that are available today differ in their predictions of the spinodal.

Solving phase equilibrium calculations has received much attention in the literature. This can be challenging, in particular for multicomponent mixtures and multiparameter EoS [49]. Determining the spinodal has a comparable degree of complexity to phase equilibrium calculations, where a set of algebraic equations have to be solved based on the underlying EoS. However, robust

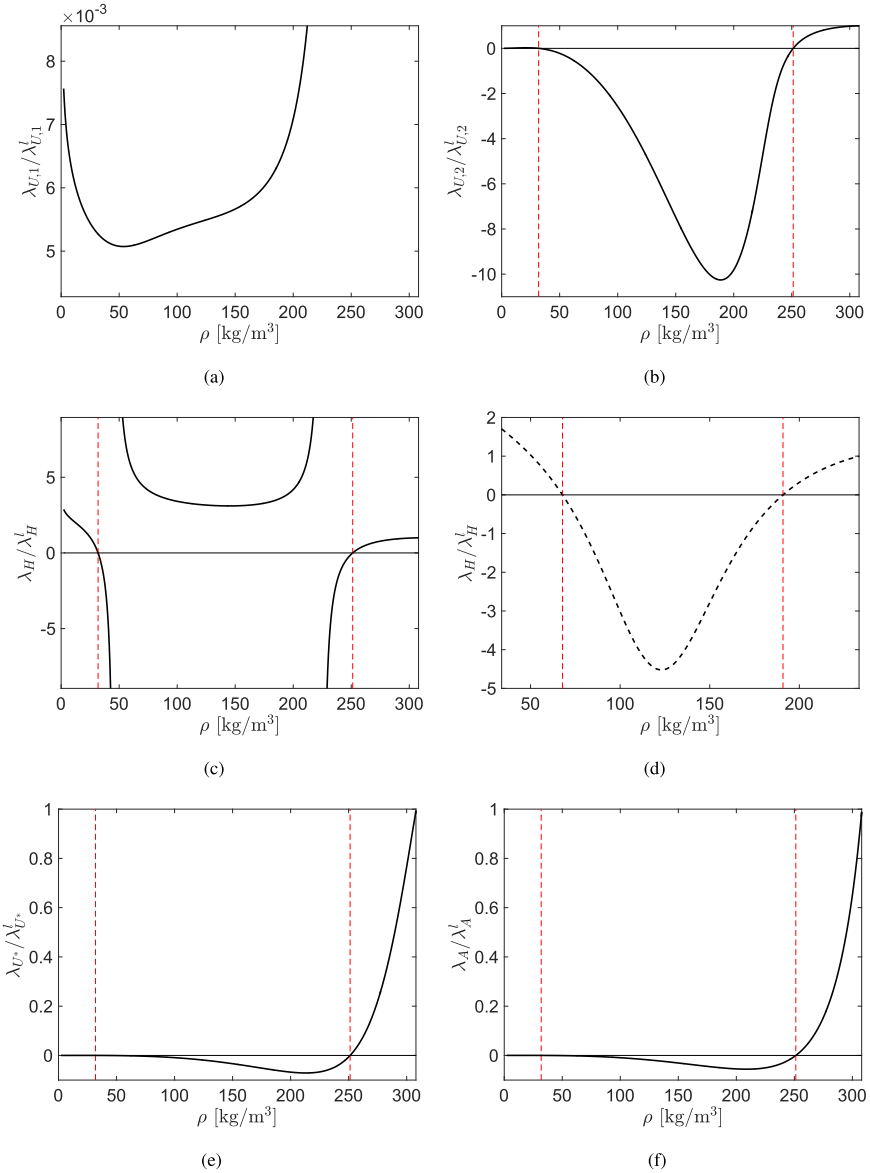

Fig. 4. A plot of the normalized eigenvalues of the energy state functions through the two-phase region in the case of methane at 92 K as predicted by the Van der Waals cubic EoS (black solid lines). The dashed line represents the eigenvalue the Hessian matrix of the enthalpy at 157 K. The vertical red dashed lines show where the quantities pass through zero. (For interpretation of the references to colour in this figure legend, the reader is referred to the web version of this article.)

and accurate methods for obtaining the spinodal have received far less attention in the literature than phase equilibrium calculations, partly due to the spinodal being less needed in engineering calculations. Previous work on the topic has mainly been limited to simple cubic EoS and pure substances [9,20–24].

In Fig. 5 we have used the methodology described in Sec. 2.2.3 to obtain the spinodal curve of a multicomponent natural gas mixture with one of the most accurate EoS available today, GERG2008 [50].

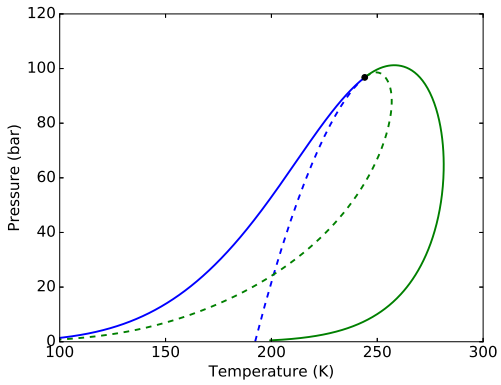

Fig. 5. Illustration of the phase envelope and spinodal curves obtained with the GERG2008 EoS for a five-component mixture of methane (75 mol-%), ethane (10 mol-%), propane (7 mol-%), butane (3 mol-%) and nitrogen (5 mol-%). The bubble line (solid blue), the dew line (solid green), the liquid spinodal (dashed blue) and the gas spinodal (dashed green) all meet in the critical point (black dot). (For interpretation of the references to colour in this figure legend, the reader is referred to the web version of this article.)

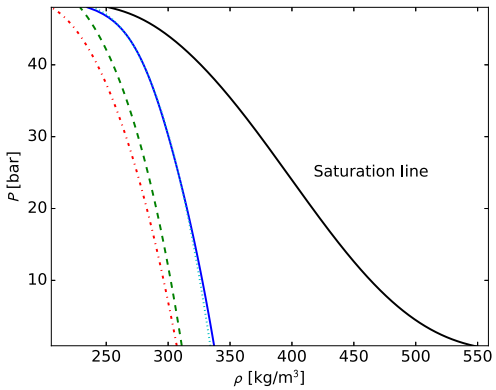

Fig. 6. The liquid density and pressure at the liquid spinodal curve for ethane, calculated using GERG2008 (solid blue), PC-SAFT (dashed green), PR (dash-dot red) and extended CSP (dotted cyan). The saturation line is given by the solid black line. (For interpretation of the references to colour in this figure legend, the reader is referred to the web version of this article.)

The figure demonstrates that the method we have presented is robust, even in the vicinity of the critical point, scalable to multi-component mixtures and applicable to complex non-analytical EoS. We observe, from a comparison of the solid and the dashed lines in Fig. 5, that there is a significant distance in the *TP* -space between the coexistence limits (solid lines) and the spinodal curves (dashed lines).

In what follows, we discuss the predicted spinodal for hydrocarbons with a selection of EoS representative of what is used in modern applications. Herein, we mainly focus on the pressure and temperature. In this discussion it is however crucial to recognize that the liquid density can change dramatically within the metastable region, even though it might only span a few degrees kelvin. An illustrative example of this is given in Fig. 6, showing the density and pressure of the liquid spinodal of ethane compared to the saturation line. At low pressures, the liquid density of the metastable fluid near the spinodal curve can be half of that at the saturation curve. Moreover, the difference in liquid density at the spinodal for different EoS can also be significant.

Fig. 7 shows the spinodal curve in the *TP* -space compared to the corresponding homogeneous nucleation limit and available experimental data for the limit of superheat for a selection of pure species. For all three substances considered here, there is a clear agreement between the limit of superheat predicted by nucleation theory and experimental data obtained from the droplet explosion method. Table 1 shows the absolute average deviation (AAD) of the experimental data points relative to the limit of superheat from classic nucleation theory for pure components and binary mixtures. The overall AAD between the predictions from CNT and the experimental measurements for the limit of superheat is only 1.0 K for pure species and 2.4 K for mixtures. Thus, even though CNT does not accurately predict the exact nucleation rates of fluids [1], it accurately reproduces the superheat limit.

The gap between the limit of superheat predicted by CNT and the liquid spinodal curve thus accurately represents the experimentally unobtainable part of the metastable region, caused by thermal fluctuations in the liquid. Overall, the liquid spinodal curves predicted using GERG2008, PC-SAFT, PR, and CSP agree within 2–3 K in the range from atmospheric to critical pressure. A notable exception is the liquid and vapor spinodals for n-pentane calculated using the PC-SAFT EoS (Fig. 7b). Here, a significant inaccuracy in the predicted critical point seems to offset the entire liquid spinodal curve by 5–10 K. This suggests that it is imperative for the EoS to reproduce the critical point of the fluid to provide reliable predictions of the spinodal. Note that while the CNT predictions depend on an estimated liquid density, surface tension, as well as the value of J_{crit}, a sensitivity analysis showed that the predicted limit of superheat matched experimental data for reasonable perturbations of ρ and σ, and for J_{crit} differing by orders of magnitude.

For the vapor spinodal there is a significantly larger span in the predicted spinodal curves from the four EoS than for the liquid spinodal. In particular, at a pressure of 0.9 bar, the difference in the vapor spinodal ranges from 42.4–85.1 K for methane, 135.5–213.6 K for n–pentane and 32.6–59.7 K for nitrogen. Table 2 shows the pressure-averaged standard deviation (with regard to EoS) in kelvin for a number of light hydrocarbons and nitrogen. The spread in predictions is higher for the vapor spinodal than the liquid spinodal, with an average standard deviation of 6.29 K for the former.

Fig. 8 shows the binary mixture liquid and vapor spinodal temperature at atmospheric pressure for the GERG2008, PC-SAFT, PR and extended CSP EoS, as a function of the second component mole fraction. The spinodal curves are compared to the bubble and dew lines, the superheat and supersaturation limits predicted by CNT, as well as available experimental data for the limit of superheat. Again, there is a good agreement between liquid superheat limit obtained in droplet explosion experiments and the limit predicted by classic nucleation theory. The predicted liquid spinodals mostly agree within 5 K. Moreover, the results indicate that for these species, a mole-weighted average of pure specie spinodal can provide an accurate estimate of the mixture spinodal.

The binary mixture vapor spinodals (Fig. 8, right) demonstrates a larger internal spread than what is the case for the liquid spinodal curves. Specifically, for an even mixture, the vapor spinodal temperature ranges from 85.9–154.7 K for ethane/propane, 108.9–177.0 K for propane/n–butane and 154.4–227.3 K for n–pentane/n–hexane. This behavior is consistent with what was

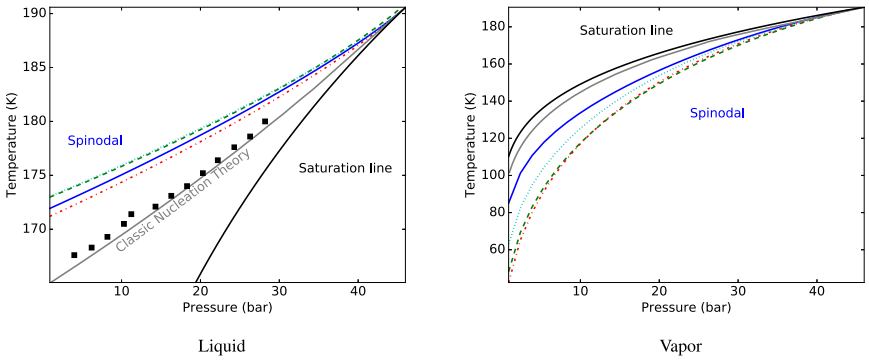

(a) Methane

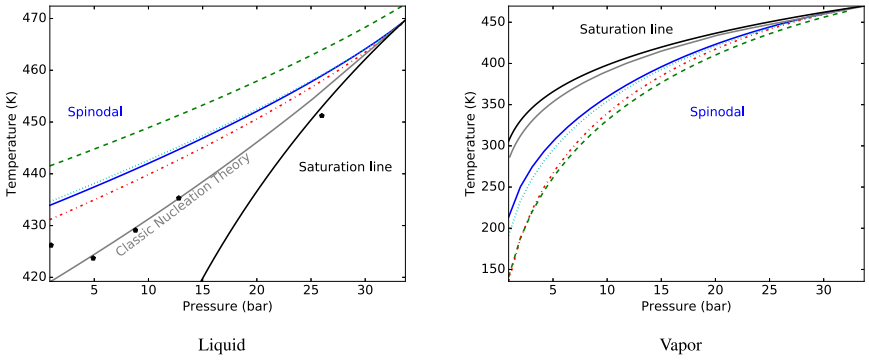

(b) n-Pentane

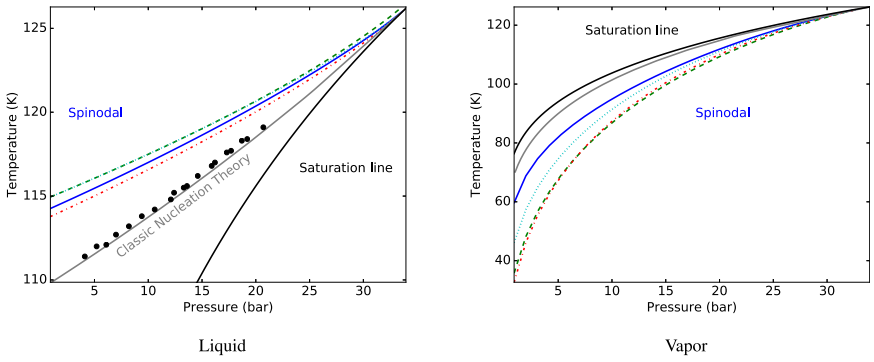

(c) Nitrogen

Fig. 7. Comparison of pure-component spinodal curves (liquid and vapor), superheat and subcool limits predicted using CNT (solid gray) and saturation line (solid black). The saturation lines are calculated with GERG2008. Spinodal curves are shown for four different EoS: GERG2008 (solid blue), PC-SAFT (dashed green), PR (dash-dot red) and extended CSP (dotted cyan). Experimental data from various studies of the limit of superheat are also shown: methane by Baidakov and Skripov [51] (squares), n-pentane compiled by Avedisian [8] (pentagons), nitrogen by Baidakov and Skripov [51] (circles). (For interpretation of the references to colour in this figure legend, the reader is referred to the web version of this article.)

Table 1
The average absolute deviation (AAD) in the temperature for the experimental data for the limit of superheat compared to classic nucleation theory for pure components and mixtures at pressure ranging from 0.9 bar to the critical pressure.

	AAD (K)
Methane	0.62
n-Pentane	0.28
Nitrogen	2.21
Ethane/Propane	4.5
Propane/n-Butane	1.2
n-Pentane/n-Hexane	1.6

Table 2
The standard deviation in the temperature with regard to EoS for the predicted spinodal. For the GERG2008, PC-SAFT, PR, and CSP EoS. Standard deviations are averaged for pressures ranging from 0.9 bar to the critical pressure.

	Liquid (K)	Vapor (K)
Methane	0.44	4.07
Ethane	1.13	6.62
Propane	1.60	7.15
n-Butane	2.19	7.99
n-Pentane	2.86	9.31
Nitrogen	0.30	2.61
Overall	1.42	6.29

observed for pure species (Fig. 7 right). The highest predictions for the vapor spinodal all come from the multiparameter GERG2008 equation, while the lowest come from the simple cubic Peng–Robinson EoS. This further illustrates the inconsistency of widely used EoS when used in the metastable domain. Table 3 shows the average (over mole fractions) standard deviation (with regard to EoS) of the predicted liquid and vapor spinodal temperatures for mixtures. Again, as for pure species, the spread in predicted spinodal temperatures is significant, especially for the vapor spinodal.

3.4. How close to the spinodals can experiments bring us?

We showed in Sec. 3.3 that the limit of superheat from experiments agreed very well with predictions from CNT, both for single-component liquids (Fig. 7) and mixtures (Fig. 8). This does not contradict that CNT is unable to reproduce experimental nucleation rates, since the limit of superheat is insensitive to the exact choice of the critical nucleation rate in Eq. (27). We can therefore use CNT to estimate the limits for how close to the spinodal it is possible to get experimentally before homogeneous nucleation occurs spontaneously. In Fig. 9, we have used methane as example and plotted the phase envelope that encloses the two-phase region (blue solid line), the limit of homogeneous nucleation as predicted by CNT (green dashed line) and the spinodals (red solid line). The spinodals, the coexistence line and the homogeneous nucleation limit all merge in the critical point.

In the following, we shall refer to the function $P = P(T, \rho)$ as the thermodynamic surface of methane. Fig. 9 shows that:

1 On a curve on the thermodynamic surface that goes from the spinodal to the coexistence limit, the distance between the spinodal and the nucleation limit relative to the corresponding distance to the coexistence limit is significant.
2 The relative distance on this curve is much larger for metastable vapor than for metastable liquid.

Point number 1 means that there is large part of the thermodynamic surface where the properties of the metastable fluid are currently experimentally unavailable, in particular for metastable vapor. In the literature, some suggestions have been put forward on how to enter the region of the thermodynamic surface that is currently experimentally unavailable.

A recent work [56] shows how small closed containers can be used to completely prevent nucleation, achieving infinitely long-lived metastable states, referred to as superstable. Experiments can be carried out in quartz inclusions, similar to Ref. [6], where speed of sound measurements in the inclusion give information about the slope of $P(\rho)$ at constant entropy, similar to Ref. [57]. Since such experiments are very challenging, the perhaps most available methodology to study the properties of highly metastable states is to use molecular dynamics simulations in the canonical ensemble. For many fluids like alkanes, carbon dioxide and nitrogen, force fields have been developed that reproduce the thermodynamic properties from experiments very accurately [58]. Molecular Dynamics simulations are then capable of generating pseudo-experimental data in the metastable regions, or to estimate the spinodals of the fluid. Eventually, hybrid data sets with both experimental data and data from computations can be exploited in the fitting of the next generation multiparameter EoS, following a procedure similar to Rutkai et al. [59]. This represents a largely unexplored research topic for the future.

Bullet point 2 agrees with the results in Figs. 7 and 8, and shows that CNT predicts the nucleation limit to be closer to the spinodal for liquids than for vapor.

4. Conclusion

In this work, we have presented a method that can be used to obtain the thermodynamic stability limit of a single-phase fluid, called the spinodal. We demonstrated that the method was robust in vicinity of the critical point, scalable to multicomponent mixtures and applicable to complex non-analytical EoS.

We next discussed the role of the spinodal, the metastable and the unstable regions of the phase diagram of the single-phase fluid in the development of modern equations of state (EoS). Since the spinodal provides a reference for an extrapolation into the metastable domain from the saturation curve, and since much is known about the thermodynamic properties of the fluid at the spinodal, information about the spinodal can be used to characterize the properties or to estimate the uncertainty of the properties of fluids in the metastable domain.

A future goal should be to develop EoS without inadmissible pseudo-stable states in the unstable domain. This is of importance, both for combining them with mass based density functional theory and to develop thermodynamically consistent mixing rules with a physical interpretation. We proposed and evaluated a set of inequality constraints that can be used for this purpose in the fitting of modern EoS for single-component fluids.

We showed that there were large inconsistencies in predicted spinodals from a wide range of EoS such as cubic EoS, extended corresponding state EoS, SAFT and multiparameter EoS. The overall standard deviation in the prediction of the spinodal temperatures were 1.4 K and 2.7 K for single- and multi-component liquid-spinodals and 6.3 K and 26.9 K for single- and multi-component vapor spinodals. However, the range between the smallest and the largest predictions were significantly larger. For example, for an even mixture of hydrocarbons, the vapor spinodal temperature ranged from 85.9–154.7 K for ethane/propane, 108.9–177.0 K for propane/n–butane and 154.4–227.3 K for n–pentane/n–hexane. In general, there was a much larger spread in the prediction of the vapor-spinodal than the liquid-spinodal.

We also discussed the relationship between the measurable limit of superheat or supersaturation and the theoretical concept of

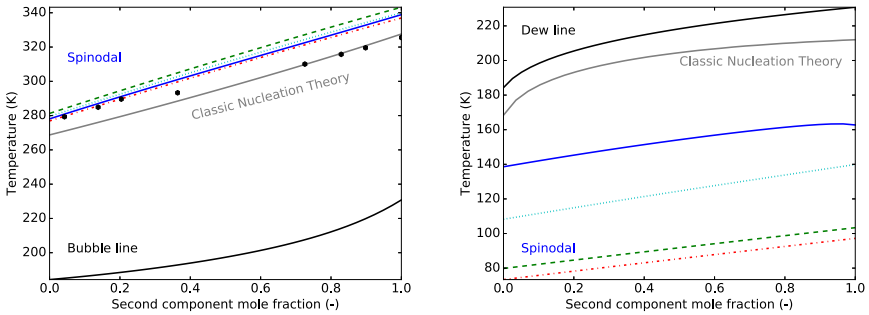

Liquid Vapor

(a) Ethane + Propane

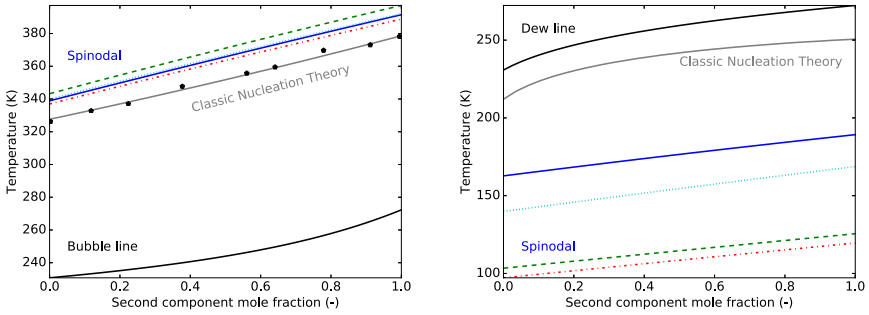

Liquid Vapor

(b) Propane + n-Butane

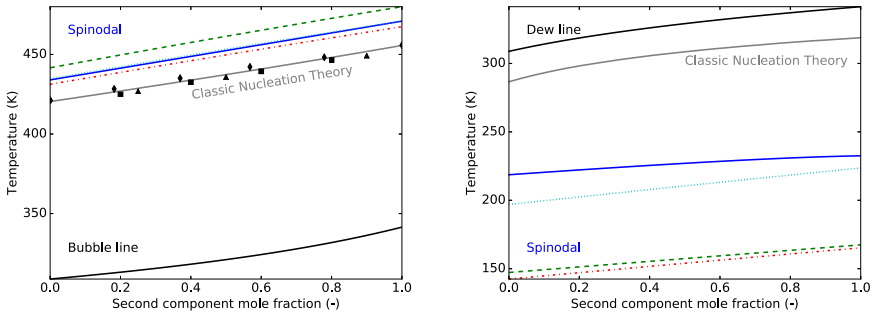

Liquid Vapor

(c) n-Pentane + n-Hexane

Fig. 8. Comparison of the spinodal curve (liquid and vapor), superheat and subcool limits predicted using CNT (solid gray), and bubble and dew lines (solid black) for some binary mixtures at 1 bar. The bubble and dew lines are computed using GERG2008. Spinodals are shown for four different EoS: GERG2008 (solid blue), PC-SAFT (dashed green), PR (dash-dot red) and extended CSP (dotted cyan). Experimental data from various studies of the limit of superheat are also shown: ethane + propane by Porteous and Blander [52] (hexagons), propane + n-butane by Renner et al. [53] (pentagons), n-pentane + n-hexane by Holden and Katz [54] (squares), Park et al. [24] (diamonds) and Skripov [55] (triangles). (For interpretation of the references to colour in this figure legend, the reader is referred to the web version of this article.)

Table 3
The standard deviation in the temperature for the predicted spinodal limit for binary mixtures at atmospheric pressure using the GERG2008, PC-SAFT, PR, and CSP EoS. Standard deviations are averaged over all mole fractions.

	Liquid (K)	Vapor (K)
Methane/Ethane	1.85	21.51
Methane/Propane	2.62	23.34
Ethane/Propane	2.05	27.22
Ethane/n-Butane	2.67	28.92
Propane/n-Butane	2.70	28.13
n-Pentane/n-Hexane	4.31	31.97
Overall	2.70	26.85

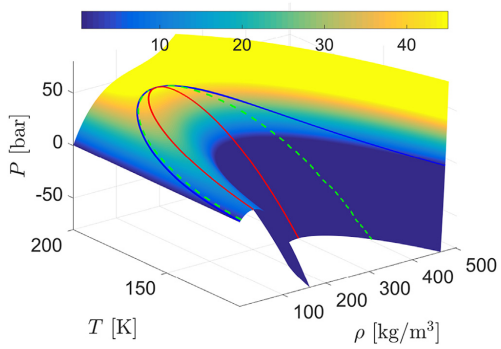

Fig. 9. A three-dimensional representation of the thermodynamic landscape of methane (relation between P, T and ρ) as predicted by the PR EoS. Here, the blue solid line encloses the two-phase region, the green dashed lines denote the states where Eq. (27) is satisfied and the homogeneous nucleation rate as predicted by CNT is so fast that the single-phase fluid appearers to decompose spontaneously into two phases. The red solid lines denote the spinodal, and enclose a region in which the single-phase fluid is unstable. (For interpretation of the references to colour in this figure legend, the reader is referred to the web version of this article.)

the spinodal. While nucleation rates from CNT can deviate orders of magnitude from experiments, we found that the limit of superheat experiments agreed within 1.0 K and 2.4 K with predictions from CNT for single- and multi-component fluids respectively.

At present, a large part of the metastable domain of the phase diagram is experimentally unavailable, in particular for metastable vapor. Novel techniques, with experimental or computational methods, should be developed to characterize the thermodynamic properties in these regions, and to identify the thermodynamic states that define the spinodal.

Acknowledgment

The authors acknowledge the support from the Research Council of Norway (project number 244076). The authors thank “The Gas Technology Centre NTNU-SINTEF” for the support.

References

[1] P.G. Debenedetti, Metastable Liquids: Concepts and Principles, Princeton University Press, Princeton, 1996.
[2] F. Caupin, E. Herbert, Cavitation in water: a review, Comptes Rendus Phys. 7 (9) (2006) 1000–1017, http://dx.doi.org/10.1016/j.crhy.2006.10.015.
[3] K. Davitt, A. Arvengas, F. Caupin, Water at the cavitation limit: density of the metastable liquid and size of the critical bubble, Europhys. Lett. 90 (2010) 16002, http://dx.doi.org/10.1209/0295-5075/90/16002.
[4] F. Caupin, A. Arvengas, K. Davitt, M. El Mekki Azouzi, K.I. Shmulovich, C. Ramboz, D.A. Sessoms, A.D. Stroock, Exploring water and other liquids at negative pressure, J. Phys. Condens. Matter 24 (28) (2012) 284110, http://dx.doi.org/10.1088/0953-8984/24/28/284110.
[5] Q. Zheng, D.J. Durben, G.H. Wolf, C.A. Angell, Liquids at large negative pressures: water at the homogeneous nucleation limit, Science 254 (5033) (1991) 829–832, http://dx.doi.org/10.1126/science.254.5033.829.
[6] M. El Mekki Azouzi, C. Ramboz, J.F. Lenain, F. Caupin, A coherent picture of water at extreme negative pressure, Nat. Phyics 9 (2013) 38–41, http://dx.doi.org/10.1038/nphys2475.
[7] A. C. Hack, A. B. Thompson, Density and viscosity of hydrous magmas and related fluids and their role in subduction zone processes, J. Petrology 52 (1333–1362). doi:10.1093/petrology/egq048.
[8] C. Avedisian, The homogeneous nucleation limits of liquids, J. Phys. Chem. Reference Data 14 (3) (1985) 695–729, http://dx.doi.org/10.1063/1.555734.
[9] J. Salla, M. Demichela, J. Casal, BLEVE: a new approach to the superheat limit temperature, J. Loss Prev. Process Industries 19 (6) (2006) 690–700, http://dx.doi.org/10.1016/j.jlp.2006.04.004.
[10] R. Bubbico, E. Salzano, Acoustic analysis of blast waves produced by rapid phase transition of LNG released on water, Saf. Sci. 47 (4) (2009) 515–521, http://dx.doi.org/10.1016/j.ssci.2008.07.033.
[11] R.K. Eckhoff, Boiling liquid expanding vapour explosions (BLEVEs): a brief review, J. Loss Prev. Process Industries 32 (2014) 30–43, http://dx.doi.org/10.1016/j.jlp.2014.06.008.
[12] H. Vehkamäki, Classical Nucleation Theory in Multicomponent Systems, Springer Verlag, Berlin, 2006.
[13] A. Obeidat, J.S. Li, G. Wilemski, Nucleation rates of water and heavy water using equations of state, J. Chem. Phys. 121 (19) (2004) 9510–9516, http://dx.doi.org/10.1063/1.1806400.
[14] A. Obeidat, G. Wilemski, Gradient theory of nucleation in polar fluids, Atmos. Res. 82 (2006) 481–488, http://dx.doi.org/10.1016/j.atmosres.2006.02.005.
[15] W. Wagner, A. Pruß, The IAPWS formulation 1995 for the thermodynamic properties of ordinary water substance for general and scientific use, J. Phys. Chem. Reference Data 31 (2002) 387–535, http://dx.doi.org/10.1063/1.1461829.
[16] Ø. Wilhelmsen, A. Aasen, G. Skaugen, P. Aursand, A. Austegard, E. Aursand, M.Aa. Gjennestad, H. Lund, G. Linga, M. Hammer, Thermodynamic Modeling with Equations of State: present Challenges for Established Models, Under Revision.
[17] H. Wakeshima, K. Takata, On the limit of superheat, J. Phys. Soc. Jpn. 13 (11) (1958) 1398–1403, http://dx.doi.org/10.1143/JPSJ.13.1398.
[18] G.R. Moore, Vaporization of superheated drops in liquids, AIChE J. 5 (4) (1959) 458–466, http://dx.doi.org/10.1002/aic.690050412.
[19] J.H. Lienhard, A. Karimi, Homogeneous nucleation and the spinodal line, J. Heat Transf. 103 (1981) 61–64, http://dx.doi.org/10.1115/1.3244431.
[20] J.H. Lienhard, N. Shamsundar, P.O. Biney, Spinodal lines and equations of state: a review, Nucl. Eng. Des. 95 (1986) 297–314, http://dx.doi.org/10.1016/0029-5493(86)90056-7.
[21] N. Shamsundar, J.H. Lienhard, Equations of state and spinodal lines – a review, Nucl. Eng. Des. 141 (1) (1993) 269–287, http://dx.doi.org/10.1016/0029-5493(93)90106-J.
[22] P.O. Biney, W.-G. Dong, J.H. Lienhard, Use of a cubic equation to predict surface tension and spinodal limits, J. Heat Transf. 108 (2) (1986) 405–410, http://dx.doi.org/10.1115/1.3246938.
[23] C. Liu, D. Zeng, K. Xing, Superheat limit of liquid mixtures, Proc. Symposium Energy Eng. 21st Century 1 (2000) 373–378.
[24] H.-C. Park, K.-T. Byun, H.-Y. Kwak, Explosive boiling of liquid droplets at their superheat limits, Chem. Eng. Sci. 60 (7) (2005) 1809–1821, http://dx.doi.org/10.1016/j.ces.2004.11.010.
[25] G. Soave, Equilibrium constants from a modified Redlich–Kwong equation of state, Chem. Eng. Sci. 27 (6) (1972) 1197–1203, http://dx.doi.org/10.1016/0009-2509(72)80096-4.
[26] D.-Y. Peng, D.B. Robinson, A new two-constant equation of state, Industrial Eng. Chem. Fundam. 15 (1) (1976) 59–64, http://dx.doi.org/10.1021/i160057a011.
[27] J. F. Ely, I. M. F. Marrucho, Equations of State for Fluid Mixtures, IUPAC, 2000, Ch. The Corresponding-states Principle, pp. 289–320.
[28] Ø. Wilhelmsen, G. Skaugen, O. Jørstad, H. Li, Evaluation of SPUNG and other equations of state for use in carbon capture and storage modelling, Energy Procedia 23 (2012) 236–245, http://dx.doi.org/10.1016/j.egypro.2012.06.024.
[29] M.L. Michelsen, J.M. Mollerup, Thermodynamic Models: Fundamentals and Computational Aspects, second ed., Tie-Line Publictions, Holte, Denmark, 2007.
[30] W.G. Chapman, K.E. Gubbins, G. Jackson, M. Radosz, SAFT: equation-of-state solution model for associating fluids, Fluid Phase Equilibria 52 (1989) 31–38, http://dx.doi.org/10.1016/0378-3812(89)80308-5.
[31] J. Gross, G. Sadowski, Perturbed-chain SAFT: an equation of state based on a perturbation theory for chain molecules, Industrial Eng. Chem. Res. 40 (4) (2001) 1244–1260, http://dx.doi.org/10.1021/ie0003887.
[32] U. Setzmann, W. Wagner, A new equation of state and tables of thermodynamic properties for methane covering the range from the melting line to 625 K at pressures up to 100 MPa, J. Phys. Chem. Reference Data 20 (6) (1991) 1061–1155, http://dx.doi.org/10.1063/1.555898.
[33] R. Span, W. Wagner, A new equation of state for carbon dioxide covering the fluid region from the triple-point temperature to 1100 K at pressures up to 800 MPa, J. Phys. Chem. Reference Data 25 (6) (1996) 1509–1596, http://

dx.doi.org/10.1063/1.555991.
[34] R. Span, E.W. Lemmon, R.T. Jacobsen, W. Wagner, A reference quality equation of state for nitrogen, Int. J. Thermophys. 19 (4) (1998) 1121–1132, http://dx.doi.org/10.1023/A:1022689625833.
[35] C. Tegeler, R. Span, W. Wagner, A new equation of state for argon covering the fluid region for temperatures from the melting line to 700 K at pressures up to 1000 MPa, J. Phys. Chem. Reference Data 28 (3) (1999) 779–850, http://dx.doi.org/10.1063/1.556037.
[36] J. Smukala, R. Span, W. Wagner, New equation of state for ethylene covering the fluid region for temperatures from the melting line to 450 K at pressures up to 300 MPa, J. Phys. Chem. Reference Data 29 (5) (2000) 1053–1121, http://dx.doi.org/10.1063/1.1329318.
[37] O. Kunz, W. Wagner, The GERG-2008 wide-range equation of state for natural gases and other mixtures: an expansion of GERG-2004, J. Chem. Eng. Data 57 (11) (2012) 3032–3091, http://dx.doi.org/10.1021/je300655b.
[38] H.B. Callen, Thermodynamics and an Introduction to Thermostatistics, second ed., Wiley, New York, 1985.
[39] J.W. Tester, M. Modell, Thermodynamics and its Applications, Prentice Hall PTR, New Jersey, 1996.
[40] B.L. Beegle, M. Modell, R.C. Reid, Thermodynamic stability criterion for pure substances and mixtures, AIChe J. 20 (1974) 1200–1206, http://dx.doi.org/10.1002/aic.690200621.
[41] E.H. Chimowitz, Introduction to Critical Phenomena in Fluids, Oxford University Press, New York, 2005.
[42] R.A. Heidemann, A.M. Khalil, The calculation of critical points, AIChE J. 26 (5) (1980) 769–779, http://dx.doi.org/10.1002/aic.690260510.
[43] M.L. Michelsen, Calculation of critical points and phase boundaries in the critical region, Fluid Phase Equilibria 16 (1) (1984) 57–76, http://dx.doi.org/10.1016/0378-3812(84)85021-9.
[44] Ø. Wilhelmsen, D. Reguera, Evaluation of finite-size effects in cavitation and droplet formation, J. Chem. Phys. 142 (2015) 064703, http://dx.doi.org/10.1063/1.4907367.
[45] R.C. Reid, J.M. Prausnitz, B.E. Poling, The Properties of Gases and Liquids, McGraw Hill Book Co., New York, NY, 1987.
[46] E.W. Lemmon, R.T. Jacobsen, A new functional form and new fitting techniques for equations of state with application to pentafluoroethane (HFC-125), J. Phys. Chem. Reference Data 34 (2005) 69–108, http://dx.doi.org/10.1063/1.1797813.
[47] E.W. Lemmon, M.O. McLinden, W. Wagner, Thermodynamic properties of propane. III. a reference equation of state for temperatures from the melting line to 650 K and pressures up to 1000 MPa, J. Phys. Chem. Reference Data 54 (2009) 3141–3180, http://dx.doi.org/10.1021/je900217v.
[48] A.E. Elhassan, R.J.B. Craven, K.M. de Reuck, The area method for pure fluids and an analysis of the two-phase region, Fluid Phase Equilibria 130 (1997) 167–187, http://dx.doi.org/10.1016/S0378-3812(96)03222-0.
[49] J. Gernert, A. Jäger, S. R, Calculation of phase equilibria for multi-component mixtures using highly accurate helmholtz energy equation of state, Fluid Phase Equilibria 375 (2014) 209–218, http://dx.doi.org/10.1016/j.fluid.2014.05.012.
[50] Software for the Reference Equation of State GERG-2008 for Natural Gases and Other Mixtures, 2016, http://www.thermo.rub.de/en/prof-w-wagner/software/gerg-2004-gerg-2008.html.
[51] V.G. Baidakov, V.P. Skripov, Superheating and surface tension of vapor nuclei in nitrogen, oxygen, and methane, Russ. J. Phys. Chem. 56 (1982) 499–501.
[52] W. Porteous, M. Blander, Limits of superheat and explosive boiling of light hydrocarbons, halocarbons, and hydrocarbon mixtures, AIChE J. 21 (3) (1975) 560–566, http://dx.doi.org/10.1002/aic.690210319.
[53] T.A. Renner, G.H. Kucera, M. Blander, Explosive boiling in light hydrocarbons and their mixtures, J. Colloid Interface Sci. 52 (2) (1975) 391–396, http://dx.doi.org/10.1016/0021-9797(75)90215-5.
[54] B.S. Holden, J.L. Katz, The homogeneous nucleation of bubbles in superheated binary liquid mixtures, AIChE J. 24 (2) (1978) 260–267, http://dx.doi.org/10.1002/aic.690240215.
[55] V.P. Skripov, Metastable Liquids, John Wiley & Sons, 1974.
[56] Ø. Wilhelmsen, D. Bedeaux, S. Kjelstrup, D. Reguera, Communication: superstabilization of fluids in nanocontainer, J. Chem. Phys. 141 (2014) 071103, http://dx.doi.org/10.1063/1.4893701.
[57] A.D. Alvarenga, M. Grimsditch, R.J. Bodnar, Elastic properties of water under negative pressures, J. Chem. Phys. 98 (1993) 8392–8396, http://dx.doi.org/10.1063/1.464497.
[58] J.J. Potoff, J. Ilja Siepmann, Vapor-liquid equilibria of mixtures containing alkanes, carbon dioxide, and nitrogen, AIChE J. 47 (2001) 1676–1682, http://dx.doi.org/10.1002/aic.690470719.
[59] G. Rutkai, M. Thol, R. Lustig, R. Span, J. Vrabec, Communication: fundamental equation of state correlation with hybrid data sets, J. Chem. Phys. 139 (2013) 041102, http://dx.doi.org/10.1063/1.4817203.

Paper II

M. Aa. Gjennestad and Ø. Wilhelmsen. Thermodynamic stability of droplets, bubbles and thick films in open and closed pores. *Fluid Phase Equilibria* 505 (2020), p. 112351. DOI: 10.1016/j.fluid.2019.112351

Fluid Phase Equilibria 505 (2020) 112351

Contents lists available at ScienceDirect

Fluid Phase Equilibria

journal homepage: www.elsevier.com/locate/fluid

Thermodynamic stability of droplets, bubbles and thick films in open and closed pores

Magnus Aa. Gjennestad [a, *], Øivind Wilhelmsen [b, c]

[a] PoreLab/Department of Physics, Norwegian University of Science and Technology, Høgskoleringen 5, NO-7491 Trondheim, Norway
[b] Department of Energy and Process Engineering, Norwegian University of Science and Technology, Kolbjørn Hejes vei 1B, NO-7491 Trondheim, Norway
[c] PoreLab/SINTEF Energy Research, P.O. box 4761 Sluppen, NO-7465 Trondheim, Norway

ARTICLE INFO

Article history:
Received 9 August 2019
Received in revised form
20 September 2019
Accepted 3 October 2019
Available online 11 October 2019

Keywords:
Thermodynamics
Stability
Droplet
Bubble
Film
Pore

ABSTRACT

A fluid in a pore can form diverse heterogeneous structures. We combine a capillary description with the cubic-plus-association equation of state to study the thermodynamic stability of droplets, bubbles and films of water at 358 K in a cylindrically symmetric pore. The equilibrium structure depends strongly on the size of the pore and whether the pore is closed (canonical ensemble) or connected to a particle reservoir (grand canonical ensemble). A new methodology is presented to analyze the thermodynamic stability of films, where the integral that describes the total energy of the system is approximated by a quadrature rule. We show that, for large pores, the thermodynamic stability limit of adsorbed droplets and bubbles in both open and closed pores is governed by their mechanical stability, which is closely linked to the pore shape. This is also the case for a film in a closed pore. In open pores, the film is chemically unstable except for very low film-phase contact angles and for a limited range in external pressure. This result emphasizes the need to invoke a complete thermodynamic stability analysis, and not restrict the discussion to mechanical stability. A common feature for most of the heterogeneous structures examined is the appearance of regions where the structure is metastable with respect to a pore filled with a homogeneous fluid. In the closed pores, these regions grow considerably in size when the pores become smaller. This can be understood from the larger energy cost of the interfaces relative to the energy gained from having two phases. Complete phase diagrams are presented that compare all the investigated structures. In open pores at equilibrium, the most stable structure is either the homogeneous phase or adsorbed droplets and bubbles, depending on the type of phase in the external reservoir. Smaller pores allow for droplets and bubbles to adsorb for a larger span in pressure. In closed pores, most of the investigated configurations can occur depending on the total density, the contact angle, the pore shape and the pore size. The analysis presented in this work is a step towards developing a thermodynamic framework to map the rich heterogeneous phase diagrams of porous media and other confined systems.

1. Introduction

Some phenomena occur exclusively in pores or under strong confinement. In porous materials, a liquid phase can form at pressures below the saturation pressure during capillary condensation [1–4], liquid water can be stretched to negative pressures exceeding 140 MPa in quartz inclusions [5,6] and giant charge reversal has been observed in confined systems filled with electrolytes [7]. The understanding of such systems is at the core of widely different topics such as porous media science [8,9], atmospheric science [10] and biology [11].

While the thermodynamics of homogeneous systems is well understood [12], this is not the case for heterogeneous systems, as evident e.g. from the large deviations between experiments, theory and simulations for the formation of drops [13,14]. Both in bulk systems and in systems under confinement, equilibrium is characterized by a minimum of an energy state function whose nature is determined by the boundary conditions. For instance, in a closed container at constant temperature, equilibrium is a minimum of the Helmholtz energy, while the Gibbs energy is minimum at

* Corresponding author.
E-mail addresses: magnus.aa.gjennestad@ntnu.no, magnus@aashammer.net (M.Aa. Gjennestad).

https://doi.org/10.1016/j.fluid.2019.112351

atmospheric conditions [12].

A complicating factor in pores, is that multiple heterogeneous structures such as films, adsorbed or free droplets and bubbles, and combinations of these, could all be stationary states of the same energy state function [15]. Such states are typically characterized by uniform temperature, equality of chemical potentials and mechanical equilibrium [12,16]. These conditions being satisfied however, does not imply a minimum, as the stationary state can also be a maximum or a saddle point [17]. To determine the equilibrium state, it is necessary to employ thermodynamic stability analysis [18], where the outcome depends strongly on the boundary conditions. For instance, bubbles and droplets are known to be unstable at atmospheric conditions, as they represent saddle points in the Gibbs energy landscape [17]. However, in confined systems, bubbles and droplets can be minima in the Helmholtz energy and thus be stable [19–21].

In the literature on the stability of heterogeneous structures, many works have studied *thin* films, often in combination with adsorbed droplets [22–24]. Films are characterized as either thin (α-films) or thick (β-films). In thin films, the thermodynamic properties of the interior deviate from bulk behavior, resulting in a non-zero disjoining pressure. Thin films have been examined by use of theory [25,26], molecular simulations [27,28], density functional theory [29] and experiments [30]. A common feature of previous works in the literature discussing the stability of films, is that they consider only stability towards perturbations of the film height. This differs from thermodynamic stability, since exchange of particles is neglected [25,26]. In this work, we show that the thermodynamic stability of the simplest type of film, the thick film, is very different for closed (canonical ensemble) and open systems (grand canonical ensemble). A new methodology to analyze the thermodynamic stability of films will be presented. This methodology can be extended to include the disjoining pressure and give new insight into thin films in future work.

We will discuss in detail the difference between the thermodynamic stability of heterogeneous structures and equilibrium configurations in *open* and *closed* pores, as well as the influence of pore size. The work is a step towards developing a thermodynamic framework to characterize heterogeneous fluid structures and equilibrium states inside porous media.

We begin by presenting the thermodynamic description of the fluid structures in Section 2. We employ a capillary description, with the rationale that it gives identical results to more sophisticated density functional theory for the thermodynamic stability of multicomponent droplets and bubbles [14]. The numerical methods are described in Section 3, before results are discussed in Section 4. Concluding remarks are provided in Section 5.

2. Models

In the following, we present thermodynamic models for the four systems illustrated in Fig. 1. The figure depicts a cylindrically symmetric pore in an incompressible and chemically inert solid matrix. The pore contains a single-component fluid that can have four different configurations, (a) a homogeneous fluid phase, (b) a free droplet or bubble that is not in contact with the pore walls, (c) a droplet or bubble filling the entire cross-section of some part of the pore and (d) a thick film (no disjoining pressure) of gas or liquid. Thin films, that are influenced by a disjoining pressure, are beyond the scope of the present work. Structures that do not have the same rotational symmetry as the pore are not considered. Examples include spherical sessile droplets and bubbles adsorbed to the pore wall. The reason for omitting these structures will be further discussed in Section 4.4. By deriving thermodynamic models for all these sub-systems with the same assumptions, it is possible to evaluate their local stability, compare their energies and thus identify the appropriate equilibrium configuration, at given conditions.

We consider a pore of length L^{p} and radius R^{p}. The radius depends on the axial coordinate $z \in [0,\, L^{\mathrm{p}}]$. Fig. 1a illustrates one possible pore geometry, but the governing equations will be derived for an arbitrary function $R^{\mathrm{p}}(z)$, which is sufficiently smooth for $\dot{R}^{\mathrm{p}} = \mathrm{d}R^{\mathrm{p}}/\mathrm{d}z$ and $\ddot{R}^{\mathrm{p}} = \mathrm{d}^2R^{\mathrm{p}}/\mathrm{d}z^2$ to be defined.

For simplicity, we will restrict the pore radii considered in the present work to functions on the form,

$$R^{\mathrm{p}}(z) = L^{\mathrm{p}}\left(0.2 - 0.075\left\{1 + \cos\left(\frac{2\pi z}{L^{\mathrm{p}}}\right)\right\}\right), \tag{1}$$

where Fig. 1 shows an example of this profile. It is assumed that the solid matrix acts as a thermal reservoir for the fluids at temperature T.

With the above assumptions, the volume of the pore is constant and can be calculated from,

$$V^{\mathrm{p}} = \pi \int_0^{L^{\mathrm{p}}} (R^{\mathrm{p}})^2 \mathrm{d}z. \tag{2}$$

Similarly, the surface area of the solid matrix is constant and equal to

$$A^{\mathrm{p}} = 2\pi \int_0^{L^{\mathrm{p}}} R^{\mathrm{p}} \sqrt{1 + \left(\dot{R}^{\mathrm{p}}\right)^2}\, \mathrm{d}z. \tag{3}$$

Three interfacial tensions will be parameters in our models. These are σ^{gs}, $\sigma^{\ell\mathrm{s}}$ and $\sigma^{\mathrm{g}\ell}$ for the gas-solid, liquid-solid and gas-liquid interfaces, respectively. In terms of the interfacial tensions, Young's equation gives the contact angle α (measured in the liquid) as

$$\cos(\alpha) = \frac{\sigma^{\mathrm{gs}} - \sigma^{\ell\mathrm{s}}}{\sigma^{\mathrm{g}\ell}}. \tag{4}$$

Due to the isothermal conditions, interfacial tensions are assumed to be constant.

The thermodynamic properties of the fluids are described by an equation of state (EOS), where any EOS capable of describing the liquid and gas phases is applicable.

In the following, we present the governing equations for all the sub-systems in Fig. 1. A clear distinction is made between whether the system is closed (canonical ensemble), or connected to a particle reservoir (grand canonical ensemble). The grand canonical ensemble is a natural representation of an open pore, which is equivalent to a system connected to a temperature and pressure reservoir for a single-component system due to the Gibbs–Duhem relation (see Ref. [21] for a discussion). Equilibrium in the canonical ensemble is a minimum of the total Helmholtz energy of the system, while equilibrium in the grand canonical ensemble is a minimum of the total grand potential energy. These energy state functions and their stationary states have to be identified for each of the configurations in Fig. 1.

2.1. Pore with a homogeneous phase

We start by considering the simplest fluid configuration possible, which is a pore filled with a single-phase fluid. This type of configuration is illustrated in Fig. 1a. The Helmholtz energy of this system is

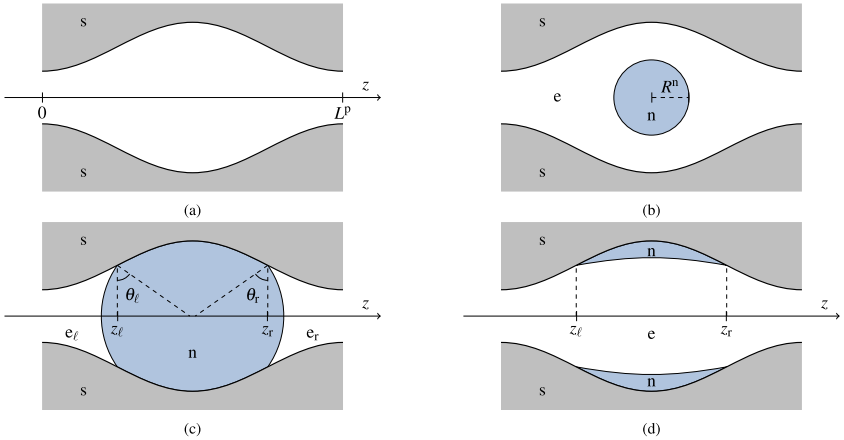

Fig. 1. Illustration of the heterogeneous fluid structures under consideration: (a) a homogeneous fluid phase, (b) a free droplet or bubble that is not in contact with the pore walls, (c) a droplet or bubble filling the entire cross-section of some part pore and (d) a thick film of gas or liquid.

$$F = -pV^{\mathrm{p}} + \mu N + \sigma A^{\mathrm{p}}, \tag{5}$$

where p is the fluid pressure, μ is the chemical potential, N is the number of particles and σ is the interfacial tension between the solid and the fluid, i.e. σ^{gs} for a pore filled with gas and σ^{ls} for a pore filled with liquid. The grand potential energy is

$$\Omega = F - \mu N. \tag{6}$$

Since the solid matrix is incompressible, chemically inert and has a constant temperature, its Helmholtz and grand potential energies are constants that can be omitted from the analysis without any further effect on the results. A stationary state of a homogeneous phase is characterized by uniform temperature, pressure and chemical potentials [12]. The phase is thermodynamically stable if its density is within the spinodal limits at the specified temperature. We refer to Aursand et al. [18] for further details on how the spinodal limits can be calculated.

2.2. Pore with a free droplet or bubble

Next, we consider a pore with a free spherical droplet or bubble that is not in contact with the pore walls. The droplet/bubble phase is labeled n, while the surrounding phase is labeled e, as illustrated in Fig. 1b.

First, we assume that the pore is a closed system with a fixed total number of particles N, total volume V^{p} and temperature T. An equilibrium state of this system is then a minimum in the total Helmholtz energy,

$$F = -p^{\mathrm{e}}V^{\mathrm{e}} + \mu^{\mathrm{e}}N^{\mathrm{e}} + \sigma^{\mathrm{es}}A^{\mathrm{es}} - p^{\mathrm{n}}V^{\mathrm{n}} + \mu^{\mathrm{n}}N^{\mathrm{n}} + \sigma^{\mathrm{en}}A^{\mathrm{en}}. \tag{7}$$

Herein, p^j is the pressure of phase j, μ^j is the chemical potential of phase j and N^j is the number of particles in phase j. The area of the interface between phase i and j is denoted by A^{ij} and the tension of this interface by σ^{ij}. Using that $V^{\mathrm{e}} + V^{\mathrm{n}} = V^{\mathrm{p}}$, $N^{\mathrm{e}} + N^{\mathrm{n}} = N$, $A^{\mathrm{es}} = A^{\mathrm{p}}$ and the Gibbs–Duhem relations for each phase, the differential of F can be written as

$$\mathrm{d}F = -(p^{\mathrm{n}} - p^{\mathrm{e}})\mathrm{d}V^{\mathrm{n}} + (\mu^{\mathrm{n}} - \mu^{\mathrm{e}})\mathrm{d}N^{\mathrm{n}} + \sigma^{\mathrm{en}}\mathrm{d}A^{\mathrm{en}}. \tag{8}$$

Since the n-phase is assumed to be spherical, A^{en} and V^{n} are not independent. We choose to describe the geometry of the droplet/bubble in terms of its radius R^{n} and get the differential

$$\mathrm{d}F = -\left(p^{\mathrm{n}} - p^{\mathrm{e}} - \frac{2\sigma^{\mathrm{en}}}{R^{\mathrm{n}}}\right)4\pi(R^{\mathrm{n}})^2\mathrm{d}R^{\mathrm{n}} + (\mu^{\mathrm{n}} - \mu^{\mathrm{e}})\mathrm{d}N^{\mathrm{n}}, \tag{9}$$

in terms of perturbations in the independent free variables of the system, R^{n} and N^{n}. The elements in the Jacobian vector of F are then

$$\left(\frac{\partial F}{\partial R^{\mathrm{n}}}\right)_{N^{\mathrm{n}}} = -4\pi(R^{\mathrm{n}})^2\left(p^{\mathrm{n}} - p^{\mathrm{e}} - \frac{2\sigma^{\mathrm{en}}}{R^{\mathrm{n}}}\right), \tag{10}$$

and

$$\left(\frac{\partial F}{\partial N^{\mathrm{n}}}\right)_{R^{\mathrm{n}}} = \mu^{\mathrm{n}} - \mu^{\mathrm{e}}. \tag{11}$$

A stationary state of F is therefore characterized by equality of the chemical potentials in the two phases and a pressure difference between the gas and liquid given by the Young–Laplace equation. The Hessian matrix of F can be found by further differentiation of the Jacobian, as shown in Ref. [14].

Let us now consider the pore in an open system at fixed total volume and temperature that is connected to a particle reservoir, such that the chemical potential of the e-phase is fixed. An equilibrium state is then a minimum of the total grand potential energy of the system,

$$\Omega = F - \mu^{\mathrm{e}}N. \tag{12}$$

By a derivation analogous to that above, one finds the Jacobian vector of Ω and that the criteria for a stationary point in the grand canonical ensemble are exactly the same as in the canonical ensemble. One subtle difference that makes the Hessian matrix of Ω different from that of F, is that μ^{e} in the open system no longer depends on the free variables of the system.

2.3. Pore with an adsorbed droplet or bubble

The next fluid configuration we consider is a pore containing a droplet or a bubble that is in contact with the pore walls and fills the entire pore cross-section for some interval on the z-axis. This type of fluid configuration is illustrated in Fig. 1c. The two fluid-fluid interfaces, in contact with the pore walls at z_ℓ and z_r, are assumed to be spherical caps. Again, the droplet/bubble phase is labeled n. The fluid phase on the left side is labeled e_ℓ and the one on the right side is labeled e_r.

The Helmholtz energy is

$$\begin{aligned} F = &-p^{e_\ell}V^{e_\ell} + \mu^{e_\ell}N^{e_\ell} + \sigma^{es}A^{e_\ell s} + \sigma^{en}A^{e_\ell n} \\ &-p^{e_r}V^{e_r} + \mu^{e_r}N^{e_r} + \sigma^{es}A^{e_r s} + \sigma^{en}A^{e_r n} \\ &-p^{n}V^{n} + \mu^{n}N^{n} + \sigma^{ns}A^{ns}. \end{aligned} \tag{13}$$

Using now that $V^{e_\ell} + V^{e_r} + V^n = V^p$, $A^{e_\ell s} + A^{ns} + A^{e_r s} = A^p$, $N^{e_\ell} + N^n + N^{e_r} = N$ and that the Gibbs–Duhem relation is satisfied for each phase, we can formulate the differential of F as

$$\begin{aligned} \mathrm{d}F = &-(p^{e_\ell} - p^n)\mathrm{d}V^{e_\ell} + (\mu^{e_\ell} - \mu^n)\mathrm{d}N^{e_\ell} \\ &+(\sigma^{es} - \sigma^{ns})\mathrm{d}A^{e_\ell s} + \sigma^{en}\mathrm{d}A^{e_\ell n} \\ &-(p^{e_r} - p^n)\mathrm{d}V^{e_r} + (\mu^{e_r} - \mu^n)\mathrm{d}N^{e_r} \\ &+(\sigma^{es} - \sigma^{ns})\mathrm{d}A^{e_r s} + \sigma^{en}\mathrm{d}A^{e_r n}. \end{aligned} \tag{14}$$

Since both fluid-fluid interfaces are assumed to be shaped like spherical caps, they can each be described by two independent variables. We therefore parameterize the six geometrical quantities V^{e_ℓ}, $A^{e_\ell s}$, $A^{e_\ell n}$, V^{e_r}, $A^{e_r s}$, $A^{e_r n}$ in terms of the four independent variables z_ℓ, z_r, θ_ℓ, and θ_r. As illustrated in Fig. 1c, z_ℓ denotes the position along the z-axis of the left three-phase contact line of the left meniscus and z_r denotes the position of the contact line of the right meniscus. The angle θ_ℓ is between a line connecting the center of the left sphere with a point on the left three-phase contact line and a line from the same point on the contact line which is perpendicular to the z-axis. The angle θ_r is defined analogously. In terms of the independent variables, we have that

$$V^{e_\ell} = \pi \int_0^{z_\ell} (R^p)^2 \mathrm{d}z - \zeta(z_\ell, \theta_\ell), \tag{15}$$

$$V^{e_r} = \pi \int_{z_r}^{L^p} (R^p)^2 \mathrm{d}z - \zeta(z_r, \theta_r), \tag{16}$$

$$A^{e_\ell s} = 2\pi \int_0^{z_\ell} R^p \sqrt{1 + \left(\dot{R}^p\right)^2}\,\mathrm{d}z, \tag{17}$$

$$A^{e_r s} = 2\pi \int_{z_r}^{L_p} R^p \sqrt{1 + \left(\dot{R}^p\right)^2}\,\mathrm{d}z, \tag{18}$$

$$A^{e_\ell n} = \pi \left\{R^p(z_\ell)\right\}^2 \left\{1 + \xi^2(\theta_\ell)\right\}, \tag{19}$$

$$A^{e_r n} = \pi \left\{R^p(z_r)\right\}^2 \left\{1 + \xi^2(\theta_r)\right\}, \tag{20}$$

where

$$\zeta(z, \theta) = \frac{\pi}{6}\left\{R^p(z)\right\}^3 \xi(\theta)\left\{3 + \xi^2(\theta)\right\}, \tag{21}$$

$$\xi(\theta) = \frac{1 - \sin(\theta)}{\cos(\theta)}. \tag{22}$$

The Helmholtz energy differential may then be expressed as

$$\begin{aligned} \mathrm{d}F = &\{\mu^{e_\ell} - \mu^n\}\mathrm{d}N^{e_\ell} + \{\mu^{e_r} - \mu^n\}\mathrm{d}N^{e_r} \\ &+\left\{(\sigma^{es} - \sigma^{ns})\frac{\partial A^{e_\ell s}}{\partial z_\ell} + \sigma^{en}\frac{\partial A^{e_\ell n}}{\partial z_\ell} - (p^{e_\ell} - p^n)\frac{\partial V^{e_\ell}}{\partial z_\ell}\right\}\mathrm{d}z_\ell \\ &+\left\{(\sigma^{es} - \sigma^{ns})\frac{\partial A^{e_r s}}{\partial z_r} + \sigma^{en}\frac{\partial A^{e_r n}}{\partial z_r} - (p^{e_r} - p^n)\frac{\partial V^{e_r}}{\partial z_r}\right\}\mathrm{d}z_r \\ &+\left\{\sigma^{en}\frac{\partial A^{e_\ell n}}{\partial \theta_\ell} - (p^{e_\ell} - p^n)\frac{\partial V^{e_\ell}}{\partial \theta_\ell}\right\}\mathrm{d}\theta_\ell \\ &+\left\{\sigma^{en}\frac{\partial A^{e_r n}}{\partial \theta_\ell} - (p^{e_r} - p^n)\frac{\partial V^{e_r}}{\partial \theta_r}\right\}\mathrm{d}\theta_r. \end{aligned} \tag{23}$$

Here, the expressions in the curly brackets are the elements of the Jacobian vector of F. The Hessian matrix can be found by further differentiation of the Jacobian vector.

In a stationary state, all the terms of (23) must vanish. Setting the last two terms equal to zero, yields

$$p^n - p^{e_\ell} = \frac{2\sigma^{en}\cos(\theta_\ell)}{R^p(z_\ell)}, \tag{24}$$

$$p^n - p^{e_r} = \frac{2\sigma^{en}\cos(\theta_r)}{R^p(z_r)}. \tag{25}$$

Since the radii of curvature of the fluid-fluid interfaces are $R^p(z_\ell)/\cos(\theta_\ell)$ and $R^p(z_r)/\cos(\theta_r)$, these two equations imply that the interfaces obey the Young–Laplace equation.

For the first two terms in equation (23) to vanish, we must have equality of the chemical potential in all fluid phases. This requires that $p^{e_\ell} = p^{e_r}$, and (24) and (25) may then be combined to give

$$\frac{\cos(\theta_\ell)}{R^p(z_\ell)} = \frac{\cos(\theta_r)}{R^p(z_r)}, \tag{26}$$

meaning that both fluid-fluid interfaces must have the same curvature. The relation between θ_i and the contact angle, measured in the n-phase, is

$$\alpha^n = \theta_i + \beta_i, \tag{27}$$

where

$$\beta_\ell = \arctan\left(\dot{R}^p(z_\ell)\right), \tag{28}$$

$$\beta_r = \arctan\left(-\dot{R}^p(z_\ell)\right). \tag{29}$$

By combining the above equations with (15-23) we find by use of trigonometric relations that both contact angles obey Young's equation (4) in a stationary state.

The grand canonical energy Ω of the system is given by (12), where (13) is used for the Helmholtz energy. The derivatives of Ω may then be found by an analogous derivation to that given above. One result from this derivation is that the criteria for a stationary state of Ω are the same as those for a stationary state of F. The Hessian matrix differs, however.

2.4. Pore with a thick film of liquid or gas

The final fluid configuration that will be considered is a pore with a wetting film consisting of either liquid or gas. The film is considered so thick that interactions between the fluid-fluid and fluid-solid interfaces, as modeled by the disjoining pressure, are negligible. We refer to excellent works in the literature for further information about the disjoining pressure [22–24]. The thick film configuration is illustrated in Fig. 1d. As for the adsorbed droplet and bubble, z_ℓ and z_r denote the positions of the left and right three-phase contact lines, respectively.

The Helmholtz energy is now

$$F = -p^e V^e + \mu^e N^e + \sigma^{es} A^{es} + \sigma^{en} A^{en} \\ -p^n V^n + \mu^n N^n + \sigma^{ns} A^{ns}. \tag{30}$$

The interfacial area between the n- and s-phases is a function of z_ℓ and z_r,

$$A^{ns} = 2\pi \int_{z_\ell}^{z_r} R^p \sqrt{1 + \left(\dot{R}^p\right)^2}\, dz \tag{31}$$

The volume of the n-phase V^n and the interfacial area between the n- and e-phases A^{en} depend on z_ℓ and z_r and on the shape of the fluid-fluid interface in between. Since the system is axisymmetric, we may express the shape of the interface by the function $R^f(z)$, which represents the distance between a point on the fluid-fluid interface to its closest point on the z-axis. The volume V^n and area A^{en} are then *functionals* of R^f,

$$A^{en} = \int_{z_\ell}^{z_r} L_{A^{en}}\left(z, R^f, \dot{R}^f\right) dz, \tag{32}$$

$$V^n = \int_{z_\ell}^{z_r} L_{V^n}\left(z, R^f, \dot{R}^f\right) dz. \tag{33}$$

The integrands of these functionals are

$$L_{A^{en}}\left(z, R^f, \dot{R}^f\right) = 2\pi R^f \sqrt{1 + \left(\dot{R}^f\right)^2}, \tag{34}$$

$$L_{V^n}\left(z, R^f, \dot{R}^f\right) = \pi\left\{(R^p)^2 - \left(R^f\right)^2\right\}. \tag{35}$$

Using that $A^{es} + A^{ns} = A^p$, $V^e + V^n = V^p$ and $N^e + N^n = N$ we proceed to eliminate A^{es}, V^e and N^e from (30) and get

$$F = (\mu^n - \mu^e)N^n - p^e V^p + \sigma^{es} A^p + \mu^e N \\ -(p^n - p^e)V^n + (\sigma^{ns} - \sigma^{es})A^{ns} + \sigma^{en} A^{en}. \tag{36}$$

Taking the differential on both sides of (36) gives

$$dF = (\mu^n - \mu^e)dN^n - (p^n - p^e)dV^n \\ +(\sigma^{ns} - \sigma^{es})dA^{ns} + \sigma^{en} dA^{en}. \tag{37}$$

The above equation shows that in a stationary state, the chemical potentials of the e- and n-phases must be the same. The Helmholtz energy of a film in a pore with a uniform chemical potential (subscript μ) can be formulated as

$$F_\mu = F_\mu^\circ + \pi \int_{z_\ell}^{z_r} 2\sigma^{en} R^f \sqrt{1 + \left(\dot{R}^f\right)^2} \\ -(p^n - p^e)\left\{(R^p)^2 - \left(R^f\right)^2\right\} \\ +2(\sigma^{ns} - \sigma^{es})R^p \sqrt{1 + \left(\dot{R}^p\right)^2}\, dz, \tag{38}$$

where we have integrated (37) and used (32) and (33). F_μ° is a constant. To have a stationary state in F_μ, the first variation with respect to the function R^f must vanish and R^f must therefore satisfy the Euler–Lagrange equation in the interval $z \in (z_\ell, z_r)$. The Euler–Lagrange equation leads to the following second-order ordinary differential equation (ODE) for R^f,

$$p^e - p^n = \sigma^{en}(\kappa_1 + \kappa_2), \tag{39}$$

where

$$\kappa_1 = \frac{1}{R^f\left(1 + \left(\dot{R}^f\right)^2\right)^{\frac{1}{2}}}, \tag{40}$$

$$\kappa_2 = -\frac{\ddot{R}^f}{\left(1 + \left(\dot{R}^f\right)^2\right)^{\frac{3}{2}}}, \tag{41}$$

are the interfacial curvatures. This ODE can be recognized as the Young–Laplace relation for the film. Since (39) is a second-order ODE, we need boundary conditions on both R^f and $\dot{R}^f$ at the free end points, z_ℓ and z_r to fully define the film. The boundary conditions on R^f are $R^f(z_\ell) = R^p(z_\ell)$ and $R^f(z_r) = R^p(z_r)$. To derive boundary conditions for $\dot{R}^f$, we must consider the *transversal conditions* at the free end points z_ℓ and z_r, see e.g. page 159 in Ref. [31]. They give that

$$\cos(\alpha^n) = \frac{\sigma^{es} - \sigma^{ns}}{\sigma^{en}}, \tag{42}$$

must be satisfied at the end points z_ℓ and z_r. Here, α^n is the contact angle measured in the film. The transversal conditions are thus satisfied when the three-phase contact angles obey Young's equation, as for the adsorbed droplet/bubble.

The grand canonical energy Ω of the pore with a film is given by (12), where (30) is used for the Helmholtz energy. As for the other systems, the criteria for a stationary state of Ω are the same as those for a stationary state of F. To analyze the thermodynamic stability of the film, one possibility is to study the second variation of e.g. F at the stationary state. As this is often challenging due to the infinite number of possible functions that can perturb the stationary state, we present in Section 3 a new methodology to analyze the stationary states of films.

3. Numerical methods

In this section, we provide details on the numerical methods used to determine the stationary states and the thermodynamic stability of the configurations in Fig. 1. For all the heterogeneous structures, one way to identify stationary states is to first determine the shape and positions of the interfaces. The outcome is a fixed value of the pressure difference $\Delta p = p^e - p^n$. For the film, this can be done by solving the Euler–Lagrange equation (39) as described in Section 3.2. Subsequently, one can calculate the phase

equilibrium with specified $\Delta p = p^{\mathrm{e}} - p^{\mathrm{n}}$, as described in Section 3.1.

3.1. Phase equilibrium calculations

All the heterogeneous structures considered in this work are characterized by the same chemical potentials in the n- and e-phases, but at a fixed pressure difference $\Delta p = p^{\mathrm{e}} - p^{\mathrm{n}}$, temperature T and phase volumes V^{e} and V^{n}. This poses an untypical phase-equilibrium problem.

To determine the remaining thermodynamic properties of the system, one can solve for the dimensionless particle numbers N^{n}/N° and N^{e}/N°. This procedure amounts to solving the non-linear system of equations $\mathbf{F}(N^{\mathrm{n}}/N^{\circ}, N^{\mathrm{e}}/N^{\circ}) = 0$, where

$$\mathbf{F}\left(\frac{N^{\mathrm{n}}}{N^{\circ}}, \frac{N^{\mathrm{e}}}{N^{\circ}}\right) = \begin{bmatrix} \dfrac{\mu^{\mathrm{e}}(T, V^{\mathrm{e}}, N^{\mathrm{e}}) - \mu^{\mathrm{n}}(T, V^{\mathrm{n}}, N^{\mathrm{n}})}{RT} \\ \dfrac{p^{\mathrm{e}}(T, V^{\mathrm{e}}, N^{\mathrm{e}}) - p^{\mathrm{n}}(T, V^{\mathrm{n}}, N^{\mathrm{n}}) - \Delta p}{p^{\circ}} \end{bmatrix}. \tag{43}$$

Herein, the functions for pressure and chemical potentials, and the derivatives required to compute the Jacobian matrix of $\mathbf{F}$, are provided by the EOS. The scaling parameters are

$$p^{\circ} = 10^5 \text{ Pa}, \tag{44}$$

$$N^{\circ} = \frac{p^{\circ} V^{\mathrm{p}}}{RT}, \tag{45}$$

and R is the universal gas constant. The system in (43) was solved using Newton's method. Initial guesses for N^{n} and N^{e} were obtained from a standard phase equilibrium calculation [18,32–34] at the specified temperature and saturation pressure. The EOS implementation used was provided by our in-house thermodynamic library presented by Wilhelmsen et al. [35].

3.2. Solving the film Euler–Lagrange equation

The ODE in (39) gives a requirement for the film profile that must be satisfied to have a vanishing first variation of the Helmholtz and grand canonical energies. Since the ODE is second-order and requires boundary conditions on both R^{f} and $\dot{R}^{\mathrm{f}}$ at z_ℓ and z_{r}, it represents a two-point boundary value problem. We solved this problem using the shooting method. The solution strategy was to first specify the position z_ℓ. Since the contact angle and pore radius at z_ℓ are known, R^{f} and $\dot{R}^{\mathrm{f}}$ are also specified. Next, a search was performed for the values of the variables $\Delta p = p^{\mathrm{e}} - p^{\mathrm{n}}$ and z_{r} that satisfy the two boundary conditions on R^{f} and $\dot{R}^{\mathrm{f}}$ at z_{r}. The shooting procedure thus amounts to solving $\mathbf{G}(\Delta p/p^{\circ}, z_{\mathrm{r}}/L^{\mathrm{p}}) = 0$, where

$$\mathbf{G}\left(\frac{\Delta p}{p^{\circ}}, \frac{z_{\mathrm{r}}}{L^{\mathrm{p}}}\right) = \begin{bmatrix} \dfrac{R^{\mathrm{f}}(z_{\mathrm{r}}) - R^{\mathrm{p}}(z_{\mathrm{r}})}{L^{\mathrm{p}}} \\ \dfrac{\dot{R}^{\mathrm{f}}(z_{\mathrm{r}}) - \tan(\theta_{\mathrm{r}})}{\max(1, |\tan(\theta_{\mathrm{r}})|)} \end{bmatrix}, \tag{46}$$

and

$$\theta_{\mathrm{r}} = \arctan\left(\dot{R}^{\mathrm{p}}(z_{\mathrm{r}})\right) + \alpha^{\mathrm{n}}. \tag{47}$$

The scaling parameter is

$$p^{\circ} = \frac{\sigma^{\mathrm{en}}}{L^{\mathrm{p}}}. \tag{48}$$

One evaluation of $\mathbf{G}$ involves one integration of (39). We used odeint from scipy's integrate module for the ODE integrations and fsolve from the optimize module to solve $\mathbf{G} = 0$ [36].

A complicating factor in the search for stationary states is that there may be many solutions to $\mathbf{G} = 0$ with the same z_ℓ. In practice, however, we have found that we can identify the one that is potentially stable and discard any other solutions in subsequent analysis. This is further explained in Appendix A.

3.3. A discrete method for describing the film

The variational formulation works well for identifying stationary states in F and Ω, where the Euler–Lagrange equation for the film (39) can be solved as described in Section 3.2. The procedure identifies stationary states, but it does not give any insight into the thermodynamic stability of the film. This information is contained in the second variation (or higher-order variations, if the second variation happens to be zero). For a stationary state of a functional to be a minimum, it is necessary to have a positive second variation for all viable perturbations, as discussed by Wilhelmsen et al. [14]. To establish that this is the case, or not, can be very demanding and it is impossible for many examples.

In this section, we present a new methodology for analyzing the thermodynamic stability of films. The approach that we follow here is to discretize the functionals for A^{en} (32) and V^{n} (33) and use the discretized functionals to represent the Helmholtz and grand canonical energies. The functionals are integrated numerically using a quadrature rule over a predefined grid, where the end points are left unspecified. This transforms the variational problem of minimizing F or Ω in the space of functions R^{f}, to an algebraic problem where F is to be minimized by a vector in $\mathbb{R}^M$. Local stability can then be evaluated by considering the eigenvalues of a Hessian matrix.

This procedure can be applied to general problems in functional optimization. We have tested it carefully and successfully reproduced well-known results from variational calculus, such as the Brachistochrone and the hanging cable problems [31], see supplementary material.

In the discrete formulation of the film, we approximate the function R^{f} by the vector

$$\mathbf{R}^{\mathrm{f}} = \left[R_1^{\mathrm{f}}, R_2^{\mathrm{f}}, \ldots, R_M^{\mathrm{f}}\right]^{\mathrm{T}}, \tag{49}$$

which represents the values of R^{f} at points on a predefined gird with M points on the z-axis, given by

$$\mathbf{z} = [z_1, z_2, \ldots, z_M]^{\mathrm{T}}. \tag{50}$$

The complete vector of geometrical unknowns, including the positions of the free end points, is then

$$\mathbf{x} = [x_1, x_2, \ldots, x_{M+2}]^{\mathrm{T}} = \left[z_\ell, z_{\mathrm{r}}, R_1^{\mathrm{f}}, R_2^{\mathrm{f}}, \ldots, R_M^{\mathrm{f}}\right]^{\mathrm{T}}. \tag{51}$$

The volume V^{n} and area A^{ne} can now be approximated by the midpoint rule,

$$V^{\mathrm{n}}(\mathbf{x}) = \sum_{i=0}^{M} L_{V^{\mathrm{n}}}\left(\overline{z}_i, \overline{R}_i^{\mathrm{f}}, \overline{\dot{R}}_i^{\mathrm{f}}\right)\Delta z_i, \tag{52}$$

$$A^{\mathrm{en}}(\mathbf{x}) = \sum_{i=0}^{M} L_{A^{\mathrm{en}}}\left(\overline{z}_i, \overline{R}_i^{\mathrm{f}}, \overline{\dot{R}}_i^{\mathrm{f}}\right)\Delta z_i. \tag{53}$$

The integrands $L_{V^{\mathrm{n}}}$ and $L_{A^{\mathrm{en}}}$ are given by (35) and (34), respectively,

and

$$\overline{z}_i = \frac{z_{i+1} + z_i}{2}, \tag{54}$$

$$\overline{R}_i^{\mathrm{f}} = \frac{R_{i+1}^{\mathrm{f}} + R_i^{\mathrm{f}}}{2}, \tag{55}$$

$$\overline{\frac{\mathrm{d}}{\mathrm{d}z}} R_i^{\mathrm{f}} = \frac{R_{i+1}^{\mathrm{f}} - R_i^{\mathrm{f}}}{\Delta z_i}, \tag{56}$$

$$\Delta z_i = z_{i+1} - z_i, \tag{57}$$

In addition, $R_0^{\mathrm{f}} = R^{\mathrm{p}}(z_\ell)$, $R_{M+1}^{\mathrm{f}} = R^{\mathrm{p}}(z_r)$, $z_0 = z_\ell$ and $z_{M+1} = z_r$.

The discretized Helmholtz energy for the film can now be calculated by introducing into (36) the discrete functionals $V^{\mathrm{n}}(\mathbf{x})$ and $A^{\mathrm{en}}(\mathbf{x})$, and the interfacial area $A^{\mathrm{ns}}(z_\ell, z_r)$ as given by (31),

$$\begin{aligned} F(\mathbf{y}) = {} & \{\mu^{\mathrm{n}} - \mu^{\mathrm{e}}\}N^{\mathrm{n}} - p^{\mathrm{e}}V^{\mathrm{p}} + \sigma^{\mathrm{es}}A^{\mathrm{p}} + \mu^{\mathrm{e}}N + \sigma^{\mathrm{en}}A^{\mathrm{en}}(\mathbf{x}) \\ & - \{p^{\mathrm{n}} - p^{\mathrm{e}}\}V^{\mathrm{n}}(\mathbf{x}) + \{\sigma^{\mathrm{ns}} - \sigma^{\mathrm{es}}\}A^{\mathrm{ns}}(z_\ell, z_r). \end{aligned} \tag{58}$$

Since, the quantities V^{n}, A^{ns} and A^{ne} depend only on the variables contained in $\mathbf{x}$, and since V^{p}, A^{p} and N are constants, the free variables of the system are the elements of $\mathbf{x}$ and the number of particles in the film N^{n},

$$\mathbf{y} = [y_1, y_2, \ldots, y_{M+3}]^{\mathrm{T}} = \left[N^{\mathrm{n}}, z_\ell, z_r, R_1^{\mathrm{f}}, R_2^{\mathrm{f}}, \ldots, R_M^{\mathrm{f}}\right]^{\mathrm{T}}. \tag{59}$$

The elements of the Jacobian vector can be obtained from (37) as

$$\frac{\partial F}{\partial y_1} = \mu^{\mathrm{n}} - \mu^{\mathrm{e}}, \tag{60}$$

and, for $i \in [2, \ldots, M+3]$,

$$\frac{\partial F}{\partial y_i} = -(p^{\mathrm{n}} - p^{\mathrm{e}})\frac{\partial V^{\mathrm{n}}}{\partial y_i} + (\sigma^{\mathrm{ns}} - \sigma^{\mathrm{es}})\frac{\partial A^{\mathrm{ns}}}{\partial y_i} + \sigma^{\mathrm{ne}}\frac{\partial A^{\mathrm{ne}}}{\partial y_i}. \tag{61}$$

The Hessian matrix can be found by further differentiation. The procedure used for calculating the derivatives of V^{n} and A^{ne} w.r.t. y_i is documented in the supplementary material. By a derivation similar to that above, we obtain the grand potential Ω, its Jacobian vector and its Hessian matrix.

The strategy to solve the discrete problem is to use the stationary state obtained from solving the ODE as described in Section 3.2 as initial guess. The stationary state for the discrete problem is then found by solving for the vector $\mathbf{y}^*$ for which the discrete Jacobian vector is zero,

$$\left.\frac{\mathrm{d}F}{\mathrm{d}\mathbf{y}}\right|_{\mathbf{y}^*} = 0. \tag{62}$$

Since we have an expression for the Hessian matrix of F and a very good initial guess for the solution to (62), this non-linear system of equations is solved with Newton's method with few number of iterations. A convergence study is reported in Appendix B, which shows that the film profiles obtained by the discrete method converge to those obtained by solving the Euler–Lagrange equation as the grid size M is increased. For a thorough exposition of the discrete approach, we refer to the supplementary material.

3.4. Stability analysis

Any stationary state identified using the procedures described above, and defined by the vector $\mathbf{y}^*$, will be stationary for both F and Ω and, therefore, in both a closed and an open pore. Since the Jacobian vector is $\mathbf{0}$, the change in, say, F in response to a small perturbation $\mathrm{d}\mathbf{y}$ of $\mathbf{y}^*$ can be expressed as

$$\mathrm{d}F = \mathrm{d}\mathbf{y}^{\mathrm{T}}\left.\frac{\mathrm{d}^2F}{\mathrm{d}\mathbf{y}^2}\right|_{\mathbf{y}^*}\mathrm{d}\mathbf{y}, \tag{63}$$

where $\mathrm{d}^2F/\mathrm{d}\mathbf{y}^2$ is the Hessian matrix. For the film, we calculate the Hessian matrices using the discrete description, see Section 3.3. The symmetric Hessian matrix can be decomposed into

$$\left.\frac{\mathrm{d}^2F}{\mathrm{d}\mathbf{y}^2}\right|_{\mathbf{y}^*} = \mathbf{Q}\mathbf{\Lambda}\mathbf{Q}^{\mathrm{T}}, \tag{64}$$

where $\mathbf{\Lambda}$ is the diagonal matrix eigenvalues and $\mathbf{Q}$ is a matrix where column i is the eigenvector $\mathbf{q}_i$ (with unit length in the L_2-norm) associated with eigenvalue λ_i. The eigenvectors are orthogonal, since the Hessian is symmetric.

A stationary state $\mathbf{y}^*$ corresponds to a minimum in F and is considered locally stable in the closed pore if all eigenvalues of the Hessian are positive. If one or more of the eigenvalues are negative, $\mathrm{d}\mathbf{y}$ can be taken in direction of the corresponding eigenvectors $\mathbf{q}_i$ (or $-\mathbf{q}_i$) to give a negative $\mathrm{d}F$. The stationary state is thus not a minimum in the Helmholtz energy and it is therefore unstable. Analogous considerations apply for Ω and stability in open pores.

The eigenvectors that correspond to the negative eigenvalues give information about the direction of the perturbations that lead to a reduction in the energy and make the system unstable. For both the adsorbed droplet/bubble and the films, we observe (see Section 4) two distinct classes of instabilities that we name (1) translation and (2) condensation/evaporation. Translation instabilities are perturbations where the n-phase moves along the z-axis and only a small number of particles are transferred to/from the e-phase(s). For condensation/evaporation instabilities on the other hand, the n-phase expands or contracts while exchanging particles with the e-phase(s), without shifting its center of mass.

Eigenvectors and eigenvalues were calculated using eigh from numpy's linalg module [36]. This function uses the *syevd routines from LAPACK, which compute the eigenvalues and eigenvectors of symmetric matrices [38].

4. Results

In the following, we will discuss the thermodynamic stability of the heterogeneous structures illustrated in Fig. 1. The focus will be on the influence of pore size, the fluid-solid interaction, as captured by the liquid contact angle α, and the difference in thermodynamic stability between closed and open systems. We restrict the discussion to two pore sizes, $L^{\mathrm{p}} = 10\ \mu\mathrm{m}$ and $L^{\mathrm{p}} = 0.01\ \mu\mathrm{m}$. Despite the small size of both pores, we will refer to the 10 μm-pore as large and the 0.01 μm-pore as small.

Water at 358 K will be used as example, inspired by the operational conditions of a proton-exchange membrane fuel cell[1] [39]. The thermodynamic properties of water are described by the cubic-plus-association modification to the Soave–Redlich–Kwong EOS (CPA-SRK). In Fig. 2, the saturation properties of water as described by both the Soave–Redlich–Kwong EOS (SRK) and CPA-SRK are

[1] Condensation of liquid water in such fuel cells may block reactant flow paths and is then severely detrimental to their performance. It is therefore of interest to know if, say, a path-blocking adsorbed droplet or a liquid film is the equilibrium configuration under the chosen operating conditions.

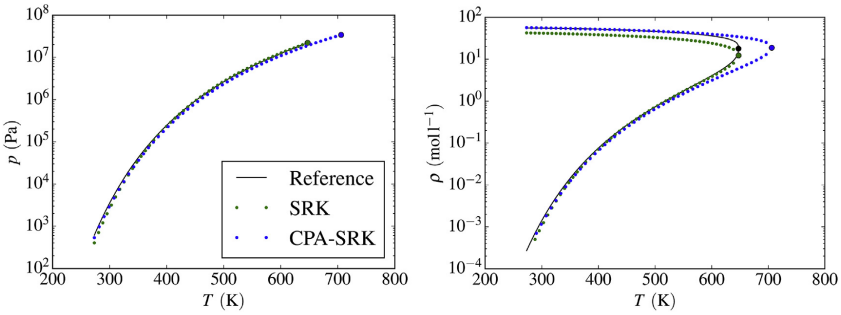

(a) (b)

Fig. 2. Saturation properties of water, as predicted by SRK (green) and CPA-SRK (blue). Reference data from Ref. [37] are shown for comparison (black). Compared to SRK, CPA-SRK is more inaccurate in the critical region, but has superior predictions of liquid densities for temperatures around 300 K.

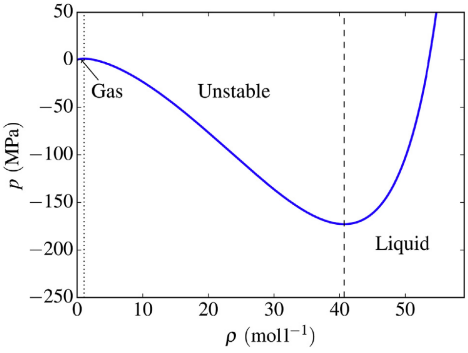

Fig. 3. CPA-SRK isotherm (solid blue) for water at 358 K. The densities at the gas spinodal (dotted line) and liquid spinodal (dashed line) are also indicated. Phases with densities between the two spinodals are unstable.

plotted together with reference data from Ref. [37]. Compared to SRK, CPA-SRK is more inaccurate in the critical region, but has superior prediction of liquid densities at lower temperatures and is therefore the preferred choice here.

The CPA-SRK isotherm for water at 358 K is shown in Fig. 3, where the gas and liquid spinodals are indicated by vertical lines. A homogeneous phase with a density between the two spinodals is thermodynamically unstable. The isotherm shows that the EOS predicts stable or metastable stretched liquid phases down to pressures of −173 MPa, consistent with the findings of Caupin et al. [5] and Azouzi et al. [6].

In the models presented in Section 2, the energies of the gas-liquid interface $\sigma^{g\ell}$, the gas-solid interface σ^{gs} and the liquid-solid interface $\sigma^{\ell s}$ are necessary input parameters. The gas-liquid surface tension of water at 358 K is 0.0616N m $^{-1}$ [37]. With this value in place, it is only the difference between the gas-solid and gas-liquid interfacial tensions that is of physical significance in the models. We therefore set $\sigma^{\ell s} = 0$ and subsequently use $\sigma^{g\ell}$ and the specified contact angle α to calculate σ^{gs} by use of Young's equation (4). Thus, only combinations of interfacial energies where Young's equation has a solution for the contact angle are studied here. Complete wetting, sometimes characterized by a positive spreading coefficient, is not considered.

4.1. Pore with a free droplet or bubble

The thermodynamic stability of free droplets and bubbles in a closed pore has been studied in previous works [17,19–21]. Our results for free bubbles in water at 358 K are shown in Fig. 4. The stability is here mapped out in terms of the relative bubble size R^n/L^p and contact angle α. The largest bubble radius that has been considered equals the radius of the pore at the widest point. Similar stability maps for free droplets are given in the supplementary information.

As expected, the thermodynamic stability of both free bubbles and droplets is independent of contact angle. For both pore sizes, large bubbles and droplets are stable and have lower Helmholtz energies than if the pores were filled with a homogeneous phase (with the same number of particles). As R^n decreases however, the configurations first become metastable w.r.t. the homogeneous phase and, eventually, unstable. The reason is that, as the volume of the n-phase becomes smaller, the reduction in energy from having both a liquid and a gas phase does not compensate for the energy cost of the gas-liquid interface. These findings are consistent with those of Wilhelmsen et al. [14]. They considered droplets and bubbles in a spherical container, where the interfacial energy between the container and the e-phase was zero. The non-zero energy of the es-interface adds a constant term to the Helmholtz energy that does not change the local stability w.r.t. to the analysis performed by Wilhelmsen et al. [14]. This is also the reason why the contact angle does not affect stability. However, it is necessary to include the contribution from the fluid-solid interface when comparing the energy of the free droplet/bubble configurations with other configurations such as adsorbed droplet/bubbles and films.

The thermodynamic stability of free bubbles and droplets in a closed system changes with pore size, which can be seen e.g. by comparing Fig. 4a with 4b. In the white region in the bottom part of the figures, the bubble radius becomes so small that the pressure difference needed to satisfy the Young−Laplace relation is too large to conform with equal chemical potential between the phases. A similar effect is observed for the free droplets. The limiting factor for the droplets is the gas spinodal and for the bubbles it is the liquid spinodal. The density range where the bubbles are

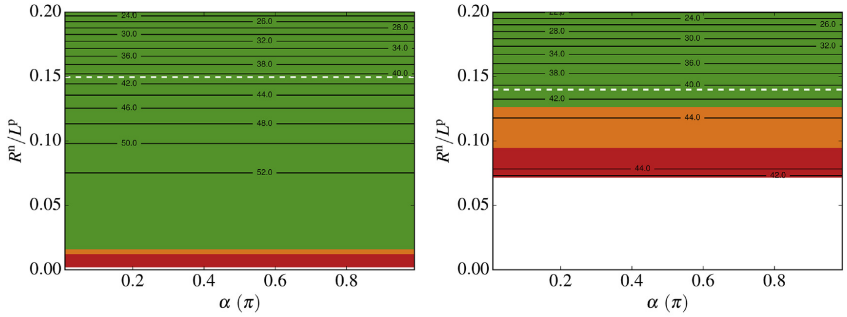

(a) Free bubbles in closed pore of 10 μm

(b) Free bubbles in closed pore of 0.01 μm

Fig. 4. Stability maps for free bubbles in closed pores of lengths (a) 10 μm and (b) 0.01 μm. The black contour lines indicate the total fluid density in mol/l. Unstable configurations are red, stable configurations are green and configurations that are locally stable, but have a larger Helmholtz energy than if the pore were filled with a single homogeneous phase, are orange. The liquid spinodal of 40.7 mol/l is shown as a dashed white line.

thermodynamically stable (the green regions) or metastable (orange regions) decreases with pore size. The transition from the metastable to the unstable region is associated, as can be seen in Fig. 4b, with a maximum in the total density. For densities above this maximum, there are no stationary bubble states. This is due to the superstabilization of the homogeneous liquid phase that occurs in small pores. We refer to Ref. [20] for an elaborate discussion of this topic.

The white dashed lines in Fig. 4 mark the states where the total density in the pore reaches the liquid spinodal limit, and the homogeneous liquid phase becomes unstable. Beyond this limit, the liquid will spontaneously decompose into two phases.

In agreement with previous work [17], we find that free droplets and bubbles are unstable in the open systems, also in the presence of a solid-fluid interface.

4.2. Pore with an adsorbed droplet or bubble

When the solid-fluid interfacial energy is lower than the gas-liquid interfacial tension, the bubbles and droplets can lower their energies by adsorbing to the pore walls. The thermodynamic stability of adsorbed bubbles and droplets, as shown in Fig. 1c, is mapped out in Fig. 5 in terms of the position of the left contact line z_ℓ and the contact angle α for open and closed pores with lengths 10 μm and 0.01 μm.

In contrast to the free droplets and bubbles, the absorbed droplets and bubbles can be stable both in open and closed pores. The general trend is that adsorbed droplets are thermodynamically stable if the liquid contact angle is high (non-wetting), while bubbles are stable when the liquid contact angle is low (wetting), and the range of stability depends on the value of the contact angle. We find that this behavior depends strongly on the pore geometry. An in-depth discussion of the influence of pore morphology on the thermodynamic stability however, is beyond the scope of the present work.

We have analyzed in detail the regions where the adsorbed droplets and bubbles become unstable. The eigenvectors associated with the negative Hessian eigenvalues in these regions reveal that an instability w.r.t. to translation of the n-phase along the z-axis, i.e. a mechanical instability, is present in the unstable regions of all the adsorbed bubble and droplet configurations. A perturbation of the position of the droplet/bubble leads to a net force that moves it further in the direction of the perturbation, not back to the original position as for the stable droplets/bubbles. The Hessian matrices of the open systems have an additional negative eigenvalue in the unstable regions. The second negative eigenvalue is associated with condensation/evaporation. This instability is also present for the droplet in the small closed pore, when the liquid pressures become large and negative. We have included figures that display where these instabilities appear in the supplementary material. Comparing the unstable regions of the droplets (left column in Fig. 5) with those of the bubbles (right column Fig. 5), these are clearly anti-symmetric. This is because the droplets with contact angles α are mechanically identical to bubbles with contact angle $\pi - \alpha$.

The white regions in the stability maps for the 10 μm-pore represent configurations where no stationary state can be found because the two menisci would have intersected or extended outside the pore. Such configurations are unfeasible and are not considered in the analysis. The same is true for the small pores. In addition, the large curvatures of some menisci in the small pores result in large, negative liquid pressures. Fig. 3 shows that the liquid spinodal poses a lower limit to how large the negative pressures of the liquid phase can be. Configurations with a lower pressure than the liquid spinodal are unfeasible.

Fig. 5e shows results for a closed pore of the small kind containing an adsorbed droplet. It has a considerable region where the droplets are metastable w.r.t. a pore with a homogeneous liquid phase (with the same number of particles). In a large closed pore, the thermodynamic stability map looks the same, except that the metastable region is stable. A figure can be found in the supplementary material. The reason for the appearance of the metastable region in the small pore is as for the free droplet/bubble; when the volumes of the bulk phases become smaller, the reduction in energy from having both a gas and a liquid does not compensate for the energy associated with the gas-liquid interface. The adsorbed bubble configurations display a similar behavior, where large bubbles (relative to pore size) become unstable w.r.t. a homogeneous gas phase. A crucial difference from the free bubbles/droplets, however, is that the transition from stable to metastable depends on the contact angle.

The orange regions for the open pores indicate where the adsorbed/droplet bubble configurations are locally stable, but have a larger grand canonical energy than if the pore were filled with a

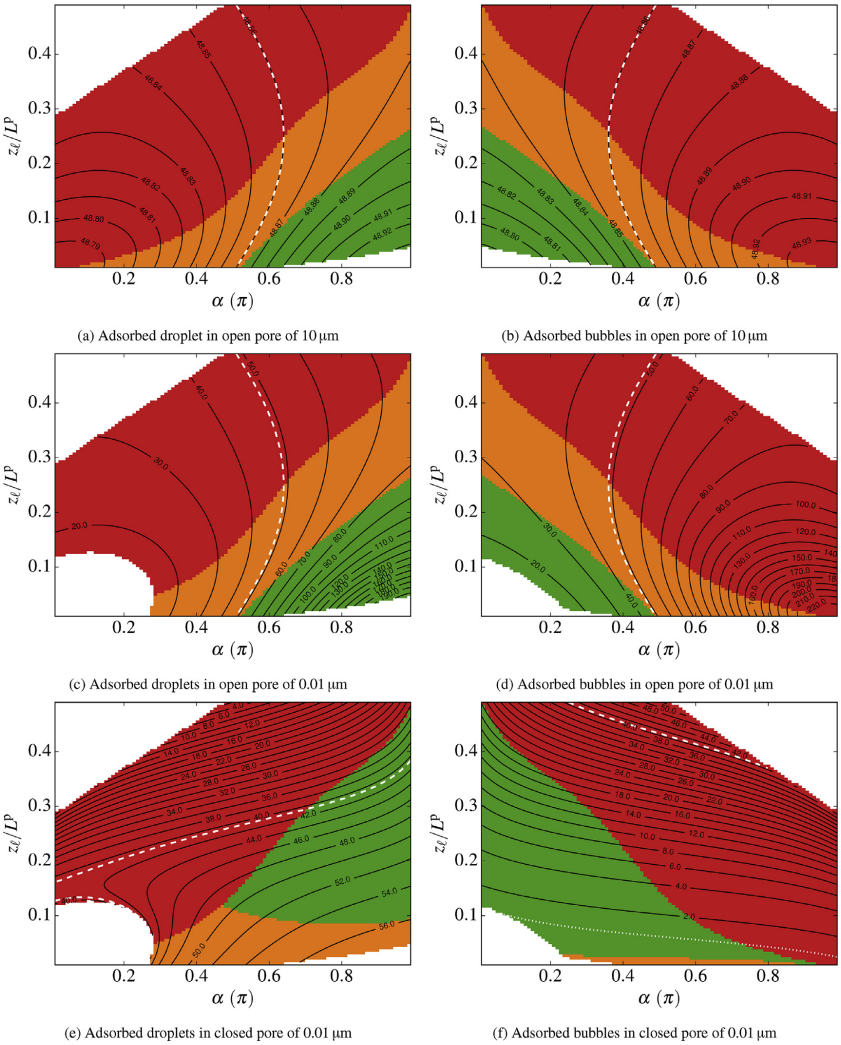

(a) Adsorbed droplet in open pore of 10 μm

(b) Adsorbed bubbles in open pore of 10 μm

(c) Adsorbed droplets in open pore of 0.01 μm

(d) Adsorbed bubbles in open pore of 0.01 μm

(e) Adsorbed droplets in closed pore of 0.01 μm

(f) Adsorbed bubbles in closed pore of 0.01 μm

Fig. 5. Stability maps of (left column) adsorbed droplets and (right column) adsorbed bubbles in open and closed pores with lengths 10 μm and 0.01 μm. For the closed pores, the black contour lines indicate the total fluid density in mol l^{-1}. Further, the gas spinodal density of 1.05 mol/l is drawn as a dotted white line and the liquid spinodal of 40.7 mol/l is shown as a dashed white line. No homogeneous phase filling the entire pore can exist for densities between the spinodals. For the open pores, the black contour lines indicate the gas phase pressure in kPa. Also, the bulk saturation pressure of 48.86 kPa is shown as a dashed white line. For all maps, unstable configurations are red, stable configurations are green and configurations that are locally stable, but have a larger energy than if the pore were filled with a single homogeneous phase, are orange.

homogeneous phase with the same intensive properties as the e-phase. The location of these regions does not change much when pore size is reduced, which is evident by comparing Fig. 5b to Fig. 5d for the bubbles, and Fig. 5a to Fig. 5c for the droplets.

Comparing the adsorbed bubbles in the large open pore (Fig. 5b) with those in the small pore (Fig. 5d), we observe that the variation of gas pressure is much larger in the small pores. In particular, when the liquid phase is sufficiently wetting, the gas pressure is lower than the bulk saturation pressure, and much more so in the small pore. Although the external phase is liquid in Fig. 5b and d, these observations are closely related to the phenomenon of capillary condensation in open pores with an external gas phase. When the liquid phase is wetting, a lower water vapor pressure is required for water to condense in the pore than in the bulk. A much lower vapor pressure is required in the small pores, meaning that water will preferentially condense in small over large pores. A study of

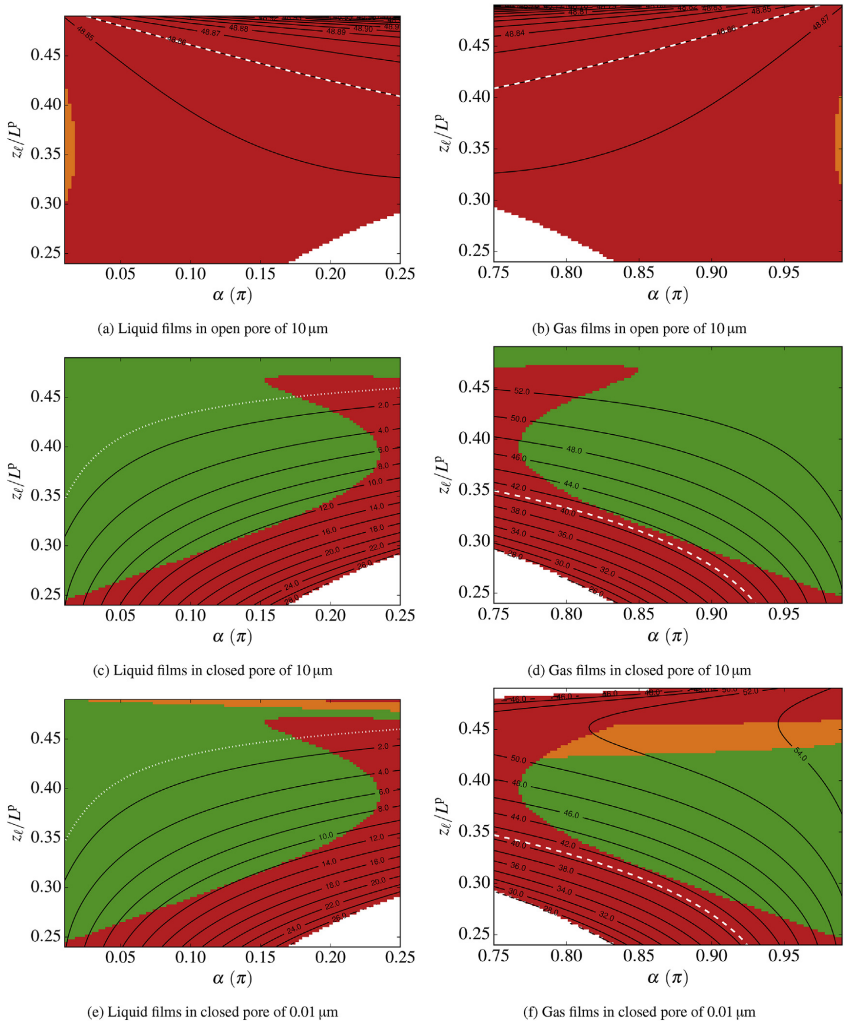

(a) Liquid films in open pore of 10 μm

(b) Gas films in open pore of 10 μm

(c) Liquid films in closed pore of 10 μm

(d) Gas films in closed pore of 10 μm

(e) Liquid films in closed pore of 0.01 μm

(f) Gas films in closed pore of 0.01 μm

Fig. 6. Stability maps of (left column) liquid films and (right column) gas films in open and closed pores of lengths 10 μm and 0.01 μm. For the closed pores, the black contour lines indicate the total fluid density in mol l^{-1}. Further, the gas spinodal density of 1.05 mol l^{-1} is drawn as a dotted white line and the liquid spinodal of 40.7 mol/l is shown as a dashed white line. No homogeneous phase filling the entire pore can exist for densities between the spinodals. For the open pores, the black contour lines indicate the gas phase pressure in kPa. Further, the bulk saturation pressure of 48.86 kPa is shown as a dashed white line. In all maps, unstable configurations are red, stable configurations are green and configurations that are locally stable, but have a larger energy than if the pore were filled with a single phase, are orange.

capillary condensation and the effects pore size and shape can be done with the models and methods presented here, which is a possible topic for future work.

4.3. Pore with a thick films of liquid or gas

The thermodynamic stability of liquid and gas films in open and closed pores is shown in Fig. 6. Configurations are here mapped in terms of the position of the left contact line z_ℓ and contact angle α.

In the open pores, most of the liquid (Fig. 6a) and gas (Fig. 6b) film configurations are unstable. The exception is when the film phase is strongly wetting. It is then possible to have a metastable film, which is evident by the orange regions in the left part of Fig. 6a and the right part of Fig. 6b. The stability map for the small pore in the open system is nearly identical to that of the large pore and is shown in the supplementary material.

Stability maps of liquid and gas films in the 10 μm closed pore are shown in Fig. 6c and d, respectively. They reveal large regions

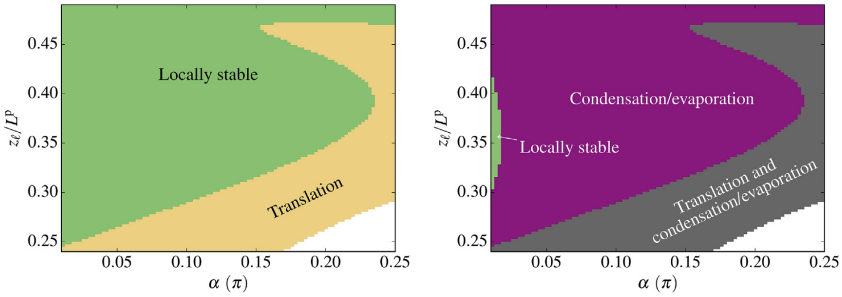

Fig. 7. Maps of instability types for liquid films in (a) the 10 μm closed pore and (b) the 10 μm open pore. Regions with no instabilities are light green, regions with only translation instabilities are cream, regions with only condensation/evaporation instabilities are magenta and regions with both types of instabilities are gray.

where both gas and liquid films are more stable than the homogeneous phase. In contrast to the adsorbed droplets, which appear when the liquid is non-wetting, the liquid films are stable only when the liquid is wetting. Analogously, the gas films in closed pores are locally stable only for a highly non-wetting liquid.

Fig. 6 reveals that the thermodynamic stability of thick films is remarkably different in open and closed pores. A deeper insight into the origin of this difference can be gained by further investigating the unstable regions. Like the adsorbed bubbles and droplets discussed in Section 4.2, a translational instability is responsible for the unstable regions in the closed system, as can be seen in Fig. 7a for the liquid film. This translation instability is also present in the same regions in the open pore (Fig. 6a and b). However, the open pore also has a condensation/evaporation instability which is present in the entire unstable region. This is illustrated in Fig. 7b for the liquid film.

As for the previous two configuration types, a metastable region appears in the closed system when the pore size is reduced, as shown in Fig. 6e and f for the liquid and gas films, respectively. The metastable configurations represent films whose small gas and liquid volumes, again, do not compensate for their interfacial energy cost. In addition, an unstable region also appears for films with small extent along the z-axis. This region is present for both, but is larger for the gas film than the liquid film. It is caused by a condensation/evaporation instability.

We emphasize that the appearance of metastable regions and of condensation/evaporation instabilities cannot be predicted form a purely mechanical analysis of the film, and a complete thermodynamic stability analysis is needed. This is important critique to nearly all previous works that evaluate the stability of films in the literature, and an important future work is thus to extend the present analysis to films that have a non-zero disjoining pressure to shed new light on the thermodynamic stability of thin films in open and closed systems.

4.4. Phase diagrams

The final results we report are phase diagrams that show the equilibrium configuration, i.e. that which has the lowest total energy at given conditions. Such phase diagrams are shown in Fig. 8 for closed pores of sizes 10 μm and 0.01 μm. The equilibrium configurations herein are determined by comparing the Helmholtz energies of the different (locally stable) fluid configurations at each value of the total density ρ and the contact angle α.

The phase diagram for the large pore in Fig. 8a exhibits a large degree of symmetry around the neutral-wetting case where $\alpha = \pi/2$. As pore-size is reduced (Fig. 8a), however, this symmetry is broken, partly due the appearance of homogeneous phases with lower Helmholtz energies than the heterogeneous structures. We note in particular the appearance of a stretched homogeneous liquid phase at the expense of the free bubble and adsorbed droplet configurations. In a similar manner, a compressed homogeneous gas phase appears as well.

For both phase diagrams, the free bubble and adsorbed droplet configurations prevail at higher densities, because locally stable configurations of these kinds allow for large liquid volume fractions. Similarly, the free droplet and adsorbed bubble are prevalent at lower densities, as these allow for large gas volume fractions. At densities around 25 mol l^{-1}, the equilibrium configuration is either a free bubble (when the liquid is wetting) or a free droplet (when the liquid is non-wetting).

Equilibrium liquid film configurations are only observed at low densities and for wetting liquids. In the 10 μm-pore, the extent of the liquid film region along the ρ-axis is smaller than the resolution used in figure. A finer resolution of the low densities, however, reveals that the region is indeed there. Its position and extent along the α-axis is indicated by a thin solid line in Fig. 8a.

The size of the liquid film region grows when the pore size is reduced (Fig. 8b). This expansion is primarily at the expense of the adsorbed bubble region and can be explained as follows. When the pore size is reduced, the liquid pressures in the adsorbed bubble configurations are also reduced. Eventually, these pressures reach the liquid spinodal, where the liquid phase can no longer exist, and it is no longer possible to have an adsorbed bubble. This is also evident from comparing the white region in the lower left corner of Fig. 5d with that in Fig. 5b. The liquid film, however, is stable in this region as it has a lower curvature than the adsorbed bubble. It therefore appears in the phase diagram as the equilibrium configuration when it is no longer possible to have an adsorbed bubble.

Like the liquid film region in the 10 μm-pore (Fig. 8a), the extent of the gas film region along the ρ-axis is smaller than the resolution. Its position is therefore also indicated with a thin solid line. The gas

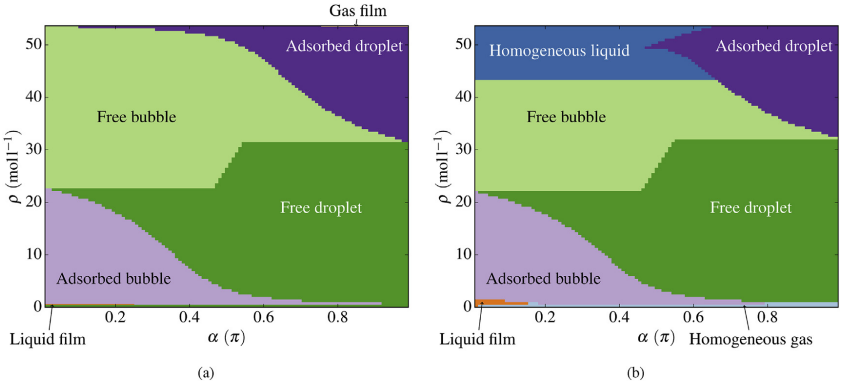

Fig. 8. Phase diagram showing equilibrium configurations in a closed pores of size (a) 10 μm and (b) 0.01 μm. Considered configurations are homogeneous gas (light blue), homogeneous liquid (blue), free bubble (light green), free droplet (green), adsorbed bubble (light purple), adsorbed droplet (purple), gas film (light orange) and liquid film (orange).

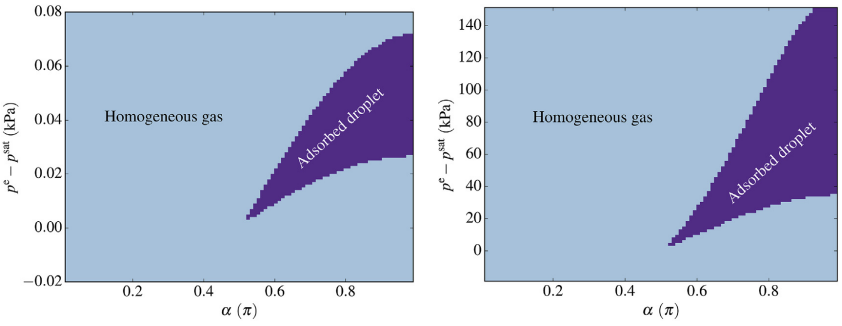

Fig. 9. Phase diagram showing equilibrium configurations in an open pore of size (a) 10 μm and (b) 0.01 μm and a gaseous external phase. Considered configurations are homogeneous gas (light blue) and adsorbed droplet (purple). External pressure minus the bulk saturation pressure, $p^{sat} = 48.86$ kPa, is indicated on the ordinate axis.

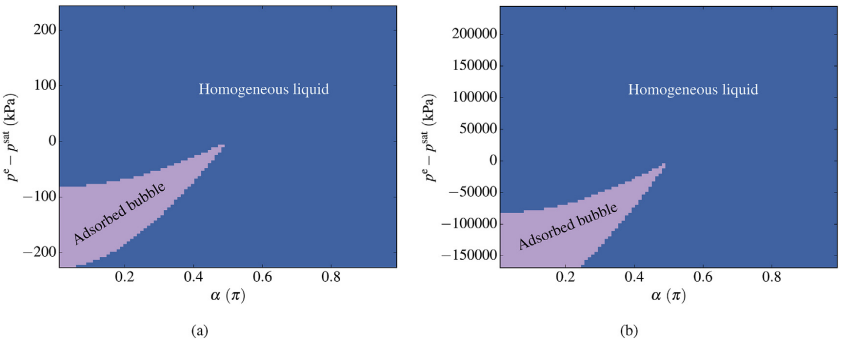

Fig. 10. Phase diagram showing equilibrium configurations in an open pore of size (a) 10 μm and (b) 0.01 μm and a liquid external phase. Considered configurations are homogeneous liquid (blue) and adsorbed bubble (light purple). External pressure minus the bulk saturation pressure, $p^{sat} = 48.86$ kPa, is indicated on the ordinate axis.

film appears at high densities, when the liquid is non-wetting. For the 0.01 μm-pore, however, we do not observe any gas films at equilibrium. The adsorbed droplet is found to always have a lower energy than the gas film. This conclusion may well change for other fluids and pore geometries.

For the closed pores at a given contact angle, a control parameter is the total density, i.e. how many particles the pore contains. For the open pores, on the other hand, a more natural choice is the external phase pressure p^e. Also, the particle reservoir connected to be pore is either gas or liquid and not both at the same time. We therefore present separate phase diagrams for cases where the external phase is gas (Fig. 9) and cases when it is liquid (Fig. 10). The equilibrium configurations are here determined by comparing the grand canonical energies of the different (locally stable) fluid configurations at each value of p^e and α.

For both pore sizes and external phase choices, a homogeneous phase is the prevailing fluid configuration. With an external gas phase, an adsorbed droplet appears as the liquid is non-wetting and, with an external liquid phase, an adsorbed bubble appears when the liquid is wetting. Compared to the phase diagrams for the closed pores, there are much fewer possible configurations. The free droplets and bubbles are absent because they are unstable for all possible contact angles and external pressures. The film configurations are absent because, even though they may be locally stable in an open pore, the homogeneous phase has a lower grand canonical energy.

As the pore size is decreased, the range of external pressures at which we find an adsorbed droplet or bubble is greatly increased. This is evident by comparing the scale of the ordinates of Fig. 9 and Fig. 10. The increase in range is due to the increased Young–Laplace pressure difference of the interface induced by the large interfacial curvatures in the small pores.

From the outset, we have restricted the discussion to fluid configurations with the same type of symmetry as the pore, i.e. rotational symmetry around the z-axis. Examples of structures that do not have this symmetry are sessile droplets and bubbles adsorbed to the pore wall. The reason for omitting these structures is as follows. The capillary modeling approach assumes a uniform pressure in the gas and liquid phases. Since fixed surface energies is also assumed, a force balance across the gas-liquid interface requires that this interface has constant mean curvature. Moreover, a stationary state must also have force balance along any liquid-solid-gas contact line(s). This requires that Young's equation (4) is satisfied along the entire contact line(s) and that the liquid-phase contact angle is constant. The combination of requirements on the interfacial curvature and the contact angle puts quite severe constraints on which fluid configurations can be stationary states in a specific pore. The considered structures all satisfy the constant contact angle requirements for the pore under consideration, due to their rotational symmetry around the z-axis.

5. Conclusion

We have studied the thermodynamic stability of free and adsorbed droplets, bubbles and gas and liquid films in open and closed pores by use of capillary models coupled to an equation of state. We used water at 358 K, as described by the CPA-SRK equation of state, as example. Emphasis was placed on the effect of fluid-solid interaction, as described by the contact angle, pore size and whether the pore is open or closed.

For free droplets and bubbles, our findings were in agreement with previous works [14,17]. These configurations were unstable in open pores, but could be stable in closed pores, if the bubbles/droplets were large enough.

In contrast to the free droplets and bubbles, adsorbed droplets and bubbles could be stable both in closed and open pores. Evidently, the interaction with the solid phase made these structures stable and in many cases, depending on contact angle and phase fractions, favorable w.r.t. a homogeneous fluid phase.

A new methodology was presented to analyze the thermodynamic stability of films, where the integral that describes the total energy of the system was approximated by a quadrature rule. The methodology allowed us to examine in detail any perturbations that made the film unstable.

Gas and liquid films were found to be unstable at most conditions in the open pores. The exception was when the fluid was nearly perfectly wetting and a liquid film could form, or nearly perfectly non-wetting, when a gas film could form. In both cases, the films were metastable with respect to the homogeneous phase. In the closed pore, both stable gas and liquid films were found. As for the free droplets and bubbles, metastable regions where a homogeneous phase was energetically preferable were observed for both adsorbed droplets and bubbles and for the gas and liquid films in the small pore. The reason was that, as the volumes of the gas and liquid phases became smaller, the energy gained from having both a liquid and a gas phase did not compensate for the energy cost of the gas-liquid interface.

Observed instabilities for the adsorbed droplets/bubbles and the films belonged to one of two distinct classes: (1) translation and (2) condensation/evaporation. Although exceptions were present, the general trend was that translation instabilities were observed in the closed pores while both translation and condensation/evaporation instabilities were observed in the open pores.

Finally, we presented phase diagrams showing equilibrium configuration types for both open and closed pores. The closed-pore phase diagrams were found to contain a larger variety of structures compared to the open-pore diagrams. Partly, this is because the open-pore diagrams can contain only structures where the external phase is gas or liquid, while the closed-pore diagrams can have both kinds of structures. Most interesting, however, is the lack of locally stable configurations of free droplets/bubbles and films with lower energy than a homogeneous phase in the open pores.

The appearance of metastable regions and of condensation/evaporation instabilities cannot be predicted form a purely mechanical analysis of systems. A complete thermodynamic stability analysis, as performed herein, is necessary. In previous literature on films, the discussion is usually limited to mechanical stability. The methodology presented in this work can be used to shed new light on the topic.

The analysis presented in this work is a step towards developing a thermodynamic framework to map the rich heterogeneous phase diagram of porous media and other confined systems.

Declaration of competing interest

None.

Acknowledgments

This work was supported by the Research Council of Norway through its Centres of Excellence funding scheme, project number 262644.

Appendix A. Solutions to the film Euler–Lagrange equation

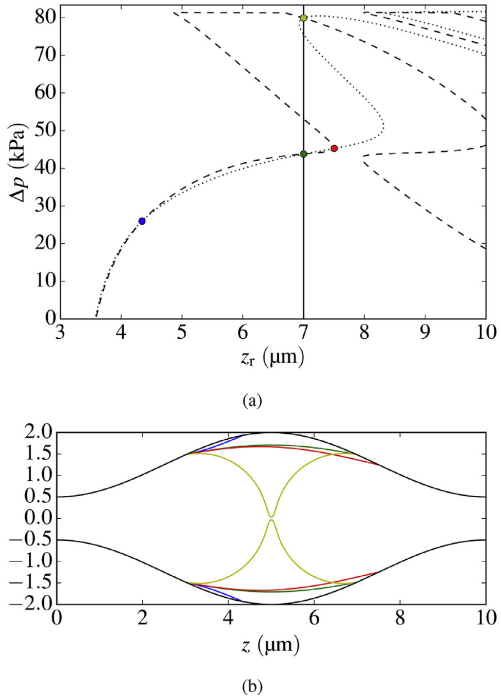

Fig. A.11. Illustration of different solutions to the film ODE (39) for a given pore, shown in (b), $z_\ell = 3$ μm and $\alpha^n = 0.07\pi$. A map of the space searched for solutions to the two-point boundary value problem $\mathbf{G} = 0$ is shown in (a). The dotted curve indicates where the first element of $\mathbf{G}$ is zero and the boundary condition on R^f is satisfied. The dashed curve indicates where the second element of $\mathbf{G}$ is zero and the boundary condition on R^f is satisfied. A solution to the two-point boundary value problem is thus a point where the two curves intersect. Four different solutions are indicated (blue, green, red and yellow). The corresponding film profiles are shown in (b).

A complicating factor in the search for stationary states for the film is that there may be many solutions to $\mathbf{G} = 0$ with a specified z_ℓ. $\mathbf{G}$ is the residual function for the two-point boundary value problem obtained by setting (46) equal to $\mathbf{0}$. One example is illustrated in Figure A.11, which displays a pore with $L^p = 10$ μm, where the shape of the pore is defined by (1) and drawn in black in Figure A.11b. Furthermore, the contact angle is $\alpha^n = 0.07\pi$, $\sigma^{en} = 0.0616$ N m^{-1} and $z_\ell = 3$ μm. Figure A.11a maps the search space. The dotted curve shows where the first element of $\mathbf{G}$ is zero and the boundary condition on R^f is satisfied, while the dashed curve shows where the second element of $\mathbf{G}$ is zero and the boundary condition on R^f is satisfied. A solution to the two-point boundary value problem is thus a point where the two curves intersect. The solid vertical line is drawn at $z_r = L^p - z_\ell$. Solutions falling on this line are symmetric or anti-symmetric with respect to the center of the pore.

Four different solutions are indicated by circles (blue, green, red and yellow) in Figure A.11a. The corresponding film configurations are shown in Figure A.11b. Of these four solutions, only the green and the yellow are symmetric. When evaluating the thermodynamic stability of these solutions, however, it turns out that only the green solution is stable in a closed system. All solutions are unstable in an open system. For a more thorough discussion on thermodynamic stability, we refer to Section 4. Since we observe that solutions that are not symmetric around the pore center are always unstable, we only need to consider the symmetric film solution with the lowest Δp, that is also feasible in the sense that $0 < R^f(z) < R^p(z)\ \forall z \in (z_\ell, z_r)$. In the analysis presented in this paper, we ignore the other solutions, even if they also represent unstable stationary states of the film. These unstable states may, however, be of interest in the theory of nucleation. For instance, the yellow profile in Figure A.11b could well be the saddle point that determines the activation barrier to the creation of a an adsorbed droplet, similar to the one depicted in Fig. 1c.

Appendix B. Convergence of the discrete film description method

In Section 3.3, we presented a discrete method to describe the Helmholtz energy of the film. Here, we perform a convergence study to show that the solutions provided by the discrete method converge to those obtained by solving the Euler–Lagrange equations when the discrete grid is refined. To this end, we consider a pore described by (1) with $L^p = 10$ μm and choose $\alpha^n = \pi/20$ and $\sigma^{en} = 0.02$ N m^{-1}. The fluid is, as in Section 4, water at 358 K, described by the CPA-SRK EOS. The film is liquid and the surrounding phase gas.

We use the variational formulation to obtain a stationary state of F where the film starts at $z_\ell = 0.3L^p$. This solution will serve both as a reference solution and to generate initial guesses for the discrete solutions. Subsequently, we solve (63) for different number of grid points, M. Relative errors in the film profile $\mathbf{R}^f$ with respect to the reference solution, as measured in the L_2- and L_∞-norms, and the corresponding estimated convergence orders are presented in Table B.1. It is clear from these results that the discrete solutions converge to the variational solution as the grid is refined, and that the convergence is second-order.

Table B.1
Relative errors in the film profile $\mathbf{R}^f$ with respect to the reference solution, as measured in the L_2- and L_∞-norms, for different discrete grid sizes M. The corresponding estimated convergence orders are also given.

M	L_2-error	L_2-order	L_∞-error	L_∞-order
25	$5.10\cdot10^{-5}$	–	$8.58\cdot10^{-4}$	–
50	$6.91\cdot10^{-6}$	2.88	$1.99\cdot10^{-4}$	2.11
100	$1.00\cdot10^{-6}$	2.79	$4.74\cdot10^{-5}$	2.07
200	$1.56\cdot10^{-7}$	2.69	$1.15\cdot10^{-5}$	2.04
400	$2.55\cdot10^{-8}$	2.61	$2.84\cdot10^{-6}$	2.02

Appendix C. Supplementary data

Supplementary data to this article can be found online at https://doi.org/10.1016/j.fluid.2019.112351.

References

[1] T. Hiratsuka, H. Tanaka, M.T. Miyahara, Comprehensive modeling of capillary condensation in open-ended nanopores: equilibrium, metastability, and spinodal, J. Phys. Chem. C 121 (48) (2017) 26877–26886, https://doi.org/10.1021/acs.jpcc.7b09631.
[2] T. Horikawa, D.D. Do, D. Nicholson, Capillary condensation of adsorbates in porous materials, Adv. Colloid Interface Sci. 169 (1) (2011) 40–58, https://doi.org/10.1016/j.cis.2011.08.003.
[3] A.V. Neimark, A. Vishnyakov, Gauge cell method for simulation studies of phase transitions in confined systems, Physical Review E 62 (4) (2000) 4611, https://doi.org/10.1103/PhysRevE.62.4611.
[4] A.V. Neimark, P.I. Ravikovitch, A. Vishnyakov, Inside the hysteresis loop:

Multiplicity of internal states in confined fluids, Physical Review E 65 (3) (2002), 031505, https://doi.org/10.1103/PhysRevE.65.031505.
[5] F. Caupin, A. Arvengas, K. Davitt, M.E.M. Azouzi, K.I. Shmulovich, C. Ramboz, D.A. Sessoms, A.D. Stroock, Exploring water and other liquids at negative pressure, J. Phys. Condens. Matter 24 (28) (2012) 284110, https://doi.org/10.1088/0953-8984/24/28/284110.
[6] M.E.M. Azouzi, C. Ramboz, J.-F. Lenain, F. Caupin, A coherent picture of water at extreme negative pressure, Nat. Phys. 9 (1) (2013) 38, https://doi.org/10.1038/nphys2475.
[7] Z.-Y. Wang, J. Wu, Ion association at discretely-charged dielectric interfaces: giant charge inversion, J. Chem. Phys. 147 (2) (2017), 024703, https://doi.org/10.1063/1.4986792.
[8] M.J. Blunt, Physically-based network modeling of multiphase flow in intermediate-wet porous media, J. Pet. Sci. Eng. 20 (3–4) (1998) 117–125, https://doi.org/10.1016/S0920-4105(98)00010-2.
[9] M. Aa. Gjennestad, M. Vassvik, S. Kjelstrup, A. Hansen, Stable and efficient time integration at low capillary numbers of a dynamic pore network model for immiscible two-phase flow in porous media, Frontiers in Physics 6 (2018), https://doi.org/10.3389/fphy.2018.00056.
[10] M. Kulmala, H. Vehkamäki, T. Petäjä, M. Dal Maso, A. Lauri, V.-M. Kerminen, W. Birmili, P. McMurry, Formation and growth rates of ultrafine atmospheric particles: a review of observations, J. Aerosol Sci. 35 (2) (2004) 143–176, https://doi.org/10.1016/j.jaerosci.2003.10.003.
[11] J.A. Huberman, A.D. Riggs, On the mechanism of DNA replication in mammalian chromosomes, J. Mol. Biol. 32 (2) (1968) 327–341, https://doi.org/10.1016/0022-2836(68)90013-2.
[12] H.B. Callen, Thermodynamics and an Introduction to Thermostatistics, John Wiley & Sons, New York, 1985.
[13] A. Fladerer, R. Strey, Homogeneous nucleation and droplet growth in supersaturated argon vapor: the cryogenic nucleation pulse chamber, J. Chem. Phys. 124 (16) (2006) 164710, https://doi.org/10.1063/1.2186327.
[14] Ø. Wilhelmsen, D. Bedeaux, S. Kjelstrup, D. Reguera, Thermodynamic stability of nanosized multicomponent bubbles/droplets: the square gradient theory and the capillary approach, J. Chem. Phys. 140 (2) (2014), 024704, https://doi.org/10.1063/1.4860495.
[15] A.I. Rusanov, Surface thermodynamics revisited, Surf. Sci. Rep. 58 (5–8) (2005) 111–239, https://doi.org/10.1016/j.surfrep.2005.08.002.
[16] F.F. Abraham, Homogenous Nucleation Theory: the Pretransition Theory of Vapor Condensation, Academic Press, New York, 1974.
[17] A.J.-M. Yang, The thermodynamical stability of the heterogeneous system with a spherical interface, J. Chem. Phys. 82 (4) (1985) 2082–2085, https://doi.org/10.1063/1.448344.
[18] P. Aursand, M. Aa. Gjennestad, E. Aursand, M. Hammer, Ø. Wilhelmsen, The spinodal of single-and multi-component fluids and its role in the development of modern equations of state, Fluid Phase Equilib. 436 (2017) 98–112, https://doi.org/10.1016/j.fluid.2016.12.018.
[19] L.G. MacDowell, V.K. Shen, J.R. Errington, Nucleation and cavitation of spherical, cylindrical, and slablike droplets and bubbles in small systems, J. Chem. Phys. 125 (3) (2006), 034705, https://doi.org/10.1063/1.2218845.
[20] Ø. Wilhelmsen, D. Bedeaux, S. Kjelstrup, D. Reguera, Communication: supersaturation of fluids in nanocontainer, J. Chem. Phys. 141 (2014), 071103, https://doi.org/10.1063/1.4893701.
[21] Ø. Wilhelmsen, D. Reguera, Evaluation of finite-size effects in cavitation and droplet formation, J. Chem. Phys. 142 (6) (2015), 064703, https://doi.org/10.1063/1.4907367.
[22] J.C. Berg, Fluid Interfaces and Capillarity. In *An Introduction to Interfaces and Colloids – The Bridge to Nanoscience*, World Scientific, Singapore, 2009 (chapter 2).
[23] L. Boinovich, A. Emelyanenko, Wetting and surface forces, Adv. Colloid Interface Sci. 165 (2) (2011) 60–69, https://doi.org/10.1016/j.cis.2011.03.002.
[24] L. Boinovich, A. Emelyanenko, The prediction of wettability of curved surfaces on the basis of the isotherms of the disjoining pressure, Colloid. Surf. Physicochem. Eng. Asp. 383 (1–3) (2011) 10–16, https://doi.org/10.1016/j.colsurfa.2010.12.020.
[25] A.V. Neimark, Thermodynamic equilibrium and stability of liquid films and droplets on fibers, J. Adhes. Sci. Technol. 13 (10) (1999) 1137–1154, https://doi.org/10.1163/156856199X00839.
[26] A.V. Neimark, K.G. Kornev, Classification of equilibrium configurations of wetting films on planar substrates, Langmuir 16 (13) (2000) 5526–5529, https://doi.org/10.1021/la000267b.
[27] D. Bhatt, J. Newman, C. Radke, Molecular simulation of disjoining-pressure isotherms for free liquid, Lennard–Jones thin films, J. Phys. Chem. B 106 (25) (2002) 6529–6537, https://doi.org/10.1021/jp0202136.
[28] H. Hu, Y. Sun, Molecular dynamics simulations of disjoining pressure effect in ultra-thin water film on a metal surface, Appl. Phys. Lett. 103 (26) (2013) 263110, https://doi.org/10.1063/1.4858469.
[29] A. Nold, D.N. Sibley, B.D. Goddard, S. Kalliadasis, Fluid structure in the immediate vicinity of an equilibrium three-phase contact line and assessment of disjoining pressure models using density functional theory, Phys. Fluids 26 (7) (2014), 072001, https://doi.org/10.1063/1.4886128.
[30] A. Checco, B.M. Ocko, M. Tasinkevych, S. Dietrich, Stability of thin wetting films on chemically nanostructured surfaces, Phys. Rev. Lett. 109 (16) (2012) 166101, https://doi.org/10.1103/PhysRevLett.109.166101.
[31] J.L. Troutman, Variational Calculus and Optimal Control, second ed., Springer, 1996.
[32] Ø. Wilhelmsen, G. Skaugen, M. Hammer, P.E. Wahl, J.C. Morud, Time efficient solution of phase equilibria in dynamic and distributed systems with differential algebraic equation solvers, Ind. Eng. Chem. Res. 52 (5) (2013) 2130–2140, https://doi.org/10.1021/ie302579w.
[33] A. Aasen, M. Hammer, G. Skaugen, J.P. Jakobsen, Ø. Wilhelmsen, Thermodynamic models to accurately describe the *PVTxy*-behavior of water/carbon dioxide mixtures, Fluid Phase Equilib. 442 (2017) 125–139, https://doi.org/10.1016/j.fluid.2017.02.006.
[34] M.L. Michelsen, J.M. Mollerup, Thermodynamic Models: Fundamentals & Computational Aspects, second ed., Tie-Line Publications, Holte, 2007.
[35] Ø. Wilhelmsen, A. Aasen, G. Skaugen, P. Aursand, A. Austegard, E. Aursand, M. Aa. Gjennestad, H. Lund, G. Linga, M. Hammer, Thermodynamic modeling with equations of state: present challenges with established methods, Ind. Eng. Chem. Res. 56 (13) (2017) 3503–3515, https://doi.org/10.1021/acs.iecr.7b00317.
[36] E. Jones, T. Oliphant, P. Peterson, et al., SciPy: open source scientific tools for Python, 2001–, URL, http://www.scipy.org/.
[37] P. Linstrom and W. Mallard, editors. NIST Chemistry WebBook, NIST Standard Reference Database Number 69. National Institute of Standards and Technology, Gaithersburg MD, 20899. doi: 10.18434/T4D303.
[38] E. Anderson, Z. Bai, C. Bischof, S. Blackford, J. Demmel, J. Dongarra, J. Du Croz, A. Greenbaum, S. Hammarling, A. McKenney, D. Sorensen, LAPACK Users' Guide, third ed., Society for Industrial and Applied Mathematics, Philadelphia, PA, 1999, ISBN 0-89871-447-8.
[39] T. Bednarek, G. Tsotridis, Issues associated with modelling of proton exchange membrane fuel cell by computational fluid dynamics, J. Power Sources 343 (2017) 550–563, https://doi.org/10.1016/j.jpowsour.2017.01.059.

Paper III

M. Aa. Gjennestad and Ø. Wilhelmsen. Thermodynamic stability of volatile droplets and thin films governed by the disjoining pressure in open and closed containers. *Langmuir* 36 (2020), pp. 7879–7893. DOI: 10.1021/acs.langmuir.0c00960

LANGMUIR

pubs.acs.org/Langmuir Article

Thermodynamic Stability of Volatile Droplets and Thin Films Governed by Disjoining Pressure in Open and Closed Containers

Magnus Aa. Gjennestad* and Øivind Wilhelmsen*

Cite This: *Langmuir* 2020, 36, 7879−7893 Read Online

ACCESS | Metrics & More | Article Recommendations

ABSTRACT: Distributed thin films of water and their coexistence with droplets are investigated using a capillary description based on a thermodynamic fundamental relation for the film Helmholtz energy, derived from disjoining pressure isotherms and an accurate equation of state. Gas−film and film−solid interfacial tensions are derived, and the latter has a dependence on film thickness. The resulting energy functionals from the capillary description are discretized, and stationary states are identified. The thermodynamic stability of configurations with thin films in systems that are closed (canonical ensemble) or connected to a particle reservoir (grand canonical ensemble) is evaluated by considering the eigenvalues of the corresponding Hessian matrices. The conventional stability criterion from the literature states that thin flat films are stable when the derivative of the disjoining pressure with respect to the film thickness is negative. This criterion is found to apply only in open systems. A closer inspection of the eigenvectors of the negative eigenvalues shows that condensation/evaporation destabilizes the film in an open system. In closed systems, thin films can be stable even though the disjoining pressure derivative is positive, and their stability is governed by mechanical instabilities of a similar kind to those responsible for spinodal dewetting in nonvolatile systems. The films are stabilized when their thickness and disjoining pressure derivative are such that the minimum unstable wavelength is larger than the container diameter. Droplets in coexistence with thin films are found to be unstable for all considered examples in open systems. In closed systems, they are found to be stable under certain conditions. The unstable droplets in both open and closed systems are saddle points in their respective energy landscapes. In the closed system, they represent the activation barrier for the transition between a stable film and a stable droplet. In the open system, the unstable droplets represent the activation barrier for the transition from a film into a bulk liquid phase. Thin films are found to be the equilibrium configuration up to a certain value of the total density in a closed system. Beyond this value, there is a morphological phase transition to stable droplet configurations.

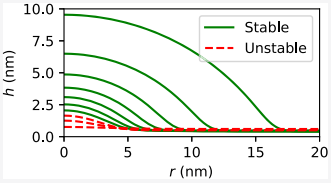

INTRODUCTION

In the literature, a distinction is made between thick (β-films) and thin films (α-films). The thermodynamic properties of thin films deviate from those of a bulk liquid phase at the same temperature and chemical potential. This deviation can be modeled by the disjoining pressure, a concept first introduced by Derjaguin in the 1930s.[1] The disjoining pressure describes the interaction between two interfaces in close proximity, such as the top and the bottom of a thin liquid film residing on a solid substrate.[2,3] The formation of films and droplets at solid interfaces is of importance in many applications. Inside porous media, thin films provide an important mode for fluid transport[4] that is often neglected or under-resolved in flow modeling.[5−7] Both droplet formation and films impact the efficiency of water removal in fuel cells[8] and are important for atmospheric water collection.[9] Thin, nanometer-thick films are key components in paint, coatings, and different lubricants.[1] They are also important in thin-film evaporation[10,11] and boiling heat transfer.[12,13]

With an emerging interest in micro-[14] and nanofluidics,[15] condensation on nanostructured surfaces,[9,16] and self-organization and pattern formation,[17−19] it becomes increasingly important to understand how thin films, often in coexistence with droplets, are influenced by confinement.[20] Previous works[21−25] have shown that the stability of heterogeneous structures is strongly affected by the choice of ensemble. For the simplest type of films, thick films with a negligible disjoining pressure, we recently showed that their thermodynamic stability was profoundly different in a closed system (canonical ensemble) and an open system (grand canonical ensemble).[25] In this work, we will study how thin films and their possible coexistence with droplets are influenced by confinement.

In the literature, thin films are often proclaimed to be unstable when $d\Pi/dh > 0$, where Π is the disjoining pressure and h is the film thickness.[1,26,27] It has, however, been pointed out that this criterion is not necessarily valid for confined systems.[20,28] In fact,

Received: April 3, 2020
Revised: June 8, 2020
Published: June 10, 2020

https://dx.doi.org/10.1021/acs.langmuir.0c00960
Langmuir 2020, 36, 7879−7893

this has been exploited in computer simulations to calculate the disjoining pressure where it has a positive slope in h.[29] The aim of this work is to compare, consistently and on equal terms, the thermodynamic stability of thin films in combination with droplets in open and closed systems. To this end, we derive a thermodynamic fundamental relation for the film phase from the disjoining pressure combined with an equation of state (EOS) that represents the bulk-phase properties. Pure water is used as an example, but the methodology is equally applicable to other fluids and can straightforwardly be extended to mixtures.

By comparing with previous results from the literature, we will explain how different assumptions in the modeling of thin films make them appear as if in an open or a closed system.[3,20,26,27,30−33] For instance, in his study of volatile films, Sharma[34] used kinetic theory to model the gas−liquid mass transfer rate as a function of the difference between vapor pressure and coexistence pressure. The coexistence pressure was modeled by an extended Kelvin equation (including effects of the disjoining pressure). Subsequently, the mass transfer rate was incorporated into a partial differential equation for the film profile to study time evolution and stationary states of films and droplets on a flat substrate. He found that flat films are unstable only when $d\Pi/dh > 0$, in agreement with the conventional stability criterion.

Dörfler et al.,[20] on the other hand, used an effective interface Hamiltonian to describe the mechanical energy of a film. They showed that the mechanical instabilities are suppressed in systems that are smaller than the critical wavelength, in agreement with earlier findings. Although their effective interface Hamiltonian did not account for particle exchange, we will show that many of their findings can be recovered by considering a closed system, since the behavior of the system is then determined by mechanical instabilities of the film−gas interface.

FUNDAMENTAL THEORY OF THIN FILMS

In the following, we present the fundamental theory that will be used to describe thin films. Starting with the original definition of the disjoining pressure by Derjaguin,[1] we derive a thermodynamic fundamental relation for the liquid film phase. Next, we show that the fundamental relation is consistent with Derjaguin's well-known relation for the macroscopic contact angle.[2] Results from the literature on the mechanical stability of thin films are briefly reviewed, which will be used in the subsequent stability analysis.

Disjoining Pressure. Since there appear to be somewhat differing interpretations of the disjoining pressure in the literature,[1,2,35] we start by describing the definition used in this work. When two interfacial regions are brought in close proximity to form a thin film, they experience either attractive or repulsive forces. These forces can be described by the disjoining pressure Π. They lead to anisotropic stresses in the film, manifested by a pressure $p^{\perp}$ normal to the interfaces that differs from the pressure $p^{\parallel}$ parallel to them.

To define the disjoining pressure, we will use the example illustrated in Figure 1. In the left container, there is a thin liquid film and a bulk gas phase with pressure p^{g}, while in the right, there is a bulk liquid phase with pressure p^{b}. The film phase in the left container is connected to, and in chemical equilibrium with, the bulk liquid phase in the right through a tube. The system is also in mechanical force balance, but the pressures p^{g} and p^{b} are, in general, different.

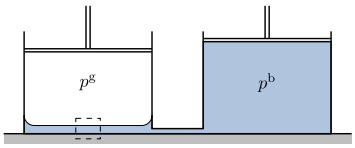

Figure 1. Two connected containers, where the left contains a thin liquid film (blue) and a bulk gas phase (white) with pressure p^{g} and the right contains a bulk liquid phase with pressure p^{b}. As indicated by the curved liquid menisci along the walls of the left container, $p^{g} \neq p^{b}$ in general. The disjoining pressure is $\Pi = p^{g} - p^{b}$. The region enclosed by dashed lines is drawn in Figure 2. Any effects of gravity have been neglected.

Inside the region enclosed by dashed lines in Figure 1, the gas−film interface has negligible curvature. Due to the force balance, the normal pressure in the film is equal to the gas pressure

$$p^{\perp} = p^{g} \tag{1}$$

The disjoining pressure is then defined, in accordance with Churaev et al.[1] (p 36), as the difference between the normal pressure in the film and the pressure in the bulk liquid phase with which the film is in chemical equilibrium. This may be expressed as

$$p^{\perp} = p^{b} + \Pi \tag{2}$$

Fundamental Relation. We will next derive a fundamental relation for the liquid film phase, i.e., the Helmholtz energy of an infinitesimally small film section. The fundamental relation may be divided by the infinitesimal substrate area covered by the film section to obtain an expression that can be integrated over the entire substrate to calculate the total Helmholtz energy of a distributed film with varying thicknesses.

Consider a section of the film covering a small area A^{fs} of a flat solid surface, as illustrated by the dotted white lines in Figure 2.

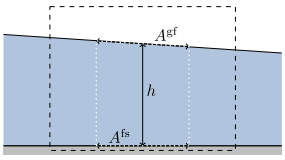

Figure 2. Enclosed by dotted white lines is the part of a film covering a small area A^{fs} of a flat solid surface. The gas−film interfacial area is A^{gf}. Since the section is small, any variations in the film thickness across it may be considered small and linear. The symbol h refers to the thickness in the middle of the film section. A somewhat exaggerated slope in the gas−film interface is used to illustrate that, in general, $A^{gf} \neq A^{fs}$.

Since the section is small, any variation in the film thickness across it may be considered small with respect to (w.r.t.) the thickness h in the middle and can be approximated as linear. The Helmholtz energy differential for the film section may then be expressed as

$$dF^{f} = -S^{f}dT + \mu^{f}dN^{f} - p^{\perp}dV^{f} + \gamma^{gf}dA^{gf} + \gamma^{fs}dA^{fs} \tag{3}$$

https://dx.doi.org/10.1021/acs.langmuir.0c00960
Langmuir 2020, 36, 7879−7893

where S^f is the entropy, T is the temperature, μ^f is the chemical potential, N^f is the number of particles, V^f is the volume of the film, and A^{gf} is the gas−film interfacial area. The interfacial tensions of the gas−film and film−solid interfaces are γ^{gf} and γ^{fs}, respectively. The reason for the appearance of $p^\perp$ in eq 3 is that the only way to change V^f at constant A^{gf} and A^{fs} is to change the film thickness h. The work required to change h must be performed against the normal pressure in the film.

The Helmholtz energy can be expressed as a function of T, V^f, A^{gf}, A^{fs}, and N^f by integrating from a thick film of volume V^f_∞, which has the desired areas A^{gf} and A^{fs} and is unaffected by the disjoining pressure, to a thin film with volume V^f

$$\begin{aligned} &F^f(T, V^f, A^{gf}, A^{fs}, N^f) \\ &\quad = F^b(T, V^f_\infty, N^f) + \gamma^{gl}_\infty A^{gf} + \gamma^{ls}_\infty A^{fs} \\ &\qquad + \int_{V^f_\infty}^{V^f} \left(\frac{\partial F^f}{\partial V^f}\right)_{T,N^f,A^{gf},A^{fs}} \mathrm{d}V^f \end{aligned} \tag{4}$$

Herein, γ^{gl}_∞ and γ^{ls}_∞ are the standard macroscopic gas−liquid and liquid−solid interfacial tensions, respectively, and F^b is a bulk-phase description of the fluid Helmholtz energy as given, e.g., by an EOS. Since the integration is performed with constant areas A^{gf} and A^{fs}, we may replace $\mathrm{d}V^f$ with $A^{fs}\,\mathrm{d}h$. Replacing the integrand in eq 4 by $p^\perp = p^b + \Pi$ from eq 2 and absorbing the resulting integral over p^b into F^b, we obtain

$$\begin{aligned} &F^f(T, V^f, A^{gf}, A^{fs}, N^f) \\ &\quad = F^b(T, V^f, N^f) + \gamma^{gl}_\infty A^{gf} + \gamma^{ls}_\infty A^{fs} - A^{fs}\int_{h_\infty}^{h} \Pi\,\mathrm{d}h \end{aligned} \tag{5}$$

where, implicitly, $h = V^f/A^{fs}$. For convenience, we introduce the shorthand notation

$$w(h) = \int_{h_\infty}^{h} \Pi\,\mathrm{d}h \tag{6}$$

that will be used in further derivations.

Equation 5 is a fundamental relation for the film section, and many other thermodynamic quantities may be derived from it by differentiation.[36] In particular, the chemical potential is

$$\mu^f = \left(\frac{\partial F^f}{\partial N^f}\right)_{T,V^f,A^{gf},A^{fs}} = \mu^b \tag{7}$$

meaning that the chemical potential of the film is the same as in a bulk liquid at the same temperature and density. This is a consequence of the disjoining pressure being a function of the film thickness only. Hence, μ^f is a function of T, V^f, and N^f. Furthermore, the gas−film interfacial tension is the same as the macroscopic gas−liquid interfacial tension

$$\gamma^{gf} = \left(\frac{\partial F^f}{\partial A^{gf}}\right)_{T,V^f,A^{fs},N^f} = \gamma^{gl}_\infty \tag{8}$$

The film−solid interfacial tension, on the other hand, becomes a function of the film thickness through the action of the disjoining pressure

$$\begin{aligned} \gamma^{fs} &= \left(\frac{\partial F^f}{\partial A^{fs}}\right)_{T,V^f,A^{gf},N^f} \\ &= \gamma^{ls}_\infty + \Pi h - w \end{aligned} \tag{9}$$

From eq 5, we observe that the Helmholtz energy is first-order Euler homogeneous in V^f, A^{gf}, A^{fs}, and N^f

$$F^f(T, \beta V^f, \beta A^{gf}, \beta A^{fs}, \beta N^f) = \beta F^f(T, V^f, A^{gf}, A^{fs}, N^f) \tag{10}$$

where β is a variable that describes a scaling of the system size. Differentiating w.r.t. β and setting $\beta = 1$ yields the Euler relation

$$F^f = \mu^f N^f - p^\perp V^f + \gamma^{gf} A^{gf} + \gamma^{fs} A^{fs} \tag{11}$$

Choosing instead $\beta = 1/A^{fs}$ yields the Helmholtz energy per area of solid substrate

$$\begin{aligned} f^f(T, h, \alpha, \Gamma) &= F^f(T, V^f/A^{fs}, A^{gf}/A^{fs}, 1, N^f/A^{fs}) \\ &= F^f(T, V^f, A^{gf}, A^{fs}, N^f)/A^{fs} \end{aligned} \tag{12}$$

where $h = V^f/A^{fs}$, $\Gamma = N^f/A^{fs}$, and $\alpha = A^{gf}/A^{fs}$. From the Euler relation (eq 11), we get

$$f^f = \mu^f\Gamma - p^\perp h + \gamma^{gf}\alpha + \gamma^{fs} \tag{13}$$

Macroscopic Wetting Properties. We previously showed that the film−solid interfacial tension is a function of the film thickness; see eq 9. This has implications for the wetting properties of a macroscopic liquid droplet on a solid surface covered by a thin film.

The spreading coefficient associated with the spreading of a thick liquid layer, whose surface tensions are unaffected by the disjoining pressure, onto a solid surface covered by a thin film is

$$\begin{aligned} \psi &= \{\gamma^{gf} + \gamma^{fs}\} - \{\gamma^{gl}_\infty + \gamma^{ls}_\infty\} \\ &= \gamma^{fs} - \gamma^{ls}_\infty \end{aligned} \tag{14}$$

since $\gamma^{gf} = \gamma^{gl}_\infty$ according to eq 8. For a given disjoining pressure isotherm, ψ is a function of h only. Young's equation for the contact angle θ results from a balance of interfacial forces. In terms of the spreading coefficient, it can be expressed as

$$\cos(\theta) = 1 + \psi(h)/\gamma^{gl}_\infty \tag{15}$$

Replacing γ^{fs} using eqs 9 and eq 3 in the equations above gives

$$\gamma^{gl}_\infty \cos(\theta) = \gamma^{gl}_\infty + \Pi h - \int_{h_\infty}^{h} \Pi\,\mathrm{d}h \tag{16}$$

This result is identical to Derjaguin's equation for the macroscopic contact angle.[1−3]

Since the droplet is macroscopic, and thus largely unaffected by the disjoining pressure and the Young−Laplace pressure difference, it is reasonable to approximate the film thickness by h_0, which is such that $\Pi(h_0) = 0$. This simplifies eq 16 to

$$\gamma^{gl}_\infty \cos(\theta_0) \approx \gamma^{gl}_\infty - \int_{h_\infty}^{h_0} \Pi\,\mathrm{d}h \tag{17}$$

as discussed in detail in the insightful review by Boinovich and Emelyanenko.[2] An alternative derivation of eq 16 based on a simplified droplet model similar to that of Dörfler et al.[20] is provided in Appendix A.

https://dx.doi.org/10.1021/acs.langmuir.0c00960
Langmuir 2020, 36, 7879−7893

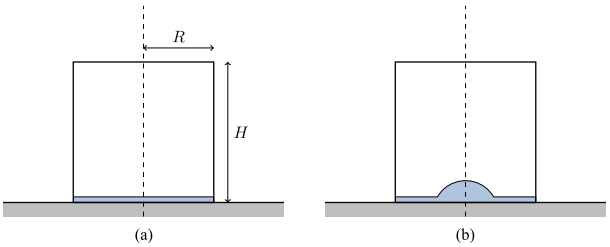

Figure 3. Illustration of the two types of fluid configurations studied in this work. (a) Flat film of uniform thickness with a gas phase above it. (b) Droplet in force balance and chemical equilibrium with a film, with a gas phase above them. All of the configurations exist in a cylindrical container of radius R and height H, which can be open or closed. The axes of symmetry are indicated by dashed lines.

Linear Stability Analysis. The mechanical stability of thin films, not taking into account condensation and evaporation, has been studied extensively in the literature.[18,20,30−33,37] One approach has been to use the film profile equation, see, e.g., refs 18 and 31, to perform a linear stability analysis and determine the growth rate of mechanical disturbances of a thin flat film with different wavelengths λ. To represent an unstable disturbance, λ must satisfy the well-known criterion

$$\lambda > \lambda_0 = 2\pi\sqrt{\frac{\gamma_\infty^{gl}}{d\Pi/dh}} \tag{18}$$

A discussion and derivation of this equation can be found in ref 18.

The criterion (eq 18) cannot be satisfied for any wavelength when $d\Pi/dh < 0$, and films corresponding to a negative slope in the disjoining pressure isotherm are therefore mechanically stable. When $d\Pi/dh > 0$, on the other hand, the interfacial tension acts to suppress disturbances with short wavelengths, while disturbances with wavelengths longer than λ_0 can grow. Films forming droplets by succumbing to such instabilities are said to undergo spinodal dewetting.[20] Locally stable films forming stable, energetically favorable droplets by overcoming some energy barrier do so through nucleation. If the substrate size is smaller than the shortest unstable wavelength, flat films may be stable even though $d\Pi/dh > 0$.[20,28]

MODELS

We will next develop models for the two composite systems illustrated in Figure 3: a distributed flat film and a droplet system. Details will be provided for the representation of the disjoining pressure and the equation of state. Water at 293.15 K will be used as the example fluid, for which $\gamma_\infty^{gl} = 0.073$ N m^{-1}. Since γ_∞^{ls} only adds a constant to the Helmholtz energy that has no qualitative effect on the results, we have set $\gamma_\infty^{ls} = 0$. In the section Fundamental Relation, V^f, A^{gf}, A^{fs}, and N^f refer to the volume, interfacial areas, and particle number of a small section of a film. From this point on, these symbols will refer to the entire distributed film.

Disjoining Pressure Model. There are many different models for the disjoining pressure isotherms, depending on the nature of the interface interactions. These vary from the classical van der Waals curves where $\Pi \propto 1/h^3$ (ref 1, p 99) to more complex curves[38] that exhibit one or more local extrema; see, e.g., Figure 3 in ref 27. Disjoining pressure isotherms are usually modeled by adding terms that account for different types of forces acting between two interfaces,[39] resulting in a plethora of possibilities for combinations of terms. We will restrict the attention to a type of model that has been used to describe water films on a solid graphite surface.[27,40] This model has two terms

$$\Pi(h) = \Pi_{VdW}(h) + \Pi_{sr}(h) \tag{19}$$

accounting for van der Waals forces and short-ranged forces, respectively. Any effects of substrate size on the disjoining pressure are neglected.[28,41] Other surfaces and fluids are likely to require different terms and parameter values.

The van der Waals term is proportional to $1/h^3$

$$\Pi_{VdW}(h) = -\frac{A}{6\pi h^3} \tag{20}$$

where A is the effective Hamaker constant. This is modeled by applying a mixing rule to the liquid and solid Hamaker constants

$$A = A^{ll} - \sqrt{A^{ll}A^{ss}} \tag{21}$$

Here, we will use $A^{ll} = 4.4 \times 10^{-20}$ J and $A^{ss} = 4.7 \times 10^{-19}$ J.[27,40]

The short-ranged contribution is, in line with previous works,[27,40] modeled by an exponential

$$\Pi_{sr}(h) = K_{sr}\exp(-h/L_{sr}) \tag{22}$$

where K_{sr} and L_{sr} are the strength and correlation length of the interactions, respectively. We will use $L_{sr} = 0.6$ nm[27,40] and consider $K_{sr} = 0$ and three different negative values of K_{sr}. The four resulting disjoining pressure curves are illustrated in Figure 4. The effect of the negative K_{sr} values is to create a minimum in

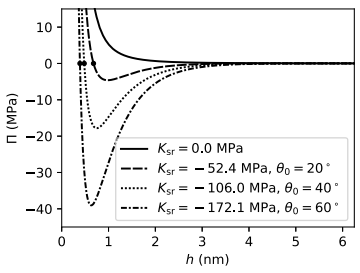

Figure 4. Disjoining pressure isotherms calculated using eq 19 for different values of the parameter K_{sr}. Contact angles θ_0 are calculated using eq 17. The dots indicate where on the isotherms $\Pi = 0$ and represent the thickness of the film a macroscopic droplet would be in force balance with.

https://dx.doi.org/10.1021/acs.langmuir.0c00960
Langmuir 2020, 36, 7879−7893

the disjoining pressure curve that makes the liquid partially wetting and allows the existence of droplets in equilibrium with thin films. For each isotherm in the figure, the legends state the contact angle θ_0 predicted by eq 17 for a macroscopic droplet in mechanical force balance with a thin film.

Equation of State for Bulk-Phase Properties. A necessary component of the models developed here is a thermodynamic description of the bulk phases. For this purpose, any EOS capable of predicting Helmholtz energies of both gas and liquid phases is applicable. We will use the cubic-plus-association modification of the Soave−Redlich−Kwong EOS.[42] This EOS is implemented in our in-house thermodynamics library.[43]

Distributed Film in a Cylindrical Container. We consider a cylindrical container with radius R, height H, and volume $V = \pi R^2 H$. Furthermore, we assume for simplicity that the film thickness h is a cylindrically symmetric function of the radial coordinate r. The film−solid interfacial area is then a constant

$$A^{\mathrm{fs}} = 2\pi \int_0^R r \, \mathrm{d}r = \pi R^2 \tag{23}$$

The film volume may be obtained by integrating h over the area A^{fs}

$$V^{\mathrm{f}} = 2\pi \int_0^R hr \, \mathrm{d}r \tag{24}$$

and, similarly

$$N^{\mathrm{f}} = 2\pi \int_0^R \Gamma r \, \mathrm{d}r \tag{25}$$

A homogeneous bulk gas phase fills the container volume that is not occupied by the film.

The container has a fixed volume V, and we will only consider the case when it is connected to a thermal reservoir with constant temperature T. If the container is closed, i.e., it is in the canonical ensemble and contains a fixed number of particles N, equilibrium is defined by the state that maximizes the total entropy of the system in the container and the reservoir subject to these constraints on T, V, and N. This is equivalently described as a minimum in the Helmholtz energy for the system.[36] Equilibrium in an open container, which also has a fixed volume V and temperature T, but where the gas phase can exchange particles with an external particle reservoir at constant chemical potential, corresponds to a minimum in the grand canonical energy Ω.

The total Helmholtz energy for the combined film-and-gas system is

$$F = F^{\mathrm{f}} + F^{\mathrm{g}} \tag{26}$$

The Helmholtz energy of the gas is

$$F^{\mathrm{g}} = \mu^{\mathrm{g}} N^{\mathrm{g}} - p^{\mathrm{g}} V^{\mathrm{g}} \tag{27}$$

$$= \mu^{\mathrm{g}} N - \mu^{\mathrm{g}} N^{\mathrm{f}} - p^{\mathrm{g}} V + p^{\mathrm{g}} V^{\mathrm{f}} \tag{28}$$

since $N^{\mathrm{g}} = N - N^{\mathrm{f}}$ and $V^{\mathrm{g}} = V - V^{\mathrm{f}}$. The Helmholtz energy of the film is obtained by integrating f^{f} over A^{fs}

$$F^{\mathrm{f}} = 2\pi \int_0^R f^{\mathrm{f}} r \, \mathrm{d}r \tag{29}$$

Inserting for f^{f} using eq 13, and subsequently combining with eqs 8, eq 4, and eq 2, we get

$$F^{\mathrm{f}} = \gamma_\infty^{\mathrm{ls}} A^{\mathrm{fs}} + 2\pi \int_0^R \{\mu^{\mathrm{f}} \Gamma + \gamma_\infty^{\mathrm{gl}} \alpha - w - p^{\mathrm{b}} h\} r \, \mathrm{d}r \tag{30}$$

where $\alpha = \sqrt{1 + \dot{h}^2}$ with $\dot{h} = \mathrm{d}h/\mathrm{d}r$. We restrict our attention to cases where there is chemical equilibrium within the film phase, i.e., μ^{f} is uniform, and thus

$$F^{\mathrm{f}} = \mu^{\mathrm{f}} N^{\mathrm{f}} + \gamma_\infty^{\mathrm{ls}} A^{\mathrm{fs}} + 2\pi \int_0^R \{\gamma_\infty^{\mathrm{gl}} \alpha - w - p^{\mathrm{b}} h\} r \, \mathrm{d}r \tag{31}$$

Adding together eqs 28 and 5, we obtain the total Helmholtz energy

$$F = \{\mu^{\mathrm{f}} - \mu^{\mathrm{g}}\} N^{\mathrm{f}} + \mu^{\mathrm{g}} N - p^{\mathrm{g}} V + \gamma_\infty^{\mathrm{ls}} A^{\mathrm{fs}} + 2\pi \int_0^R \{\gamma_\infty^{\mathrm{gl}} \alpha - w - \{p^{\mathrm{b}} - p^{\mathrm{g}}\} h\} r \, \mathrm{d}r \tag{32}$$

This expression is a functional of h and a function of N^{f}.

Assuming chemical equilibrium, i.e., $\mu^{\mathrm{g}} = \mu^{\mathrm{f}}$, at a given value of $\Delta p = p^{\mathrm{g}} - p^{\mathrm{b}}$, mechanical equilibrium is defined by a minimum of the functional

$$F_\mu = F_\mu^\circ + 2\pi \int_0^R L(r, h, \dot{h}) \, \mathrm{d}r \tag{33}$$

where F_μ° is a constant and the integrand is

$$L(r, h, \dot{h}) = \{\gamma_\infty^{\mathrm{gl}} \alpha - w - \{p^{\mathrm{b}} - p^{\mathrm{g}}\} h\} r \tag{34}$$

We observe that F_μ closely resembles an effective interface Hamiltonian as presented, e.g., by MacDowell[28] and Dörfler et al.[20]

A film profile at mechanical equilibrium must have a vanishing first variation of F_μ and satisfy the Euler−Lagrange equation[44]

$$\frac{\partial L}{\partial h} - \frac{\mathrm{d}}{\mathrm{d}r}\left\{\frac{\partial L}{\partial \dot{h}}\right\} = 0 \tag{35}$$

We differentiate L and insert into the Euler−Lagrange equation to get

$$p^{\mathrm{g}} - p^{\mathrm{b}} = \Pi + \gamma_\infty^{\mathrm{gl}} \{\kappa_1 + \kappa_2\} \tag{36}$$

where

$$\kappa_1 = \frac{\dot{h}}{r\sqrt{1 + \dot{h}^2}} \tag{37}$$

$$\kappa_2 = \frac{\ddot{h}}{\{1 + \dot{h}\}^{3/2}} \tag{38}$$

are the curvatures of the film−gas interface.

Equation 36 is the augmented Young−Laplace equation for the film. It is a second-order ordinary differential equation that may be solved to yield a film profile that satisfies the mechanical force balance. Solving eq 36 requires two boundary conditions. The first is a homogeneous Neumann boundary condition at $r = 0$

$$\dot{h}|_{r=0} = 0 \tag{39}$$

which follows from the cylindrical symmetry of the problem. The second is a Dirichlet condition at $r = R$

$$h|_{r=R} = h_R \tag{40}$$

where h_R is some specified constant value.

https://dx.doi.org/10.1021/acs.langmuir.0c00960
Langmuir 2020, 36, 7879−7893

For a given value of h_R, the Euler−Lagrange equation may have several solutions. We will consider two qualitatively different types of solutions. The first type is the trivial solution where h is a constant. This corresponds to a flat film (Figure 3a). In this case, the curvature terms in eq 36 are zero and $\Delta p = p^g - p^b$ is equal to Π, which is constant along the film profile. The other type of solution is a droplet and a film, as illustrated in Figure 3b. In this case, the disjoining pressure and curvature terms vary along the film profile, but their sum remains constant. Crucially, as the gas−liquid interface of the droplet approaches the solid surface, the disjoining pressure term balances the curvature terms in such a way that the gas−liquid interface flattens into a flat film.

The grand canonical energy can be calculated from the Helmholtz energy by

$$\Omega = F - \mu^g N \tag{41}$$

The criteria for a stationary state in Ω are the same as for F. However, the stability of these stationary points, i.e., whether they are minima, maxima, or saddle points, is likely to differ.

NUMERICAL METHODS

In this section, we will describe the numerical methods used to solve the models presented. This amounts to identifying stationary states of the two energy functionals, F and Ω, and determining their stability by characterizing them as maxima, minima, or saddle points.

To identify stationary states, we adopt the same strategy as described in ref 25. We first find states that are in mechanical force balance by solving eq 36, the Euler−Lagrange equation. The solution specifies the geometry of the film configuration, i.e., the thickness h as a function or r, and corresponds to a specific value of $\Delta p = p^g - p^b$, the difference between the gas phase pressure and the pressure of the hypothetical bulk liquid phase with which the film would be in chemical equilibrium. A phase equilibrium calculation is performed next, where equality of the chemical potentials is used to determine the number of particles in the film and gas phases.

The next step after determining a stationary state is to evaluate its stability. To this end, we discretize the Helmholtz and grand canonical energy functionals and examine the eigenvalues of their Hessian matrices.

Phase Equilibrium Calculations. Any film profile in mechanical force balance satisfies eq 36 for a specific value of $\Delta p = p^g - p^b$. Through eq 24, the film profile also specifies the volumes V^f and V^g. Phase equilibrium for a particular film profile can therefore be determined by finding the particle numbers N^f and N^g that give the necessary pressure difference and equality of the film and gas chemical potentials. This is accomplished by solving the nonlinear system of equations

$$\mathbf{F}\left(N^f/N^\circ, N^g/N^\circ\right) = 0 \tag{42}$$

where

$$\mathbf{F}\left(\frac{N^f}{N^\circ}, \frac{N^g}{N^\circ}\right) = \begin{bmatrix} \dfrac{\mu^g(T, V^g, N^g) - \mu^b(T, V^f, N^f)}{RT} \\ \dfrac{p^g(T, V^g, N^g) - p^b(T, V^f, N^f) - \Delta p}{p^\circ} \end{bmatrix} \tag{43}$$

and $\mu^b = \mu^f$ according to eq 7. The pressures, chemical potentials, and the derivatives required to compute $\mathbf{F}$ and its Jacobian are provided by the EOS. The scaling quantities are

$$p^\circ = 10^5 \text{ Pa} \tag{44}$$

$$N^\circ = \frac{p^\circ V}{RT} \tag{45}$$

where R is the universal gas constant.

The nonlinear system defined by eq 42 was solved using Newton's method. Initial guess values for N^f and N^g were obtained by a standard phase equilibrium calculation[45,46] at the specified temperature and saturation pressure.

Solving the Euler−Lagrange Equation. The Euler−Lagrange equation for the film eq 36 was solved to obtain film profiles in mechanical force balance. This equation is a second-order ordinary differential equation that has two boundary conditions, one at $r = 0$ and the other at $r = R$. Together, these boundary conditions and eq 36 constitute a two-point boundary value problem, which was solved using solve_bvp from Scipy's `integrate` module.[47]

Discrete Description of the Distributed Film. Following the procedures described above results in stationary states of the Helmholtz and grand canonical energy functionals. These are states that have a vanishing first variation for any perturbation of the film profile. However, these procedures do not give any information about whether or not the stationary states are stable. This information is contained in the second variation or higher-order variations if the second variation is zero. A stationary state is a minimum if the second variation is positive for any perturbation of the film profile. To evaluate this numerically, we use a discrete approach similar to Gjennestad and Wilhelmsen.[25] The idea is to represent the continuous function $h(r)$ by its values at discrete points and then use a quadrature rule to approximate the functional integrals. Stability of the stationary states can then be determined by considering the eigenvalues of a Hessian matrix, as will be described in the section Stability Analysis.

An equivalent way of expressing the Helmholtz energy of the distributed film model (eq 32) is

$$F = \{\mu^f - \mu^g\}N^f + \mu^g N - p^g V + \gamma_\infty^{ls} A^{fs} + \gamma_\infty^{gl} A^{gf} - W - \{p^b - p^g\}V^f \tag{46}$$

where A^{gf}, W, and V^f are functionals of h. Specifically

$$A^{gf} = 2\pi \int_0^R r\sqrt{1 + \dot{h}^2}\, \mathrm{d}r \tag{47}$$

$$W = 2\pi \int_0^R rw\, \mathrm{d}r \tag{48}$$

and V^f is given by eq 24.

Let now the function h be approximated by the vector

$$\mathbf{h} = [h_1,\ h_2,\ \ldots,\ h_M]^T \tag{49}$$

which gives its values at M discrete points along the r-axis

$$\mathbf{r} = [r_1,\ r_2,\ \ldots,\ r_M]^T \tag{50}$$

The functional A^{gf} may then be approximated by the sum

$$A^{gf}(\mathbf{h}) = 2\pi \sum_{i=0}^{M} \overline{r}_i \sqrt{1 + \dot{\overline{h}}_i^{\,2}}\ \Delta r_i \tag{51}$$

where

$$\overline{r}_i = \frac{r_{i+1} + r_i}{2} \tag{52}$$

$$\overline{h}_i = \frac{h_{i+1} + h_i}{2} \tag{53}$$

$$\dot{\overline{h}}_i = \frac{h_{i+1} - h_i}{\Delta r_i} \tag{54}$$

$$\Delta r_i = r_{i+1} - r_i \tag{55}$$

The boundary conditions dictate that $h_0 = h_1$ and $h_{M+1} = h_M$. Analogous definitions apply for $W(\mathbf{h})$ and $V^f(\mathbf{h})$.

The Helmholtz energy functional may now be approximated by

$$F(\mathbf{x}) = \{\mu^f - \mu^g\}N^f + \mu^g N - p^g V = \gamma_\infty^{ls} A^{fs} + \gamma_\infty^{gl} A^{gf}(\mathbf{h}) - W(\mathbf{h}) - \{p^b - p^g\}V^f(\mathbf{h}) \tag{56}$$

where the vector of unknowns $\mathbf{x}$ includes N^f in addition to $\mathbf{h}$

https://dx.doi.org/10.1021/acs.langmuir.0c00960
Langmuir 2020, 36, 7879−7893

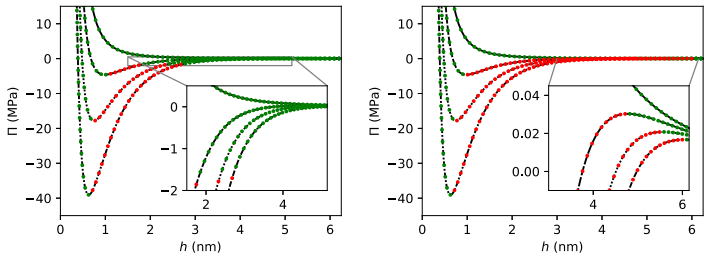

(a) Closed (b) Open

Figure 5. Stability of flat films of different thicknesses with each of the four disjoining pressure curves from Figure 4, in (a) a closed and (b) an open container. Locally stable films are indicated by green dots and unstable films by red dots.

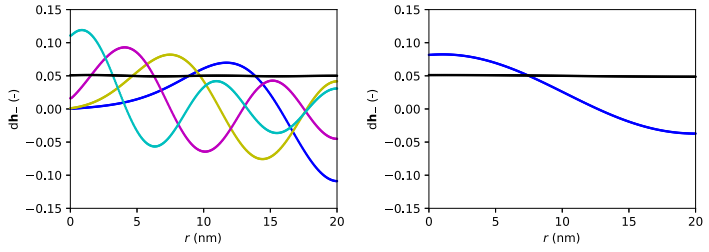

(a) $h = 1.06$ nm (b) $h = 2.68$ nm

Figure 6. Flat film instability modes $\mathbf{dh}_-$ for the $\theta_0 = 60°$ disjoining pressure isotherm in the open container. In (a) the film thickness is $h = 1.06$ nm and in (b) it is $h = 2.68$ nm. Instabilities have zero (black), one (blue), three (magenta), or four (cyan) internal extrema. The plotted vectors $\mathbf{dh}_-$ have been normalized so that their length is 1 in the L_2-norm. Instabilities in the closed system are similar, except that the zero-extrema mode (black) is absent.

$$\mathbf{x} = [x_1,\ x_2,\ x_3,\ ...,\ x_{M+1}]^{\mathrm{T}} = [N^{\mathrm{f}},\ h_1,\ h_2,\ ...,\ h_M]^{\mathrm{T}} \tag{57}$$

The Jacobian vector of the discretized Helmholtz energy can be shown to be

$$\frac{\partial F}{\partial x_1} = \mu^{\mathrm{f}} - \mu^{\mathrm{g}} \tag{58}$$

and

$$\frac{\partial F}{\partial x_i} = \gamma_\infty^{\mathrm{gl}} \frac{\partial A^{\mathrm{gf}}}{\partial x_i} - \frac{\partial W}{\partial x_i} - \{p^{\mathrm{b}} - p^{\mathrm{g}}\}\frac{\partial V^{\mathrm{f}}}{\partial x_i} \tag{59}$$

for $i \in \{2, M + 1\}$. The Hessian matrix may be found by further differentiation. Details of the procedure for calculating the derivatives of A^{gf}, W, and V^{f} w.r.t. x_i and a validation of the discretization procedure are given in ref 25 and its accompanying Supporting Information. An analogous procedure is applied to obtain a discrete approximation of the grand canonical energy and its derivatives.

Stability Analysis. Stationary states $\mathbf{x}^*$ obtained with the above procedures will have Jacobian vectors equal to zero for both F and Ω. The change in, e.g., F due to a small perturbation $\mathbf{dx}$ of the stationary state $\mathbf{x}^*$ is thus determined by the Hessian matrix of F

$$\mathrm{d}F = \mathbf{dx}^{\mathrm{T}} \left.\frac{\mathrm{d}^2 F}{\mathbf{dx}^2}\right|_{\mathbf{x}^*} \mathbf{dx} \tag{60}$$

The Hessian matrix is symmetric and can therefore be decomposed as

$$\left.\frac{\mathrm{d}^2 F}{\mathbf{dx}^2}\right|_{\mathbf{x}^*} = \mathbf{Q}\mathbf{\Lambda}\mathbf{Q}^{\mathrm{T}} \tag{61}$$

where the matrix $\mathbf{\Lambda}$ is a diagonal matrix of eigenvalues and $\mathbf{Q}$ is a matrix whose column i is the eigenvector $\mathbf{q}^{(i)}$ corresponding to the eigenvalue $\Lambda^{(i)}$. We will use the convention that all eigenvectors $\mathbf{q}^{(i)}$ have length 1 in the L_2-norm. Since the Hessian is symmetric, the eigenvectors are orthogonal.[25]

The stationary state $\mathbf{x}^*$ is locally stable in a closed container and represents a local minimum in F if all of the eigenvalues of the Hessian matrix $\Lambda^{(i)}$ are positive. On the other hand, if one or more eigenvalues are negative, it is possible to choose the perturbation $\mathbf{dx}$ along one of the associated eigenvectors $\mathbf{q}_-^{(i)}$. The subscripted minus sign indicates the negative eigenvalue. In this case, we choose $\mathbf{dx} = \mathbf{dx}_- \propto \mathbf{q}_-^{(i)}$ and this will give a negative $\mathrm{d}F$. The stationary state $\mathbf{x}^*$ is then not a local minimum and is considered locally unstable. Stability in open containers is evaluated in a similar manner. Unstable states with both positive and negative eigenvalues are called saddle points, while only negative eigenvalues characterize a maximum.

The eigenvectors associated with negative eigenvalues give information about the direction in configuration space that the system can go to reduce its energy and hence what causes an instability to the stationary state.

Before the calculation of eigenvalues and eigenvectors, it was ensured that the discrete Jacobian vectors of the stationary states obtained by the methods in sections Solving the Euler−Lagrange Equation and Phase Equilibrium Calculations were indeed zero. This was accomplished through a small number of iterations with Newton's method using the Jacobian vectors and Hessian matrices defined by the discrete approach.

https://dx.doi.org/10.1021/acs.langmuir.0c00960
Langmuir 2020, 36, 7879−7893

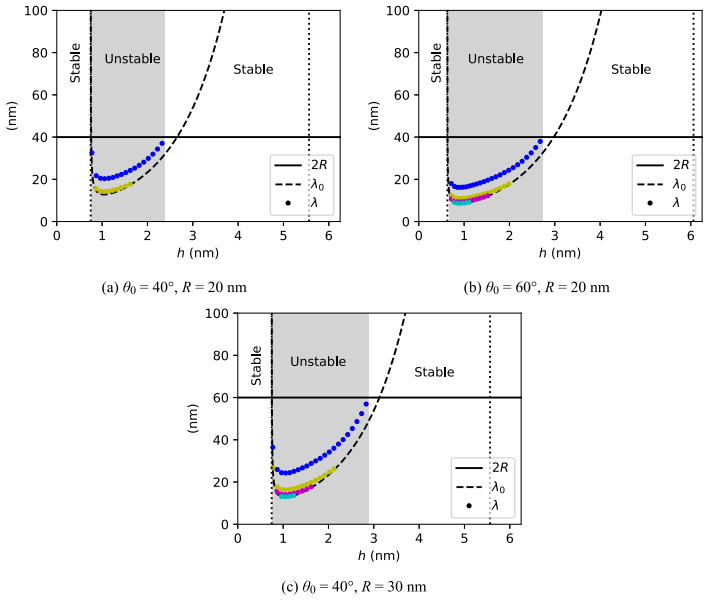

(a) $\theta_0 = 40°$, $R = 20$ nm (b) $\theta_0 = 60°$, $R = 20$ nm

(c) $\theta_0 = 40°$, $R = 30$ nm

Figure 7. Wavelengths λ of mechanical instability modes (dots) for different film thicknesses h, disjoining pressure isotherms, and container radii R. The modes have one (blue), two (yellow), three (magenta), or four (cyan) internal maxima. In (a) and (b), the container radius is $R = 20$ nm and in (c) it is $R = 30$ nm. In (a) and (c) $\theta_0 = 40°$ and in (b) $\theta_0 = 60°$. Also plotted are the container diameters $2R$ (solid lines) and a linear approximation, computed from eq 18, of the minimum wavelength λ_0 of film profile perturbations that have a positive growth rate (dashed lines). The dotted vertical lines mark the asymptotes where $\lambda_0 \to \infty$. The shaded gray regions indicate the intervals of film thicknesses where the films were found to be unstable in the closed system.

Eigenvalues and eigenvectors were calculated with `eigh` from the `linalg` module in Numpy.[48] This function again uses the *`syevd` routines from LAPACK.[49]

RESULTS

We first discuss the thermodynamic stability of flat films and droplet configurations. Next, we compare the energies of the two types of configuration and study the morphological phase transition between them.

Except where explicitly stated otherwise, we consider a container with $R = 20$ nm and $H = 10$ nm. The number of grid points used in the discrete approximation is $M = 400$.

Flat Films. Figure 5 compares the local stability of flat films as a function of film thickness for four different disjoining pressure isotherms. Stability in a closed container is illustrated in Figure 5a, while Figure 5b displays stability in an open container. In the open container, films are stable when $d\Pi/dh < 0$. This is in agreement with the conventional stability condition presented in the literature; see, e.g., the review paper by Boinovich and Emelyanenko[2] (or ref 1, p 56). A similar result was also obtained through dynamic considerations by Sharma,[34] assuming a constant gas pressure and a model for the evaporation rate. In the closed container, on the other hand, some films are found to be stable even if $d\Pi/dh > 0$.

Eigenvectors $\mathbf{q}_-^{(i)}$ of Hessian matrices that are associated with negative eigenvalues correspond to perturbations $d\mathbf{x}_- \propto \mathbf{q}_-^{(i)}$ that the film is unstable against. An unstable stationary state may have one or more such negative eigenvalues. The vectors $d\mathbf{x}_-$ are composed of two parts: dN_-^f, the component describing the perturbation of the number of particles in the film; and $d\mathbf{h}_-$, a vector representing the perturbation of the film profile. The vectors $d\mathbf{h}_-$ are here referred to as instability modes.

Figure 6 compares the instability modes for the $\theta_0 = 60°$ isotherm and two different film thicknesses in an open container. Specifically, Figure 6 displays the instability modes obtained when $h = 1.06$ nm. This film thickness is well into the unstable region of the disjoining pressure isotherm with $d\Pi/dh > 0$. Each mode has resemblance to a sinusoidal function with some wavelength and corresponds to a specific number of internal extrema, indicated by their color (black, 0; blue, 1; yellow, 2; etc.). Instabilities in the closed system are similar, except that the zero-extrema mode (black) is absent. By moving along this mode, the open system can reduce its energy by condensing or evaporating the film while the film retains its flat profile. We call this mode a condensation−evaporation instability and find that it is present in the open system whenever the derivative of the disjoining pressure curve is positive. This type of mode thus causes the open system to be unstable whenever $d\Pi/dh > 0$. The other instability modes involve some degree of rearrangement of the film profile, and we therefore call these mechanical instability modes. The stability of the closed system is determined by this kind of instability. We emphasize that the mechanical instabilities also involve some exchange of particles. The distinction between condensation/evaporation and mechanical instabilities is based on whether or not the alteration of the gas−film interface shape occurs. We further observe that the

https://dx.doi.org/10.1021/acs.langmuir.0c00960
Langmuir 2020, 36, 7879−7893

exchange of particles is larger in the open system than in the closed system, which is due to the constrained total number of particles in the closed system.

As the film thickness is increased, the number of unstable mechanical modes is gradually reduced. They disappear in order of decreasing number of internal maxima (i.e., cyan first, then magenta, etc.) until there is only one left. As the film thickness is increased further and approaches the end of the unstable interval for the closed container (Figure 5a), the maximum of the mode with a single internal extremum moves toward the center of the container. Figure 6 shows the instability modes for a film of thickness h = 2.68 nm in an open container. This thickness corresponds to the rightmost red dot on the $\theta_0 = 60°$ isotherm of the closed container displayed in Figure 5a. The mechanical instability mode resembles in this case a sinusoidal function with a wavelength close to the diameter of the container. For thicker films, there are no unstable modes in the closed system and it is stable. In the open system however, the condensation/evaporation instability persists until the disjoining pressure derivative again becomes negative. The existence of condensation/evaporation inabilities in open systems and their absence in closed systems have recently been reported also for thick films in pores.[25]

The mechanical instabilities seen here are of a similar kind as those that cause spinodal dewetting. As shown, e.g., by Dörfler et al.,[20] the mechanical instabilities must have wavelengths λ that are smaller than the diameter of the container. The finite extent of the container makes instabilities with longer wavelengths impossible. Furthermore, the wavelengths of unstable perturbations must be bounded from below by the surface tension. Perturbations with very short wavelengths will require the creation of a large amount of surface area, relative to the amount of energy than can be gained from the disjoining pressure by shifting the liquid around. In a translationally invariant system of infinite extent, this lower bound is given by eq 18. A consequence of eq 18 is that $d\Pi/dh > 0$ is a necessary condition for mechanical instabilities. This results in specific intervals of film thicknesses where mechanical instabilities may occur.

To show that these two effects indeed constrain the mechanical instabilities observed here, we estimate for each unstable state the wavelengths of the mechanical instability modes. For the modes with many extrema, the horizontal crest-to-trough distance changes slightly along the r-axis. We therefore estimate the wavelength as the distance from the container sidewall to the nearest internal extremum, multiplied by a factor 2. Figure 7 displays the resulting wavelengths as functions of film thickness. Results are presented for disjoining pressure isotherms with $\theta_0 = 40°$ (Figure 7a) and $\theta_0 = 60°$ (Figure 7b). Figure 7c displays results for the 40° isotherm and a wider container. The figures also show the container diameter $2R$ (solid horizontal line) and the shortest unstable wavelength λ_0 as predicted by eq 18 (dashed line). The dotted vertical lines indicate where $d\Pi/dh = 0$ and $\lambda_0 \to \infty$. The disjoining pressure derivative is positive between them and, according to the linear stability analysis, mechanical instabilities should thus occur only for film thicknesses in between these lines.

All measured wavelengths correspond to film thicknesses between the dotted lines, i.e., where $d\Pi/dh > 0$. We observe no mechanical instabilities with wavelengths longer than $2R$. As a concrete illustration, compare Figure 7a where R = 20 nm with Figure 7c where the container size is increased to R = 30 nm. In the latter case, the increased container size gives room for instabilities with longer wavelengths. This results in an increased interval of film thicknesses where films are mechanically unstable. The larger container also gives room for a larger number of extrema in instabilities with a given wavelength. For instance, the shortest-wavelength instabilities in Figure 7a have two internal extrema, whereas instabilities with approximately the same wavelength in Figure 7c have four. For both container sizes, it is clear that the mechanical instabilities with the longest wavelength disappear when they reach the $2R$-bound.

In addition to being smaller than $2R$, the measured unstable wavelengths are longer than λ_0. Although derived with an assumption of translational invariance that does not apply in the present example, eq 18 appears to provide an accurate estimate for the lower bound for the unstable wavelengths.

From the form of eq 18, we may expect that instabilities of shorter wavelengths are possible when the disjoining pressure derivatives are larger. This is indeed what we observe, e.g., when comparing results from the $\theta_0 = 40°$ isotherm (Figure 7a) to results from the $\theta_0 = 60°$ isotherm (Figure 7b). The latter disjoining pressure curve extends to larger negative values for the disjoining pressure. This results in unstable modes with shorter wavelengths and a larger number of internal extrema.

In large closed containers, more mechanical instability modes will be present as the upper bound of $2R$ increases. The films will then become mechanically unstable for a larger part of the interval where $d\Pi/dh > 0$. However, the dotted lines in Figure 7 display the film thicknesses for which the estimated lower bound for unstable wavelengths λ_0 diverges. The divergence of λ_0 means that there may be an interval on the h-axis where a finite container is not large enough to support sufficiently long wavelengths for the film to be unstable no matter how large the container is. However, this region quickly becomes narrow as the container diameter is increased. As an example, consider the $\theta_0 = 40°$ isotherm and a container with $2R$ = 1 μm. The lower bound, λ_0, is larger than 1 μm only for film thicknesses between 5.41 nm and the thickness for which λ_0 diverges, 5.56 nm. The effect of mechanical stabilization due to finite container size is therefore expected to be small for large containers.

In summary, we find that the criterion for thermodynamic stability of films provided in the literature, $d\Pi/dh < 0$, applies only to open systems due to a condensation/evaporation instability that is present whenever this criterion is not satisfied. The stability of films in closed systems is governed by mechanical instabilities of a similar kind as those responsible for spinodal dewetting in nonvolatile systems. Similar to nonvolatile films,[20] we find that films in small closed containers may be stable even though $d\Pi/dh > 0$ due to the finite size of the container.

Droplets and Films. We shall next compare the thermodynamic stability of a thin film in coexistence with a droplet in an open and a closed system. The stability of different droplet configurations in a closed container is shown in Figure 8 for the $\theta_0 = 60°$ isotherm. Here, the configurations with the largest droplets are stable. As the droplet size is reduced, the contact angle decreases and the film thickness increases. Thus, the droplet configurations gradually converge to a flat film as the film thickness approaches the minimum on the disjoining pressure curve where $d\Pi/dh|_{h=h_a} = 0$. At some point before the disjoining pressure in the thin-film part of the configurations reaches this minimum, however, the droplets become unstable. As we shall see in the next section, this point is associated with a minimum in the total density in the container. A similar behavior was obtained also for the $\theta_0 = 40°$ isotherm.

https://dx.doi.org/10.1021/acs.langmuir.0c00960
Langmuir 2020, 36, 7879−7893

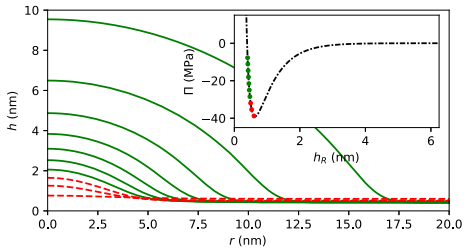

Figure 8. Thermodynamic stability of droplets in coexistence with films of different thicknesses for the disjoining pressure curve with $\theta_0 = 60°$. The film thickness marked on the disjoining pressure isotherm is h_R, i.e., the thickness measured at the container wall where $r = R$. Stable configurations are shown in solid green and unstable configurations in dashed red.

Dörfler et al.[20] found that stable nonvolatile droplets eventually became unstable if the substrate size was increased by making the film-covered substrate area larger while keeping the size of the droplet fixed. We observe the same for the droplets in a closed system studied here.

If the container is open instead of closed, then all of the droplet configurations in Figure 8 are unstable.

The unstable droplet states have one negative Hessian eigenvalue, in both the open and the closed container. The unstable droplets thus represent saddle points in both free energy landscapes, and the systems can reduce their energies by moving along (or against) one particular direction given by the associated eigenvector. Examples of instability modes $\mathbf{dh}_-$ are shown in Figure 9. These modes are similar for the open and

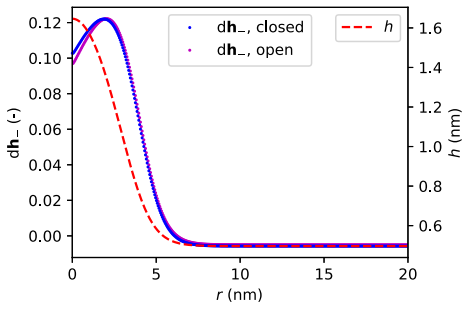

Figure 9. Droplet instability modes $\mathbf{dh}_-$ for the $\theta_0 = 60°$ disjoining isotherm and $h_R = 0.50$ nm, in the closed (blue) and the open (magenta) container. For reference, the film thickness h is also shown (dashed red line). The plotted vectors $\mathbf{dh}_-$ have been normalized so that their length is 1 in the L_2-norm.

closed systems. However, as discussed for the flat film, the unstable perturbations $\mathbf{dx}_- \propto \mathbf{q}_-^{(i)}$ for the open system involve a larger degree of particle exchange with the gas phase.

By initially perturbing the unstable droplets in the open system along the unstable eigenvector $\mathbf{dx}_- \propto \mathbf{q}_-^{(i)}$, we were able to form a path in the configuration space, with monotonically decreasing grand canonical energy, to a homogeneous liquid phase filling the entire container. By perturbing the system in the opposite direction, a path to a stable flat film was obtained. Sharma[34] observed a similar behavior by use of dynamic considerations. He assumed a constant gas pressure and a model for the evaporation rate. Time-stationary droplet solutions were then unstable, and droplets slightly smaller than the time-stationary state evaporated, shrunk, and eventually became a flat film, while slightly bigger droplets condensed further and grew in size. The unstable droplets in the open system thus represent activation barriers in the energy landscape, which correspond to stationary states with gas pressures above the saturation pressure.

By perturbing the unstable droplets in the closed system, we were able to form paths with monotonically decreasing Helmholtz energy to either a larger stable droplet or a stable flat film. The unstable droplets in the closed system therefore represent the activation barrier for wetting/dewetting of the solid surface.

A notable difference between the paths in the open and closed systems was that in the closed system, the number of particles in the film phase N^f changed very little. As an example, the decay of the unstable droplet in Figure 9 to a flat film resulted in a 5.5% reduction in N^f in the open system and only a 0.074% reduction in the closed system. A consequence of this is that the assumption of a nonvolatile film phase in the effective interface Hamiltonian approach used, e.g., by Dörfler et al.[20] appears reasonable for water in a closed system at the current temperature. However, this might not be the case for fluids closer to their critical temperature.

Film−Droplet Transition. By comparing the Helmholtz energy of different locally stable flat film and droplet configurations with the same total density $\rho = N/V$, we determine the equilibrium configuration in a closed system. This comparison is shown in Figure 10 for the $\theta_0 = 60°$ isotherm. The

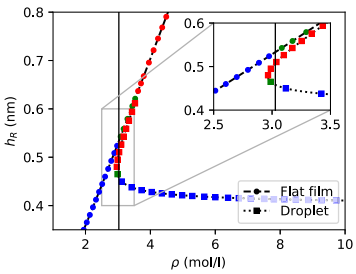

Figure 10. Film thicknesses h_R (at the container sidewall) plotted against the total density ρ in a closed container for the disjoining pressure isotherm with $\theta_0 = 60°$. Flat film configurations are shown as circles on a dashed line, while droplet configurations are shown as squares on a dotted line. Unstable states are shown in red and locally stable in green. Equilibrium states, which are locally stable and have the lowest Helmholtz energy of the stable configurations at that density, are shown in blue. The solid vertical line indicates the film−droplet transition density.

film thickness h_R at the container sidewall is plotted as a function of the total density for both types of configurations. Unstable configurations are indicated by red markers, locally stable configurations are indicated in green, and stable configurations that represent the lowest Helmholtz energy for a particular value of ρ are shown in blue. The gas spinodal density at the considered temperature is 0.35 mol L^{-1}, and the liquid spinodal

https://dx.doi.org/10.1021/acs.langmuir.0c00960
Langmuir 2020, 36, 7879−7893

density is 43 mol L^{-1}. Since the total densities of the configurations lie between the gas and liquid spinodals, a homogeneous fluid phase can be ruled out as a possible alternative equilibrium state since it is thermodynamically unstable.[46]

Figure 10 shows that the point on the dotted line where droplet configurations go from stable to unstable occurs at a minimum in the total density. Below this minimum, no stationary droplet states can be found. A similar effect has been observed for free bubbles and droplets in a closed system.[22,23] The unstable branch of droplet configurations converges toward the flat film configurations. The two types of configurations merge at the film thickness corresponding to a minimum in the disjoining pressure curves.

The flat films are stable at low densities. They are also the equilibrium configuration up to a certain value of the total density, indicated by the vertical solid line in Figure 10, where there is a morphological phase transition and the equilibrium state becomes a stable droplet configuration. The transition density is 3.03 mol L^{-1}, a value that depends both on the size and on the shape of the container.

Tracing the blue markers from left to right in Figure 10 shows that in a closed container at equilibrium, the system will initially consist of a thin flat film that grows in thickness as the number of particles is increased. Eventually, a droplet will form when the transition density is exceeded. The formation of a droplet will deplete liquid from the thin-film region such that the film thickness is reduced. This transition, from a stable film state to a stable droplet state, occurs through dewetting by nucleation.

The nucleation regime corresponds to the interval of densities in Figure 10 for which there are three possible stationary states: one stable flat film state and two droplet states. The two droplet states correspond to a small droplet, which is unstable, and a larger droplet, which is stable. An example of three such states at ρ = 3.1 mol L^{-1} is shown in Figure 11b. A transition from the stable flat film to the stable droplet state will pass through the unstable droplet, as it represents a saddle point in the thermodynamic energy landscape.

In Figure 11a, the Helmholtz energy difference ΔF between the droplet configurations and the corresponding film configuration with the same total density is plotted. Like in Figure 10, the stationary droplet states fork out into a stable and an unstable branch. The Helmholtz energy of the unstable branch is always larger than the stable branch. Furthermore, the Helmholtz energy of the unstable branch approaches that of the flat film as the total density in increased.

The Helmholtz energy differences ΔF of the three states in Figure 11b are indicated by markers of corresponding colors in Figure 11a. It is clear that the large droplet has the lowest Helmholtz energy and is the equilibrium configuration. However, a transition from the stable flat configuration, which passes through the unstable small-droplet configuration, must overcome an energy barrier through an activated nucleation process. The probability of the transition to occur increases as the energy barrier decreases and eventually goes to zero as the total density is increased. The opposite transition, from a large droplet to a flat film, may also occur as an activated nucleation process below the transition density. A similar analysis for the θ_0 = 40° isotherm gives qualitatively similar results but a somewhat higher transition density of 3.88 mol L^{-1}. Since the activation barriers for the film−droplet transition displayed in Figure 11a are rather small, we expect for this example that the morphological change will occur close to the transition density.

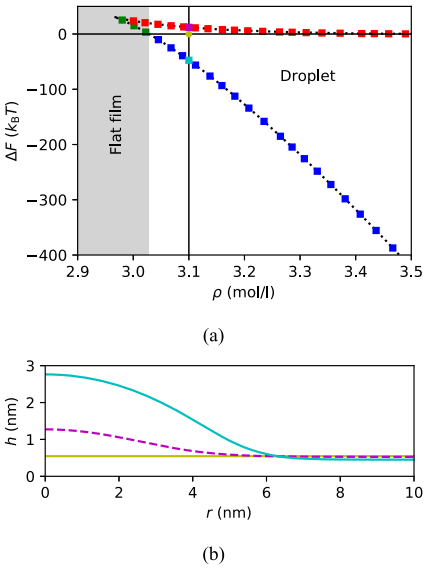

Figure 11. In (a), the Helmholtz energies of droplet configurations, relative to the flat film configuration with the same density, are shown as squares on a dotted line. As in Figure 10, θ_0 = 60° and unstable droplet states are marked by red squares, locally stable states by green squares, and stable states that have the lowest Helmholtz energy at the given density are shown in blue. The flat film configurations are stable for the entire range of densities plotted. Values of ΔF for the three possible stationary configurations at ρ = 3.1 mol L^{-1}, one flat film state (yellow dot) and two droplet states (magenta and cyan squares), are indicated. The corresponding film profiles are shown in (b).

CONCLUSIONS

The thermodynamic properties of thin films deviate from those of a bulk liquid phase at the same temperature and chemical potential. This deviation can be modeled by the disjoining pressure. Thin films occur in a variety of applications, such as in flow through porous media, fuel cells, in evaporation as well as in micro- and nanofluidics.

This work is a study of thin films of spatially varying thicknesses and their coexistence with droplets, in open systems and under confinement. Based on Derjaguin's concept of a disjoining pressure Π, which is dependent on film thickness h, and the existing bulk-phase equations of state, we derived a thermodynamic fundamental relation for a thin liquid film phase. From this fundamental relation, the film−gas and film−solid interfacial tensions were obtained, the latter of which was dependent on the film thickness. We verified that Derjaguin's equation for the contact angle of a macroscopic droplet was reproduced by the fundamental relation, and it was next employed to derive a capillary model for a distributed film of varying thicknesses, with a homogeneous gas phase above it.

The model was used to study the thermodynamic stability of stationary states that represent flat films and droplets of water in closed systems (canonical ensemble) or connected to a particle reservoir (grand canonical ensemble). The stationary states were found by solving the Euler−Lagrange equations derived

https://dx.doi.org/10.1021/acs.langmuir.0c00960
Langmuir 2020, 36, 7879−7893

from the Helmholtz energy functional (closed system) or the grand canonical energy functional (open system). By discretizing the energy functionals, the thermodynamic stability of the configurations could be inferred from the eigenvalues of the corresponding Hessian matrices.

In closed systems, the flat films were occasionally stable even when the conventional stability criterion often presented in the literature, $d\Pi/dh < 0$, was not satisfied. A closer inspection of the eigenvectors associated with the negative eigenvalues revealed that the stability was governed by mechanical instabilities of a similar kind as those responsible for spinodal dewetting in nonvolatile systems. In line with earlier works,[20,28] the films were stabilized when their thickness and disjoining pressure derivatives were such that the minimum unstable wavelength became larger than the container diameter.

Flat films in open systems, on the other hand, were found to follow the conventional stability criterion. The reason for this was the presence of an additional type of instability whenever the criterion was not satisfied. This type of instability corresponded to condensation/evaporation of the film while the film profile remained flat. This instability was not present in the closed systems.

Droplets in coexistence with thin films were found to be unstable for all considered examples in open systems. In closed systems, they were stable under certain conditions. When two different droplet states were possible at the same density, the large droplet was stable and the small droplet was unstable. Smaller and smaller droplets exhibited smaller and smaller contact angles and eventually converged to flat films.

The unstable droplets in both open and closed systems were found to be saddle points in their respective energy landscapes. In the closed system, they represent the activation barrier for the transition between a stable flat film and a stable droplet. This activation barrier was quantified by evaluating the Helmholtz energies of both the stable and unstable stationary states. In the open system, the unstable droplets represent the activation barrier for the transition from a flat film to a bulk liquid phase through condensation.

In a closed system, flat films were found to be the equilibrium configuration up to a certain value for the total density. Beyond this value, there was a morphological phase transition to stable droplet configurations.

The framework presented can readily be extended to study thin-film configurations in multicomponent systems and in different geometries such as around fibers and within porous media.

APPENDIX A. MACROSCOPIC DROPLET MODEL

In this section, we derive a simplified model for a macroscopic droplet configuration. This model serves two purposes. (1) Analysis of the macroscopic model will provide an alternative way to derive Derjaguin's relation for the macroscopic contact angle (eq 16), using the fundamental relation for the film phase, that does not presume a balance of interfacial forces. (2) Since the macroscopic model is consistent with a known result, Derjaguin's contact angle relation, it provides an opportunity to validate the distributed model and the discrete approach used to solve it. We will show that the two give the same interface profiles in the large-droplet limit.

We consider a cylindrical container of base radius R, base area $A = \pi R^2$, and height H, giving a total volume $V = AH$. It contains a spherical droplet, large enough for the pressure inside it to be unaffected by the disjoining pressure, covering part of A, while a thin film covers the rest. A gas phase occupies the remaining container volume. The gas−liquid interface of the droplet is a spherical cap, and the droplet volume can be expressed as

$$V^{\mathrm{d}}(a, b) = \frac{\pi b}{6}\{3a^2 + b^2\} \tag{A.1}$$

where a is the base-area radius and b is the height of the spherical cap. The parameters a and b are related to the radius of curvature in the droplet, r, and the contact angle θ through

$$r^2 = a^2 + \{r - b\}^2 \tag{A.2}$$

$$\cos(\theta) = \{r - b\}/r \tag{A.3}$$

The gas−liquid interfacial area of the droplet is

$$A^{\mathrm{gd}}(a, b) = \pi\{a^2 + b^2\} \tag{A.4}$$

and the solid−liquid interfacial area is

$$A^{\mathrm{ds}}(a) = \pi a^2 \tag{A.5}$$

The film area is

$$A^{\mathrm{f}}(a) = A - A^{\mathrm{ds}}(a) \tag{A.6}$$

and the film volume is

$$V^{\mathrm{f}}(h, a) = hA^{\mathrm{f}}(a) \tag{A.7}$$

where h is the film thickness. The gas volume is

$$V^{\mathrm{g}} = V - V^{\mathrm{f}} - V^{\mathrm{d}} \tag{A.8}$$

In a closed container in contact with a thermal reservoir, equilibrium is a stationary state of the Helmholtz energy. Using the capillary model approach, the Helmholtz energy differential for the system is

$$\mathrm{d}F = \mathrm{d}F^{\mathrm{g}} + \mathrm{d}F^{\mathrm{d}} + \mathrm{d}F^{\mathrm{f}} \tag{A.9}$$

$$= -S\,\mathrm{d}T - p^{\mathrm{g}}\mathrm{d}V^{\mathrm{g}} + \mu^{\mathrm{g}}\mathrm{d}N^{\mathrm{g}} - p^{\mathrm{d}}\mathrm{d}V^{\mathrm{d}} + \mu^{\mathrm{d}}\,\mathrm{d}N^{\mathrm{d}} + \gamma_{\infty}^{\mathrm{gl}}\,\mathrm{d}A^{\mathrm{gd}} + \gamma_{\infty}^{\mathrm{ls}}\,\mathrm{d}A^{\mathrm{ds}} - p^{\mathrm{f}}\,\mathrm{d}V^{\mathrm{f}} + \mu^{\mathrm{f}}\,\mathrm{d}N^{\mathrm{f}} + \gamma^{\mathrm{f}}\,\mathrm{d}A^{\mathrm{f}} \tag{A.10}$$

Herein, γ^{f} is the film tension, i.e.,

$$\gamma^{\mathrm{f}} = \gamma^{\mathrm{gf}} + \gamma^{\mathrm{fs}} \tag{A.11}$$

$$= \gamma_{\infty}^{\mathrm{gl}} + \gamma_{\infty}^{\mathrm{ls}} + \Pi h - \int_{h_{\infty}}^{h} \Pi\,\mathrm{d}h \tag{A.12}$$

Using now that $\mathrm{d}V^{\mathrm{g}} = -\mathrm{d}V^{\mathrm{f}} - \mathrm{d}V^{\mathrm{d}}$, $\mathrm{d}N^{\mathrm{g}} = -\mathrm{d}N^{\mathrm{f}} - \mathrm{d}N^{\mathrm{d}}$, and $\mathrm{d}A^{\mathrm{f}} = -\mathrm{d}A^{\mathrm{ds}}$, the differential may be expressed as

$$\mathrm{d}F = -S\,\mathrm{d}T - \{p^{\mathrm{d}} - p^{\mathrm{g}}\}\,\mathrm{d}V^{\mathrm{d}} + \{\mu^{\mathrm{d}} - \mu^{\mathrm{g}}\}\,\mathrm{d}N^{\mathrm{d}} + \gamma_{\infty}^{\mathrm{gl}}\,\mathrm{d}A^{\mathrm{gd}} + \{\gamma_{\infty}^{\mathrm{ls}} - \gamma^{\mathrm{f}}\}\,\mathrm{d}A^{\mathrm{ds}} - \{p^{\mathrm{f}} - p^{\mathrm{g}}\}\,\mathrm{d}V^{\mathrm{f}} + \{\mu^{\mathrm{f}} - \mu^{\mathrm{g}}\}\,\mathrm{d}N^{\mathrm{f}} \tag{A.13}$$

The areas and volumes are determined by three free parameters, e.g., h, a, and b. This enables further manipulation of the differential to obtain

https://dx.doi.org/10.1021/acs.langmuir.0c00960
Langmuir 2020, 36, 7879−7893

$$
\begin{aligned}
\mathrm{d}F = & -S\,\mathrm{d}T + \{\mu^{\mathrm{d}} - \mu^{\mathrm{g}}\}\,\mathrm{d}N^{\mathrm{d}} + \{\mu^{\mathrm{f}} - \mu^{\mathrm{g}}\}\,\mathrm{d}N^{\mathrm{f}} \\
& + \left\{-\{p^{\mathrm{d}} - p^{\mathrm{g}}\}\frac{\partial V^{\mathrm{d}}}{\partial a} - \{p^{\mathrm{f}} - p^{\mathrm{g}}\}\frac{\partial V^{\mathrm{f}}}{\partial a}\right. \\
& \left. + \gamma_{\infty}^{\mathrm{gl}}\frac{\partial A^{\mathrm{gd}}}{\partial a} + \{\gamma_{\infty}^{\mathrm{ls}} - \gamma^{\mathrm{f}}\}\frac{\partial A^{\mathrm{ds}}}{\partial a}\right\}\mathrm{d}a \\
& + \left\{-\{p^{\mathrm{d}} - p^{\mathrm{g}}\}\frac{\partial V^{\mathrm{d}}}{\partial b} + \gamma_{\infty}^{\mathrm{gl}}\frac{\partial A^{\mathrm{gd}}}{\partial b}\right\}\mathrm{d}b \\
& + \left\{-\{p^{\mathrm{f}} - p^{\mathrm{g}}\}\frac{\partial V^{\mathrm{f}}}{\partial h}\right\}\mathrm{d}h
\end{aligned}
\tag{A.14}
$$

In a stationary state, all terms in A.14 must be zero. The first two terms then give that a stationary state requires chemical equilibrium

$$
\mu^{\mathrm{d}} = \mu^{\mathrm{g}} = \mu^{\mathrm{f}} \tag{A.15}
$$

Having the last term equal to zero requires

$$
p^{\mathrm{g}} = p^{\mathrm{f}} = p^{\mathrm{b}} + \Pi \tag{A.16}
$$

i.e., mechanical equilibrium between the gas and film phases. The two remaining terms give

$$
p^{\mathrm{d}} - p^{\mathrm{g}} = \frac{2\gamma_{\infty}^{\mathrm{gl}}}{r} \tag{A.17}
$$

the Young−Laplace equation for the droplet and

$$
\cos(\theta) = \frac{\gamma^{\mathrm{f}} - \gamma_{\infty}^{\mathrm{ls}}}{\gamma_{\infty}^{\mathrm{gl}}} \tag{A.18}
$$

which is Young's equation for the contact angle of the droplet. Inserting eq A.12 into eq A.18, we recover Derjaguin's equation (eq 16) for the contact angle of a macroscopic droplet.

The procedure above can also be applied in an open isothermal system. The result is that the criteria for a stationary state in the grand canonical energy Ω are the same as those for a stationary state in F.

As a validation of the discrete approach described in the section Discrete Description of the Distributed Film, we here confirm that the film profiles obtained with this method converge to those obtained by the macroscopic model as the droplet size is increased. To this end, we compute stationary droplet states with the macroscopic model and $a = R/2$ for progressively increasing values of R. For each of these states, we compute the stationary state that has the same number of particles using the discrete approach with 600 grid points. We use the same fluid EOS and interfacial tensions as in the main paper and use the disjoining pressure isotherm with a macroscopic contact angle of $\theta_0 = 60°$. Two examples are shown in Figure 12a,b for $R = 10$ and 640 nm, respectively. There is a large discrepancy between the film profiles for the small container. In the large container, the two profiles are identical within the accuracy of the plots.

As a more formal comparison, we compute the L_2-norm of the relative difference between the film profiles obtained with the two different models. This is plotted in Figure 13 against the container radius. This shows that the film profiles obtained with the discrete method converge to those from the macroscopic model as the container size is increased.

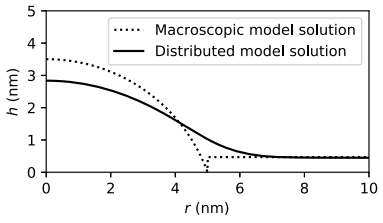

(a)

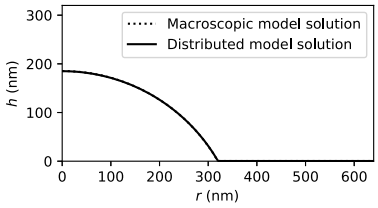

(b)

Figure 12. Solutions of the macroscopic model (dotted) and the distributed model (solid) for container sizes (a) $R = 10$ nm and (b) $R = 640$ nm.

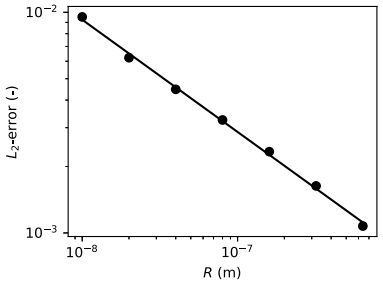

Figure 13. L_2-error between macroscopic and distributed model solutions vs the container radius.

AUTHOR INFORMATION

Corresponding Authors

Magnus Aa. Gjennestad − *PoreLab/Department of Physics, Norwegian University of Science and Technology, 7491 Trondheim, Norway;* orcid.org/0000-0002-2164-5874; Email: magnus@aashammer.net, magnus.aa.gjennestad@ntnu.no

Øivind Wilhelmsen − *PoreLab/SINTEF Energy Research, 7034 Trondheim, Norway; Department of Energy and Process Engineering, Norwegian University of Science and Technology, 7491 Trondheim, Norway;* orcid.org/0000-0003-4631-0349; Email: oivind.wilhelmsen@sintef.no

Complete contact information is available at: https://pubs.acs.org/10.1021/acs.langmuir.0c00960

Notes

The authors declare no competing financial interest.

https://dx.doi.org/10.1021/acs.langmuir.0c00960
Langmuir 2020, 36, 7879−7893

■ ACKNOWLEDGMENTS

This work was partly supported by the Research Council of Norway through its Centres of Excellence funding scheme, project number 262644.

■ REFERENCES

(1) Churaev, N. V.; Derjaguin, B. V.; Muller, V. M. *Surface Forces*; Springer: New York, 1987.
(2) Boinovich, L.; Emelyanenko, A. Wetting and surface forces. *Adv. Colloid Interface Sci.* **2011**, *165*, 60−69.
(3) Boinovich, L.; Emelyanenko, A. The prediction of wettability of curved surfaces on the basis of the isotherms of the disjoining pressure. *Colloids Surf., A* **2011**, *383*, 10−16.
(4) Moura, M.; Flekkøy, E. G.; Måløy, K. J.; Schäfer, G.; Toussaint, R. Connectivity enhancement due to film flow in porous media. *Phys. Rev. Fluids* **2019**, *4*, No. 094102.
(5) Zhao, B.; MacMinn, C. W.; Primkulov, B. K.; Chen, Y.; Valocchi, A. J.; Zhao, J.; Kang, Q.; Bruning, K.; McClure, J. E.; Miller, C. T.; Fakhari, A.; Bolster, D.; Hiller, T.; Brinkmann, M.; Cueto-Felgueroso, L.; Cogswell, D. A.; Verma, R.; Prodanović, M.; Maes, J.; Geiger, S.; Vassvik, M.; Hansen, A.; Segre, E.; Holtzman, R.; Yang, Z.; Yuan, C.; Chareyre, B.; Juanes, R. Comprehensive comparison of pore-scale models for multiphase flow in porous media. *Proc. Natl. Acad. Sci. U.S.A.* **2019**, *116*, 13799−13806.
(6) Gjennestad, M. Aa.; Vassvik, M.; Kjelstrup, S.; Hansen, A. Stable and efficient time integration at low capillary numbers of a dynamic pore network model for immiscible two-phase flow in porous media. *Front. Phys.* **2018**, *6*, No. 56.
(7) Gjennestad, M. Aa.; Winkler, M.; Hansen, A. Pore network modeling of the effects of viscosity ratio and pressure gradient on steady-state incompressible two-phase flow in porous media. *Transp. Porous Media* **2020**, *132*, 355−379.
(8) Spernjak, D.; Prasad, A. K.; Advani, S. G. Experimental investigation of liquid water formation and transport in a transparent single-serpentine PEM fuel cell. *J. Power Sources* **2007**, *170*, 334−344.
(9) Thickett, S. C.; Neto, C.; Harris, A. T. Biomimetic surface coatings for atmospheric water capture prepared by dewetting of polymer films. *Adv. Mater.* **2011**, *23*, 3718−3722.
(10) Xiao, R.; Maroo, S. C.; Wang, E. N. Negative pressures in nanoporous membranes for thin film evaporation. *Appl. Phys. Lett.* **2013**, *102*, No. 123103.
(11) Zhao, J.-J.; Duan, Y.-Y.; Wang, X.-D.; Wang, B.-W. Effects of superheat and temperature-dependent thermophysical properties on evaporating thin liquid films in microchannels. *Int. J. Heat Mass Transfer* **2011**, *54*, 1259−1267.
(12) Ju, Y. S.; Kaviany, M.; Nam, Y.; Sharratt, S.; Hwang, G. S.; Catton, I.; Fleming, E.; Dussinger, P. Planar vapor chamber with hybrid evaporator wicks for the thermal management of high-heat-flux and high-power optoelectronic devices. *Int. J. Heat Mass Transfer* **2013**, *60*, 163−169.
(13) Kandlikar, S. G. Fundamental issues related to flow boiling in minichannels and microchannels. *Exp. Therm. Fluid Sci.* **2002**, *26*, 389−407.
(14) Setu, S. A.; Dullens, R. P. A.; Hernández-Machado, A.; Pagonabarraga, I.; Aarts, D. G. A. L.; Ledesma-Aguilar, R. Super-confinement tailors fluid flow at micro-scales. *Nat. Commun.* **2015**, *6*, No. 7297.
(15) McGraw, J. D.; Bäumchen, O.; Klos, M.; Haefner, S.; Lessel, M.; Backes, S.; Jacobs, K. Nanofluidics of thin polymer films: Linking the slip boundary condition at solidliquid interfaces to macroscopic pattern formation and microscopic interfacial properties. *Adv. Colloid Interface Sci.* **2014**, *210*, 13−20.
(16) Snustad, I.; Røe, I. T.; Brunsvold, A.; Ervik, A.; He, J.; Zhang, Z. A review on wetting and water condensation - Perspectives for CO_2 condensation. *Adv. Colloid Interface Sci.* **2018**, *256*, 291−304.
(17) Reiter, G. Dewetting of thin polymer films. *Phys. Rev. Lett.* **1992**, *68*, 75.
(18) Mukherjee, R.; Sharma, A. Instability, self-organization and pattern formation in thin soft films. *Soft Matter* **2015**, *11*, 8717−8740.
(19) Bhandaru, N.; Das, A.; Mukherjee, R. Confinement induced ordering in dewetting of ultra-thin polymer bilayers on nanopatterned substrates. *Nanoscale* **2016**, *8*, 1073−1087.
(20) Dörfler, F.; Rauscher, M.; Dietrich, S. Stability of thin liquid films and sessile droplets under confinement. *Phys. Rev. E* **2013**, *88*, No. 012402.
(21) MacDowell, L. G.; Shen, V. K.; Errington, J. R. Nucleation and cavitation of spherical, cylindrical, and slablike droplets and bubbles in small systems. *J. Chem. Phys.* **2006**, *125*, No. 034705.
(22) Wilhelmsen, Ø.; Bedeaux, D.; Kjelstrup, S.; Reguera, D. Communication: Superstabilization of fluids in nanocontainer. *J. Chem. Phys.* **2014**, *141*, No. 071103.
(23) Wilhelmsen, Ø.; Reguera, D. Evaluation of finite-size effects in cavitation and droplet formation. *J. Chem. Phys.* **2015**, *142*, No. 064703.
(24) Yang, A. J.-M. The thermodynamical stability of the heterogeneous system with a spherical interface. *J. Chem. Phys.* **1985**, *82*, 2082−2085.
(25) Gjennestad, M. Aa.; Wilhelmsen, Ø. Thermodynamic stability of droplets, bubbles and thick films in open and closed pores. *Fluid Phase Equilib.* **2020**, *505*, No. 112351.
(26) Neimark, A. V.; Kornev, K. G. Classification of equilibrium configurations of wetting films on planar substrates. *Langmuir* **2000**, *16*, 5526−5529.
(27) Neimark, A. V. Thermodynamic equilibrium and stability of liquid films and droplets on fibers. *J. Adhes. Sci. Technol.* **1999**, *13*, 1137−1154.
(28) MacDowell, L. G. Computer simulation of interface potentials: Towards a first principle description of complex interfaces. *Eur. Phys. J.: Spec. Top.* **2011**, *197*, 131−145.
(29) MacDowell, L. G.; Benet, J.; Katcho, N. A. Capillary fluctuations and film-height-dependent surface tension of an adsorbed liquid film. *Phys. Rev. Lett.* **2013**, *111*, No. 047802.
(30) Pahlavan, A. A.; Cueto-Felgueroso, L.; Hosoi, A. E.; McKinley, G. H.; Juanes, R. Thin films in partial wetting: Stability, dewetting and coarsening. *J. Fluid Mech.* **2018**, *845*, 642−681.
(31) Kheshgi, H. S.; Scriven, L. Dewetting: Nucleation and growth of dry regions. *Chem. Eng. Sci.* **1991**, *46*, 519−526.
(32) Ruckenstein, E.; Jain, R. K. Spontaneous rupture of thin liquid films. *J. Chem. Soc., Faraday Trans. 2* **1974**, *70*, 132−147.
(33) Silin, D.; Virnovsky, G. A variational model of disjoining pressure: Liquid film on a nonplanar surface. *Transp. Porous Media* **2010**, *82*, 485−505.
(34) Sharma, A. Equilibrium and dynamics of evaporating or condensing thin fluid domains: Thin film stability and heterogeneous nucleation. *Langmuir* **1998**, *14*, 4915−4928.
(35) Berg, J. C. *An Introduction to Interfaces & Colloids: The Bridge to Nanoscience*; World Scientific, 2010.
(36) Callen, H. B. *Thermodynamics and an Introduction to Thermostatistics*, 2nd ed.; John Wiley & Sons, 1985.
(37) Vrij, A. Possible mechanism for the spontaneous rupture of thin, free liquid films. *Discuss. Faraday Soc.* **1966**, *42*, 23−33.
(38) MacDowell, L. G.; Benet, J.; Katcho, N. A.; Palanco, J. M. Disjoining pressure and the film-height-dependent surface tension of thin liquid films: New insight from capillary wave fluctuations. *Adv. Colloid Interface Sci.* **2014**, *206*, 150−171.
(39) Boinovich, L. DLVO forces in thin liquid films beyond the conventional DLVO theory. *Curr. Opin. Colloid Interface Sci.* **2010**, *15*, 297−302.
(40) Thiele, U.; Mertig, M.; Pompe, W. Dewetting of an evaporating thin liquid film: Heterogeneous nucleation and surface instability. *Phys. Rev. Lett.* **1998**, *80*, 2869.
(41) Emelyanenko, K. A.; Emelyanenko, A. M.; Boinovich, L. B. Van der waals forces in free and wetting liquid films. *Adv. Colloid Interface Sci.* **2019**, 357−369.
(42) Kontogeorgis, G. M.; Voutsas, E. C.; Yakoumis, I. V.; Tassios, D. P. An equation of state for associating fluids. *Ind. Eng. Chem. Res.* **1996**, *35*, 4310−4318.

(43) Wilhelmsen, Ø.; Aasen, A.; Skaugen, G.; Aursand, P.; Austegard, A.; Aursand, E.; Gjennestad, M. Aa.; Lund, H.; Linga, G.; Hammer, M. Thermodynamic modeling with equations of state: present challenges with established methods. *Ind. Eng. Chem. Res.* **2017**, *56*, 3503−3515.
(44) Troutman, J. L. *Variational Calculus and Optimal Control*, 2nd ed.; Springer, 1996.
(45) Michelsen, M. L.; Mollerup, J. M. *Thermodynamic Models: Fundamentals & Computational Aspects*, 2nd ed.; Tie-Line Publications, 2007.
(46) Aursand, P.; Gjennestad, M. Aa.; Aursand, E.; Hammer, M.; Wilhelmsen, Ø. The spinodal of single-and multi-component fluids and its role in the development of modern equations of state. *Fluid Phase Equilib.* **2017**, *436*, 98−112.
(47) Kierzenka, J.; Shampine, L. F. A BVP solver based on residual control and the Maltab PSE. *ACM Trans. Math. Software (TOMS)* **2001**, *27*, 299−316.
(48) Jones, E.; Oliphant, T.; Peterson, P. et al. SciPy: Open source scientific tools for Python, 2001. http://www.scipy.org/.
(49) Anderson, E.; Bai, Z.; Bischof, C.; Blackford, S.; Demmel, J.; Dongarra, J.; Du Croz, J.; Greenbaum, A.; Hammarling, S.; McKenney, A.; Sorensen, D. *LAPACK Users' Guide*, 3rd ed.; Society for Industrial and Applied Mathematics: Philadelphia, PA, 1999.

https://dx.doi.org/10.1021/acs.langmuir.0c00960
Langmuir 2020, 36, 7879−7893

Paper IV

M. Aa. Gjennestad, M. Vassvik, S. Kjelstrup, and A. Hansen. Stable and efficient time integration at low capillary numbers of a dynamic pore network model for immiscible two-phase flow in porous media. *Frontiers in Physics* 6 (2018), p. 56. DOI: 10.3389/fphy.2018.00056

frontiers in Physics

ORIGINAL RESEARCH
published: 13 June 2018
doi: 10.3389/fphy.2018.00056

Stable and Efficient Time Integration of a Dynamic Pore Network Model for Two-Phase Flow in Porous Media

Magnus Aa. Gjennestad[1]*, *Morten Vassvik*[1], *Signe Kjelstrup*[2] *and Alex Hansen*[1]

[1] PoreLab, Department of Physics, Norwegian University of Science and Technology, Trondheim, Norway, [2] PoreLab, Department of Chemistry, Norwegian University of Science and Technology, Trondheim, Norway

We study three different time integration methods for a dynamic pore network model for immiscible two-phase flow in porous media. Considered are two explicit methods, the forward Euler and midpoint methods, and a new semi-implicit method developed herein. The explicit methods are known to suffer from numerical instabilities at low capillary numbers. A new time-step criterion is suggested in order to stabilize them. Numerical experiments, including a Haines jump case, are performed and these demonstrate that stabilization is achieved. Further, the results from the Haines jump case are consistent with experimental observations. A performance analysis reveals that the semi-implicit method is able to perform stable simulations with much less computational effort than the explicit methods at low capillary numbers. The relative benefit of using the semi-implicit method increases with decreasing capillary number Ca, and at Ca $\sim 10^{-8}$ the computational time needed is reduced by three orders of magnitude. This increased efficiency enables simulations in the low-capillary number regime that are unfeasible with explicit methods and the range of capillary numbers for which the pore network model is a tractable modeling alternative is thus greatly extended by the semi-implicit method.

Keywords: porous media, two-phase flow, pore network model, numerical methods, time integration, stability, low capillary number

OPEN ACCESS

Edited by:
Romain Teyssier,
Universität Zürich, Switzerland

Reviewed by:
Daniele Chiappini,
Università degli Studi Niccolò Cusano, Italy
Christian F. Klingenberg,
Universität Würzburg, Germany

***Correspondence:**
Magnus Aa. Gjennestad
magnus@aashammer.net

Specialty section:
This article was submitted to Computational Physics, a section of the journal Frontiers in Physics

Received: *19 January 2018*
Accepted: *17 May 2018*
Published: *13 June 2018*

Citation:
Gjennestad MA, Vassvik M, Kjelstrup S and Hansen A (2018) Stable and Efficient Time Integration of a Dynamic Pore Network Model for Two-Phase Flow in Porous Media. Front. Phys. 6:56. doi: 10.3389/fphy.2018.00056

1. INTRODUCTION

Different modeling approaches have been applied in order to increase understanding of immiscible two-phase flow in porous media. On the pore scale, direct numerical simulation approaches using e.g. the volume of fluid method [1] or the level-set method [2, 3] to keep track of the fluid interface locations, have been used. The lattice-Boltzmann method is another popular choice, see e.g. Ramstad et al. [4]. These methods can provide detailed information on the flow in each pore. They are, however, computationally intensive and this restricts their use to relatively small systems.

Pore network models have proven to be useful in order to reduce the computational cost [5], or enable the study of larger systems, while still retaining some pore-level detail. In these models, the pore space is partitioned into volume elements that are typically the size of a single pore or throat. The average flow properties in these elements are then considered, without taking into account the variation in flow properties within each element.

Pore network models are typically classified as either quasi-static or dynamic. The quasi-static models are intended for situations where flow rates are low, and viscous pressure drops are

neglected on the grounds that capillary forces are assumed to dominate at all times. In the quasi-static models by Lenormand et al. [6], Willemsen [7], and Blunt [8], the displacement of one fluid by the other proceeds by the filling of one pore at the time, and the sequence of pore filling is determined by the capillary entry pressure alone.

The dynamic models, on the other hand, account for the viscous pressure drops and thus capture the interaction between viscous and capillary forces. As three examples of such models, we mention those by Hammond and Unsal [5], Joekar-Niasar et al. [9], and Aker et al. [10]. A thorough review of dynamic pore network models was performed by Joekar-Niasar and Hassanizadeh [11].

The pore network model we consider here is of the dynamic type that was first presented by Aker et al. [10]. Since the first model was introduced, it has been improved upon several times. Notably, it was extended to include film and corner flow by Tørå et al. [12]. The model considered here does not contain this extension. This class of models, which we call the Aker-type models, is different from the majority of other pore network models [5, 9] in that both the pore body and pore throat volumes are assigned to the links, and no volume is assigned to the nodes. Fluid interface locations are tracked explicitly as they move continuously through the pore space. This is in contrast to the model by Hammond and Unsal [5], where interfaces are moved through whole volume elements at each time step, and to the model of Joekar-Niasar et al. [9], where interface locations are only implicitly available through the volume element saturation. One of the advantages of the Aker-type model is that a detailed picture of the fluid configuration is provided at any time during a simulation. Dynamic phenomena, such as the retraction of the invasion front after a Haines jump [13–16], are thus easily resolved.

Since 1985, numerical instabilities at low capillary numbers have been known to occur for various types of dynamic pore network models [17]. A whole section is devoted to the topic in the review by Joekar-Niasar and Hassanizadeh [11]. It is important to address such stability problems rigorously, as many of the practical applications of two-phase porous media flow are in the low capillary number regime. Examples include most parts of the reservoir rock during CO_2 sequestration, flow of liquid water in fuel cell gas diffusion layers and studies of Haines jump dynamics, see e.g. Armstrong and Berg [15].

When Aker-type pore network models are used, the numerical instabilities are observed as oscillations in the positions of the fluid interfaces. Some efforts to avoid these oscillations have been made by introduction of modifications to the model. Medici and Allen [18] used a scheme where water was allowed to flow in the forward direction only in order to study water invasion in fuel cell gas diffusion layers. While this approach led to interesting results, it has some downsides. First, the interface movement is artificially restricted, and certain dynamic effects can not be resolved. This includes e.g. invasion front retraction after a Haines jump. Second, the method can only be used in cases with transient invasion. Studies of steady-state flow, such as those performed by Knudsen et al. [21] and Savani et al. [19], are not possible.

Because the oscillations originate in the numerical methods, rigorous attempts to remove them should focus on these methods rather than the models themselves. Joekar-Niasar et al. [9] followed this avenue and achieved stabilization using a linearized semi-implicit method. Their work, however, concerned a different type of pore network model than that considered here.

In this work, we present three numerical methods that can be utilized to perform stable simulations of two-phase flow in porous media with pore network models of the Aker type. The stability problems previously observed are thus solved without the need to resort to model modifications that restrict interface movement or preclude steady-state flow simulations. Two explicit methods are discussed, the forward Euler method and the midpoint method. These are stabilized by a new time step criterion derived herein. The third method is a new semi-implicit method. Thorough verifications of all methods are performed, confirming correct convergence properties and stability. Finally, we compare the methods in terms of performance.

The rest of this paper is structured as follows. Section 2 contains background information on the pore network model. Section 3 presents briefly the nomenclature, used in subsequent sections to describe the time integration methods. In section 4, we recapitulate how the forward Euler method is used to integrate the model and we present a new time step criterion that stabilizes both forward Euler and the midpoint method at low capillary numbers. We briefly review the midpoint method in section 5. The new semi-implicit method is described in detail in section 6. Some remarks about the numerical implementation are made in section 7. Section 8 contains a description of the cases simulated. Numerical experiments, including a Haines jump case, that show convergence and stability are given in section 9 and a comparison of the method performances are made in section 10. Section 11 summarizes and concludes the paper.

2. PORE NETWORK MODEL

We consider incompressible flow of two immiscible fluids in a porous medium, where one fluid is more wetting toward the pore walls than the other. We call the less wetting fluid non-wetting (n) and the more wetting fluid we call wetting (w). The porous medium is represented in the model by a network of N nodes connected by M links. Each node is given an index $i \in [0, N-1]$, and each link is identified by the indices of the two nodes it connects. An example pore network is shown in **Figure 1**. The nodes are points that have no volume and, consequently, all fluid is contained in the links. The links therefore represent both the pore and the throat volumes of the physical porous medium. In this respect, the pore network model studied here differ from most other pore network models [11]. Each fluid is assumed to fill

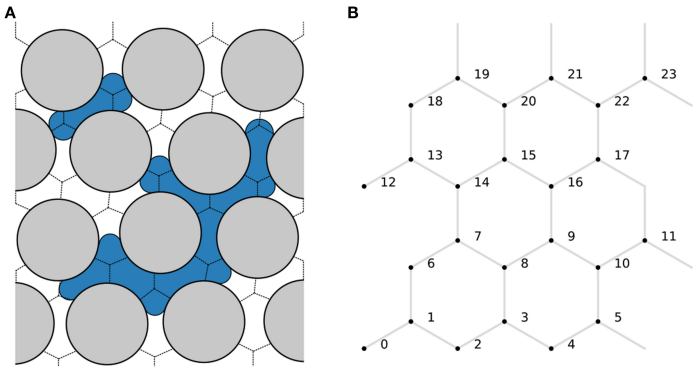

FIGURE 1 | Illustration of **(A)** a physical pore network with wetting (white) and non-wetting fluid (blue) and **(B)** its representation in the pore network model. The void space volumes separated by dashed lines in **(A)** are each represented as one link in **(B)**. The node points in the model representation **(B)** is assumed to be located at the intersection points of the dashed lines in **(A)**. Each fluid is assumed to fill the entire link cross section. The interface positions are therefore each represented in the model by a single number, giving its location along the link length.

the entire link cross section. The interface positions are therefore each represented in the model by a single number, giving its location along the link length.

The flow in each link is treated in a one-dimensional manner, where the flow is averaged over the link cross section. As we consider flow in relatively small cross sections only, we neglect any inertial effects and the volume flow rate ($m^3\ s^{-1}$) from node j to node i through the link connecting then is given by Washburn [20]

$$q_{ij} = -g_{ij}\left(\mathbf{z}_{ij}\right)\left\{p_i - p_j - c_{ij}\left(\mathbf{z}_{ij}\right)\right\}. \tag{1}$$

Herein, p_i (Pa) is the pressure in node i, g_{ij} ($m^3\ s^{-1}\ Pa^{-1}$) is the link mobility, c_{ij} (Pa) is the link capillary pressure and $\mathbf{z}_{ij}$ (m) is a vector containing the positions of any fluid interfaces present in the link. Both the link mobility and the capillary pressure depend on the fluid interface positions in the link. If two nodes i and j are *not* connected by a link, then $g_{ij} = 0$. Due to mass conservation, the net flow rate into every node i is zero

$$\sum_j q_{ij} = 0. \tag{2}$$

While the mobilities are symmetric with respect to permutation of the indices, the capillary pressures are anti-symmetric,

$$g_{ij} = g_{ji}, \tag{3}$$
$$c_{ij} = -c_{ji}. \tag{4}$$

Introducing this into Equation (1), we obtain the immediately intuitive result

$$q_{ij} = -q_{ji}. \tag{5}$$

The cross-sectional area of link ij is denoted a_{ij} (m^2). Interface positions are advected with the flow according to

$$\frac{\mathrm{d}}{\mathrm{d}t}\mathbf{z}_{ij} = \frac{q_{ij}}{a_{ij}}, \tag{6}$$

when they are sufficiently far away from the nodes. Near the nodes, however, the interfaces are subject to additional modeling to account for interface interactions in the pores. This is discussed further in section 2.3.

The form of the expressions for the mobilities and capillary pressures depends on the shape of the links, and many different choices and modeling approaches are possible. Here, we will use models similar to those previously presented and used by e.g. Knudsen et al. [21] and Aker et al. [10]. However, the treated time integration methods are more general and can be applied to other models as well.

2.1. Link Mobility Model

We apply a cylindrical link model when computing the mobilities, so that

$$g_{ij}(\mathbf{z}_{ij}) = \frac{\pi r_{ij}^4}{8 L_{ij}\mu_{ij}\left(\mathbf{z}_{ij}\right)}. \tag{7}$$

Here, r_{ij} (m) is the link radius and L_{ij} (m) is the link length. The viscosity μ_{ij} (Pa s) is the volume-weighted average of the fluid viscosities and can be computed from the wetting and non-wetting fluid viscosities μ_w and μ_n and the wetting fluid saturation s_{ij},

$$\mu_{ij}\left(\mathbf{z}_{ij}\right) = \mu_w s_{ij}\left(\mathbf{z}_{ij}\right) + \mu_n\left\{1 - s_{ij}\left(\mathbf{z}_{ij}\right)\right\}. \tag{8}$$

2.2. Capillary Pressure Model

In each link ij, there may be zero, one or more interfaces present. These are located at the positions specified in $\mathbf{z}_{ij}$. As the interfaces may be curved, there may be a discontinuity in pressure at these interface locations. The capillary pressure c_{ij} is the sum of interfacial pressure discontinuities in the link ij. When computing the capillary pressures, we assume that the links are wide near each end, and therefore that interfaces located near a link end have negligible curvature and no pressure discontinuity, while the links have narrow throats in the middle. The link capillary pressures are thus modeled as

$$c_{ij}\left(\mathbf{z}_{ij}\right) = \frac{2\sigma_{\mathrm{wn}}}{r_{ij}} \sum_{z \in \mathbf{z}_{ij}} (\pm 1)\left\{1 - \cos\left(2\pi\,\chi_{ij}\left(z\right)\right)\right\}. \tag{9}$$

The interfacial tension between the fluids is denoted σ_{wn} (N m^{-1}) and

$$\chi_{ij}\left(z\right) = \begin{cases} 0 & z < \alpha r_{ij}, \\ \frac{z - \alpha r_{ij}}{L_{ij} - 2\alpha r_{ij}} & \alpha r_{ij} < z < L_{ij} - \alpha r_{ij}, \\ 1 & z > L_{ij} - \alpha r_{ij}. \end{cases} \tag{10}$$

The χ_{ij}-function ensures zones of length αr_{ij} at both ends of each link with zero capillary pressure across any interface located there. Choosing $\alpha = 0$ is equivalent to replacing χ_{ij} with z/L_{ij} in (9).

2.3. Fluid Interface Interaction Models

The equations discussed so far in this section describe how the fluids and the fluid interfaces move through the links. In addition, we rely on models for how they behave close to the nodes. The purpose of these are to emulate interface interactions in the pore spaces.

The following is assumed about the fluid behavior near the nodes and is accounted for by the fluid interface interaction models.

- The mass of each fluid is conserved at every node. This means that at all times, all wetting and non-wetting fluid flowing into a node from one subset of its neighboring links must flow out into another disjoint subset of its neighboring links.
- The network nodes in the model have no volume. However, due to the finite size of the physical pore void spaces, wetting fluid flowing into a pore space must be able to flow freely past any non-wetting fluid occupying the node point if the non-wetting fluid does not extend far enough into the pore void space cut the wetting fluid off. An example is illustrated in **Figure 2**. We consider a link ij to be cut off from free outflow of wetting fluid if the non-wetting fluid continuously extends a length at least αr_{ij} into the link. Non-wetting fluid may freely flow past wetting fluid, or not, the same manner.
- In each link ij, interfacial tension will prevent droplets with length smaller than αr_{ij} from forming by separation from larger droplets. An example is illustrated in **Figure 3**.

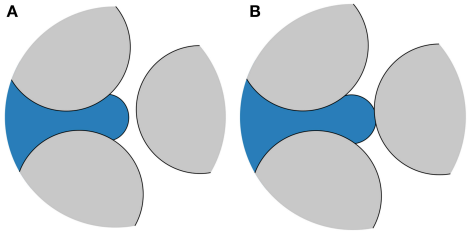

FIGURE 2 | Network node connected to three links. The node point, located near the middle of the pore space, is occupied by non-wetting fluid (blue). **(A)** The non-wetting fluid extends only a short distance into the links containing wetting fluid (white). The wetting fluid therefore remains connected and may flow freely through the pore space. **(B)** Non-wetting fluid protrudes far enough into all links to block the pore space for wetting fluid. The wetting fluid must now displace the non-wetting fluid in order to flow through.

2.4. Boundary Conditions

We consider only networks where the nodes and links can be laid out in the two-dimensional x-y plane. These networks will be periodic in both the x- and y-direction. However, the model is also applicable to networks that extend in three dimensions [22], and the presented numerical methods are also compatible both with networks in three dimensions and with other, non-periodic boundary conditions [23].

We will here apply two types of boundary conditions to the flow. With the first type, a specified pressure difference ΔP (Pa) will be applied across the network in the y-direction. This pressure difference will be equal to the sum of all link pressure differences in any path spanning the network once in the y-direction, ending up in the same node as it started. With the other type of boundary condition, we specify a total flow rate Q (m^3 s^{-1}) across the network. This flow rate will be equal to the sum of link flow rates flowing through any plane drawn through the network normal to the y-axis.

3. TEMPORAL DISCRETIZATION

In the following three sections, we describe the different time integration methods considered. These methods are applied to Equation (6), where evaluation of the right hand side involves simultaneously solving the mass conservation equation (2) and the constitutive equation (1) to obtain all unknown link flow rates and node pressures.

The discretized times (s) are denoted with a superscript where n is the time step number,

$$t^{(n)} = t^{(0)} + \sum_{i=0}^{n-1} \Delta t^{(i)}. \tag{11}$$

The time step $\Delta t^{(i)}$ is the difference between $t^{(i+1)}$ and $t^{(i)}$ and the time $t^{(0)}$ is the initial time in a simulation. Similarly,

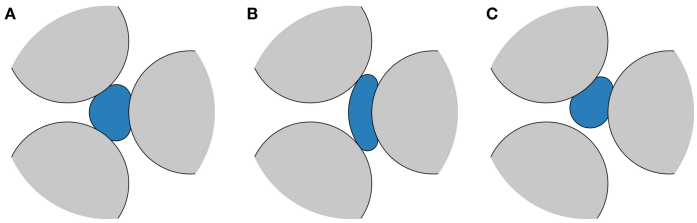

FIGURE 3 | (A) Small non-wetting bubble (blue) whose volume is small compared to the link volumes and is prevented from splitting by interfacial tension. This limits the minimum size of non-wetting bubbles, which will either **(B)** be stuck or **(C)** move through one of the links without splitting.

quantities evaluated at the discrete times are denoted with time step superscripts, e.g.

$$q_{ij}^{(n)} = q_{ij}\left(t^{(n)}\right). \tag{12}$$

Mobilities and capillary pressures with superscripts are evaluated using the interface positions at the indicated time step,

$$g_{ij}^{(n)} = g_{ij}\left(\mathbf{z}_{ij}^{(n)}\right), \tag{13}$$

$$c_{ij}^{(n)} = c_{ij}\left(\mathbf{z}_{ij}^{(n)}\right). \tag{14}$$

4. FORWARD EULER METHOD

The forward Euler method is the simplest of the time integration methods considered here and is the one used most frequently in previous works, see e.g. Knudsen et al. [21] and Sinha and Hansen [24]. We include its description here for completeness and to provide context for the proposed new capillary time step criterion that is introduced to stabilize the method at low capillary numbers.

The ordinary differential equation (ODE) (6) is discretized in a straightforward manner for each link *ij* using forward Euler,

$$\mathbf{z}_{ij}^{(n+1)} = \mathbf{z}_{ij}^{(n)} + \Delta t^{(n)} \frac{q_{ij}^{(n)}}{a_{ij}}. \tag{15}$$

The flow rates are calculated by inserting Equation (1), evaluated with the current known interface positions,

$$q_{ij}^{(n)} = -g_{ij}^{(n)}\left\{p_i^{(n)} - p_j^{(n)} - c_{ij}^{(n)}\right\}, \tag{16}$$

into the mass conservation equation (2). This results in the a system of linear equations consisting of one equation,

$$\sum_j g_{ij}^{(n)} p_j^{(n)} - p_i^{(n)} \sum_j g_{ij}^{(n)} = -\sum_j g_{ij}^{(n)} c_{ij}^{(n)}, \tag{17}$$

for each node *i* with unknown pressure. This linear system can be cast into matrix form,

$$\mathbf{A} \cdot \mathbf{x} = \mathbf{b}, \tag{18}$$

where the vector $\mathbf{x}$ contains the unknown node pressures, e.g.

$$\mathbf{x} = \begin{bmatrix} p_0^{(n)} \\ p_1^{(n)} \\ \vdots \\ p_{N-1}^{(n)} \end{bmatrix}. \tag{19}$$

The matrix elements are

$$A_{ij} = \left\{1 - \delta_{ij}\right\} g_{ij}^{(n)} - \delta_{ij} \sum_k g_{ik}^{(n)}, \tag{20}$$

and the elements of the constant vector are

$$b_i = -\sum_k g_{ik}^{(n)} c_{ik}^{(n)}. \tag{21}$$

The node pressures are obtained by solving this linear equation system. The flow rates are subsequently evaluated using Equation (16) and the interface positions are then updated using Equation (15) and the interface interaction models.

4.1. Time Step Restrictions

In previous works [10, 21], the time step length was chosen from a purely advective criterion,

$$\Delta t_{\mathrm{a}}^{(n)} = C_{\mathrm{a}} \min_{ij}\left(\frac{a_{ij} L_{ij}}{q_{ij}^{(n)}}\right). \tag{22}$$

The parameter C_{a} corresponds to the maximum fraction of a link length any fluid interface is allowed to move in a single forward Euler time step. The value of C_{a} must be chosen based on the level of accuracy desired from the simulation.

However, selecting the time step based on the advective criterion only, often results in numerical instabilities at low capillary numbers, where viscous forces are small relative to the capillary forces. This is demonstrated in section 9.2. The origins of the numerical instabilities can be identified by performing analysis on a linearized version of the governing equations. This is done in Appendix A. This analysis also leads to a new time step criterion, whereby the time step length is restricted by the

sensitivity of the capillary forces to perturbations in the current interface positions,

$$\Delta t_{\mathrm{c}}^{(n)} = C_{\mathrm{c}} \min_{ij} \left(\frac{2a_{ij}}{g_{ij}^{(n)} \left| \sum_{z \in \mathbf{z}_{ij}^{(n)}} \frac{\partial c_{ij}}{\partial z} \right|} \right). \tag{23}$$

For the particular choice of capillary pressure model given by (9), we obtain

$$\Delta t_{\mathrm{c}}^{(n)} = C_{\mathrm{c}} \min_{ij} \left(\frac{a_{ij} r_{ij} L_{ij}}{2\pi g_{ij}^{(n)} \sigma_{\mathrm{wn}} \left| \sum_{z \in \mathbf{z}_{ij}^{(n)}} (\pm 1) \sin\left(2\pi \chi_{ij}(z)\right) \frac{\mathrm{d}\chi_{ij}}{\mathrm{d}z} \right|} \right). \tag{24}$$

According to the linear analysis, numerical instabilities are avoided if the parameter C_{c} is chosen such that $0 < C_{\mathrm{c}} < 1$. However, we must regard (23) as an approximation when we apply it to the full non-linear model in simulations and, consequently, we may have to chose C_{c} conservatively to ensure stability for all cases.

At each step in the simulation, the time step used is then taken as

$$\Delta t^{(n)} = \min\left(\Delta t_{\mathrm{c}}^{(n)}, \Delta t_{\mathrm{a}}^{(n)} \right), \tag{25}$$

to comply with both the advective and the capillary time step criteria. The capillary time step restriction (23) is independent of flow rate. It therefore becomes quite severe, demanding relatively fine time steps, when flow rates are low.

4.2. Boundary Conditions

The periodic boundary conditions, specifying a total pressure difference ΔP across the network, can be incorporated directly into the linear equation system (18). For each node i, a term $g_{ij}^{(n)} \Delta P$ is added to or subtracted from b_i for any link ij that crosses the periodic boundary.

With the specified ΔP condition implemented, we can use it to obtain the node pressures and link flow rates corresponding to a specified total flow rate Q. Due to the linear nature of the model, the total flow rate is linear in ΔP [10], so that

$$Q = C_1 \Delta P + C_2, \tag{26}$$

for some unknown coefficients C_1 and C_2, that are particular to the current fluid configuration.

We choose two different, but otherwise arbitrary, pressure drop values ΔP_1 and ΔP_2 and, using the above procedure, we solve the network model once for each pressure difference and calculate the corresponding total flow rates Q_1 and Q_2. The coefficients C_1 and C_2 are then determined by,

$$C_1 = \frac{Q_2 - Q_1}{\Delta P_2 - \Delta P_1}, \tag{27}$$

$$C_2 = \frac{Q_2 \Delta P_1 - Q_1 \Delta P_2}{\Delta P_1 - \Delta P_2}. \tag{28}$$

The pressure difference ΔP required to obtain the specified flow rate Q is determined by solving Equation (26) for ΔP. Subsequently, the network model is solved a third time with pressure drop ΔP to obtain the desired node pressures and link flow rates.

5. MIDPOINT METHOD

The forward Euler method is first-order accurate in time. To obtain smaller numerical errors, methods of higher order are desirable. We therefore include in our discussion the second-order midpoint method. This method is identical to that used by Aker et al. [10], except with respect to choice of time step length.

The ODE (6) is discretized as

$$\mathbf{z}_{ij}^{(n+1)} = \mathbf{z}_{ij}^{(n)} + \Delta t^{(n)} \frac{q_{ij}^{(n+1/2)}}{a_{ij}}, \tag{29}$$

where $q_{ij}^{(n+1/2)}$ is the flow rate at the midpoint in time between point n and $n+1$. This flow rate is calculated in the same manner as described in section 4. The interface positions at $n + 1/2$ are obtained by taking a forward Euler step with half the length of the whole time step,

$$\mathbf{z}_{ij}^{(n+1/2)} = \mathbf{z}_{ij}^{(n)} + \frac{1}{2} \Delta t^{(n)} \frac{q_{ij}^{(n)}}{a_{ij}}. \tag{30}$$

5.1. Time Step Restrictions

Since the forward Euler stability region is contained within the stability region for the midpoint method, we use the same time step restrictions for the midpoint method as for forward Euler, see section 4.1.

5.2. Boundary Conditions

Both the specified ΔP and the specified Q boundary conditions are incorporated into the midpoint method by applying the procedures described in section 4.2 for each evaluation of the right hand side of Equation (6).

6. SEMI-IMPLICIT METHOD

To avoid both the numerical instabilities and the time step restriction (23), which becomes quite severe at low flow rates, we here develop a new semi-implicit time stepping method. Simulation results indicate that this method is stable with time steps determined by the advective criterion (22) only, and much longer time steps are therefore possible than with the forward Euler and midpoint methods at low capillary numbers.

The ODE (6) is now discretized according to

$$\mathbf{z}_{ij}^{(n+1)} = \mathbf{z}_{ij}^{(n)} + \Delta t^{(n)} \frac{q_{ij}^{(n+1)}}{a_{ij}}. \tag{31}$$

The semi-implicit nature of this discretization comes from the flow rate used,

$$q_{ij}^{(n+1)} = -g_{ij}^{(n)} \left\{ p_i^{(n+1)} - p_j^{(n+1)} - c_{ij}^{(n+1)} \right\}. \tag{32}$$

Herein, the link mobility is evaluated at time step n, while the node pressures and the capillary pressure are evaluated time step $n+1$.

The link mobilities could of course also have been evaluated at time step $n+1$, thus creating a fully implicit backward Euler scheme. As is shown in Appendix A, we may expect backward Euler to be stable with any positive $\Delta t^{(n)}$. The backward Euler scheme may therefore seem like a natural choice for performing stable simulations with long time steps. However, to evaluate the mobilities at time step $n+1$ complicates the integration procedure and was found to be unnecessary in practice. A semi-implicit alternative is therefore preferred.

To obtain the node pressures, we solve the mass conservation equations,

$$F_i = \sum_k q_{ik}^{(n+1)} = 0. \tag{33}$$

Again, we have one equation for each node i with unknown pressure. However, because the capillary pressures now depend on the flow rates,

$$c_{ij}^{(n+1)} = c_{ij}\left(\mathbf{z}_{ij}^{(n)} + \Delta t^{(n)}\frac{q_{ij}^{(n+1)}}{a_{ij}}\right), \tag{34}$$

the mass conservation equations are now a system of non-linear equations, rather than a system of linear equations. This system can be cast in the form

$$\mathbf{F}(\mathbf{x}) = \mathbf{0}, \tag{35}$$

where $\mathbf{x}$ contains the unknown pressures, e.g.

$$\mathbf{x} = \begin{bmatrix} p_0^{(n+1)} \\ p_1^{(n+1)} \\ \vdots \\ p_{N-1}^{(n+1)} \end{bmatrix}. \tag{36}$$

In order to solve Equation (35) using the numerical method described in section 7, it is necessary to have the Jacobian matrix of $\mathbf{F}$. Details on how the Jacobian matrix is calculated are given in Appendix B.

The calculation of link flow rates from node pressures, and thus every evaluation of $\mathbf{F}$ and its Jacobian, involves solving one non-linear equation for each link flow rate,

$$G_{ij}\left(q_{ij}^{(n+1)}\right) = q_{ij}^{(n+1)} + g_{ij}^{(n)}\left\{p_i^{(n+1)} - p_j^{(n+1)} - c_{ij}^{(n+1)}\right\} = 0. \tag{37}$$

The derivative of G_{ij} with respect to $q_{ij}^{(n+1)}$ is

$$\frac{\mathrm{d}G_{ij}}{\mathrm{d}q_{ij}^{(n+1)}} = 1 - g_{ij}^{(n)}\frac{\mathrm{d}c_{ij}^{(n+1)}}{\mathrm{d}q_{ij}^{(n+1)}}. \tag{38}$$

The procedure for updating the interface positions with the semi-implicit method may be summarized as follows. The non-linear equation system (35) is solved to obtain the unknown node pressures. In every iteration of the solution procedure, the flow rates are evaluated by solving Equation (37) for each link. When a solution to Equation (35) is obtained, the interface positions are updated using Equation (31) and the interface interaction models.

6.1. Time Step Restrictions

We aim to select the time steps such that

$$\Delta t^{(n)} = \Delta t_{\mathrm{a}}^{(n+1)}. \tag{39}$$

However, to solve the non-linear system (35) is challenging in practice and requires initial guess values for the link flow rates and node pressures that lie sufficiently close to the solution. For this purpose, we here use values from the previous time step. This turns out to be a sufficiently good choice for most time steps, but our numerical solution procedure does not always succeed. As the link flow rates and node pressures at two consecutive points in time become increasingly similar as the time interval between them is reduced, we may expect the guess values to lie closer to the solution if we reduce the time step. Thus, if our solution procedure is unable to succeed, our remedy is to shorten $\Delta t^{(n)}$. This will sometimes lead to time steps shorter than $\Delta t_{\mathrm{a}}^{(n+1)}$. If, for a given time step, $\Delta t^{(n)}$ must be reduced to less than twice the time step length allowed by the explicit methods, we revert to forward Euler for that particular step. As we demonstrate in section 10, however, this does not prevent the semi-implicit method from being much more efficient than the explicit methods at low capillary numbers.

6.2. Boundary Conditions

As with the explicit methods, the specified ΔP boundary condition can be incorporated directly into the mass balance equation system, in this case Equation (35). This is done by adding to or subtracting from the right hand sides of Equation (32) and Equation (37) a term $g_{ij}^{(n)}\Delta P$ for each link ij crossing the periodic boundary.

The specified flow rate boundary condition is incorporated by including ΔP as an additional unknown and adding an additional equation

$$F_m = \left\{\sum_{ij\in\Omega} q_{ij}^{(n+1)}\right\} - Q = 0, \tag{40}$$

to the non-linear equation system (35). Herein, Ω is the set of links crossing the periodic boundary, with i being the node on the downstream side and j being the node on the upstream side. Thus, Equation (40) is satisfied when the total flow rate through the network is equal to Q.

7. IMPLEMENTATION

The non-linear equation system (35) is solved using a Newton-type solution method that guarantees convergence to a local

minimum of $\mathbf{F} \cdot \mathbf{F}$, see Press et al. [25, p. 477]. However, a local minimum of $\mathbf{F} \cdot \mathbf{F}$ is not necessarily a solution to Equation (35), and good initial guess values for the node pressures and link flow rates are therefore crucial. For this purpose, we use the values from the previous time step and reduce the length of the current time step if the solution method fails, as discussed in section 6.1.

Solving Equation (37) is done using a standard Newton solver [26]. For robustness, a bisection solver [26] is used if the Newton solver fails.

The Newton-type solver for non-linear systems and the explicit time integration methods require methods for solving linear systems of equations. We use the conjugate gradient method in combination with the LU preconditioner implemented in the PETSc library, see Balay et al. [27]. An introduction to solving systems of Kirchhoff-type equations numerically can be found in Batrouni and Hansen [28].

8. CASE DESCRIPTIONS

In this section, we describe the two simulated cases. One is a test case where a single bubble is contained in a network consisting of links connected in series, while the other is designed to capture a single Haines jump in a small network where fluids flow at a specified rate.

8.1. Links-in-Series Test Case

The verification will include comparison of results from the various numerical methods applied to a test case. The test case is chosen such that it can be set up as a single ODE with a closed expression for the right-hand side. An accurate reference solution can thus be easily obtained using a high-order Runge–Kutta method. As our test case, we consider a network consisting of $M = 3$ identical links connected in series. The network contains a single bubble of length ℓ (m) with center position z (m). In the capillary pressure model, we choose $\alpha = 0$. The ODE (6) can then be restated as an equivalent equation for the bubble position,

$$\frac{\mathrm{d}z}{\mathrm{d}t} = \frac{Q}{a}, \tag{41}$$

where Q is the flow through the network and a is the link cross-sectional area. The model equations can be reduced to the following expression for flow rate.

$$Q = -\frac{g}{M}\left\{\Delta P + \frac{4\sigma_{\mathrm{wn}}}{r}\sin\left(\frac{\pi\ell}{L}\right)\sin\left(\frac{2\pi z}{L}\right)\right\} \tag{42}$$

Here, g is the mobility of a single link, $L = 1.0 \cdot 10^{-3}$ m is the length of a single link and $r = 1.0 \cdot 10^{-4}$ m is the link radius. The bubble has length $\ell = 4.8 \cdot 10^{-4}$ m and is initially located at $z = 2.4 \cdot 10^{-4}$ m. The fluid parameters used in all simulations are given in **Table 1**. The pressure difference ΔP will be stated for each simulation.

8.2. Haines Jump Case

The Haines jump was first reported almost 90 years ago [13]. It refers to the sudden drops in driving pressure observed in drainage experiments when non-wetting fluid breaks through a throat and invades new pores. This process was studied experimentally and numerically by Måløy et al. [16] and, more recently, it was imaged directly and analyzed in detail by Armstrong and Berg [15] for flow in a micromodel and by Berg et al. [14] for flow in a sample of Berea sandstone. The Haines jump case simulated here captures one such break-through and subsequent pressure drop.

TABLE 1 | Fluid properties corresponding to water (w) and decane (n) at atmospheric pressure and 298 K.

Parameter	Value	Unit	References
μ_{w}	$8.9 \cdot 10^{-4}$	Pa s	[29]
μ_{n}	$8.5 \cdot 10^{-4}$	Pa s	[29]
σ_{wn}	$5.2 \cdot 10^{-2}$	$\mathrm{N\,m^{-1}}$	[30]

Among the findings in the study by Måløy et al. [16] was that pore drainage is a non-local event, meaning that as one pore is drained, imbibition occurs in nearby neck regions. This was also observed by Armstrong and Berg [15], and was explained as follows. When the imposed flow rates are low, the non-wetting fluid that fills the newly invaded pores needs to be supplied from nearby locations rather than the external feed. Armstrong and Berg [15] also found, for their range of investigated parameters, that pore drainage occurred on the same time-scale, regardless of the externally imposed flow rate.

We consider a hexagonal network consisting $N = 24$ nodes and $M = 36$ links. All links have length $1.0 \cdot 10^{-3}$ m, while the link radii are drawn randomly from a uniform distribution between 0.1 and 0.4 link lengths. In the capillary pressure model, we choose $\alpha = 1$. The fluid parameters μ_{w}, μ_{n} and σ_{wn} are the same as in the links-in-series test case, see **Table 1**. With these fluid parameters and network length scales, the case mimics the flow of water (w) and decane (n) in a Hele-Shaw cell filled with glass beads similar to those used in e.g. Måløy et al. [16, 31] and Tallakstad et al. [32]. The linear dimensions are ~ 10 times bigger in this network compared to the micromodel of Armstrong and Berg [15]. Initially, the fluids are distributed in the network as shown in **Figure 4**, with the non-wetting fluid in a single connected ganglion.

Simulations are run at different specified flow rates Q until a net fluid volume equivalent to 5% of the total pore volume has flowed through the network. The flow dynamics will, of course, depend upon the specified flow rate. At low flow rates, however, the flow will exhibit some relatively fast fluid redistribution events and one relatively slow pressure build-up and subsequent Haines jump event. The Haines jump will occur as the non-wetting fluid breaks through the link connecting nodes 9 and 16 and invades node 16, see **Figure 4**.

It was mentioned by Armstrong and Berg [15] that the large local flow velocities that they observed as a pore was filled with non-wetting fluid during a Haines jump has implications for how such processes must be numerically simulated. Specifically, the time resolution of the simulation needs to be fine enough during these events to capture them. This poses a challenge when externally applied flow rates are low and there is thus a large difference in the large time

scale that governs the overall flow of the system and the small time scale than governs the local flow during Haines jumps.

9. VERIFICATION

In this section, we verify that the time integration methods presented correctly solve the pore network model equations and that the time step criteria presented give stable solutions.

9.1. Convergence Tests

All time integration methods presented should, of course, give the same solution for vanishingly small time steps. Furthermore, the difference between the solution obtained with a given finite time step and the fully converged solution should decrease as the time steps are refined, and should do so at a rate that is consistent with the order of the method. In this section, we verify that all three time integration methods give solutions that converge to the reference solution for the links-in-series test case and thus that the methods correctly solve the model equations for this case.

We choose the pressure difference to be $\Delta P = -3200\,\text{Pa}$. This value is large enough to overcome the capillary forces and push the non-wetting bubble through the links. We therefore expect a flow rate Q that varies in time, but is always positive.

As measures of the numerical error, we consider both the relative error in the flow rate Q and the relative error in bubble position z between the numerical solutions and reference solutions at the end of the simulation. Time integration is performed from $t = 0\,\text{s}$ to $t = 0.001\,44\,\text{s}$. To have control over the time step lengths, we ignore all time step criteria for now and instead set a constant Δt for each simulation.

In **Figure 5**, flow rates are plotted for each of the time integration methods. Results using a coarse time step, $\Delta t = 4 \cdot 10^{-5}\,\text{s}$, and a fine time step, $\Delta t = 1 \cdot 10^{-5}\,\text{s}$, are shown along with the reference solution.

For the forward Euler and the semi-implicit method, there is considerable discrepancy between the numerical and the reference solution with the coarse time step. The flow rate obtained from forward Euler lags behind the reference solution, while that from the semi-implicit method lies ahead of it. This may be expected, however, since forward Euler at each time step uses current information in the right hand side evaluation, whereas the semi-implicit method uses a combination of current and future information. With the fine time step, there is less difference between the reference and the numerical solutions.

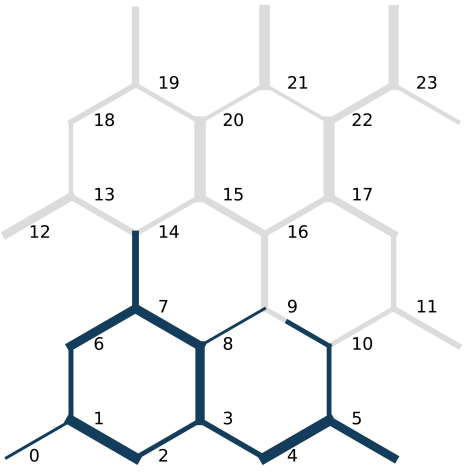

FIGURE 4 | Initial fluid configuration in the Haines jump case. The non-wetting fluid is blue while the wetting fluid is gray. The link radii are not drawn to scale with the link lengths. Node indices are indicated in black.

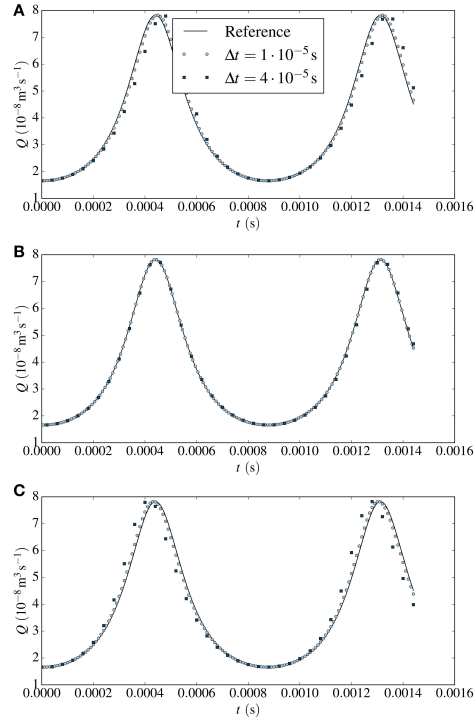

FIGURE 5 | Flow rates Q plotted against time for two different time steps Δt for the links-in-series test case with Δ P = −3200 Pa. Results from the forward Euler method are given in **(A)**, results from the midpoint method in **(B)** and results from the semi-implicit method in **(C)**. The solid line represents the reference solution.

With the more accurate midpoint method, the coarse-stepped numerical solution lies only marginally ahead of the reference solution while there is no difference between the fine-stepped numerical solution and the reference solution at the scale of representation.

The convergence of the numerical solutions to the reference solution upon time step refinement is quantified in **Tables 2–4**. Herein, the numerical errors and estimated convergence orders are given for the forward Euler, midpoint and semi-implicit method, respectively. For all methods considered, the numerical errors decrease when the time step is refined and do so at the rate that is expected. The forward Euler and the semi-implicit method exhibit first-order convergence, while the midpoint method shows second-order convergence. We note that the errors in both z and Q are similar in magnitude for the forward Euler and the semi-implicit method. The errors obtained with the midpoint method are smaller. The difference is one order of magnitude for $\Delta t = 1 \cdot 10^{-5}$ s.

In summary, we have verified that the presented time integration methods correctly solve the pore network model equations for the links-in-series test case and that the numerical errors decrease upon time step refinement at the rate that is consistent with the expected order of the methods.

TABLE 2 | Relative errors in bubble position z and flow rate Q at $t = 0.001\,44$ s and estimated convergence orders for the links-in-series test case computed with the forward Euler method.

Δt (s)	z-error	z-order	Q-error	Q-order
$4 \cdot 10^{-5}$	$1.55 \cdot 10^{-2}$		$1.33 \cdot 10^{-1}$	
$2 \cdot 10^{-5}$	$7.44 \cdot 10^{-3}$	1.06	$6.41 \cdot 10^{-2}$	1.06
$1 \cdot 10^{-5}$	$3.66 \cdot 10^{-3}$	1.02	$3.15 \cdot 10^{-2}$	1.02
$5 \cdot 10^{-5}$	$1.82 \cdot 10^{-3}$	1.01	$1.57 \cdot 10^{-2}$	1.01

TABLE 3 | Relative errors in bubble position z and flow rate Q at $t = 0.001\,44$ s and estimated convergence orders for the links-in-series test case computed with the midpoint method.

Δt (s)	z-error	z-order	Q-error	Q-order
$8 \cdot 10^{-5}$	$1.67 \cdot 10^{-2}$		$1.44 \cdot 10^{-1}$	
$4 \cdot 10^{-5}$	$4.24 \cdot 10^{-3}$	1.98	$3.65 \cdot 10^{-3}$	1.98
$2 \cdot 10^{-5}$	$1.08 \cdot 10^{-3}$	1.97	$9.33 \cdot 10^{-3}$	1.97
$1 \cdot 10^{-5}$	$2.86 \cdot 10^{-4}$	1.92	$2.46 \cdot 10^{-3}$	1.92

TABLE 4 | Relative errors in bubble position z and flow rate Q at $t = 0.001\,44$ s and estimated convergence orders for the links-in-series test case computed with the semi-implicit method.

Δt (s)	z-error	z-order	Q-error	Q-order
$4 \cdot 10^{-5}$	$1.39 \cdot 10^{-2}$		$1.18 \cdot 10^{-1}$	
$2 \cdot 10^{-5}$	$6.98 \cdot 10^{-3}$	0.99	$5.97 \cdot 10^{-2}$	0.98
$1 \cdot 10^{-5}$	$3.51 \cdot 10^{-3}$	0.99	$3.01 \cdot 10^{-2}$	0.99
$5 \cdot 10^{-5}$	$1.76 \cdot 10^{-3}$	1.00	$1.5 \cdot 10^{-2}$	1.00

9.2. Stability Tests

In this section, we demonstrate that the proposed capillary time step criterion (23) stabilizes the forward Euler method and the midpoint method at low flow rates. We simulated two different cases and varied C_c. Simulations run with low C_c turned out to be free of spurious oscillations, indicating that the proposed criterion stabilizes the methods, while simulations run with C_c significantly larger than unity produced oscillations, indicating that the proposed criterion is not unnecessarily strict.

First, consider the links-in-series test case with $\Delta P = 0$ Pa. With no applied pressure difference, the flow is driven purely by the imbalance of capillary forces on the non-wetting bubble. Therefore, there should only be flow initially and the bubble should eventually reach an equilibrium position where both interfaces experience the same capillary force and the flow rate is zero. Simulations were run with $C_a = 0.1$ and C_c equal to 2.0, 1.0, and 0.5. Results from forward Euler are shown in **Figure 6A** and results from the midpoint method are shown in **Figure 6B**. In both figures, the reference solution is also shown.

The forward Euler results are stable and qualitatively similar to the reference solution with $C_c = 0.5$. With $C_c = 1.0$, there are some oscillations initially that are dampened and eventually vanish. From comparison with the reference solution, it is clear that such oscillations have no origin in the model equations and are artifacts of the numerical method. With $C_c = 2.0$, the oscillations are severe and do not appear to be dampened by the method. Instead the non-wetting bubble keeps oscillating around its equilibrium position in a manner that is clearly unphysical.

The results from the midpoint method in **Figure 6B** follow a qualitatively similar trend as those from forward Euler with regard to stability. Results computed with $C_c = 0.5$ are stable and results with $C_c = 2.0$ exhibit severe oscillations. Still, the results from the midpoint method lie much closer to the reference solution than the results from the forward Euler method, as we would expect since the midpoint method is second-order. Both methods are, however, unstable with $C_c = 2.0$, indicating that the while the midpoint method has improved accuracy over forward Euler, it is unable to take significantly longer time steps without introducing oscillations. This is consistent with the analysis in Appendix A, since the two methods have identical stability regions in real space.

Next, consider the Haines jump case with $Q = 10^{-9}\,\mathrm{m^3\,s^{-1}}$, corresponding to $\mathrm{Ca} = 1.2 \cdot 10^{-5}$. This case was run using the forward Euler method, $C_a = 0.1$ and three different values of C_c, equal to 4.0, 2.0, and 1.0. The required pressure difference to drive the flow at the specified rate is shown in **Figure 7A**. **Figure 7B** shows the pressure from **Figure 7A** in greater detail.

For all three values of C_c, the main qualitative features of the flow are captured. We observe short transient pressure drops at $t \approx 0.08$ s and $t \approx 0.20$ s. These correspond to fluid redistribution events on the upstream side of the non-wetting ganglion, where the fluid rearranges itself to a more stable configuration with little change to the interface positions on the downstream side. The event at $t \approx 0.20$ s is illustrated in **Figure 8**. The fluid redistribution is driven by capillary forces and less external

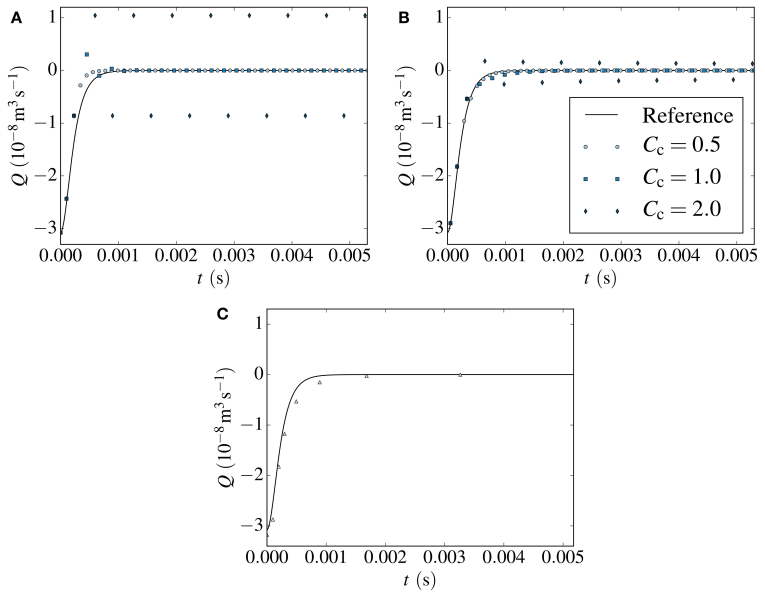

FIGURE 6 | Flow rate plotted against time in the link-in-series test case with $\Delta P = 0$ Pa. Results from the forward Euler method **(A)** and the midpoint method **(B)** are shown for different values of C_c. Severe numerical instabilities arise when $C_c = 2.0$. Results from the semi-implicit method are shown are shown in **(C)**. These are stable, even if the capillary time step criterion is not used. The solid black line represents a reference solution.

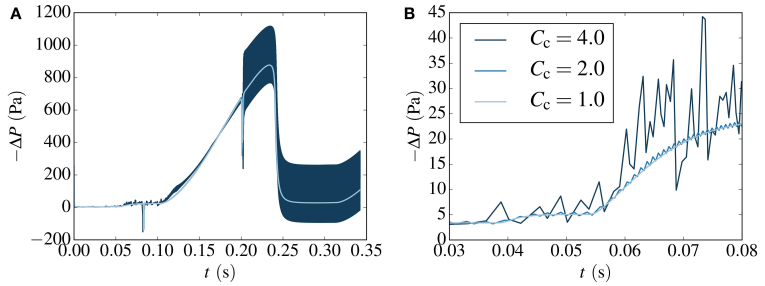

FIGURE 7 | Pressure difference required to drive the flow in the Haines jump case at a rate of $Q = 10^{-9}$ m^3 s^{-1}, corresponding to Ca $= 1.2 \cdot 10^{-5}$. In **(B)**, the results from **(A)** are shown in greater detail. Results are computed with the forward Euler method for different values of the capillary time step restriction parameter C_c. Numerical instabilities are seen to occur for $C_c > 1$.

pressure is therefore required to drive the flow during these events.

We also observe the slow pressure build-up from $t \approx 0.10$ s to $t \approx 0.23$ s, when the driving pressure becomes large enough to overcome the capillary forces and cause break-through of non-wetting fluid in the link connecting nodes 9 and 16, and we observe the subsequent Haines jump. The fluid configurations before and after the Haines jump are shown in **Figure 9**. Notice also that non-wetting fluid at the downstream end of the moving ganglion retracts during the Haines jump in links near to where the break-through occurs. This is seen e.g. in the links downstream of nodes 10 and 14. That such local imbibition occurs near the drained pore is in agreement with the observations of

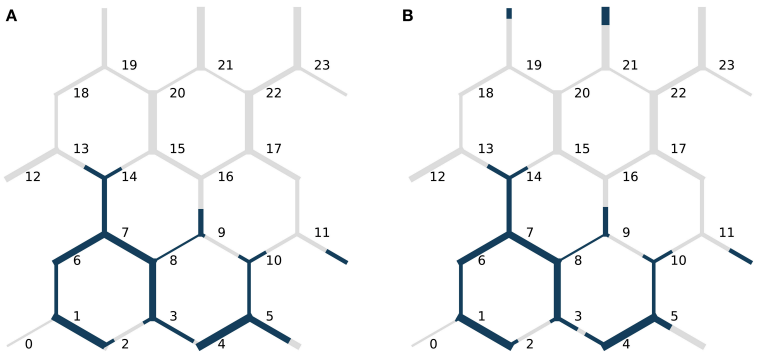

FIGURE 8 | Fluid distribution in the Haines jump case, **(A)** at $t = 0.19$ s and **(B)** at $t = 0.21$ s, before and after the fluid redistribution event at $t \approx 0.20$ s. The link radii are not drawn to scale with the link lengths. Node indices are indicated in black.

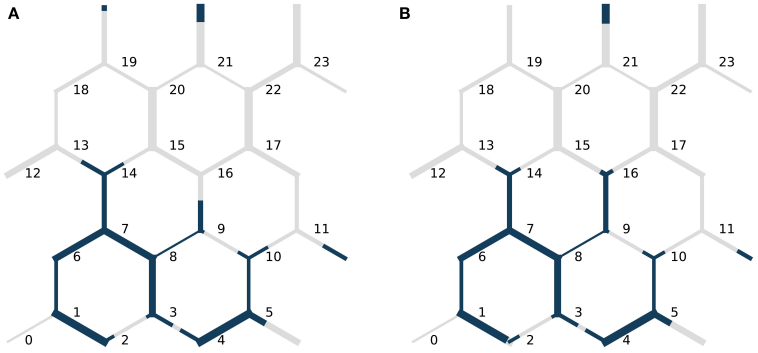

FIGURE 9 | Fluid distribution in the Haines jump case **(A)** at $t = 0.23$ s and **(B)** at $t = 0.27$ s, before and after the Haines jump. During the jump, non-wetting fluid breaks-through the link connecting nodes 9 and 16 and invades node 16. Also, non-wetting fluid in other links at the downstream end of the moving ganglion retracts. This is seen e.g. in the links downstream of nodes 10 and 14. The link radii are not drawn to scale with the link lengths. Node indices are indicated in black.

Armstrong and Berg [15], and shows that the model is able to capture the non-local nature of pore drainage events in a numerically stable manner when the new numerical methods are used.

As in the links-in-series case, the solution exhibits oscillations for the values of C_c that are larger than unity. With $C_c = 1.0$, the results are free from oscillations and appear stable. This indicates that the stability criterion (23) is valid and not unnecessarily strict also for a network configuration that is much more complex than links in series.

Both the links-in-series case and the Haines jump case were simulated with the semi-implicit method and produced stable results with the advective time step criterion (22) only. The results from the links-in-series test case are shown in **Figure 6C**. For brevity, the results from the Haines jump case are omitted here. The reader is referred to **Figure 10A** in section 10, where stable results are shown for a lower flow rate.

To summarize, both the forward Euler and midpoint methods produce stable results for the cases considered when the capillary time step criterion (23) is used in addition to Equation (22) to select the time step lengths. By running simulations with different C_c, we have observed a transition from stable to unstable results for values of C_c near 1, in order of magnitude. In the Haines jump case, all methods presented are able to capture both the fast capillary-driven fluid redistribution events, and the slow pressure build-up before a Haines jump.

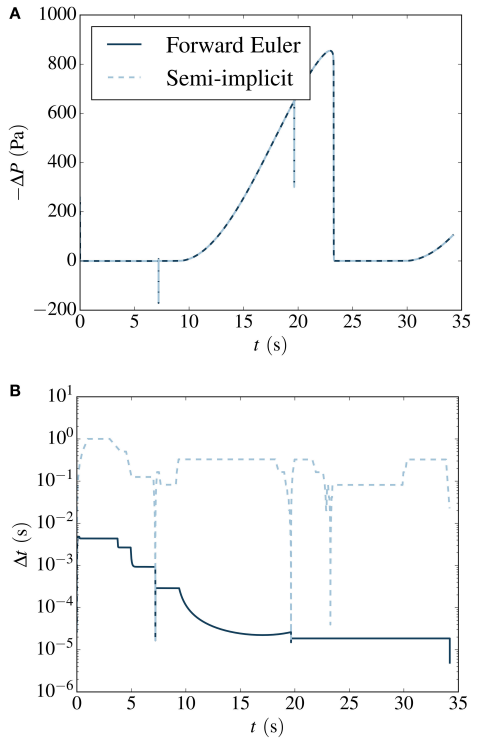

FIGURE 10 | (A) Pressure difference required to drive the flow at $Q = 10^{-11}$ m^3 s^{-1}, corresponding to Ca $= 1.2 \cdot 10^{-7}$, in the Haines jump case. Results are plotted for the forward Euler method (solid dark blue) and the semi-implicit method (dashed light blue). These lines coincide at the scale of representation. The time steps lengths used by each method are plotted in **(B)**.

10. PERFORMANCE ANALYSIS

In this section, we analyze and compare the performance of the time integration methods. In doing so, we consider the number of time steps and the wall clock time required to perform stable simulations of the Haines jump case with each of the methods at different specified flow rates Q. The flow rates simulated were 10^{-7} m^3 s^{-1}, 10^{-8} m^3 s^{-1}, 10^{-9} m^3 s^{-1}, 10^{-10} m^3 s^{-1}, 10^{-11} m^3 s^{-1}, and 10^{-12} m^3 s^{-1}. The accuracy of the methods was studied Section 9.1, and will not be part of the performance analysis. Instead, stable simulations are considered sufficiently accurate.

First, we look more closely at the results for $Q = 10^{-11}$ m^3 s^{-1}, corresponding to Ca $= 1.2 \cdot 10^{-7}$. The pressure difference required to drive the flow is shown in **Figure 10A**, and the time step lengths used are shown in **Figure 10B**. From the latter Figure, we see that the semi-implicit method is able to take longer time steps than forward Euler for most of the simulation. During the pressure build-up phase, the difference is four orders of magnitude. During the fast capillary-driven fluid redistribution events, however, the length of the semi-implicit time steps drop to the level of those used by forward Euler. This is because we here have relatively large flow rates in some links, even though Q is low, and the advective time step criterion (22) becomes limiting for both the semi-implicit method and forward Euler.

It was mentioned by Armstrong and Berg [15] that any accurate numerical simulation on the pore scale must have a time resolution fine enough to capture the fast events. The semi-implicit method accomplishes this by providing a highly dynamic time resolution, which is refined during the fast events. The method is therefore able to resolve these events, while time resolution can be coarsened when flow is governed by the slow externally applied flow rate, saving computational effort.

The time duration of the Haines jump pressure drops for all except the two largest externally applied flow rates were around 10 ms. This is in qualitative agreement with the results presented by Armstrong and Berg [15]. They found that, for their investigated range of parameters, pores were drained on the millisecond time scale regardless of externally applied flow rate. However, we stress that although we consider the same fluids, the pore network used here was approximately one order of magnitude larger in the linear dimensions than that of Armstrong and Berg [15].

The number of time steps and wall clock time required to simulate the Haines jump case at different specified flow rates Q are shown in **Figures 11A,B**, respectively.

For the explicit methods, both the number of time steps and the wall time are proportional to Ca^{-1} at low capillary numbers. This is because the capillary time step criterion (23) dictates the time step at low capillary numbers (except during fast fluid redistribution events). The criterion depends on the fluid configuration, while it is independent of the flow rate. At low enough flow rates, the system will pass through roughly the same fluid configurations during the simulation, regardless of the applied Q. The speed at which the system passes through these configurations, however, will be inversely proportional to Q and therefore, so will the required wall time and number of time steps. As the forward Euler and the midpoint method are subject to the same time step criteria, these require roughly the same number of time steps at all considered flow rates. However, since the midpoint method is a two-step method, the wall time it requires is longer and approaches twice that required by the forward Euler for long wall times.

For the semi-implicit method, on the other hand, the number of time steps required to do the simulation becomes effectively independent of the specified flow rate at capillary numbers smaller than approximately 10^{-4}. The result is that low-capillary number simulations can be done much more efficiently than with the explicit methods, in terms of wall time required to perform stable simulations. This is seen in **Figure 11B**. At Ca $\sim 10^{-5}$, the computational time needed by all three methods are similar in magnitude. The relative benefit of using the semi-implicit method increases at lower capillary numbers. For the lowest capillary number considered, the difference in wall time between

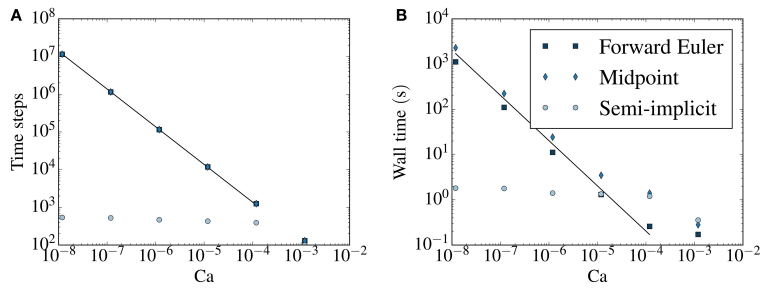

FIGURE 11 | (A) Number of time steps and **(B)** wall clock time required to simulate the Haines jump case at at different specified flow rates. In each simulation, the same volume of fluid (5% of the pore volume) flows through a network. Results from the forward Euler method (squares), the midpoint method (diamonds) and the semi-implicit method (circles) are shown. In **(A,B)**, the black lines are inversely proportional to Ca.

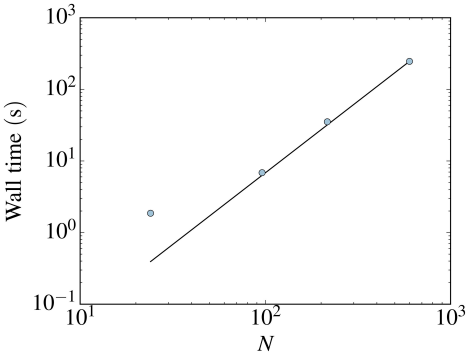

FIGURE 12 | Wall clock time time required to simulate the Haines jump case with the semi-implicit method for different network sizes. All simulations were run at Ca $\sim = 10^{-7}$ and N denotes the number of nodes in the network. The wall time is seen to increase proportionally to N^2 for the three largest networks.

the explicit methods and the semi-implicit is three orders of magnitude.

The increased efficiency of the semi-implicit method over explicit methods at low capillary numbers means that one can use the semi-implicit method to perform simulations in the low capillary number regime that are unfeasible with explicit methods. Thus, the range of capillary numbers for which the pore network model is a tractable modeling alternative is extended to much lower capillary numbers. This includes e.g. simulations of water flow in fuel cell gas diffusion layers, where capillary numbers are can be 10^{-8} [33].

Finally, to study the effect of an increase in network size on the wall time required by the semi-implicit method, the Haines jump case was run on three scaled-up versions of the network with $N = 24$ nodes considered so far, illustrated in **Figure 4**. All simulations were run at Ca $\sim 10^{-7}$. In **Figure 12** the wall clock time time required is plotted against the number of nodes N for the different networks. The wall time is seen to increase proportionally to N^2.

11. CONCLUSION

We have studied three different time integration methods for a pore network model for immiscible two-phase flow in porous media. Two explicit methods, the forward Euler and midpoint methods, and a new semi-implicit method were considered. The explicit methods have been presented and used in other works [10, 21, 24], and were reviewed here for completeness. The semi-implicit method was presented here for the first time, and therefore in detail.

The explicit methods have previously suffered from numerical instabilities at low capillary numbers. Here, a new time-step criterion was suggested in order to stabilize them and numerical experiments were performed demonstrating that stabilization was achieved.

It was verified that all three methods converged to a reference solution to a selected test case upon time step refinement. The forward Euler and semi-implicit methods exhibited first-order convergence and the midpoint method showed second-order convergence.

Simulations of a single Haines jump were performed. These showed that the all three methods were able to resolve both pressure build-up events and fluid redistribution events, including interfacial retraction after a Haines jump, which may occur at vastly different time scales when capillary numbers are low. The results from the Haines jump case were consistent with experimental observations made by Armstrong and Berg [15]. Fluid redistribution events cannot be properly captured when using solution methods that have previously been used at low capillary numbers that e.g. do not allow backflow [18].

A performance analysis revealed that the semi-implicit method was able to perform stable simulations with much less

computational effort than the explicit methods at low capillary numbers. For the case considered, the computational time needed was approximately the same for all three methods at Ca $\sim 10^{-5}$. At lower capillary numbers, the computational time needed by the explicit methods increased inversely proportional to the capillary number, while the time needed by the semi-implicit method was effectively constant. At Ca $\sim 10^{-8}$, the computational time needed by the semi-implicit methods was therefore three orders of magnitude smaller than those needed by the explicit methods.

The superior efficiency of the new semi-implicit method over the explicit methods at low capillary numbers enables simulations in this regime that are unfeasible with explicit methods. Thus, the range of capillary numbers for which the pore network model is a tractable modeling alternative is extended to much lower capillary numbers. This includes e.g. simulations of water flow in fuel cell gas diffusion layers, where capillary numbers are can be 10^{-8} [33].

In summary, use of Aker-type pore network models were previously restricted to relatively high capillary numbers due to numerical instabilities in the explicit methods used to solve them. With the new time step criterion presented here, these stability problems are removed. However, simulations at low capillary numbers still take a long time and the computational time needed increases inversely proportional to the capillary number. This problem is solved by the new semi-implicit method. With this method, the computational time needed becomes effectively independent of the capillary number, when capillary numbers are low.

AUTHOR CONTRIBUTIONS

To pursue low capillary number simulations with Aker-type pore network models was proposed by SK, MG, and AH in collaboration. MV developed the particular variation of the pore network model used. MG developed the new numerical methods and performed the simulations. MG wrote the manuscript, aided by comments and suggestions from MV, SK, and AH.

ACKNOWLEDGMENTS

The authors would like to thank Dick Bedeaux, Santanu Sinha, and Knut Jørgen Måløy for fruitful discussions. Special thanks are also given to Jon Pharoah for inspiring discussions and comments. This work was partly supported by the Research Council of Norway through its Centres of Excellence funding scheme, project number 262644.

SUPPLEMENTARY MATERIAL

The Supplementary Material for this article can be found online at: https://www.frontiersin.org/articles/10.3389/fphy.2018.00056/full#supplementary-material

REFERENCES

1. Raeini AQ, Blunt MJ, Bijeljic B. Modelling two-phase flow in porous media at the pore scale using the volume-of-fluid method. *J Comput Phys.* (2012) **231**:5653–68. doi: 10.1016/j.jcp.2012.04.011
2. Jettestuen E, Helland JO, Prodanović M. A level set method for simulating capillary-controlled displacements at the pore scale with nonzero contact angles. *Water Resour Res.* (2013) **49**:4645–61. doi: 10.1002/wrcr.20334
3. Gjennestad MA, Munkejord ST. Modelling of heat transport in two-phase flow and of mass transfer between phases using the level-set method. *Energy Proc.* (2015) **64**:53–62. doi: 10.1016/j.egypro.2015.01.008
4. Ramstad T, Øren PE, Bakke S. Simulation of two-phase flow in reservoir rocks using a lattice Boltzmann method. *SPE J.* (2010) **15**:917–27. doi: 10.2118/124617-PA
5. Hammond PS, Unsal E. A dynamic pore network model for oil displacement by wettability-altering surfactant solution. *Transport Porous Media* (2012) **92**:789–817. doi: 10.1007/s11242-011-9933-4
6. Lenormand R, Touboul E, Zarcone C. Numerical models and experiments on immiscible displacements in porous media. *J Fluid Mech.* (1988) **189**:165–87. doi: 10.1017/S0022112088000953
7. Wilkinson D, Willemsen JF. Invasion percolation: a new form of percolation theory. *J Phys A Math Gen.* (1983) **16**:3365. doi: 10.1088/0305-4470/16/14/028
8. Blunt MJ. Physically-based network modeling of multiphase flow in intermediate-wet porous media. *J Petroleum Sci Eng.* (1998) **20**:117–25. doi: 10.1016/S0920-4105(98)00010-2
9. Joekar-Niasar V, Hassanizadeh SM, Dahle H. Non-equilibrium effects in capillarity and interfacial area in two-phase flow: dynamic pore-network modelling. *J Fluid Mech.* (2010) **655**:38–71. doi: 10.1017/S0022112010000704
10. Aker E, Måløy KJ, Hansen A, Batrouni GG. A two-dimensional network simulator for two-phase flow in porous media. *Transport Porous Media* (1998) **32**:163–86. doi: 10.1023/A:1006510106194
11. Joekar-Niasar V, Hassanizadeh S. Analysis of fundamentals of two-phase flow in porous media using dynamic pore-network models: a review. *Crit Rev Environ Sci Technol.* (2012) **42**:1895–976. doi: 10.1080/10643389.2011.574101
12. Tørå G, Øren PE, Hansen A. A dynamic network model for two-phase flow in porous media. *Transport Porous Media* (2012) **92**:145–64. doi: 10.1007/s11242-011-9895-6
13. Haines WB. Studies in the physical properties of soil. v. the hysteresis effect in capillary properties, and the modes of moisture distribution associated therewith. *J Agric Sci.* (1930) **20**:97–116. doi: 10.1017/S002185960008864X
14. Berg S, Ott H, Klapp SA, Schwing A, Neiteler R, Brussee N, et al. Real-time 3D imaging of Haines jumps in porous media flow. *Proc Natl Acad Sci USA* (2013) **110**:3755–9. doi: 10.1073/pnas.1221373110
15. Armstrong RT, Berg S. Interfacial velocities and capillary pressure gradients during haines jumps. *Phys Rev E* (2013) **88**:043010. doi: 10.1103/PhysRevE.88.043010
16. Måløy KJ, Furuberg L, Feder J, Jøssang T. Dynamics of slow drainage in porous media. *Phys Rev Lett.* (1992) **68**:2161. doi: 10.1103/PhysRevLett.68.2161
17. Koplik J, Lasseter T. Two-phase flow in random network models of porous media. *Soc Petrol Eng J.* (1985) **25**:89–100. doi: 10.2118/11014-PA
18. Medici E, Allen J. The effects of morphological and wetting properties of porous transport layers on water movement in PEM fuel cells. *J Electrochem Soc.* (2010) **157**:B1505–14. doi: 10.1149/1.3474958
19. Savani I, Sinha S, Hansen A, Bedeaux D, Kjelstrup S, Vassvik M. A Monte Carlo algorithm for immiscible two-phase flow in porous media. *Transport Porous Media* (2017) **116**:869–88. doi: 10.1007/s11242-016-0804-x
20. Washburn EW. The dynamics of capillary flow. *Phys Rev.* (1921) **17**:273. doi: 10.1103/PhysRev.17.273
21. Knudsen HA, Aker E, Hansen A. Bulk flow regimes and fractional flow in 2D porous media by numerical simulations. *Transport Porous Media* (2002) **47**:99–121. doi: 10.1023/A:1015039503551

22. Sinha S, Bender AT, Danczyk M, Keepseagle K, Prather CA, Bray JM, et al. Effective rheology of two-phase flow in three-dimensional porous media: experiment and simulation. *Transport Porous Media* (2017) **119**:77–94. doi: 10.1007/s11242-017-0874-4
23. Erpelding M, Sinha S, Tallakstad KT, Hansen A, Flekkøy EG, Måløy KJ. History independence of steady state in simultaneous two-phase flow through two-dimensional porous media. *Phys Rev E* (2013) **88**:053004. doi: 10.1103/PhysRevE.88.053004
24. Sinha S, Hansen A. Effective rheology of immiscible two-phase flow in porous media. *Europhys Lett.* (2012) **99**:44004. doi: 10.1209/0295-5075/99/44004
25. Press WH, Flannery BP, Teukolsky SA, Vetterling WT. *Numerical Recipes: The Art of Scientific Computing, 3rd Edn*. New York, NY: Cambridge University Press (2007).
26. Süli E, Mayers D. *An Introduction to Numerical Analysis*. Cambridge: Cambridge University Press (2006).
27. Balay S, Abhyankar S, Adams MF, Brown J, Brune P, Buschelman K, et al. *PETSc Web Page* (2016). Available online at: http://www.mcs.anl.gov/petsc
28. Batrouni GG, Hansen A. Fourier acceleration of iterative processes in disordered systems. *J Stat Phys.* (1988) **52**:747–73. doi: 10.1007/BF01019728
29. Linstrom P, Mallard W, (eds.). *NIST Chemistry WebBook, NIST Standard Reference Database Number 69*. Gaithersburg, MD: National Institute of Standards and Technology (2017).
30. Zeppieri S, Rodríguez J, López de Ramos A. Interfacial tension of alkane + water systems. *J Chem Eng Data* (2001) **46**:1086–8. doi: 10.1021/je000245r
31. Måløy KJ, Feder J, Jøssang T. Viscous fingering fractals in porous media. *Phys Rev Lett.* (1985) **55**:2688. doi: 10.1103/PhysRevLett.55.2688
32. Tallakstad KT, Knudsen HA, Ramstad T, Løvoll G, Måløy KJ, Toussaint R, et al. Steady-state two-phase flow in porous media: statistics and transport properties. *Phys Rev Lett.* (2009) **102**:074502. doi: 10.1103/PhysRevLett.102.074502
33. Sinha PK, Wang CY. Pore-network modeling of liquid water transport in gas diffusion layer of a polymer electrolyte fuel cell. *Electrochim Acta* (2007) **52**:7936–45. doi: 10.1016/j.electacta.2007.06.061

Conflict of Interest Statement: The authors declare that the research was conducted in the absence of any commercial or financial relationships that could be construed as a potential conflict of interest.

Appendix A. Capillary time step criterion

In this section, we identify the cause of the numerical instabilities that explicit methods suffer from at low flow rates when the capillary time step criterion (23) is not obeyed. We also derive this criterion. The contents of this section are not intended to constitute a formal proof of the stability of the presented time integration methods. The results derived herein are based on a linearized approximation of the pore network model. Although the application of results from a linearized analysis to general cases is somewhat simplistic, it is useful for highlighting key difficulties, see e.g. [26] pp. 347., and for deriving results that can be found to work in practice. For evidence of the actual stability of the time integration methods, it is therefore referred to the numerical tests performed in Section 9.

Consider a single link ij in a network and assume that p_i and p_j are given. Then the ODE (6) for the interface positions in the link is

$$\frac{\mathrm{d}\mathbf{z}_{ij}}{\mathrm{d}t} = \frac{q_{ij}\left(\mathbf{z}_{ij}\right)}{a_{ij}}. \tag{A.1}$$

We further assume that the flow rate in this link is low. This means that the node and capillary pressures almost balance at the current interface positions $\mathbf{z}_{ij}^*$, and thus $q_{ij}\left(\mathbf{z}_{ij}^*\right) \approx 0$. Also, we neglect the dependence of g_{ij} on the interface positions. Now rewrite (A.1) in terms $\Delta\mathbf{z}_{ij} = \mathbf{z}_{ij} - \mathbf{z}_{ij}^*$ and linearize the right hand side around $\mathbf{z}_{ij}^*$ to get

$$\frac{\mathrm{d}}{\mathrm{d}t}\Delta\mathbf{z}_{ij} \approx \frac{q_{ij}\left(\mathbf{z}_{ij}^*\right)}{a_{ij}} + \frac{g_{ij}\left(\mathbf{z}_{ij}^*\right)}{a_{ij}}\left(\sum_{z\in\mathbf{z}_{ij}^*}\frac{\partial c_{ij}}{\partial z}\right)\Delta\mathbf{z}_{ij}, \tag{A.2}$$

$$\approx \frac{g_{ij}\left(\mathbf{z}_{ij}^*\right)}{a_{ij}}\left(\sum_{z\in\mathbf{z}_{ij}^*}\frac{\partial c_{ij}}{\partial z}\right)\Delta\mathbf{z}_{ij}, \tag{A.3}$$

$$= \lambda\Delta\mathbf{z}_{ij}. \tag{A.4}$$

We can now read off the approximate ODE eigenvalue as

$$\lambda = \frac{g_{ij}\left(\mathbf{z}_{ij}^*\right)}{a_{ij}}\left(\sum_{z\in\mathbf{z}_{ij}^*}\frac{\partial c_{ij}}{\partial z}\right). \tag{A.5}$$

Without loss of generality, we may assume that $\lambda < 0$. If this is not the case, we interchange the indices i and j and redefine our spatial coordinate so that $z \to -z$ to get an ODE with negative λ. We therefore write the eigenvalue as

$$\lambda = -\frac{g_{ij}\left(\mathbf{z}_{ij}^*\right)}{a_{ij}}\left|\sum_{z\in\mathbf{z}_{ij}^*}\frac{\partial c_{ij}}{\partial z}\right|. \tag{A.6}$$

If the forward Euler method is to be stable on the linearized ODE, $\lambda\Delta t$ must lie in the stability region of the forward Euler method [26],

$$-2 < \lambda\Delta t < 0. \tag{A.7}$$

This is satisfied if we choose the time step such that

$$\Delta t < \frac{2a_{ij}}{g_{ij}\left(\mathbf{z}^*_{ij}\right)\left|\sum_{z\in\mathbf{z}^*_{ij}} \frac{\partial c_{ij}}{\partial z}\right|}. \tag{A.8}$$

The criterion (23) is obtained by demanding that (A.8) be satisfied for all links in the network. If the advective criterion (22) is used by itself and the link flow rates are low, then (A.8) is not necessarily satisfied for all links and we must expect numerical instabilities from the forward Euler method.

As the midpoint method has the same real-space stability region as the forward Euler method (A.7), the above reasoning and the criterion (23) can be applied for the midpoint method also.

The backward Euler method, on the other hand, is stable if [26]

$$\lambda\Delta t < 0, \tag{A.9}$$

and, because λ is negative, it is stable with any positive Δt for this linearized problem.

Appendix B. Jacobian matrix for the semi-implicit method

In order to solve (35) using the numerical method described in Section 7, it is necessary to have the Jacobian matrix of $\mathbf{F}$. This matrix may be written as

$$\frac{\partial F_i}{\partial p_j^{(n+1)}} = \delta_{ij} \sum_k \frac{\partial q_{ik}^{(n+1)}}{\partial p_i^{(n+1)}} + \left\{1-\delta_{ij}\right\} \frac{\partial q_{ij}^{(n+1)}}{\partial p_j^{(n+1)}}. \tag{B.1}$$

The derivative of $q_{ik}^{(n+1)}$ with respect to $p_i^{(n+1)}$ can be found by differentiation of (32) with respect to $p_i^{(n+1)}$ and application of the chain rule,

$$\frac{\partial q_{ij}^{(n+1)}}{\partial p_i^{(n+1)}} = -g_{ij}^{(n)} + g_{ij}^{(n)} \frac{\partial c_{ij}^{(n+1)}}{\partial p_i^{(n+1)}}, \tag{B.2}$$

$$= -g_{ij}^{(n)} + g_{ij}^{(n)} \frac{\mathrm{d}c_{ij}^{(n+1)}}{\mathrm{d}q_{ij}^{(n+1)}} \frac{\partial q_{ij}^{(n+1)}}{\partial p_i^{(n+1)}}. \tag{B.3}$$

This can be solved for the desired derivative to yield

$$\frac{\partial q_{ij}^{(n+1)}}{\partial p_i^{(n+1)}} = -\frac{g_{ij}^{(n)}}{1 - g_{ij}^{(n)} \frac{\mathrm{d}c_{ij}^{(n+1)}}{\mathrm{d}q_{ij}^{(n+1)}}}. \tag{B.4}$$

Herein, the derivative of capillary pressure with respect to flow rate is

$$\frac{\mathrm{d}c_{ij}^{(n+1)}}{\mathrm{d}q_{ij}^{(n+1)}} = \frac{2\sigma_{\mathrm{wn}}}{r_{ij}} \sum_{z\in\mathbf{z}_{ij}^{(n+1)}} (\pm 1) \sin\left(2\pi\chi_{ij}(z)\right) \frac{\mathrm{d}\chi_{ij}}{\mathrm{d}z} \frac{2\pi\Delta t^{(n)}}{a_{ij}}, \tag{B.5}$$

for the specific choice of capillary pressure model given by (9).

As the pore network model is linear in the node pressures, it is intuitive that the effect on the link flow rate of increasing the pressure in the node at one end of a link is the same as decreasing it, by the same amount, in the node at the other end. Thus we may write

$$\frac{\partial q_{ij}^{(n+1)}}{\partial p_j^{(n+1)}} = -\frac{\partial q_{ij}^{(n+1)}}{\partial p_i^{(n+1)}}. \tag{B.6}$$

This equation may be more formally derived by differentiating (32) with respect to $p_j^{(n+1)}$ to get

$$\frac{\partial q_{ij}^{(n+1)}}{\partial p_j^{(n+1)}} = g_{ij}^{(n)} + g_{ij}^{(n)} \frac{\partial c_{ij}^{(n+1)}}{\partial p_j^{(n+1)}}, \tag{B.7}$$

$$= g_{ij}^{(n)} + g_{ij}^{(n)} \frac{\mathrm{d}c_{ij}^{(n+1)}}{\mathrm{d}q_{ij}^{(n+1)}} \frac{\partial q_{ij}^{(n+1)}}{\partial p_j^{(n+1)}}, \tag{B.8}$$

and, solving for the desired derivative,

$$\frac{\partial q_{ij}^{(n+1)}}{\partial p_j^{(n+1)}} = \frac{g_{ij}^{(n)}}{1 - g_{ij}^{(n)} \frac{\mathrm{d}c_{ij}^{(n+1)}}{\mathrm{d}q_{ij}^{(n+1)}}}. \tag{B.9}$$

Comparison of (B.4) and (B.9) gives the intuitive result (B.6).

The addition of F_m (40) to the non-linear system for the specified flow rate boundary condition, introduces some new terms in the Jacobian matrix of $\mathbf{F}$. The derivatives of F_m with respect to the node pressures are

$$\frac{\partial F_m}{\partial p_k^{(n+1)}} = \sum_{ij \in \Omega} \left\{ \delta_{ki} \frac{\partial q_{kj}^{(n+1)}}{\partial p_k^{(n+1)}} + \delta_{kj} \frac{\partial q_{ik}^{(n+1)}}{\partial p_k^{(n+1)}} \right\}, \tag{B.10}$$

where link flow rate derivatives are calculated using (B.4) and (B.6) and the derivative with respect to ΔP is

$$\frac{\partial F_m}{\partial (\Delta P)} = -\sum_{ij \in \Omega} \frac{g_{ij}^{(n)}}{1 - g_{ij}^{(n)} \frac{\mathrm{d}c_{ij}^{(n+1)}}{\mathrm{d}q_{ij}^{(n+1)}}}. \tag{B.11}$$

The additional terms corresponding to the derivatives with respect to ΔP of the mass balance equations for each node k with unknown pressures are

$$\frac{\partial F_k}{\partial (\Delta P)} = \sum_{ij \in \Omega} \left\{ \delta_{kj} - \delta_{ki} \right\} \frac{g_{ij}^{(n)}}{1 - g_{ij}^{(n)} \frac{\mathrm{d}c_{ij}^{(n+1)}}{\mathrm{d}q_{ij}^{(n+1)}}}. \tag{B.12}$$

Paper V

S. Sinha, M. Aa. Gjennestad, M. Vassvik, M. Winkler, A. Hansen, and E. G. Flekkøy. Rheology of high-capillary number flow in porous media. *Frontiers in Physics* 7 (2019), p. 65. DOI: 10.3389/fphy.2019.00065

frontiers in Physics

ORIGINAL RESEARCH
published: 07 May 2019
doi: 10.3389/fphy.2019.00065

Rheology of High-Capillary Number Two-Phase Flow in Porous Media

Santanu Sinha[1,2]*, *Magnus Aa. Gjennestad*[2], *Morten Vassvik*[2], *Mathias Winkler*[2], *Alex Hansen*[2,1] *and Eirik G. Flekkøy*[3]

[1] *Beijing Computational Science Research Center, Beijing, China,* [2] *PoreLab, Department of Physics, Norwegian University of Science and Technology (NTNU), Trondheim, Norway,* [3] *PoreLab, Department of Physics, University of Oslo, Oslo, Norway*

Flow of immiscible fluids in porous media at high capillary numbers may be characterized by an effective viscosity. We demonstrate that the effective viscosity is well-described by the Lichtenecker-Rother equation. Depending on the pore geometry, wettability, and viscosity of the fluids, the exponent α in this equation can have different values. We find $\alpha = 1$ when fluids are well-mixed with small bubbles, $\alpha = 0.6$ in two- and 0.5 in three-dimensional systems when there is less mixing with the appearance of big bubbles, and $\alpha = -0.5$ when lubrication layers are formed along the pore walls. Our arguments are based on analytical and numerical methods.

Keywords: porous media, two-phase flow, effective viscosity, pore-network modeling, lattice-boltzman method (LBM)

OPEN ACCESS

Edited by:
Josè S. Andrade Jr., Universidade Federal do Ceará, Brazil

Reviewed by:
Wenzheng Yue, China University of Petroleum, Beijing, China
Bikas K. Chakrabarti, Saha Institute of Nuclear Physics, India

***Correspondence:**
Santanu Sinha
santanu@csrc.ac.cn

Specialty section:
This article was submitted to Interdisciplinary Physics, a section of the journal Frontiers in Physics

Received: *11 January 2019*
Accepted: *15 April 2019*
Published: *07 May 2019*

Citation:
Sinha S, Gjennestad MA, Vassvik M, Winkler M, Hansen A and Flekkøy EG (2019) Rheology of High-Capillary Number Two-Phase Flow in Porous Media. Front. Phys. 7:65. doi: 10.3389/fphy.2019.00065

1. INTRODUCTION

The hydrodynamics of real systems very often happens at small scale, such as in a porous medium [1]. This is the case in a wide variety of biological, geological, and technological systems where there are often several immiscible fluids present. The challenge of describing such systems in a unified way, however, is largely unsolved. An important reason for this is the lack of a length scale above which the system may be averaged. Such a length scale gives rise to the representative elementary volume (REV) which is the conceptual basis for conventional theories that seek to up-scale the description of flow in porous media. However, since the fluid structures in question are often fractal, the REV average of intensive quantities, such as saturations, will depend on the size of the REV.

An important and rather general exception where this is not a problem, is the case of steady state flow [2, 3]. Steady state flow is characterized by potentially strong fluctuations at the pore scale, but with steady averages at the REV scale. Steady state configurations have much in common with ensembles in equilibrium statistical mechanics. Steady state flow implicitly assumed in conventional descriptions of porous media flows that take the existence of a REV for granted.

When the flow in question contains immiscible phases that are strongly forced in the sense that viscous forces dominate capillary forces, the description of the steady state simplifies to the description of a single fluid. This is the subject of the present work, and we show how the emergent description is manifestly incompatible with the conventional theories that have been in use for more than 80 years, most notably perhaps by the petroleum industry.

2. THEORY

The first and still leading theory describing immiscible two-phase flow in porous media is that of Wyckoff and Botset [4]. They based their theory of *relative permeability* on the idea that when the porous medium is seen from the viewpoint of one of the fluids, the pore volume accessible to this

fluid would be the pore volume of the porous medium minus the pore volume occupied by the other fluid. This reduces the effective permeability seen by either fluid and the relative reduction factor is the relative permeability. In order to account for the surface tension between the immiscible fluids in the pores, the concept of capillary pressure was introduced [5]. The central equations in relative permeability theory are

$$\vec{v}_j = -\frac{K}{\mu_j}\, k_{r,j}(S_j)\, \vec{\nabla} P_j \,, \tag{1}$$

where the subscript j either refers to the wetting fluid ($j = w$) or the non-wetting fluid ($j = n$). $\vec{v}_w$ and $\vec{v}_n$ are superficial velocities of the two fluids, defined as the volumetric flow rates of each fluid entering a REV divided by the area of entry. K is the permeability of the porous medium, μ_w and μ_n are the wetting and non-wetting viscosities. $k_{r,w}(S_w)$ and $k_{r,n}(S_w)$ are the relative permeabilities and they are both functions of the wetting saturation S_w only. The corresponding non-wetting saturation is $S_n = 1 - S_w$. The wetting and non-wetting pressure fields P_w and P_n are related through the capillary pressure function $P_c(S_w) = P_n - P_w$. We define a total superficial velocity $\vec{v}$ given by,

$$\vec{v} = \vec{v}_w + \vec{v}_n \,. \tag{2}$$

$\vec{v}$ is defined as the volumetric flow rate of all fluids entering the REV divided by the area of entry.

Let us now consider the case when the flow rates are so large that the capillary pressure may be ignored. Hence, we have $P_n = P_w = P$ and we may combine the relative permeability Equation (1) with Equation (2) to find

$$\vec{v} = -K\left[\frac{k_{r,w}(S_w)}{\mu_w} + \frac{k_{r,n}(S_n)}{\mu_n}\right]\vec{\nabla} P = -\frac{K}{\mu_{\rm eff}(S_w)}\vec{\nabla} P \,, \tag{3}$$

where we have defined an *effective viscosity* $\mu_{\rm eff}$ as

$$\frac{1}{\mu_{\rm eff}(S_w)} = \frac{k_{r,w}(S_w)}{\mu_w} + \frac{k_{r,n}(S_n)}{\mu_n} \,. \tag{4}$$

There have been many suggestions as to what functional form the relative permeabilities $k_{r,w}(S_w)$ and $k_{r,n}(S_w)$ take. The most common choice is to use those of Brooks and Corey assuming $k_{r,w}(S_w) = k^0_{r,w} S_w^{n_w}$ and $k_{r,n}(S_w) = S_n^{n_n}$ where $0 \le k^0_{r,w} \le 1$ and the Corey exponents n_w and n_n being typically in the range 2–6 [6, 7].

Equation (4) is problematic. When $\mu_w = \mu_n$, a dependency of $\mu_{\rm eff}$ on the saturation is predicted when n_w and/or n_n are larger than 1 when using the Brook–Corey relative permeabilities. Other functional forms for the relative permeabilities give similar dependencies. Clearly, such behavior is not physical.

McAdams et al. [8] proposed an effective viscosity for two-phase flow by assuming a saturation-weighted *harmonic* average

$$\frac{1}{\mu_{\rm eff}} = \frac{S_w}{\mu_w} + \frac{S_n}{\mu_n} \,. \tag{5}$$

Cicchitti et al. [9] proposed an effective viscosity based on the saturation-weighted *arithmetic* average

$$\mu_{\rm eff} = \mu_w S_w + \mu_n S_n \,. \tag{6}$$

Both of these expressions become saturation-independent when $\mu_w = \mu_n$ as they should. There are several other proposals for the functional form of the effective viscosity $\mu_{\rm eff}$ in the literature [10].

A one-dimensional porous medium, e.g., a capillary tube where the two fluids move as bubbles in series [11] constitutes a series coupling and the arithmetic average (6) is appropriate. If the capillary tubes forms a parallel bundle, each filled with either only the wetting or the non-wetting fluid, we have a parallel coupled system and Equation (5) is appropriate. We now consider a capillary bundle, where each capillary i in the bundle is filled with a bubble train with a corresponding wetting saturation $S_{w,i}$. The probability distribution for finding a capillary having this saturation, $S_{w,i}$, is $p(S_{w,i})$ so that

$$S_w = \int_0^1 dS\, p(S)\, S \,. \tag{7}$$

The capillary bundle is essentially a parallel combination of tubes, each filled with a series of bubbles. The effective viscosity for the capillary bundle is therefore given by,

$$\frac{1}{\mu_{\rm eff}} = \int_0^1 \frac{p(S)\, dS}{\mu_w S + \mu_n (1 - S)} \,. \tag{8}$$

As a model for the distribution $p(S_{w,i})$, we may take a Gaussian with a narrow width σ centered around S_w: $p(S_{w,i}) = \exp[-(S_{w,i} - S_w)^2/2\sigma^2]/\sqrt{2\pi\sigma^2}$. Using this distribution for saturation we can integrate Equation (8) using a saddle point approximation and we find to order σ^2 that,

$$\mu_{\rm eff} = \mu_w S_w + \mu_n S_n - \frac{(\mu_n - \mu_w)^2}{\mu_w S_w + \mu_n S_n}\, \sigma^2 \,. \tag{9}$$

We now consider a wide distribution of saturations in the capillaries. Considering a uniform distribution for $p(S_{w,i})$ in Equation (8) rather than a Gaussian, we find for an average wetting saturation $S_w = 1/2$,

$$\mu_{\rm eff} = \left|\frac{\mu_w - \mu_n}{\ln\left(\frac{\mu_w}{\mu_n}\right)}\right| \,. \tag{10}$$

The functional form of the latter equation is very different from the one for the Gaussian distribution, Equation (9).

For the extreme case when the capillaries are filled completely by either the wetting or the non-wetting fluids given by $p(S_{w,i}) = S_w \delta(S_{w,i} - 1) + S_n \delta(S_{w,i})$, we find the effective viscosity according to Equation (5), as already pointed out. We may study this either-or situation in a more complex network, namely a square lattice. We assume that the wetting saturation is set to $S_w = 1/2$, which defines the bond percolation threshold and that the links are

randomly filled with either fluid. We may then use Straley's exact result [12] leading to an effective viscosity

$$\mu_{\text{eff}} = \sqrt{\mu_w \mu_n}\,. \tag{11}$$

We may calculate the effective viscosity of a regular lattice by using Kirkpatrick's mean field theory [13]. The mobility between nodes i and j is K_{ij}/μ_{ij} where K_{ij} is the permeability and μ_{ij} is the effective viscosity of the link given by $\mu_{ij} = \mu_w S_{w,ij} + \mu_n S_{n,ij}$. Here $S_{w,ij}$ and $S_{n,ij}$ are the local wetting and non-wetting saturations in the links between the nodes. This form of μ_{ij} is due to the fluids being connected in series in one link. Kirkpatrick's theory is based on the idea that the network with link mobilities K_{ij}/μ_{ij} may be replaced by a network with a uniform mobility K/μ_{eff} such that the total network mobility remains the same. In that case, the value of K/μ_{eff} is given by [13]

$$\left\langle \frac{\frac{K}{\mu_{\text{eff}}} - \frac{K_{ij}}{\mu_{ij}}}{\frac{K_{ij}}{\mu_{ij}} + \left[\left(\frac{z}{2}\right) - 1\right]\frac{K}{\mu_{\text{eff}}}} \right\rangle = 0, \tag{12}$$

where z is the coordination number of the lattice. Considering the wetting saturation distribution $p(S_{w,ij})$ fulfilling Equation (7), the ensemble average is given by, $\langle ... \rangle = \int_0^\infty dK_{ij} P(K_{ij}) \int_0^1 dS_{w,ij} p(S_{w,ij}) ...$, where $P(K_{ij})$ is the permeability distribution. We assume a square lattice so that $z = 4$. By assuming that the saturation distribution is a narrowly peaked Gaussian with width σ, we may again use the saddle point approximation to get,

$$\mu_{\text{eff}} = \mu_w S_w + \mu_n S_n + \mathcal{O}\left(|\mu_n - \mu_w|\sigma^2\right). \tag{13}$$

This is similar to that found for the parallel capillary bundle, Equation (9).

From the systems giving rise to Equations (9), (10), (11), and (13), the form of μ_{eff} is not clear. Does it depend on the details of the porous medium or is there a general form? We may generalize Equations (5) and (6) by writing them in the form

$$\mu_{\text{eff}}^{\alpha} = \mu_w^{\alpha} S_w + \mu_n^{\alpha} S_n, \tag{14}$$

where $\alpha = -1$ for parallel coupling and $\alpha = +1$ for series coupling. Equation (14) has been used for estimating the effective electrical permittivity of heterogeneous conductors and in connection with permeability homogenization in porous media and is known as the Lichtenecker–Rother equation [14–17]. The effective viscosity in (11) corresponds to $\alpha \to 0$, whereas Equations (9) and (13) suggest $\alpha = 1$. Only Equation (10) does not fit this form.

In order to test Equation (14) in case of a porous medium, we now present two numerical approaches in the following: dynamic pore-network modeling and lattice Boltzmann simulations.

3. PORE-NETWORK MODELING

The dynamic pore-network model used here has successfully explained several experimental and theoretical results for both the transient and steady-state two-phase flow in porous media over decades [18–21]. During the transients, the model shows the different regimes of two-phase flow, namely the capillary fingering, viscous fingering, and the stable displacement pattern while changing the capillary number and viscosity ratio [18]. In the steady state, the crossover from linear Darcy regime to a quadratic regime that was observed experimentally have also been studied with this pore-network model [19, 22]. The model have also shown the experimental observation of history independence in the steady-state two-phase flow at higher capillary numbers [20]. Recently, relations between steady-state seepage velocities in porous media was obtained analytically by introducing of a new velocity function, the co-moving velocity. These relations were also established numerically with this model [23].

In the model, the porous medium is represented by a network of links, connected at nodes. In the links, two immiscible fluids, separated by interfaces, are transported. We consider both two-dimensional (2D) and three-dimensional (3D) networks for our simulations. For 2D, regular square and honeycomb networks with disordered link radii are used, whereas for 3D, reconstructed pore networks extracted from real samples are used [19]. The flow rate inside a link between two neighboring nodes i and j with respective pressures p_i and p_j obeys

$$q_{ij} = -\frac{g_{ij}}{l_{ij}}\left(p_j - p_i\right), \tag{15}$$

where l_{ij} is the link length and g_{ij} is the link mobility which is inversely proportional to the link viscosity given by $\mu_{ij} = \mu_w S_{w,ij} + \mu_n S_{n,ij}$ [24, 25]. There is no contribution to the pressure from interfaces as the surface tension (γ) is zero. This sets the capillary number, defined as the ratio of viscous to capillary forces given by $\text{Ca} = u\mu_r/\gamma$, to infinity. Here u is the Darcy velocity and μ_r is the viscosity of the more viscous fluid. Simulations are performed with a constant global pressure drop ΔP across the network and the local pressures (p_i) are determined by solving the Kirchhoff equations. Flow rates q_{ij} through each link are then calculated using Equation (15) and the interfaces are moved with small time steps.

A crucial point here is how to distribute the two fluids after they mix at the nodes. Whether the system will allow high or low fragmentation of the fluids will depend on the geometry and nature of the pore space [26, 27]. This will have impact on the size of the bubbles and the number of interfaces inside a link. As small bubbles of either fluid may not necessarily imply a large number of interfaces or *vice versa*, we implemented two different algorithms for the interface dynamics. In the *bubble-controlled* algorithm, we decide the minimum size of a bubble before entering a link and in the *interface-controlled* algorithm we decide the maximum number of interfaces that can exist in a link. We considered two different possibilities for each algorithm: for the bubble-controlled case, (A) small bubbles are allowed, with minimum sizes $b_{\min} = 0.02 r_{ij}$, (B) bubbles with sizes at least equal to the respective pore radii ($b_{\min} = r_{ij}$) are allowed. For the interface-controlled algorithm, we study two cases, (C) one with

maximum four and (D) another with maximum two interfaces per link. Our model does not include lubrication layers, and the simulations therefore cannot capture the wetting film effects at the pore walls. More details of the interface algorithm is provided in the **Supplementary Material**.

4. LATTICE BOLTZMANN SIMULATIONS

We then turn to lattice Boltzmann simulations which have no explicit parameters for the bubble size or for the number of interfaces and permits arbitrary shapes of the fluid domains within the link. The lattice Boltzmann model applied here is based on the original triangular lattice and the interaction rules first introduced by Gunstensen et al. [28]. It models the Navier–Stokes equation for two immiscible fluids within a 2D pore geometry of rectangular pipes of equal width, and in the pores the fluids organize only according to the flow and geometry of the system. The two fluids are represented by different colors, here red (more viscous) and blue (less viscous), and their respective densities ρ_r and ρ_b define a local color gradient. The surface tension is introduced by the application of two steps, first a perturbation of the mass distribution that is proportional to the magnitude of the color gradient, thus increasing the mass in the directions transverse to a fluid-fluid interface, and second, a re-coloring step that sends red toward red and blue toward blue. Both steps conserve the local momentum, the first step creates the change in the stress tensor which is responsible for the surface tension, and the last step causes an anti-diffusive flux of both phases. The solid obstacles are represented by the bounce-back rule, which ensures the hydrodynamic no-slip condition and the wetting property is controlled by coloring the solid obstacles with the same saturations as in the bulk fluid. The aim is to simulate flows that are not governed by surface tension effects and this wetting rule creates a relatively neutral wetting property that does not affect the flow as much as full wetting of one phase. The model also allows for tuning of the surface tension γ, so that the capillary number given by $\mathrm{Ca} = \frac{u\mu_r}{\gamma}$, is set to high values. Here, u is the overall Darcy velocity and μ_r is the viscosity of the red fluid with higher viscosity. In all the simulations $\mathrm{Ca} > 9$. For the more viscous wetting fluid, the wetting saturation $S_w = \rho_r/(\rho_r + \rho_b)$ controls the viscosity according to the local rule

$$\mu = \left[S_w + M(1 - S_w)\right]\mu_r, \tag{16}$$

where $M = \mu_b/\mu_r$ here and the pressure gradient is implemented as a constant body force in the diagonal direction point to upper right corner of the simulation domain. The body force is introduced as a constant momentum input at every time step and at every lattice site.

Initially, the flow velocity is zero everywhere and ρ_r and ρ_b initialized according to the specified value of S_w but with a small random component added. This randomness then triggers an initial phase separation which is responsible for the subsequent distribution of bubbles. Unlike the network modeling, the wetting effects of the pore walls are included here [29]. For the neutral wetting condition and for more viscous wetting fluid, we choose a rectangular pore network to emulate the network model. For the case of complete wetting with less viscous wetting fluid, the wetting layers are important and we therefore avoid the singular sharp corners. The model is implemented on a 128×128 biperiodic lattice with the pressure gradient implemented as a constant body force in the diagonal direction pointing to the upper right corner.

5. RESULTS AND DISCUSSION

We perform simulations under constant external pressure drop ΔP and the systems are evolved to the steady state. The results here are in the high capillary number regime and therefore do not depend on the history or the initial preparation of the system [20]. In the steady state, we compare the results with $(\mu_{\mathrm{eff}}/\mu_w)^\alpha = S_w + M^\alpha S_n$ (Equation 14), where $M = \mu_n/\mu_w$. In the network model, we measure the total flow rate Q as a function of the saturations S_w. As $Q = -\frac{KA}{L\mu_{\mathrm{eff}}}\Delta P$, we measure μ_{eff}/μ_w by calculating Q_w/Q where Q_w is the total flow rate at $S_w = 1$. In the lattice Boltzmann simulations, the μ_{eff} is calculated by measuring the effective permeability, obtained by measuring the total flux Q through the system and dividing by the forcing or average pressure gradient. We chose $M = 2$, 5, and 10 here. Higher values of M increase the computational cost and do not change the conclusions of this study for the network model with $\gamma = 0$. Simulations with M and $1/M$ produce the same results due to symmetric bubble rules and the absence of film flow in the network model. Depending on the pore geometry, wettability and viscosities of the fluids, we find three flow regimes. All can be characterized by Equation (14) with three different values of α. When smaller bubbles (model A) or more interfaces (model C) are allowed in the network model, we find $\alpha = 1$ for both 2D and 3D systems as shown in **Figures 1**, **2**, respectively were the fluids are well mixed. This regime is also observed in the lattice Boltzmann simulations for neutral wetting properties, or when the wetting fluid is more viscous. This is shown in **Figure 3**, where the straight lines confirm $\alpha = 1$ in Equation (14). Here the continuous merging and break-up of droplets give rise to a flow where each pore channel contains a sequence of individual drops. The fluids effectively behave as if they are arranged in series, and on the average the life-time of the droplets does not have any impact on the up-scaled behavior.

When we allow only larger bubbles with the size of the order of the pore size (model B) or few interfaces (model D) in the network model, we find $\alpha = 0.6$ for 2D and $\alpha = 0.5$ for 3D that are consistent with Equation (14). Results are plotted in **Figures 4**, **5**, respectively. Here the steady-state fluid distribution shows less mixing and larger clusters compared to **Figure 1**. This also affects the fractional flow, making the less viscous fluid to flow with higher velocity (**Supplementary Material**). So far, we could not find a set of suitable parameters or pore geometry for the lattice Boltzmann simulations that can reproduce this regime of flow.

When the wetting fluid is made less viscous in the lattice Boltzmann simulations, it produces lubrication layers of the

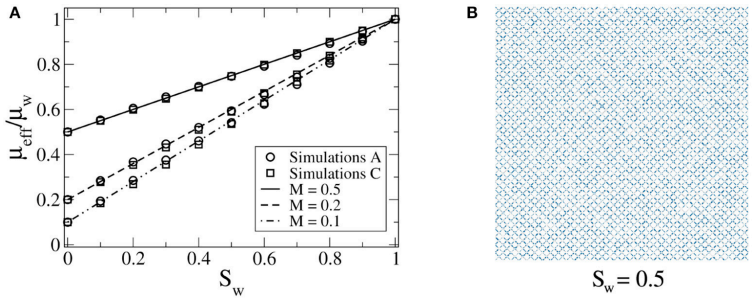

FIGURE 1 | (A) Plot of $(\mu_{eff}/\mu_w)^{\alpha}$ obtained from 2D network simulations (symbols) with small bubbles (A) or with many interfaces (C). Results are consistent with Equation (14) (straight lines) with $\alpha = 1$. A steady-state snapshot for model C is shown in **(B)**, where gray and blue are the wetting and non-wetting fluids respectively. Here the wetting fluid is more viscous and the results for less viscous wetting fluid are the same for the network model due to the symmetry in the interface rules and the lack of film flow mechanism in the model.

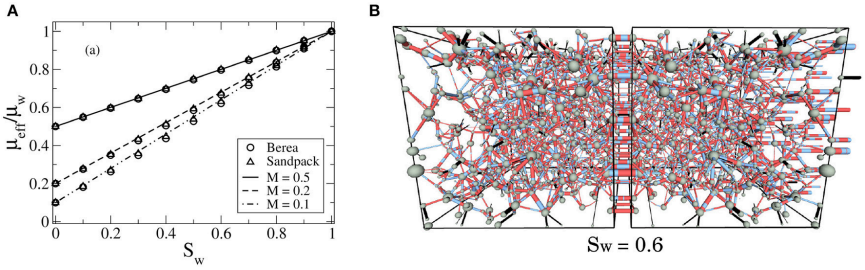

FIGURE 2 | (A) Plot of $(\mu_{eff}/\mu_w)^{\alpha}$ for 3D networks reconstructed from Berea sandstone and sandpack samples for the simulations with four interfaces (C). Results are consistent with Equation (14) (straight lines) with $\alpha = 1$, similar to the 2D networks. A snapshot of fluids in Berea sandstone in the steady state for model C is shown in **(B)**, where blue and red are the wetting and non-wetting fluids respectively.

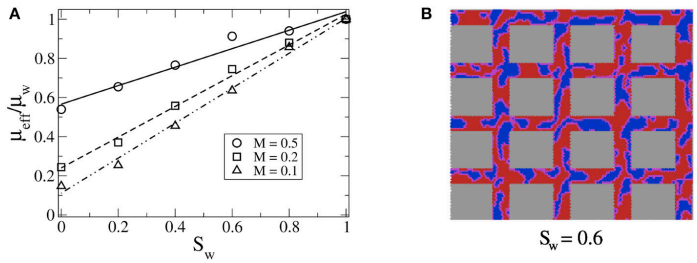

FIGURE 3 | (A) Plot of $(\mu_{eff}/\mu_w)^{\alpha}$ obtained from lattice Boltzmann simulations with more viscous wetting fluid which shows $\alpha = 1$ when compared with Equation (14). **(B)** Typical steady-state distribution of the fluids, where the blue and red are the more viscous (wetting) and less-viscous (non-wetting) fluids, respectively.

wetting fluid along the pore walls. This introduces a third regime with a negative value of α. The results are shown in **Figure 6** which indicate a robust $\alpha = -0.5$ behavior over a range of M values. This means that, due to the lubrication layers flow comes close to the parallel-coupling scenario, which is described by $\alpha = -1$, but there is still a significant difference. The flow paths that appear in parallel are not stationary as they would be in a parallel coupled

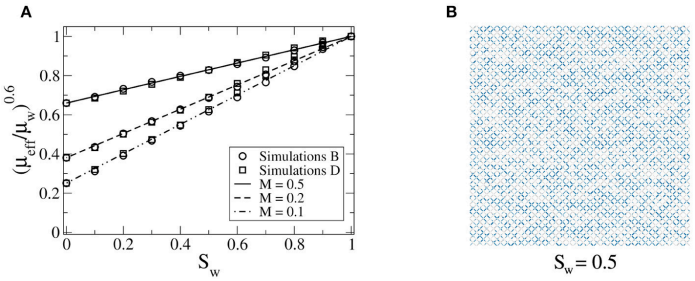

FIGURE 4 | (A) Plot of $(\mu_{eff}/\mu_w)^{\alpha}$ obtained from network simulations with larger bubbles (B) or few interfaces (D) which shows $\alpha = 0.6$ for 2D. **(B)** Typical steady-state snapshot for model D, showing less mixing of fluids and larger clusters compared to **Figure 1B**.

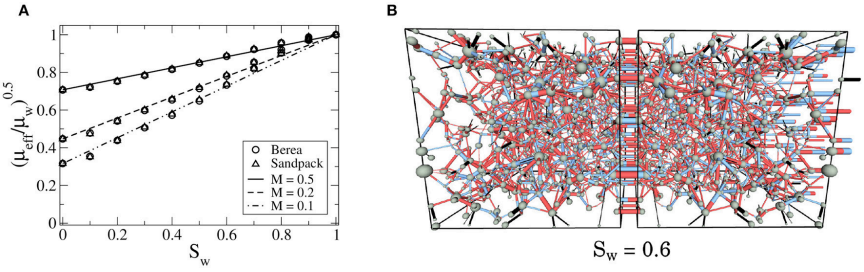

FIGURE 5 | (A) Plot of $(\mu_{eff}/\mu_w)^{\alpha}$ for 3D networks reconstructed from Berea sandstone and sandpack samples for the simulations with two interfaces (D). Results are consistent with Equation (14) (straight lines) with $\alpha = 0.5$. A steady-state snapshot of Berea sandstone for model D is shown in **(B)**, where blue and red are the wetting and non-wetting fluids respectively.

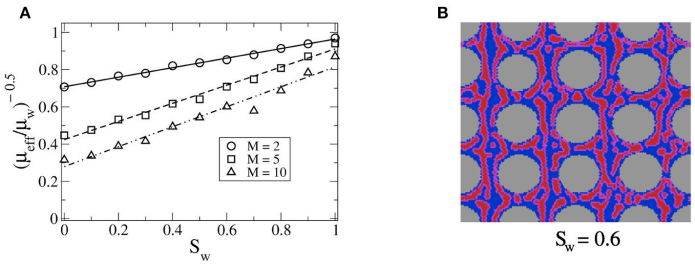

FIGURE 6 | (A) Plot of $(\mu_{eff}/\mu_w)^{\alpha}$ from lattice Boltzmann simulations with less viscous wetting fluid where we find $\alpha = -0.5$. The steady state is dominated by lubrication layers of less viscous blue fluid as seen in **(B)**. The end points close to $S_w = 1$ fall a little below 1, which could have several explanations, one being finite Reynolds numbers, an effect that is likely to increase with increasing M the way the simulations are done.

system, they break up and merge continuously. We could not study this regime with our network model as the model does not contain film flow. It will be interesting to study this in the future with a network model that includes the film flow [30].

6. CONCLUSION

In summary, we show that immiscible two-phase flow in porous media at high capillary number limit can be characterized by measuring the effective viscosity in the steady state. We find that

the Lichtenecker–Rother Equation (14) describes the effective viscosity well for different flow configurations. We identified three flow regimes characterized by the exponent α, which depend on the organization of the two fluids in the pores. When the fluids are well mixed, we find a result which is consistent with the Kirkpatrick's mean field theory [13] with $\alpha = 1$. This is observed in both the network model and lattice Boltzmann simulations, by allowing small bubbles or more interfaces in the network model, and with the neutral wetting condition or more viscous wetting fluid in the lattice Boltzmann simulations. When only larger bubbles or fewer interfaces are allowed, we find the second regime with $\alpha = 0.6$ in 2D and $\alpha = 0.5$ in 3D with the network model. Third, when the wetting fluid is less viscous, lubrication layers are formed at the pore walls, and we find $\alpha = -0.5$ from the lattice Boltzmann simulations.

Finally, we like to point out that in the network model, we have varied the minimum bubble size over the range $0.02r_{ij}$ to $0.5r_{ij}$ finding α decreasing gradually from 1 to 0.6. Taking into account that $r_{ij} \leq 0.4\ l$, where l is the link length, this shift of α from 1 to 0.6 occurs over the narrow range from 0.008 l to 0.2 l, indicating that we see a crossover. In case of the lattice Boltzmann simulation there is no gradual transition with different wetting properties from $\alpha = 1$ to $\alpha = -0.5$. The former is observed in the neutrally wetting case or in the case when the viscous fluid is the completely wetting. The latter is observed in the case of complete wetting of the less viscous fluid.

AUTHOR CONTRIBUTIONS

MG and SS did the network model computations. EF did the Lattice Boltzmann computations. AH wrote the first draft of the manuscript. All the authors contributed in developing the theory and developing the manuscript to its final form.

ACKNOWLEDGMENTS

The authors thank Dick Bedeaux, Carl Fredrik Berg, Signe Kjelstrup, Knut Jørgen Måløy, Per Arne Slotte, and Ole Torsæter for interesting discussions. EF and AH thank the Beijing Computational Science Research Center (CSRC) and Hai-Qing Lin for hospitality. SS was supported by the National Natural Science Foundation of China under grant number 11750110430. This work was partly supported by the Research Council of Norway through its Centers of Excellence funding scheme, project number 262644.

SUPPLEMENTARY MATERIAL

The Supplementary Material for this article can be found online at: https://www.frontiersin.org/articles/10.3389/fphy.2019.00065/full#supplementary-material

REFERENCES

1. Bear J. *Dynamics of Fluids in Porous Media*. Mineola, NY: Dover (1988).
2. Tallakstad KT, Knudsen HA, Ramstad T, Løvoll G, Måløy KJ, Toussaint R, et al. Steady-state two-phase flow in porous media: statistics and transport properties. *Phys Rev Lett.* (2009) **102**:074502. doi: 10.1103/PhysRevLett.102.074502
3. Aursjø O, Erpelding M, Tallakstad KT, Flekkøy EG, Hansen A, Måløy KJ. Film flow dominated simultaneous flow of two viscous incompressible fluids through a porous medium. *Front Phys.* (2014) **2**:63. doi: 10.3389/fphy.2014.00063
4. Wyckoff RD, Botset HG. The flow of gasliquid mixtures through unconsolidated sands. *J Appl Phys.* (1936) **7**:325. doi: 10.1063/1.1745402
5. Leverett MC. Capillary behavior in porous solids. *Trans AIME.* (1941) **142**:152. doi: 10.2118/941152-G
6. Brooks RH, Corey AT. Hydraulic properties of porous media. In: Corey AT, Dils RE and Yevdjevich VM, editors. *Hydrology Papers 3*. Fort Collins, CO: Colorado State University (1964). p. 27.
7. Lake LW. *Enhanced Oil Recovery*. Englewood Cliffs, NJ: Prentice Hall (1989).
8. McAdams WH, Woods WK, Heroman LC Jr. Vaporization inside horizontal tubes-II: Benzene-oil mixtures. *Trans ASME.* (1942) **64**:193.
9. Cicchitti A, Lombardi C, Silvestri M, Soldaini G, Zavattarelli R. Two-phase cooling experiments: Pressure drop, heat transfer and burnout measurements. *Energia Nucl.* (1960) **7**:407.
10. Awad M, Muzychka YS. Effective property models for homogeneous two-phase flows. *Exp Therm Fluid Sci.* (2008) **33**:106. doi: 10.1016/j.expthermflusci.2008.07.006
11. Sinha S, Hansen A, Bedeaux D, Kjelstrup S. Effective rheology of bubbles moving in a capillary tube. *Phys Rev E.* (2013) **87**:025001. doi: 10.1103/PhysRevE.87.025001
12. Straley JP. Critical exponents for the conductivity of random resistor lattices. *Phys Rev B.* (1977) **15**:5733. doi: 10.1103/PhysRevB.15.5733
13. Kirkpatrick S. Percolation and conduction. *Rev Mod Phys.* (1973) **45**:574. doi: 10.1103/RevModPhys.45.574
14. Lichtenecker K, Rother K. Die Herleitung des logarithmischen Mischungsgesetzes aus allgemeinen Prinzipien der stationären Strömung. *Phys Z.* (1931) **32**:255.
15. Guéguen Y, Palciauskas V. *Introduction to the Physics of Rocks*. Princeton, NJ: Princeton University Press (1994).
16. Todd MG, Shi FG. Complex permittivity of composite systems: a comprehensive interphase approach. *IEEE Trans Dielectr Electr Insul.* (2005) **12**:601. doi: 10.1109/TDEI.2005.1453466
17. Brovelli A, Cassiani C. A combination of the Hashin-Shtrikman bounds aimed at modelling electrical conductivity and permittivity of variably saturated porous media. *Geophys J Int.* (2010) **180**:225. doi: 10.1111/j.1365-246X.2009.04415.x
18. Aker E, Måløy KJ, Hansen A, Batrouni GG. A two-dimensional network simulator for two-phase flow in porous media. *Transp Porous Media.* (1998) **32**:163. doi: 10.1023/A:1006510106194
19. Sinha S, Bender AT, Danczyk M, Keepseagle K, Prather CA, Bray JM, et al. Effective rheology of two-phase flow in three-dimensional porous media: Experiment and simulation. *Transp Porous Media.* (2017) **119**:77. doi: 10.1007/s11242-017-0874-4
20. Erpelding M, Sinha S, Tallakstad KT, Hansen A, Flekkøy EG, Måløy KJ. History independence of steady state in simultaneous two-phase flow through two-dimensional porous media. *Phys Rev E.* (2013) **88**:053004. doi: 10.1103/PhysRevE.88.053004
21. Gjennestad MA, Vassvik M, Kjelstrup S, Hansen A. Stable and efficient time integration of a dynamic pore network model for two-phase flow in porous media. *Front Phys.* (2018) **13**:56. doi: 10.3389/fphy.2018.00056
22. Sinha S, Hansen A. Effective rheology of immiscible two-phase flow in porous media. *Europhys Lett.* (2012) **99**:44004. doi: 10.1209/0295-5075/99/44004
23. Hansen A, Sinha S, Bedeaux D, Kjelstrup S, Gjennestad MA, Vassvik M. Relations between seepage velocities in immiscible, incompressible two-phase flow in porous media. *Transp Porous Media.* (2018) **125**:565. doi: 10.1007/s11242-018-1139-6

24. Langglois WE. *Slow Viscous Flow*. New York, NY: The Macmillan Company (1964).
25. Jia P, Dong M, Dai L, Yao J. Slow viscous flow through arbitrary triangular tubes and its application in modelling porous media flows. *Transp Porous Media*. (2008) **74**:153. doi: 10.1007/s11242-007-9187-3
26. Ody CP, Baroud CN, de Langre E. Transport of wetting liquid plugs in bifurcating microfluidic channels. *J Colloid Interface Sci*. (2007) **308**:231. doi: 10.1016/j.jcis.2006.12.018
27. Liu X, Zhang C, Yu W, Deng Z, Chen Y. Bubble breakup in a microfluidic T-junction. *Sci Bull*. (2016) **61**:811. doi: 10.1007/s11434-016-1067-1
28. Gunstensen AK, Rothman DH, Zaleski S, Zanetti G. Lattice Boltzmann model of immiscible fluids. *Phys Rev A*. (1991) **43**:4320. doi: 10.1103/PhysRevA.43.4320
29. Rothman DH, Zaleski S. *Lattice-Gas Cellular Automata: Simple Models of Complex Hydrodynamics*. Cambridge: Cambridge University Press (2004).
30. Tørå G, Øren PE, Hansen A. A dynamic network model for two-phase flow in porous media. *Transp Porous Media*. (2012) **92**:145. doi: 10.1007/s11242-011-9895-6

Conflict of Interest Statement: The authors declare that the research was conducted in the absence of any commercial or financial relationships that could be construed as a potential conflict of interest.

Paper VI

M. Aa. Gjennestad, M. Winkler, and A. Hansen. Pore network modeling of the effects of viscosity ratio and pressure gradient on steady-state incompressible two-phase flow in porous media. *Transport in Porous Media* 132 (2020), pp. 355–379. DOI: 10.1007/s11242-020-01395-z

Transport in Porous Media
https://doi.org/10.1007/s11242-020-01395-z

Pore Network Modeling of the Effects of Viscosity Ratio and Pressure Gradient on Steady-State Incompressible Two-Phase Flow in Porous Media

Magnus Aa. Gjennestad[1] · **Mathias Winkler**[1] · **Alex Hansen**[1]

Received: 18 November 2019 / Accepted: 19 February 2020

Abstract
We perform steady-state simulations with a dynamic pore network model, corresponding to a large span in viscosity ratios and capillary numbers. From these simulations, dimensionless steady-state time-averaged quantities such as relative permeabilities, residual saturations, mobility ratios and fractional flows are computed. These quantities are found to depend on three dimensionless variables, the wetting fluid saturation, the viscosity ratio and a dimensionless pressure gradient. Relative permeabilities and residual saturations show many of the same qualitative features observed in other experimental and modeling studies. The relative permeabilities do not approach straight lines at high capillary numbers for viscosity ratios different from 1. Our conclusion is that this is because the fluids are not in the highly miscible near-critical region. Instead they have a viscosity disparity and intermix rather than forming decoupled, similar flow channels. Ratios of average mobility to their high capillary number limit values are also considered. Roughly, these vary between 0 and 1, although values larger than 1 are also observed. For a given saturation, the mobilities are not always monotonically increasing with the pressure gradient. While increasing the pressure gradient mobilizes more fluid and activates more flow paths, when the mobilized fluid is more viscous, a reduction in average mobility may occur.

Keywords Porous media · Two-phase flow · Steady-state · Pore network model

1 Introduction

A number of different modeling approaches have been applied to study two-phase flow in porous media. These include direct numerical simulations (DNS), which employ, e.g., the volume-of-fluid method (Raeini et al. 2012) or the level-set method (Jettestuen et al. 2013; Gjennestad and Munkejord 2015) to keep track of the fluid interfaces, lattice-Boltzmann methods (Ramstad et al. 2012; Armstrong et al. 2016) and pore network models. Recently, several of these methods were compared in a benchmark study

✉ Magnus Aa. Gjennestad
magnus.aa.gjennestad@ntnu.no; magnus@aashammer.net

[1] PoreLab and Department of Physics, Norwegian University of Science and Technology, Trondheim, Norway

Published online: 07 March 2020

by Zhao et al. (2019), where participants were asked to reproduce experimentally studied transient fluid displacement processes at different capillary numbers and wettability conditions. This benchmark study, and the bulk of works in the literature, focuses on transient processes. Less attention has been given to pore-scale modeling and experiments on steady-state flow. In steady state, fluids may flow and interfaces move on the pore scale. However, the total flow rates and average pressure drop for a sufficiently large representative elementary volume fluctuate around well-defined time-averaged values (Erpelding et al. 2013; Rücker et al. 2015; Hansen et al. 2018). Our focus here is on such states and their corresponding time-averaged steady-state properties.

On the modeling side, part of the explanation for the limited focus on steady state is probably that steady-state simulations require longer simulation times compared to transient processes. While breakthrough of the invading phase typically happens for simulation times corresponding to much less than one pore volume of flow in transient cases, several pore volumes may be required to obtain decent time averages of steady-state quantities.

In spite of this, some studies on steady-state two-phase flow have been carried out. Avraam and Payatakes (1995) performed quasi-2D micro-model experiments, varied the capillary number, the viscosity ratio and the flow rate ratio, and found four different flow regimes. They also studied relative permeabilities. Steady-state simulations with a pore network model of the Aker type (Aker et al. 1998b) have also been performed by Knudsen et al. (2002), Knudsen and Hansen (2002), Ramstad and Hansen (2006), Tørå et al. (2009), Sinha et al. (2017) and Sinha et al. (2019b). In particular, Knudsen et al. (2002) performed simulations with equal viscosities and one value for the interfacial tension, and studied the effect of changing total flow rate on fractional flow and relative permeabilities. Results for equal viscosities are interesting and applicable in some cases, e.g., for oil and water (Oak et al. 1990). For other applications, e.g., sequestration of supercritical CO_2 (Bennion and Bachu 2005) and gas–liquid flows such as in fuel cells, viscosity contrast should be taken into account.

The aim of this work is to shed light on how different steady-state flow properties behave as pressure gradients are increased from values corresponding to moderate capillary numbers around 10^{-3}–10^{-4} to the high capillary number limit. Furthermore, we aim to assess the impact of viscosity ratio in this context. To this end, we perform steady-state simulations using a dynamic pore network model of the Aker type (Aker et al. 1998b; Sinha et al. 2019a) to represent a block of porous material. In each simulation, the time evolution of the fluid configurations in the network is resolved, yielding a time series of total flow rates and average pressure drops for the entire network. These time series are subsequently time-averaged to obtain steady-state values that are used to calculate quantities such as relative permeabilities, fractional flow and capillary number. We give results from more than 6000 such steady-state simulations that cover a large range of viscosity ratios and capillary numbers. To aid further research, the simulation data are published along with this article.

In the simulations, we utilize a new time step criterion in the numerical solution method (Gjennestad et al. 2018) to perform numerically stable simulations at low and moderate capillary numbers. The new methodology has an important effect on capillary numbers below 10^{-3}. In addition, we make extensive use of results from a recent study of the high capillary number regime (Sinha et al. 2019b) in the analysis of the results.

The discussion is restricted to capillary numbers above 10^{-4}, where history-dependence of the steady-state quantities is negligible (Knudsen et al. 2002; Erpelding et al. 2013). At lower capillary numbers, steady-state quantities are harder to define and calculate. To allow for a discussion which is as general as possible, and which allows for comparison with

other studies of slightly different systems, we focus on dimensionless steady-state quantities, such as relative permeabilities, mobility ratios and fractional flow.[1]

The chosen pore network model is of the Aker type (Aker et al. 1998b). It has several properties that are advantageous when computing steady-state quantities. First, it is dynamic and thus captures the effects of both viscous and capillary forces. Second, it can be solved in a numerically stable manner at arbitrarily low capillary numbers (Gjennestad et al. 2018). Third, it is possible to apply periodic boundary conditions, keeping the saturation constant and eliminating effects of saturation gradients. Furthermore, it is computationally cheap, making the study of large enough systems over long enough times possible.

In spite of these advantages, however, the model also has some limitations. In particular, film flow is not accounted for. An extension of the model that includes film flow has been developed (Tørå et al. 2012), but it is computationally more demanding than the present model and is therefore not used here. While film flow effects could, in principle, also be captured, e.g., by a DNS or lattice-Boltzmann simulations, very high spatial resolution is required to resolve such films properly (Zhao et al. 2019). This makes such an approach prohibitively expensive for steady-state calculations, especially when a large number of them are desired.

The rest of the paper is structured as follows. In Sect. 2, we describe the system under consideration, define some important steady-state flow properties and discuss the high capillary number limit. In Sect. 3, we describe the pore network model used, the numerical methods used to solve it and the procedures used to obtain steady-state time averages in some detail. Results are presented and discussed in Sect. 4, and concluding remarks are given in Sect. 5.

2 Steady-State Flow

In this section, we define the system under study, some quantities that will be used to describe steady-state flow and discuss the high capillary number limit.

The system we consider is a block of porous material, as illustrated in Fig. 1. It has cross-sectional area A and thickness Δx in the direction of flow (the x-direction). The volume of the block is

$$V = A\Delta x. \tag{1}$$

The pore space volume in the block is V_p, so that the porosity is

$$\varphi = V_\mathrm{p}/V. \tag{2}$$

The pore space is occupied by two fluids, where one is more wetting toward the pore walls than the other. In the following, we will call the more wetting fluid wetting (w) and the less wetting fluid non-wetting (n). The fluids are assumed to be incompressible and S_w is the wetting fluid saturation, i.e., the fraction of the pore space volume occupied by the wetting fluid.

[1] These quantities are used to provide a familiar framework of dimensionless quantities in which results are presented and discussed. However, other quantities could also, in principle, be used to convey the same information. One example is the velocities presented by Hansen et al. (2018).

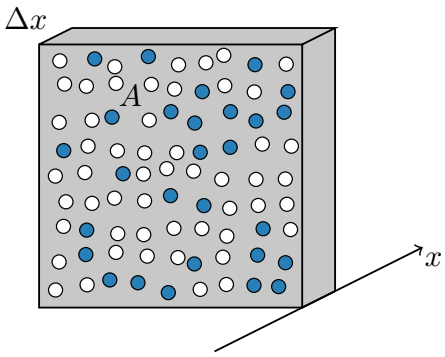

Fig. 1 Illustration of the system under consideration, a block of porous material. The porous matrix is shown in gray, pores occupied by the wetting fluid in white and pores filled by the non-wetting fluid in blue. The block has thickness Δx in the x-direction and cross-sectional area A

A pressure difference, either constant or fluctuating, exists across the porous block. This causes the wetting and non-wetting fluids to flow at time-dependent rates $\tilde{Q}_\mathrm{w}(t)$ and $\tilde{Q}_\mathrm{n}(t)$, respectively. In a steady-state $\tilde{Q}_\mathrm{w}$ and $\tilde{Q}_\mathrm{n}$ may fluctuate, but do so around a well-defined time-averaged value (Erpelding et al. 2013; Rücker et al. 2015; Hansen et al. 2018). We shall be most concerned with such time averages, which we call the steady-state flow properties. The steady-state wetting flow rate is defined as

$$Q_\mathrm{w} = \frac{1}{t_2 - t_1} \int_{t_1}^{t_2} \tilde{Q}_\mathrm{w}(t)\, \mathrm{d}t, \tag{3}$$

where $[t_1, t_2]$ is the time period of averaging. The steady-state non-wetting flow rate and the steady-state pressure difference Δp are defined analogously.[2] The steady-state total flow rate is,

$$Q = Q_\mathrm{w} + Q_\mathrm{n}, \tag{4}$$

and the fractional flow of wetting fluid is

$$F_\mathrm{w} = Q_\mathrm{w}/Q. \tag{5}$$

The volume-averaged fluid velocity in the pore space, the seepage velocity, is

$$v = Q/\varphi A, \tag{6}$$

and the average mobility is

$$m = -v/(\Delta p/\Delta x). \tag{7}$$

In the literature, description of two-phase flow in porous media is typically done in terms of the relative permeabilities $\kappa_\mathrm{w}^\mathrm{r}$ and $\kappa_\mathrm{n}^\mathrm{r}$. These are related to the steady-state properties Q_w, Q_n and Δp by

[2] We use tildes to distinguish the time time-dependent, possibly fluctuating $\tilde{Q}$, $\tilde{Q}_\mathrm{w}$, $\tilde{Q}_\mathrm{n}$ and $\Delta\tilde{p}$ from the time-averaged or constant Q, Q_w, Q_n and Δp.

$$\frac{Q_{\mathrm{w}}}{A} = -\frac{\kappa_{\mathrm{w}}^{\mathrm{r}}\kappa}{\mu_{\mathrm{w}}}\frac{\Delta p}{\Delta x}, \tag{8}$$

$$\frac{Q_{\mathrm{n}}}{A} = -\frac{\kappa_{\mathrm{n}}^{\mathrm{r}}\kappa}{\mu_{\mathrm{n}}}\frac{\Delta p}{\Delta x}. \tag{9}$$

Herein, μ_{w} and μ_{n} are the viscosities of the wetting and non-wetting fluids, respectively, and κ is the absolute permeability of the porous medium.

When measuring relative permeabilities (Oak et al. 1990; Bennion and Bachu 2005) and when using relative permeability models to do continuum-scale calculations, it is often only their dependence on S_{w} which is considered. It is, however, well established that variation with viscosity ratio $M = \mu_{\mathrm{n}}/\mu_{\mathrm{w}}$ and capillary number Ca cannot, in general, be neglected (Avraam and Payatakes 1995; Bardon and Longeron 1980; Datta et al. 2014; Armstrong et al. 2016; Guo et al. 2015).

2.1 The High Capillary Number Limit

Even though the relative permeabilities are dependent on capillary number, there seems to be general agreement in the literature that this dependence disappears at high capillary numbers (Bardon and Longeron 1980; Avraam and Payatakes 1995; Whitson et al. 2003; Ramstad et al. 2012; Schechter and Haynes 1992; Sinha et al. 2019b). We call this the high-Ca limit.

In particular, Sinha et al. (2019b) studied the high-Ca limit obtained when the two fluids are driven through the porous medium by a large pressure gradient while retaining their immiscibility. For a pore network model and 2D lattice-Boltzmann simulations, they showed that the fluid velocity in this limit could be described by

$$v_{\mathrm{D}} = \lim_{\mathrm{Ca}\to\infty} v = -\frac{\kappa}{\bar{\mu}\varphi}\frac{\Delta p}{\Delta x}, \tag{10}$$

with an effective viscosity

$$\bar{\mu}^{\alpha} = S_{\mathrm{w}}\mu_{\mathrm{w}}^{\alpha} + S_{\mathrm{n}}\mu_{\mathrm{n}}^{\alpha}. \tag{11}$$

The exponent α depended on the degree of intermixing of the fluids, induced by the flow through the porous medium. Intermixing here means that the fluids flow as many small disconnected structures when well intermixed, while they flow as larger structures when less well intermixed. For highly intermixed flows containing small droplets, it was found that $\alpha = 1$, while for less well intermixed flows α was shown to decrease. For a flow regime with lubrication layers, where the two fluids flowed in parallel through the pores, $\alpha = -0.5$ was obtained.

These results for α may be illustrated by considering the following two examples. First, an exponent $\alpha = -1$ would be obtained if the porous medium were modeled by a bundle of identical capillary tubes, where each tube contains only one or the other of the two fluids. In this case, the fluids are not intermixed at all and their flows are completely decoupled. Second, consider the case where the tubes in the model each contain a train of bubbles, with the same saturation in each tube. In this case, the fluids must be considered well intermixed and there is strong coupling between their flows. They are in fact forced to have same velocity. The corresponding exponent would be $\alpha = 1$. The degree of intermixing

between the flow of the two fluids, resulting in the coupling between their flows being strong or weak, thus determines α. In a real porous medium and in a network model, one might expect partial coupling of the flows and an exponent somewhere in between -1 and 1. This was indeed what was found by Sinha et al. (2019b). For the pore network model and porous medium studied here, it was shown that $\alpha = 0.6$.

Many other works in the literature refer to the more general idea of a high-Ca limit (Avraam and Payatakes 1995; Whitson et al. 2003; Ramstad et al. 2012; Armstrong et al. 2016). However, the prevailing view seems to be that the relative permeabilities approach straight lines at high capillary numbers (Bardon and Longeron 1980; Avraam and Payatakes 1995; Whitson et al. 2003; Ramstad et al. 2012; Schechter and Haynes 1992), i.e.,

$$\lim_{\mathrm{Ca}\to\infty} \kappa_{\mathrm{w}}^{\mathrm{r}} = S_{\mathrm{w}}, \tag{12}$$

$$\lim_{\mathrm{Ca}\to\infty} \kappa_{\mathrm{n}}^{\mathrm{r}} = S_{\mathrm{n}}. \tag{13}$$

To show how straight-line relative permeabilities are compatible with the results from Sinha et al. (2019b), we introduce (8), (9), (12) and (13) and into (6) and express the flow velocity in the high-Ca limit as

$$v_{\mathrm{D}} = -\frac{\kappa}{\varphi}\left(\frac{S_{\mathrm{w}}}{\mu_{\mathrm{w}}} + \frac{S_{\mathrm{n}}}{\mu_{\mathrm{n}}}\right)\frac{\Delta p}{\Delta x}. \tag{14}$$

This result is a special case of (10) with $\alpha = -1$.

Some of the experimental studies carried out that obtain straight-line relative permeabilities consider two phases near the mixture's critical point, see, e.g., Bardon and Longeron (1980); Schechter and Haynes (1992). In these cases, the interfacial tension approaches zero, and the capillary number infinity, as the phases are brought closer to the critical point. At the same time, the physical properties (e.g., composition, density and viscosity) of the two phases converge and they become chemically miscible. The two-phase flow then converges toward a literal single-phase flow, where the two phases have the same average velocity. The relative permeabilities approach (12) and (13) as a result. Furthermore, as $\mu_{\mathrm{n}} \to \mu_{\mathrm{w}}$ in this kind of miscible high-Ca limit, (14) reduces to the single-phase Darcy equation and the α-exponent becomes meaningless. This paper is concerned with immiscible two-phase flow and we therefore do not seek to approach the high-Ca limit through small interfacial tensions.

Another way one might obtain the straight-line relative permeabilities, in the event that the high-Ca limit is approached while the fluids retain their immiscibility, is if the two fluids occupy similar, but separate and decoupled parts of the porous medium. In this case, the porous medium can essentially be described by the capillary tube model that gave $\alpha = -1$ above. The relative permeability of each fluid is then proportional to the cross-sectional area of the porous medium available to it, i.e., proportional to the saturation. Such a flow configuration seems compatible with one of the basic assumptions in the relative permeability framework, namely the fluids flow through connected pathways and the fluid–fluid interfaces behave as rigid partitions between them (Armstrong et al. 2016).

While the view that relative permeabilities are straight lines at high capillary numbers seems to be the prevailing one, there are also studies which indicate that this may not always be the case (Delshad 1981; Fulcher et al. 1985; Armstrong et al. 2016). A particularly illustrative example is the lattice-Boltzmann simulations by Armstrong et al. (2016), where the wetting and non-wetting relative permeabilities seem

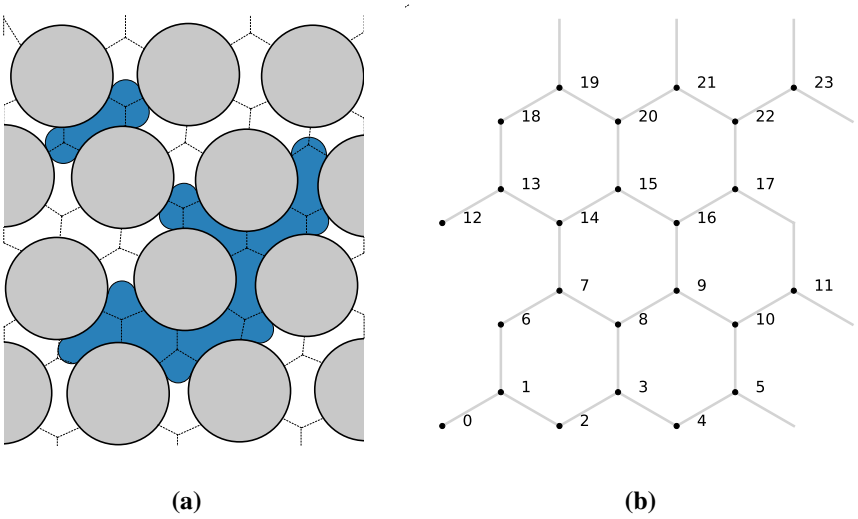

Fig. 2 Illustration of **a** wetting (white) and non-wetting fluid (blue) in a physical pore network and **b** the representation of this network in the model. The dashed lines in **a** indicate sections of the pore space volume that are each represented by one link in **b**. The intersection points of the dashed lines in **a** show the node locations in the model representation (**b**). Figures **a** and **b** are reproduced from Gjennestad et al. (2018)

to approach curves that are concave up and concave down, respectively. High capillary numbers were simulated by varying interfacial tension, viscosity and driving force. Armstrong et al. (2016) show conclusively that ganglion motion and intermixing of fluids occur in a manner that is clearly inconsistent with the idea that the two fluids flow through static pathways. The latter point is part of a discussion that goes back to the flow regime micro-model studies of flow regimes by Avraam and Payatakes (1995).

3 Pore Network Simulations

In this section, we describe in some detail the pore network model used in this study, the numerical methods used to solve it and the procedure for calculating the time-averaged quantities described in the previous section.

The pore network model is a dynamic model that takes both viscous and capillary forces into account. It keeps track of the fluid–fluid interface locations and evolves these in time according to the calculated pressures and flow rates in each pore. This provides a time series of the fluctuating total quantities $\tilde{Q}_{\mathrm{w}}$, $\tilde{Q}_{\mathrm{n}}$ and $\Delta\tilde{p}$ for the entire network, in steady state. Subsequently, these time series are averaged to get time-averaged steady-state flow properties.

Validation of the pore network modeling approach is provided through earlier works. These include Aker et al. (1998a, 2000), Erpelding et al. (2013), Sinha et al. (2017) and the benchmark study by Zhao et al. (2019).

3.1 Pore Network Model

The model describes flow of two incompressible and immiscible fluids (w and n) in a porous medium. The porous medium is represented by a network consisting of N nodes that are connected by M links. The nodes are each given an index $i \in [0, \ldots, N-1]$, and the links are identified by the two nodes ij that they connect. An example pore network is shown in Fig. 2. The nodes have no volume, and the pore space volume is thus assigned to the links. Furthermore, it is assumed that each fluid fills the entire link cross sections. The location of a fluid–fluid interface can then be described by a single number which gives its position in the link. For each link, the vector $\mathbf{z}_{ij}$ contains the positions of the fluid interfaces in that link.

The flow in each link is treated in a one-dimensional fashion, averaged over the link cross sections. We consider flows in relatively small cross sections only and therefore neglect any effects of fluid inertia. The volumetric flow rate from node j to node i through the link connecting the two nodes is then given by,

$$q_{ij} = -\lambda_{ij}(\mathbf{z}_{ij})\{p_i - p_j - c_{ij}(\mathbf{z}_{ij})\}. \tag{15}$$

Herein, p_i is the pressure in node i, λ_{ij} is the link's mobility and c_{ij} is the net pressure difference across the link due to its fluid interfaces. Both λ_{ij} and c_{ij} depend on the interface positions $\mathbf{z}_{ij}$. For two nodes i and j not connected by a link, $\lambda_{ij} = 0$. Applying mass conservation at each node i yields,

$$\sum_j q_{ij} = 0. \tag{16}$$

The cross-sectional area of link ij is a_{ij}. The interface positions $\mathbf{z}_{ij}$ therefore evolve in time according to the advection equation,

$$\frac{\mathrm{d}}{\mathrm{d}t}\mathbf{z}_{ij} = \frac{q_{ij}}{a_{ij}}, \tag{17}$$

when sufficiently far away from the nodes. Close to the nodes, they are subject to additional models that account for interface interactions in the nodes. This is further described in Gjennestad et al. (2018).

3.1.1 Link Mobility Model

The link mobility depends on link geometry and fluid viscosities. We assume cylindrical links when computing the mobilities and thus

$$\lambda_{ij}(\mathbf{z}_{ij}) = \frac{\pi r_{ij}^4}{8 L_{ij} \mu_{ij}(\mathbf{z}_{ij})}. \tag{18}$$

Here, L_{ij} is the link length, r_{ij} is the link radius and $\mu_{ij}(\mathbf{z}_{ij})$ is the volume-weighted average of the fluid viscosities μ_w and μ_n.

3.1.2 Interfacial Pressure Discontinuity Model

There may be zero, one or more interfaces in each link. Their positions along the link are contained in $\mathbf{z}_{ij}$. Each element in $\mathbf{z}_{ij}$ is thus between 0 and L_{ij}. The symbol c_{ij} denotes the

sum of the interfacial pressure discontinuities in link ij. We assume that the links are much wider near the ends than in the middle and that the pressure discontinuities become negligibly small for interfaces near the ends. The pressure discontinuities are therefore modeled by

$$c_{ij}\left(\mathbf{z}_{ij}\right) = \frac{2\sigma_{\text{wn}}}{r_{ij}} \sum_{z \in \mathbf{z}_{ij}} (\pm 1)\{1 - \cos\left(2\pi\chi(z)\right)\}. \tag{19}$$

Herein, σ_{wn} is the interfacial tension and

$$\chi(z) = \begin{cases} 0, & \text{if } z < r_{ij}, \\ \frac{z - r_{ij}}{L_{ij} - 2r_{ij}}, & \text{if } r_{ij} < z < L_{ij} - r_{ij}, \\ 1, & \text{if } z > L_{ij} - r_{ij}. \end{cases} \tag{20}$$

The effect of the χ-function is to introduce zones of length r_{ij} at each end of the links where the pressure discontinuity of any interface is zero.

3.2 Numerical Solution Method

Solving the pore network model numerically involves stepping the fluid–fluid interface locations forward in time, from one discrete point in time to the next. This is be accomplished by applying a Runge–Kutta method to the M ODEs, one for each link, given by (17). Each evaluation of the right-hand sides during the integration requires simultaneously solving the mass conservation equations (16) and the constitutive equations (15) for the flow rate in each link.

The time at the discrete point n is

$$t^{(n)} = \sum_{i=0}^{n-1} \Delta t^{(i)}, \tag{21}$$

where the time step length $\Delta t^{(i)}$ is the difference between $t^{(i+1)}$ and $t^{(i)}$. For ease of notation, we let quantities evaluated at the discrete time points be denoted by their associated time point index in superscript, e.g.,

$$q_{ij}^{(n)} = q_{ij}\left(t^{(n)}\right). \tag{22}$$

Mobilities and pressure discontinuities with superscripts are evaluated with the interface positions at the time point indicated,

$$\lambda_{ij}^{(n)} = \lambda_{ij}\left(\mathbf{z}_{ij}^{(n)}\right), \tag{23}$$

$$c_{ij}^{(n)} = c_{ij}\left(\mathbf{z}_{ij}^{(n)}\right). \tag{24}$$

In this work, we use the forward Euler method to integrate the ODEs (17). However, other and more sophisticated solution methods can also be used (Gjennestad et al. 2018). Applying the forward Euler method to (17), we get

$$\mathbf{z}_{ij}^{(n+1)} = \mathbf{z}_{ij}^{(n)} + \Delta t^{(n)} \frac{q_{ij}^{(n)}}{a_{ij}}. \tag{25}$$

The link flow rates herein are calculated by introducing the constitutive equation (15), evaluated at the current interface positions,

$$q_{ij}^{(n)} = -\lambda_{ij}^{(n)} \left\{ p_i^{(n)} - p_j^{(n)} - c_{ij}^{(n)} \right\}, \tag{26}$$

into the mass conservation equations (16). This yields a system of linear equations, with one equation

$$\sum_j \lambda_{ij}^{(n)} p_j^{(n)} - p_i^{(n)} \sum_j \lambda_{ij}^{(n)} = -\sum_j \lambda_{ij}^{(n)} c_{ij}^{(n)}, \tag{27}$$

for each node i with an unknown pressure.

One forward Euler time step is then taken by first obtaining the pressure in each node by solving the linear system, using the current interface positions. Subsequently, the link flow rates are calculated using (26) and the interface positions updated according to (25).

3.2.1 Time Step Restrictions

Since we use the explicit forward Euler method to integrate the interface positions in time, short enough time steps must be chosen to ensure numerical stability. The length of time step n is set according to the criteria in Gjennestad et al. (2018),

$$\Delta t^{(n)} = \min \left(\Delta t_{\mathrm{c}}^{(n)}, \Delta t_{\mathrm{a}}^{(n)} \right), \tag{28}$$

where

$$\Delta t_{\mathrm{a}}^{(n)} = C_{\mathrm{a}} \min_{ij} \left(\frac{a_{ij} L_{ij}}{q_{ij}^{(n)}} \right), \tag{29}$$

$$\Delta t_{\mathrm{c}}^{(n)} = C_{\mathrm{c}} \min_{ij} \left(\frac{2 a_{ij}}{\lambda_{ij}^{(n)} \left| \sum_{z \in \mathbf{z}_{ij}^{(n)}} \frac{\partial c_{ij}}{\partial z} \right|} \right), \tag{30}$$

and the parameters C_{a} and C_{c} are set to 0.1 and 0.9, respectively.

3.2.2 Boundary Conditions

We carry out simulations in a network that can be laid out in two dimensions, as illustrated in Fig. 2b. The network is periodic both in the flow direction and in the transverse direction. Two different boundary conditions are explored: (1) A constant pressure difference of Δp is applied across the periodic boundary in the flow direction, and (2) a constant total flow rate Q is prescribed. The length of the network in the flow direction is denoted Δx and the average pressure gradient in the network is thus $\Delta p / \Delta x$.

The boundary conditions corresponding to a constant applied Δp can be incorporated directly into the linear system (27) when this is solved during each time step. This is done by adding to or subtracting from each equation i in the linear system a term $\lambda_{ij}^{(n)}\Delta p$ for each link ij that extends across the periodic boundary.

The boundary conditions corresponding to a prescribed flow rate Q are applied as follows. Since the model is linear, the total flow rate is related to the current pressure drop by

$$Q = C_1 + C_2\Delta\tilde{p}, \tag{31}$$

where the constants C_1 and C_2 depend on the current interface positions in a non-trivial way. By selecting two different, but otherwise arbitrary, pressure drops $\Delta\tilde{p}_1$ and $\Delta\tilde{p}_2$ and solving the linear system (27) for both of them, we obtain the corresponding total flow rates Q_1 and Q_2. The quantities C_1 and C_2 can then be calculated from,

$$C_1 = \frac{Q_2 - Q_1}{\Delta\tilde{p}_2 - \Delta\tilde{p}_1}, \tag{32}$$

$$C_2 = \frac{Q_2\Delta\tilde{p}_1 - Q_1\Delta\tilde{p}_2}{\Delta\tilde{p}_1 - \Delta\tilde{p}_2}. \tag{33}$$

Subsequently, (31) can be solved for the pressure difference $\Delta\tilde{p}$ necessary to get the prescribed total flow rate Q, and a forward Euler time step can be taken with this pressure difference incorporated into the linear system (27).

3.3 Computation of Steady-State Time Averages from Network Simulations

The porous medium we consider is modeled by a network of links, and the total volume of the links is the pore volume V_p. The network is embedded in a three-dimensional block of solid material with thickness Δx in the flow direction and cross-sectional area A. The volume V of the porous block and its porosity φ are then easily calculated by (1) and (2), respectively.

The saturation S_w may be computed at any time during the simulation, by adding up the fluid volumes for all links. However, since we use periodic boundary conditions, S_w is a constant in each simulation. So is $S_\mathrm{n} = 1 - S_\mathrm{w}$.

In the case of constant applied pressure gradient $\Delta p/\Delta x$, the quantities that we need to compute from the actual simulations are Q, Q_w and Q_n. These are time averages of the fluctuating quantities $\tilde{Q}$, $\tilde{Q}_\mathrm{w}$ and $\tilde{Q}_\mathrm{n}$. The model is stepped forward in time as described in the previous section. We approximate the time-average Q by summing over the total flow rates $\tilde{Q}^{(n)}$ at each time step n (after steady state has been reached),

$$Q = \frac{\sum_n \tilde{Q}^{(n)}\Delta t^{(n)}}{\sum_n \Delta t^{(n)}}. \tag{34}$$

The time-averaged quantities Q_w and Q_n are calculated from $\tilde{Q}_\mathrm{w}^{(n)}$ and $\tilde{Q}_\mathrm{w}^{(n)}$ in an analogous manner.

The instantaneous flow rate $\tilde{Q}^{(n)}$ can be computed by constructing a plane cutting through the network, transverse to the flow direction, and adding together the flow rates $q_{ij}^{(n)}$ of all links intersecting the plane. We denote the set of intersecting links by B and add up,

$$\tilde{Q}^{(n)} = \sum_{ij \in B} q_{ij}^{(n)}. \tag{35}$$

Since the fluids are incompressible, it does not matter where this cut is made.

The instantaneous flow rate $\tilde{Q}_{\mathrm{w}}^{(n)}$ is computed by making several cuts, denote the set of cuts by C, and computing the sum

$$\tilde{Q}_{\mathrm{w}}^{(n)} = \frac{1}{|C|} \sum_{B \in C} \sum_{ij \in B} s_{ij}^{(n)} q_{ij}^{(n)}. \tag{36}$$

Herein, $|C|$ denotes the number of elements in C, i.e., the number of cuts, and $s_{ij}^{(n)}$ is the volume fraction of wetting fluid in the volume of fluid that flowed past the middle of link ij during time step n. $\tilde{Q}_{\mathrm{n}}^{(n)}$ is computed in an analogous manner. Having computed the time averages Q, Q_{w} and Q_{n} we may the obtain the time-averaged flow velocity, mobility, fractional flow and relative permeabilities using (6), (7), (5), (8) and (9).

If Q is fixed instead of $\Delta p/\Delta x$, the time-averaged value of the pressure gradient is computed by

$$\frac{\Delta p}{\Delta x} = \frac{\sum_n \Delta \tilde{p}^{(n)} \Delta t^{(n)}}{\Delta x \sum_n \Delta t^{(n)}}, \tag{37}$$

where $\Delta \tilde{p}^{(n)}$ is the pressure difference across the network during time step n.

Using steady-state averages calculated as described above, the capillary number is computed according to,

$$\mathrm{Ca} = \frac{\mu |Q|}{\varphi A \sigma_{\mathrm{wn}}}, \tag{38}$$

where the average viscosity μ is defined as,

$$\mu = S_{\mathrm{w}} \mu_{\mathrm{w}} + S_{\mathrm{n}} \mu_{\mathrm{n}}. \tag{39}$$

3.4 Dimensional Analysis

As can be surmised from the description above, the network and five numbers are given as input to steady-state simulations. In the case of constant pressure-difference boundary conditions, the five numbers are the fluid viscosities μ_{w} and μ_{n}, the fluid–fluid interfacial tension σ_{wn}, the pressure gradient $\Delta p/\Delta x$ and the saturation S_{w}. Any change in the steady-state averages is the response of the model to variations in these inputs. If we consider the network topology and aspect ratios fixed, and only allow for a linear scaling of the network size, any variations in the network can be described by a single length scale. We choose the average pore radius $\bar{r}$.

By the Buckingham π theorem (Rayleigh 1892), the total of six dimensional input variables can be reduced to three dimensionless variables. This means that any combination of the six inputs that give the same three dimensionless variables is similar and differs only in scale. Any dimensionless output from the model is therefore the same for the same values of the dimensionless input variables. One choice of dimensionless variables is

$$S_{\mathrm{w}}, \tag{40}$$

Table 1 Range of input parameters used in the steady-state pore network model simulations. For each combination of the input parameters listed, 21 values of S_w, evenly spaced on the interval [0, 1], were used. The corresponding ranges of the dimensionless variables M, Π and Ca are also given

Quantity	Minimum value	Maximum value	Unit
μ_w	5.0×10^{-4}	1.0×10^{-2}	Pa s
μ_n	5.0×10^{-4}	1.0×10^{-2}	Pa s
σ_{wn}	2.0×10^{-2}	3.0×10^{-2}	N m^{-1}
$-\Delta p/\Delta x$	3.9×10^{3}	8.0×10^{5}	Pa m^{-1}
$\bar{r}$	2.5×10^{-4}	7.8×10^{-4}	m
M	5.0×10^{-2}	2.0×10^{1}	–
Π	6.1×10^{-3}	8.1×10^{1}	–
Ca	4.0×10^{-4}	6.1×10^{-1}	–

$$M = \frac{\mu_n}{\mu_w}, \tag{41}$$

$$\Pi = \left|\frac{\Delta p}{\Delta x}\right| \frac{\bar{r}^2}{2\sigma_{wn}}, \tag{42}$$

where M is the viscosity ratio. The variable Π is a dimensionless pressure gradient. It represents the ratio of the average pressure drop over a length $\bar{r}$ to the Young–Laplace pressure difference over an interface in a pore of radius $\bar{r}$. In particular, when $\Pi = 1$, we have

$$\left|\frac{\Delta p}{\Delta x}\right| \bar{r} = \frac{2\sigma_{wn}}{\bar{r}}, \tag{43}$$

and the average pressure drop over the length $\bar{r}$ is equal to the typical Young–Laplace pressure difference.

Since it relates the average pressure drop to the capillary forces, Π may be expected to play a similar role as the capillary number. This should be true at least when capillary numbers are high and the average pressure drop is dominated by viscous contributions. However, Π is perhaps even more closely related to the ganglion mobilization number. This was defined by Avraam and Payatakes (1995) as the ratio between the driving force exerted on a ganglion and its resistance to motion resulting from capillary forces.

3.5 Simulations

Steady-state simulations were performed using the pore network model described in this section. All simulations were run on 72×48 hexagonal networks, similar to that shown in Fig. 2b. These networks consisted of 3456 nodes and 5184 links. All links had the same length L, and link radii were uniformly distributed between $0.1L$ and $0.4L$. For each of the 288 combinations of the input parameters listed in Table 1, 21 values of S_w were used, evenly spaced on the interval $[0, 1]$. In total, $288 \times 21 = 6048$ simulations were run. As this paper is concerned with immiscible two-phase flow, we do not use vanishingly small values of the interfacial tension. Time-averaged quantities were calculated from simulation results as described in Sect. 3.3. The averaging time corresponded to 10 pore volumes of flow.

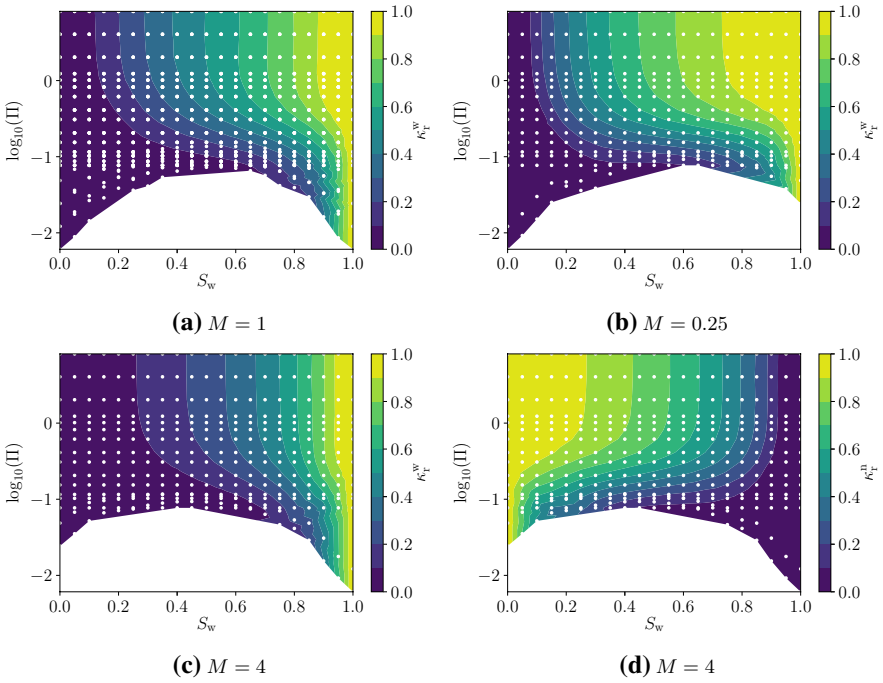

(a) $M = 1$ **(b)** $M = 0.25$

(c) $M = 4$ **(d)** $M = 4$

Fig. 3 Relative permeabilities for the wetting phase for **a** $M = 1$, **b** $M = 0.25$ and **c** $M = 4$. Relative permeabilities for the non-wetting phase and $M = 4$ are shown in **d**. Parameters where simulations have been performed are indicated by white dots, while values in between are obtained by interpolation. **a** Contains data from 1365 simulations, while **b**, **c** and **d** each contain data from 336

4 Results

In this section, we present and discuss the simulation results. We look first at relative permeabilities (Sect. 4.1), then residual saturations (Sect. 4.2), average flow velocities and mobilities (Sect. 4.3) and, finally, fractional flows (Sect. 4.4).

4.1 Relative Permeabilities

Relative permeabilities κ_w^r and κ_n^r are perhaps the most extensively studied properties in two-phase flow in porous media, and the most obvious dimensionless steady-state quantities to calculate from the pore network model. In Fig. 3, computed relative permeabilities are plotted against saturation S_w and the non-dimensional pressure gradient Π for three subsets of the simulations. Specifically, Fig. 3a, b, c shows relative permeabilities for the wetting phase and viscosity ratios M of 1, 0.25 and 4, respectively. Relative permeabilities for the non-wetting phase and a viscosity ratio of 4 are shown in Fig. 3d.

For each value of M, the relative permeability data fall on a single well-defined surface. This shows that the relative permeabilities produced by the model are indeed determined by the three dimensionless variables S_w, M and Π, in agreement with the dimensional analysis in Sect. 3.4. Bardon and Longeron (1980) mention that gravity

(Bond number), wettability (contact angle) and inertia (Reynolds number) could also affect the relative permeabilities. These effects are not considered in the present study, though gravity could be included in the model with relative ease.

When measuring relative permeabilities (Oak et al. 1990; Bennion and Bachu 2005) and when using relative permeability models for continuum-scale calculations, it is often only their dependence on S_w which is considered. Here, the calculated relative permeabilities are strongly dependent on Π, and they increase with increasing Π. There is a very strong correlation between Π and the capillary number, where high values of Π are also associated with high values of Ca. Thus, the results are consistent with those of Bardon and Longeron (1980), Avraam and Payatakes (1995), Armstrong et al. (2016) and Datta et al. (2014), who find that relative permeabilities increase with capillary number. This dependence seems to disappear, however, as $\Pi \to \infty$. For the viscosity ratios considered here, it disappears at $\Pi \sim 1$, where the contours in Fig. 3 approach vertical lines. At this Π-value, the average pressure drop over the length $\bar{r}$ is equal to the typical Young–Laplace interfacial pressure difference, as discussed in Sect. 3.4. The fact that the relative permeabilities become independent of the pressure gradient as capillary numbers increase is consistent with the high-Ca limit.

The general consensus in the literature (Bardon and Longeron 1980; Fulcher et al. 1985; Avraam and Payatakes 1995; Whitson et al. 2003; Ramstad et al. 2012; Schechter and Haynes 1992) seems to be that relative permeabilities approach straight lines (12) and (13), at high capillary numbers. In the equal-viscosity pore network simulations by Knudsen et al. (2002), this was found to be the case. Here, however, we find straight lines, i.e., equidistant contour lines in Fig. 3 for $\Pi \gtrsim 1$, only for $M \sim 1$. When M is different from unity, relative permeabilities converge to nonlinear functions of S_w (and M) in the high-Ca limit.

As discussed in Sect. 2.1, relative permeabilities form straight lines in the high-Ca limit if this is realized by approaching a mixture critical point. In such a case $\mathrm{Ca} \to \infty$ would necessarily happen at the same time as $M \to 1$ and our results would seemingly be in agreement with the literature consensus. However, our model assumes immiscible flow and it is questionable whether it can be relied on when the fluids become miscible.

Straight-line relative permeabilities could be obtained also in the immiscible high-Ca limit if the fluids flow in similar, decoupled flow channels. By visual inspection of fluid configurations, however, such decoupled flow channels are not found here (see, e.g., Fig. 10 in "Appendix" section). Instead, the fluids exhibit a large degree of intermixing and move as droplets or small ganglia at high capillary numbers. This was observed also by Sinha et al. (2019b), both in pore network model and lattice-Boltzmann simulations. Disconnected non-wetting droplets were also observed at high capillary numbers in the experiments by Avraam and Payatakes (1995), and were found to contribute significantly to the total flow rate, although connected pathways were also present.

We therefore conclude that our relative permeabilities deviate from straight lines at high capillary numbers because the fluids are not in the highly miscible near-critical region. Instead they have a viscosity disparity and intermix instead of forming decoupled flow channels. The effect of this on total mobility and fractional flow is discussed further in Sects. 4.3 and 4.4, respectively.

One example from the literature where relative permeabilities do not seem to form straight lines is found in Armstrong et al. (2016). Instead, they found a concave down κ_n^r and a concave up κ_w^r, similar to our results with $M > 1$ (see Fig. 3c, d). Their viscosity ratio was not given.

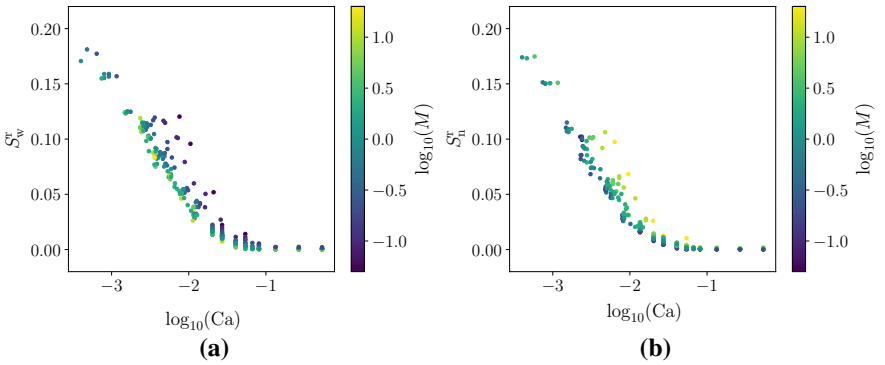

Fig. 4 Residual saturations for **a** the wetting fluid and **b** the non-wetting fluid. **a** and **b** each contain 288 data points, one for each of the 288 combinations of input parameters (see Sect. 3.5)

From Fig. 3, it is evident that the relative permeabilities follow a nonlinear curve not unlike those produced by the classical Corey-type correlations for the lowest values of Π, i.e., the lowest capillary numbers. When working with such correlations, it is typically assumed that there exists a low capillary number limit below which relative permeabilities become independent of the flow rate, and the correlations are therefore valid (for the fluids used in the measurements). Ramstad et al. (2012) mention that viscous forces start to influence the fluid transport at capillary numbers around 10^{-5}. This is consistent with the findings here, which are that relative permeabilities have a dependence on Π down to the lowest capillary numbers considered of approximately 10^{-4}. We emphasize that the definition of capillary number used here differs from that used in Ramstad et al. (2012), since it includes the porosity. Adoption of the definition from Ramstad et al. (2012) would reduce all capillary numbers reported here by approximately half an order of magnitude.

Qualitatively, the changes in the relative permeability curves with Ca in Armstrong et al. (2016) are similar to those found here for $M > 1$. In particular, their κ_n^r-curve shifts from a concave up shape at low Ca to a concave down shape at high Ca. We find the same here when $M > 1$ (Fig. 3d).

Avraam and Payatakes (1995) find from their experiments that both relative permeabilities increase with M. This is not the case here, at least not at high capillary numbers. They attribute this to the existence of films of the wetting fluid, which are not included in our model.

4.2 Residual Saturations

For both the wetting and non-wetting fluids, there are regions in Fig. 3 where the relative permeabilities are zero. This was seen by Knudsen et al. (2002) also, for $M = 1$. These regions correspond to irreducible/residual saturations, two other ubiquitous dimensionless quantities in two-phase porous media flow. The residual saturations are often defined as the saturation of one fluid that remains after flooding with the other. This property, defined in this way, is somewhat difficult to measure using the type of steady-state pore network model simulations performed here. Therefore, we have chosen to define the residual saturation of the wetting fluid as the saturation on the fractional flow curve (F_w plotted vs. S_w, all other input parameters kept constant) where the wetting fluid fractional flow falls below

a threshold value[3] of 10^{-4}. The residual non-wetting saturation is defined in an analogous manner.

Computed residual wetting and non-wetting saturations are shown in Fig. 4. Residual saturations increase as capillary numbers are reduced, in accordance with findings of Ramstad et al. (2012), Bardon and Longeron (1980), Datta et al. (2014) and Fulcher et al. (1985). Furthermore, they reach zero at capillary numbers around 0.1. This means that it is possible to flush out all of one fluid from the network model through flooding with the other, provided that the flow rate is high enough.

Bardon and Longeron (1980) observed that residual saturations were insensitive to changes in M, which is in agreement with our findings. However, wetting residual saturations are somewhat higher when the wetting fluid is more viscous and non-wetting residual saturations are a little higher when the non-wetting fluid is more viscous. It would seem that mobility of the minority fluid is impeded when it is more viscous than the majority fluid.

4.3 Average Flow Velocity and Mobility

The average mobility m and the average flow velocity v are other important quantities in two-phase flow. They are related through (7) and are discussed together here for reasons that will become apparent below.

Sinha et al. (2019b) studied the high-Ca limit of two-phase porous media flow. They found that, at high capillary numbers, the average flow velocity followed a Darcy-type equation (10), with an effective viscosity (11). The existence of this high-Ca limit motivates the study of the average flow velocity and the average mobility, relative to their limit values. Dividing (7) by (10) gives

$$v/v_{\mathrm{D}} = m/m_{\mathrm{D}}, \tag{44}$$

where m_{D} is the mobility in the high-Ca limit. The two quantities v/v_{D} and m/m_{D} are thus identical. Moreover, they are dimensionless and may be expected to vary, roughly, between 0 and 1. In particular, they should be 1 in the two single-phase cases, $S_{\mathrm{w}} = 1$ and $S_{\mathrm{n}} = 1$, and in the high-Ca limit.

Figure 5 shows v/v_{D} for $M = 1$, $M = 0.25$ and $M = 4$, plotted against S_{w} and Π. As expected, all data points collapse to 1 in both single-phase cases. Furthermore, each value of M corresponds to a single well-defined v/v_{D}-surface, in accordance with the dimensional analysis. Each constant-M surface reaches values close to 1 at the highest values of Π, in agreement with the findings of Sinha et al. (2019b) for the high-Ca limit.

Interestingly, there are some values of v/v_{D} that are larger than 1. This means that, at a given saturation, the average mobility is higher at some lower capillary number than in the high-Ca limit. This somewhat counter-intuitive effect occurs for the more disparate viscosity ratios, at saturations where the more viscous fluid is in minority. Figure 6a shows v/v_{D} plotted against Π, for $S_{\mathrm{w}} = 0.15$ and three different viscosity ratios, 0.25, 1 and 4. The data points with $M = 1$ converge to 1, the limit value, from below and relatively fast as Π increases. The data points with $M = 4$ also approach 1 from below, but

[3] The value of this threshold is based on the observation that fractional flow curves yielded by the pore network model for moderate capillary numbers are close to zero at low saturations before they increase sharply as saturation is increased. A threshold of 10^{-4} provides a reasonable estimate for where this occurs.

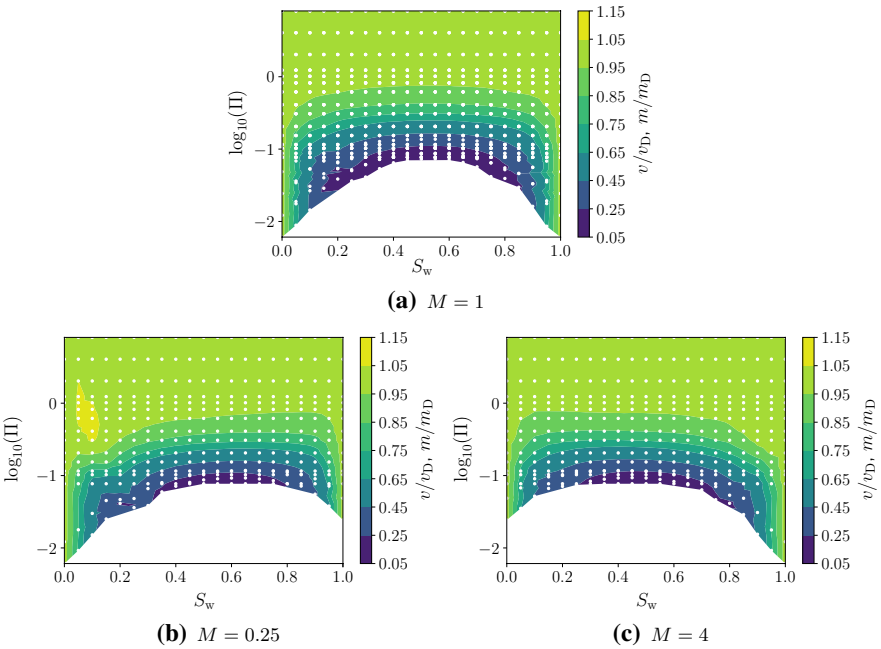

Fig. 5 Simulated values of v/v_D for viscosity ratios **a** $M = 1$, **b** $M = 0.25$ and **c** $M = 4$. Parameters where simulations have been performed are indicated by white dots, while values in between are obtained by interpolation. **a** Contains data from 1365 simulations, while **b** and **c** each contain data from 336

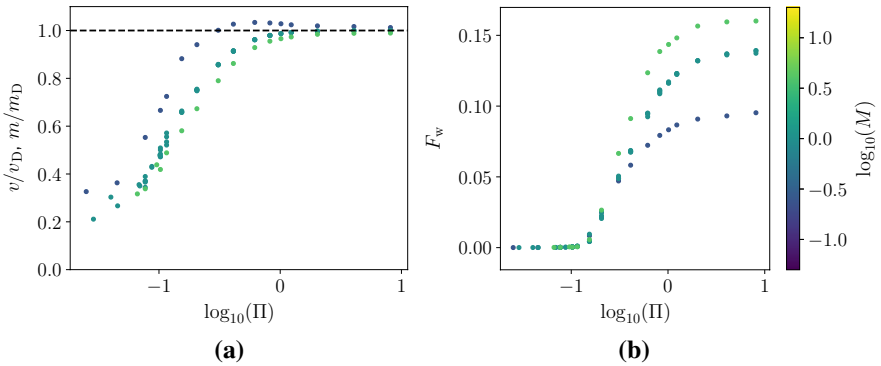

Fig. 6 **a** Calculated values of v/v_D for $S_w = 0.15$ and viscosity ratios of 0.25, 1 and 4. **b** Fractional flow for the same set of simulations as in **a**. Data in both **a** and **b** represent the $S_w = 0.15$ subsets of those in Fig. 5

slower. For the lower viscosity ratio $M = 0.25$, on the other hand, v/v_D increases fast, overshoots and then approaches 1 from above.

In Fig. 6b is shown the fractional flow for the same data points as in Fig. 6a. For the data points with $M = 1$, convergence of v/v_D to the limit value occurs as the fractional

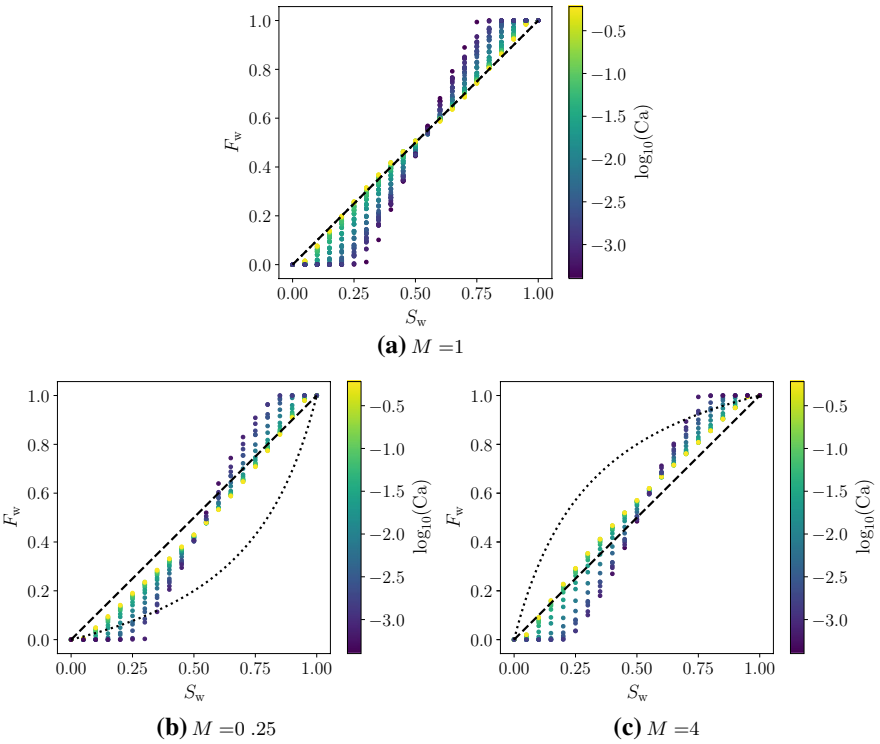

(a) $M = 1$

(b) $M = 0.25$

(c) $M = 4$

Fig. 7 Fractional flow data for **a** $M = 1$, **b** $M = 0.25$ and **c** $M = 4$. The dashed lines represent $F_w = S_w$ and the dotted lines represent the fractional flow obtained if the relative permeabilities were $\kappa_w^r = S_w$, see (12), and $\kappa_n^r = 1 - S_w$, see (13). **a** Contains data from 1365 simulations, while **b** and **c** each contain data from 336

flow approaches its limit value. The same is true for $M = 0.25$ and $M = 4$, although convergence is not yet complete for the largest Π-values considered.

In terms of mobility ratios m/m_D these observations may be understood as follows. At low pressure gradients, all wetting fluid is stuck, in the sense that $F_w = 0$, and the non-wetting fluid flows around it (see Fig. 6b). As the pressure gradient is increased, some of the wetting fluid is mobilized and F_w increases above zero. This results in more active flow paths for both fluids and a sharp increase in the average mobility for all three viscosity ratios. An example of such mobilization can be seen by comparing Figs. 8 and 9 in "Appendix" section.

For $M = 0.25$, average mobility reaches a maximum before all wetting fluid is mobilized, i.e., before F_w converges to its value in the high-Ca limit. This maximum is caused by the competition between two different effects. First, an increase in pressure gradient makes more flow paths available, increasing mobility. Second, F_w increases and the more viscous wetting fluid makes up a larger fraction of the flowing fluid. Thus, the average viscosity of the flowing fluid increases, reducing the average mobility. Eventually, a point is reached where the latter effect becomes more important and a further increase in the pressure gradient reduces the average mobility.

For $M = 1$, there is no such competition to generate a maximum, as the wetting and non-wetting fluids are equally viscous and mobilization of the wetting fluid does not affect the average viscosity.

For $M = 4$, the two effects are again present. However, since the wetting fluid is now less viscous, they both lead to an increase in mobility with an increase in pressure gradient and we see no maximum.

4.4 Fractional Flow

The fractional flow for three subsets of the performed simulations is shown in Fig. 7, for viscosity ratios 1, 4, and 0.25. The data in Fig. 7a for $M = 1$ are in qualitative agreement with those from Knudsen et al. (2002). They find $F_w \sim S_w$ at high capillary numbers and that deviation from the diagonal line representing $F_w = S_w$ increases as the capillary number is reduced. Furthermore, curves for a specific capillary number are asymmetric w.r.t. $S_w = 0.5$ and cross the diagonal line at $S_w > 0.5$, meaning that more of the curve lies below the diagonal than above it. This observation was explained by Knudsen et al. (2002) by the propensity for the wetting fluid to occupy narrower pores where the flow rate is lower.

By comparing Fig. 7b, c we may deduce some of the impact of the viscosity ratio on the fractional flow. At high capillary numbers, $F_w > S_w$ when $M > 1$, i.e., when the wetting fluid is less viscous. Conversely, $F_w < S_w$ when $M < 1$ and the wetting fluid is more viscous. The latter was observed also by Avraam and Payatakes (1995), at low viscosity ratios and high capillary number, the fractional flow curves tended to be concave up.

The dotted lines in Fig. 7b, c represent the fractional flows obtained if the relative permeabilities were $\kappa_w^r = S_w$ and $\kappa_n^r = 1 - S_w$, i.e., what would be expected at high capillary numbers if the fluids followed separate, similar flow channels. The fractional flows from the network model in this limit curve the same way as the dotted lines, but lie much closer to the diagonal. As noted before, our pore network model gives instead a large degree of fluid intermixing in the high-Ca regime (see, e.g., Fig. 10). In such an intermixed state, fluid velocities will be more tightly coupled. We therefore propose that, in the event that fluids intermix rather than form decoupled flow channels, the tighter coupling causes the fluids to flow with velocities that are more similar. Thus, the fractional flow curves lie closer to the diagonal.

At lower capillary numbers, the fractional flow curves obtain the classical S-shape, as in the case for $M = 1$. Also, as is intuitive and was observed by Avraam and Payatakes (1995), fractional flow for a given saturation and capillary number increases with viscosity ratio.

5 Conclusion

We have performed more than 6000 steady-state simulations with a dynamic pore network model of the Aker type, corresponding to a large span in viscosity ratios and capillary numbers. From these simulations, dimensionless time-averaged steady-state quantities such as relative permeabilities, residual saturations, mobility ratios and fractional flows were computed and discussed. By a dimensional analysis of the model, all dimensionless output was found to be functions of the saturation S_w, the viscosity ratio M and the dimensionless pressure gradient Π. Effects of wettability, gravity and inertia were not considered. These effects may add additional dimensionless variables whose impact could be studied in future work.

Calculated relative permeabilities and residual saturations showed many of the same qualitative features observed in other experimental and modeling studies. In particular, the relative permeabilities increased with capillary numbers and converged to a limit, dependent on M and S_w, at high capillary numbers. However, while consensus in the literature seems to be that relative permeabilities converge to straight lines at high capillary numbers, this was not the case for the results of the network model when $M \neq 1$.

Our conclusion is that our relative permeabilities deviate from straight lines at high capillary numbers because the fluids are not in the highly miscible near-critical region. Instead they have a viscosity disparity and intermix rather than forming decoupled, similar flow channels. Such intermixing behavior has been observed previously in pore network and lattice-Boltzmann simulations (Sinha et al. 2019b) and, to some extent, in experiments (Avraam and Payatakes 1995). However, it would be very interesting to see whether experimental studies specifically designed to induce intermixing and measure steady-state properties at high capillary numbers would produce relative permeability curves that are nonlinear in S_w.

Ratios of average mobility to their high capillary number limit values were also considered. These ratios varied, roughly, between 0 and 1, but values larger than 1 were also observed. For a given saturation, the mobilities were not always monotonically increasing with the pressure gradient. While increasing the pressure gradient mobilizes more fluid and activates more flow paths, when the mobilized fluid is more viscous, a reduction in average mobility may occur instead.

Acknowledgements Open Access funding provided by NTNU Norwegian University of Science and Technology (incl St. Olavs Hospital - Trondheim University Hospital. The authors would like to thank Signe Kjelstrup and Santanu Sinha for discussions and encouragement. This work was partly supported by the Research Council of Norway through its Centres of Excellence funding scheme, Project Number 262644.

Appendix: Example Fluid Distributions

In this section, we show example fluid distributions from steady-state simulations at different sets of parameters. We show two examples for each set of parameters, with a time difference between them corresponding to one pore volume of flow. For ease of viewing and discussion, the networks used in these illustrations are 12×8, much smaller than those used in the steady-state simulations described in Sect. 3.5.

Figures 8, 9 and 10 show example fluid configurations obtained during simulations with $S_w = 0.85$ and $M = 1$ and different dimensionless pressure gradients. Comparing them illustrates how more and more of the non-wetting fluid is mobilized as the magnitude of Π is increased.

In Fig. 8, $\log_{10}(\Pi) = -1.0$ and all interfaces remain stationary. Only the wetting fluid is moving ($F_w = 1.0$) and necessarily does so through connected pathways.

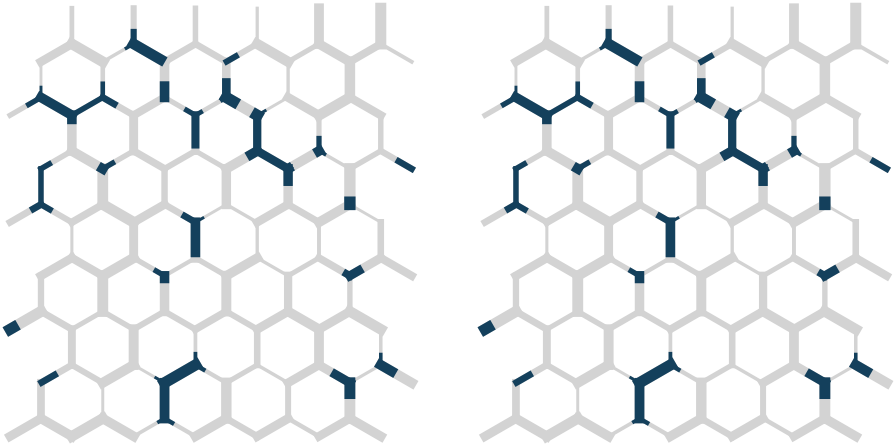

Fig. 8 Example fluid distributions for $S_w = 0.85$, $M = 1$ and $\log_{10}(\Pi) = -1.0$. Non-wetting fluid is blue, and wetting fluid is gray. The time difference between **a** and **b** corresponds to one pore volume of flow. All interfaces are stationary. Only the wetting fluid is moving ($F_w = 1.0$) through connected pathways. Drawn link widths are chosen for illustrative purposes and are not to scale

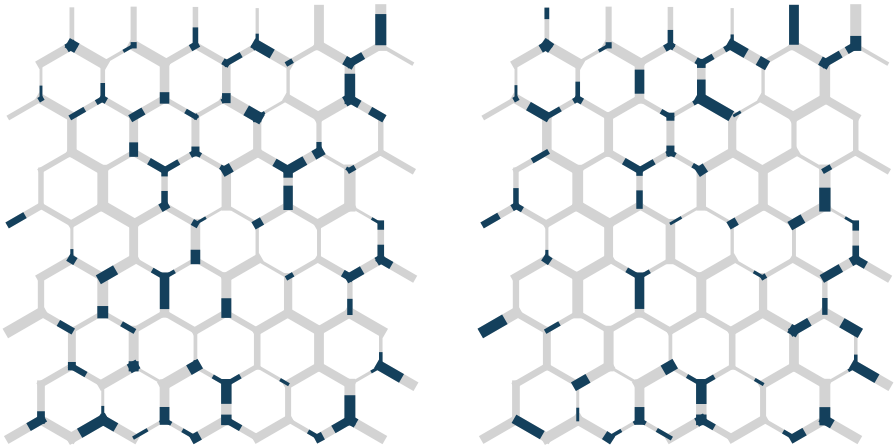

Fig. 9 Example fluid distributions for $S_w = 0.85$, $M = 1$ and $\log_{10}(\Pi) = -0.7$. The time difference between **a** and **b** corresponds to one pore volume of flow. Some interfaces remain stationary, while others are moving. The non-wetting fluid is partially mobilized ($F_w = 0.94$) and moves in droplets or small ganglia. Drawn link widths are chosen for illustrative purposes and are not to scale

In Fig. 9, $\log_{10}(\Pi) = -0.7$ and some interfaces remain stationary while others are moving. The non-wetting fluid is partially mobilized ($F_w = 0.94$) and moves in droplets or small ganglia.

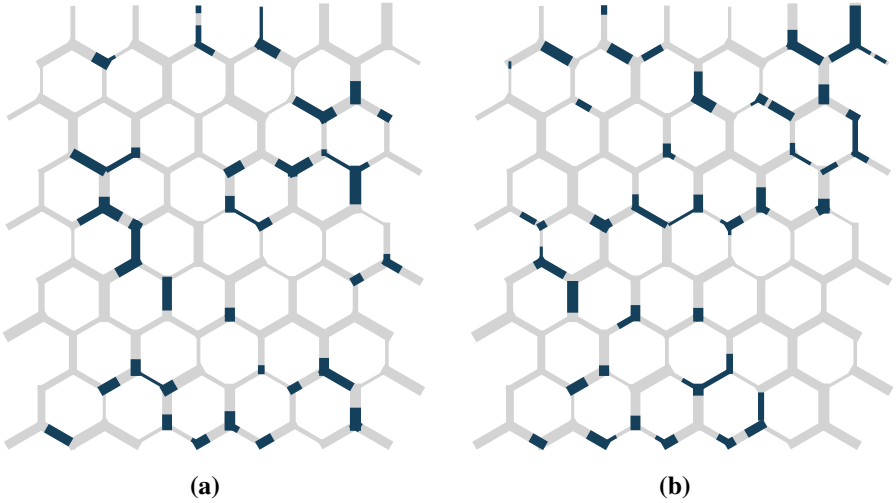

Fig. 10 Example fluid distributions for $S_w = 0.85$, $M = 1$ and $\log_{10}(\Pi) = 1.2$. Non-wetting fluid is blue, and wetting fluid is gray. The time difference between **a** and **b** corresponds to one pore volume of flow. Almost no interfaces remain stationary, and most of the non-wetting fluid is moving through moving droplets or small ganglia. The fractional flow is $F_w = 0.88$. Drawn link widths are chosen for illustrative purposes and are not to scale

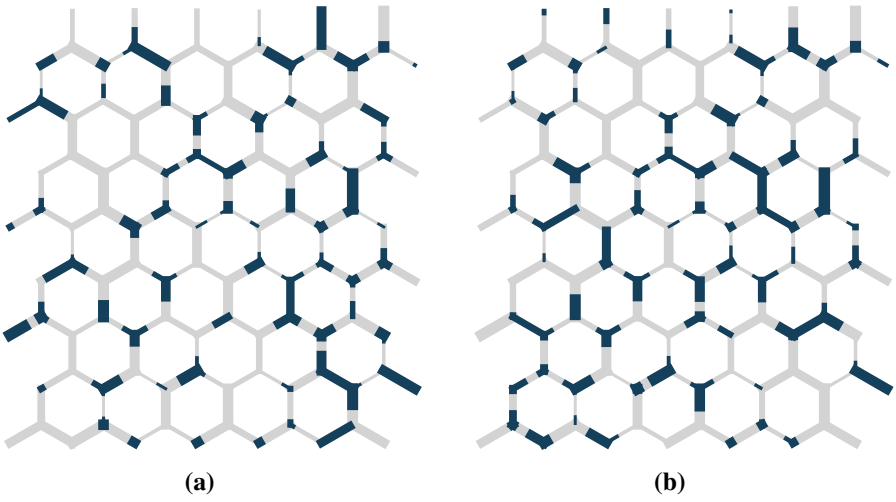

Fig. 11 Example fluid distributions for $S_w = 0.75$, $M = 1$ and $\log_{10}(\Pi) = -1.0$. Non-wetting fluid is blue, and wetting fluid is gray. Some of the non-wetting fluid is mobilized, while some remains stationary. The fractional flow is $F_w = 0.84$. Drawn link widths are chosen for illustrative purposes and are not to scale

In Fig. 10, $\log_{10}(\Pi) = 1.2$ and the system starts to approach the high-Ca limit. Almost no interfaces remain stationary, and most of the non-wetting fluid is moving through droplets or ganglia. The fractional flow is $F_w = 0.88$.

Figure 11 shows example fluid configurations when more non-wetting fluid is introduced, $S_w = 0.75$, while $M = 1$ and the pressure gradient $\log_{10}(\Pi) = -1.0$ is the same as in Fig. 8. As more non-wetting fluid is added, some of it is mobilized, while some remains stationary ($F_w = 0.84$). The non-wetting fluid moves as droplets or small ganglia.

References

Aker, E., Måløy, K.J., Hansen, A.: Simulating temporal evolution of pressure in two-phase flow in porous media. Phys. Rev. E **58**(2), 2217 (1998a). https://doi.org/10.1103/PhysRevE.58.2217

Aker, E., Måløy, K.J., Hansen, A., Batrouni, G.G.: A two-dimensional network simulator for two-phase flow in porous media. Transp. Porous Media **32**(2), 163–186 (1998b). https://doi.org/10.1023/A:1006510106194

Aker, E., Måløy, K.J., Hansen, A., Basak, S.: Burst dynamics during drainage displacements in porous media: simulations and experiments. EPL (Europhys. Lett.) **51**(1), 55 (2000). https://doi.org/10.1209/epl/i2000-00331-2

Armstrong, R.T., McClure, J.E., Berrill, M.A., Rücker, M., Schlüter, S., Berg, S.: Beyond Darcy's law: the role of phase topology and ganglion dynamics for two-fluid flow. Phys. Rev. E **94**(4), 043113 (2016). https://doi.org/10.1103/PhysRevE.94.043113

Avraam, D., Payatakes, A.: Flow regimes and relative permeabilities during steady-state two-phase flow in porous media. J. Fluid Mech. **293**, 207–236 (1995). https://doi.org/10.1017/S0022112095001698

Bardon, C., Longeron, D.G.: Influence of very low interfacial tensions on relative permeability. Soc. Petrol. Eng. J. **20**(05), 391–401 (1980). https://doi.org/10.2118/7609-PA

Bennion, B., Bachu, S.: Relative permeability characteristics for supercritical CO_2 displacing water in a variety of potential sequestration zones. In: SPE Annual Technical Conference and Exhibition, Society of Petroleum Engineers (2005). https://doi.org/10.2118/95547-MS

Datta, S.S., Ramakrishnan, T., Weitz, D.A.: Mobilization of a trapped non-wetting fluid from a three-dimensional porous medium. Phys. Fluids **26**(2), 022002 (2014). https://doi.org/10.1063/1.4866641

Delshad, M.: Measurement of relative permeability and dispersion for micellar fluids in Berea rock. Master's thesis, The University of Texas at Austin (1981)

Erpelding, M., Sinha, S., Tallakstad, K.T., Hansen, A., Flekkøy, E.G., Måløy, K.J.: History independence of steady state in simultaneous two-phase flow through two-dimensional porous media. Phys. Rev. E **88**(5), 053004 (2013). https://doi.org/10.1103/PhysRevE.88.053004

Fulcher, R., Ertekin, T., Stahl, C., et al.: Effect of capillary number and its constituents on two-phase relative permeability curves. J. Petrol. Technol. **37**(02), 249–260 (1985). https://doi.org/10.2118/12170-PA

Gjennestad, M.A., Munkejord, S.T.: Modelling of heat transport in two-phase flow and of mass transfer between phases using the level-set method. Energy Proc. **64**, 53–62 (2015). https://doi.org/10.1016/j.egypro.2015.01.008

Gjennestad, M.A., Vassvik, M., Kjelstrup, S., Hansen, A.: Stable and efficient time integration at low capillary numbers of a dynamic pore network model for immiscible two-phase flow in porous media. Front. Phys. (2018). https://doi.org/10.3389/fphy.2018.00056

Guo, H., Dou, M., Hanqing, W., Wang, F., Yuanyuan, G., Yu, Z., Yansheng, W., Li, Y., et al.: Review of capillary number in chemical enhanced oil recovery. In: SPE Kuwait Oil and Gas Show and Conference, Society of Petroleum Engineers (2015). https://doi.org/10.2118/175172-MS

Hansen, A., Sinha, S., Bedeaux, D., Kjelstrup, S., Gjennestad, M.A., Vassvik, M.: Relations between seepage velocities in immiscible, incompressible two-phase flow in porous media. Transp. Porous Media **125**, 565–587 (2018). https://doi.org/10.1007/s1124

Jettestuen, E., Helland, J.O., Prodanović, M.: A level set method for simulating capillary-controlled displacements at the pore scale with nonzero contact angles. Water Resour. Res. **49**(8), 4645–4661 (2013). https://doi.org/10.1002/wrcr.20334

Knudsen, H.A., Hansen, A.: Relation between pressure and fractional flow in two-phase flow in porous media. Phys. Rev. E **65**(5), 056310 (2002). https://doi.org/10.1103/PhysRevE.65.056310

Knudsen, H.A., Aker, E., Hansen, A.: Bulk flow regimes and fractional flow in 2D porous media by numerical simulations. Transp. Porous Media **47**(1), 99–121 (2002). https://doi.org/10.1023/A:1015039503551

Oak, M.J., Baker, L.E., Thomas, D.C.: Three-phase relative permeability of Berea sandstone. J. Petrol. Technol. **42**(08), 1054–1061 (1990). https://doi.org/10.2118/17370-PA

Raeini, A.Q., Blunt, M.J., Bijeljic, B.: Modelling two-phase flow in porous media at the pore scale using the volume-of-fluid method. J. Comput. Phys. **231**(17), 5653–5668 (2012). https://doi.org/10.1016/j.jcp.2012.04.011

Ramstad, T., Hansen, A.: Cluster evolution in steady-state two-phase flow in porous media. Phys. Rev. E **73**(2), 026306 (2006). https://doi.org/10.1103/PhysRevE.73.026306

Ramstad, T., Idowu, N., Nardi, C., Øren, P.E.: Relative permeability calculations from two-phase flow simulations directly on digital images of porous rocks. Transp. Porous Media **94**, 487–504 (2012). https://doi.org/10.1007/s11242-011-9877-8

Rayleigh, R.: On the question of the stability of the flow of fluids. Lond., Edinb., Dublin Philos. Mag. J. Sci. **34**(206), 59–70 (1892). https://doi.org/10.1080/14786449208620167

Rücker, M., Berg, S., Armstrong, R., Georgiadis, A., Ott, H., Simon, L., Enzmann, F., Kersten, M., de With, S.: The fate of oil clusters during fractional flow: trajectories in the saturation-capillary number space. In: Conference: International Symposium of the Society of Core Analysts , vol. 7 (2015)

Schechter, D.S., Haynes, J.: Relative permeabilities of a near critical binary fluid. Transp. Porous Media **9**(3), 241–260 (1992). https://doi.org/10.1007/BF00611969

Sinha, S., Bender, A.T., Danczyk, M., Keepseagle, K., Prather, C.A., Bray, J.M., Thrane, L.W., Seymour, J.D., Codd, S.L., Hansen, A.: Effective rheology of two-phase flow in three-dimensional porous media: experiment and simulation. Transp. Porous Media **119**(1), 77–94 (2017). https://doi.org/10.1007/s11242-017-0874-4

Sinha, S., Gjennestad, M.A., Vassvik, M., Hansen, A.: A dynamic network simulator for immiscible two-phase flow in porous media (2019a). arXiv:1907.12842

Sinha, S., Gjennestad, M.A., Vassvik, M., Winkler, M., Hansen, A., Flekkøy, E.G.: Rheology of high-capillary number flow in porous media. Front. Phys. (2019b). https://doi.org/10.3389/fphy.2019.00065

Tørå, G., Ramstad, T., Hansen, A.: Anomalous diffusion on clusters in steady-state two-phase flow in porous media in two dimensions. EPL (Europhys. Lett.) **87**(5), 54002 (2009). https://doi.org/10.1209/0295-5075/87/54002

Tørå, G., Øren, P.E., Hansen, A.: A dynamic network model for two-phase flow in porous media. Transp. Porous Media **92**(1), 145–164 (2012). https://doi.org/10.1007/s11242-011-9895-6

Whitson, C.H., Fevang, Ø., Sævareid, A.: Gas condensate relative permeability for well calculations. Transp. Porous Media **52**(2), 279–311 (2003). https://doi.org/10.1023/A:1023539527573

Zhao, B., MacMinn, C.W., Primkulov, B.K., Chen, Y., Valocchi, A.J., Zhao, J., Kang, Q., Bruning, K., McClure, J.E., Miller, C.T., Fakhari, A., Bolster, D., Hiller, T., Brinkmann, M., Cueto-Felgueroso, L., Cogswell, D.A., Verma, R., Prodanović, M., Maes, J., Geiger, S., Vassvik, M., Hansen, A., Segre, E., Holtzman, R., Yang, Z., Yuan, C., Chareyre, B., Juanes, R.: Comprehensive comparison of pore-scale models for multiphase flow in porous media. Proc. Nat. Acad. Sci. **116**(28), 13799–13806 (2019). https://doi.org/10.1073/pnas.1901619116